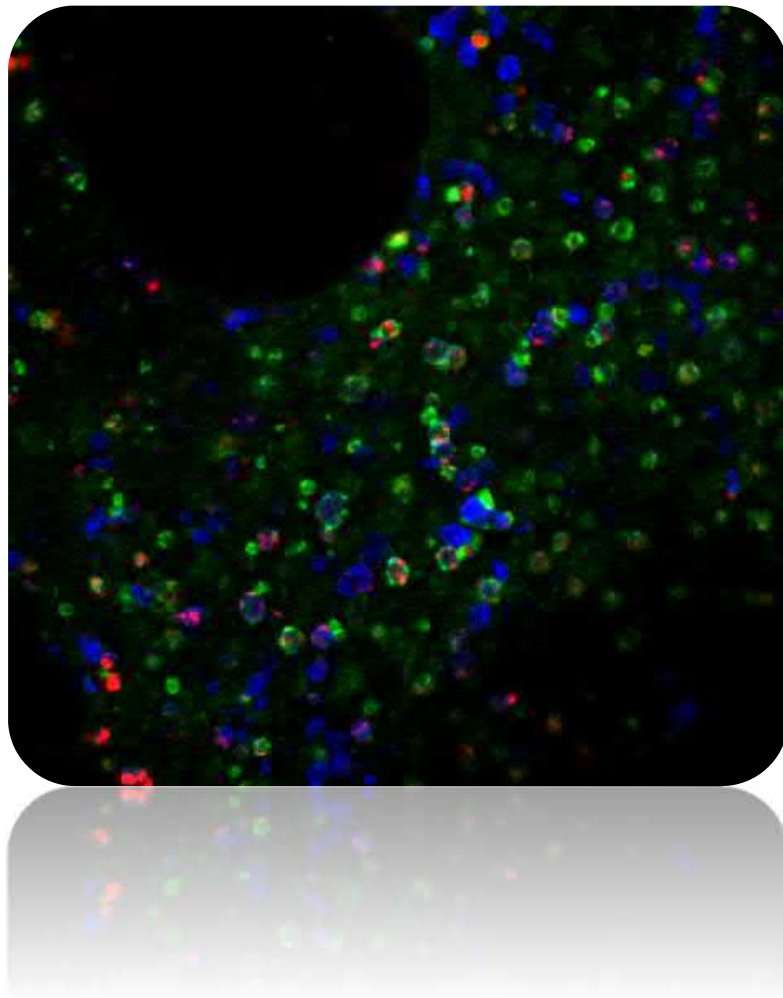


Intracellular trafficking of polymeric nanocarriers in eukaryotic cells with emphasis on transcytotic processes

Doctoral thesis

Jonas Reinholz

Max Planck Institute for Polymer Research, Mainz





MAX-PLANCK-GESELLSCHAFT

JOHANNES GUTENBERG
UNIVERSITÄT MAINZ



Intracellular trafficking of polymeric nanocarriers in eukaryotic cells with emphasis on transcytotic processes

Dissertation

In fulfillment of the requirements for the degree of

Doktor rerum naturalium (**Dr. rer. nat**)

Submitted to

THE FACULTY OF BIOLOGY

JOHANNES GUTENBERG UNIVERSITY, MAINZ

This doctoral thesis has been carried out at the

MAX PLANCK INSTITUTE FOR POLYMER RESEARCH, MAINZ

Jonas Reinholz

Born on 13 October 1988 in Mainz, Germany

Mainz, 2018

Dean: Prof. Dr. Walter Stöcker

1. Reviewer: Prof Dr. Volker Mailänder

Physical Chemistry of Polymers

Max Planck Institute for Polymer Research, Mainz

2. Reviewer: PD Dr. Joachim Urban

Institute of Genetics

Johannes Gutenberg-University, Mainz

Table of contents

I	Abbreviations.....	vii
II	List of Figures.....	xi
III	List of Tables.....	xiv
IV	Abstract.....	xv
V	Deutscher Abstract.....	xvi
1	Introduction	1
1.1	Introduction into nanomedicine	1
1.2	Why do we need oral drug delivery via nanocarriers?.....	2
1.3	Natural barriers of the human body and their implications for oral drug delivery via nanocarriers	5
1.4	Endocytosis in epi- and endothelial cells	8
1.5	Transcytosis of nanomaterials.....	11
1.6	Exocytosis of nanomaterials	14
1.7	Dendritic cells and nanoparticle induced vaccination.....	18
1.8	Next Generation Sequencing and RNA-Seq	19
1.9	Aims	24
2	Materials and Methods	25
2.1	Materials.....	25
2.1.1	Chemicals and buffers	25
2.1.2	Media and sera.....	28
2.1.3	Consumables and kits.....	29
2.1.4	Enzymes	31
2.1.5	Pharmacological inhibitors.....	31
2.1.6	Nanoparticles	32

TABLE OF CONTENTS

2.1.7	Primers.....	33
2.1.8	Plasmids.....	36
2.1.9	Bacteria.....	36
2.1.10	Cell lines.....	36
2.1.11	Instruments	37
2.1.12	Software and bioinformatics	39
2.2	Methods.....	40
2.2.1	Cell culture techniques	40
2.2.2	Nanoparticle synthesis.....	41
2.2.3	Zeta potential and size determination of nanoparticles	42
2.2.4	Nanoparticle filtration	42
2.2.5	Cell viability assays.....	43
2.2.6	Endotoxin determination	44
2.2.7	In vitro Transcytosis Assay	45
2.2.8	Adjustment of the pH value in DMEM.....	46
2.2.9	RNA extraction.....	46
2.2.10	cDNA synthesis	47
2.2.11	Quantification of nucleic acids.....	48
2.2.12	Primer design.....	48
2.2.13	Polymerase chain reaction.....	49
2.2.14	Agarose gel electrophoresis.....	50
2.2.15	DNA extraction from agarose gels	50
2.2.16	DNA restriction	51
2.2.17	In-Fusion® HD Cloning.....	52
2.2.18	Heat shock transformation.....	52
2.2.19	Colony PCR.....	53
2.2.20	Plasmid isolation	53

2.2.21	Sanger Sequencing	54
2.2.22	Generation of lentiviral particles	54
2.2.23	Stable transduction of eGFP-/ ZsGreen- and mCherry-tagged proteins ...	55
2.2.24	Fluorescence microscopy	55
2.2.25	Transient transfection	56
2.2.26	Fluorescence spectroscopy	56
2.2.27	Lentiviral titer detection	56
2.2.28	Confocal laser scanning microscopy	57
2.2.29	Cell fixation.....	57
2.2.30	Cell membrane staining.....	57
2.2.31	Quantification of co-localization.....	58
2.2.32	Automatic quantification via Fiji script.....	59
2.2.33	Cryo high pressure freezing transmission electron microscopy.....	62
2.2.34	Super-resolution Microscopy	63
2.2.35	Nanoparticle treatment of cells.....	64
2.2.36	Desorption of proteins from nanoparticles	64
2.2.37	Flow cytometry.....	65
2.2.38	SDS-PAGE.....	66
2.2.39	Determination of protein concentrations	66
2.2.40	Nanoparticle functionalization	67
2.2.41	Generation of BMDCs.....	67
2.2.42	Quantitative real time polymerase chain reaction	67
2.2.43	Statistical analysis	69
2.2.44	Preparation of RNA-Seq samples.....	69
2.2.45	Illumina Sequencing.....	69
2.2.46	Quantification of NGS data sets	70
2.2.47	Pathway analysis	71

3	Results and discussion.....	72
3.1	Endocytosis and Transcytosis of PS-NP in Caco-2 cells	72
3.1.1	Caco-2 cells establishing a cellular monolayer	72
3.1.2	Cytotoxicity of different nanoparticle systems	75
3.1.3	Nanoparticle uptake in Caco-2 cells.....	77
3.1.4	Nanoparticle uptake in transwell system.....	80
3.1.5	Nanoparticle transcytosis in transwell system.....	81
3.1.6	Uptake of differently charged nanoparticles	83
3.1.7	Transcytosis of differently charged and sized nanoparticles.....	84
3.1.8	Effect of apical pH value on transcytosis.....	86
3.1.9	Nanoparticle coatings	87
3.1.10	Transcytosis efficiencies of different coated PS-NP	90
3.1.11	Obstacles of transcytosis determination	92
3.2	Intracellular trafficking of polystyrene nanoparticles in Caco-2 cells	97
3.2.1	Mass spectrometry analysis of transcytosed nanoparticles	97
3.2.2	RNA extractions from Caco-2 cells	101
3.2.3	Amplification of different cDNAs	102
3.2.4	Generation of fluorescent lentiviral vectors	104
3.2.5	Co-Localization analysis of nanoparticle-treated Caco-2 cells.....	107
3.2.6	Lysosomes as final fate for nanocarriers.....	111
3.2.7	Trafficking profiles were established	115
3.2.8	Double transgenic cell lines confirm trafficking profiles.....	121
3.3	Transcriptomic analysis of dendritic cells after nanoparticle addition	125
3.3.1	RNA extractions of bone marrow derived dendritic cells.....	126
3.3.2	Next Generation Sequencing of ovalbumin nanocapsule-treated dendritic cells.....	129
3.3.3	NGS results were partially confirmed via qPCR.....	134

3.3.4	Pathway reconstruction after ovalbumin nanocapsule treatment	137
4	Summary and conclusion	140
5	Deutsche Zusammenfassung	143
6	Bibliography	147
7	Supplementary data	177
7.1	NICOMP Distribution	177
7.2	Zeta potential analysis	179
7.3	Fluorescent dyes	180
7.4	Toxicity tests	182
7.5	Determination of endotoxin contaminations	183
7.6	Calibration curves	184
7.7	Transcytosis in different transwell plates	185
7.8	Transcytosis of differently charged SDS-stabilized nanoparticles	186
7.9	Endocytosis inhibition by various pharmacological inhibitors	187
7.10	Choice of Rab3a as representative for the Rab3 family	187
7.11	Amplification of putative transcytosis relevant cDNAs	188
7.12	Vector maps	189
7.13	Analysis of potential bleed through	194
7.14	Close-ups of co-localization studies	196
7.15	Nanoparticle treatment on transwell filters	209
7.16	GSD Microscopy	211
7.17	Double transgenic cells	214
7.18	Fiji analysis	217
7.19	Double transgenic cells without nanoparticles	221
7.20	Scanning electron microscopy	226
7.21	Nanoparticles in cell culture medium	228

TABLE OF CONTENTS

7.22	Proposed KEGG-pathways of downregulated genes after ovalbumin-nanocapsule treatment.....	229
8	Curriculum vitae	230
9	Publications.....	231
10	Affidavit.....	232
11	Acknowledgements.....	233

I Abbreviations

°C	Degree Celsius
μg	Microgram
μl	Microliter
μm	Micrometer
μmol	Micromole
A	Adenine
A5	Annexin V
AA	Amino acid
Bp	Base pair
BSA	Bovine serum albumin
C	Cytosine
Ca	Calcium
Caco-2	Human epithelial colorectal adenocarcinoma cells
Cav1	Caveolin-1
CD	Cluster of differentiation
cDNA	Complementary DNA
CDS	Coding sequence
CHAPS	3-[(3-Cholamidopropyl)dimethylammonio]-1-propanesulfonate
cLSM	Confocal laser scanning microscopy
CME	Clathrin-mediated endocytosis
CO ₂	Carbon dioxide
COOH	Carboxylic acid
Cpne1	Copine-1
CPP	Cell penetrating peptide
Cyt D	Cytochalasin D
Da	Dalton
DC	Dendritic cell
DLS	Dynamic light scattering
DMEM	Dulbecco's Modified Eagle Medium
DMSO	Dimethyl sulfoxide
IFU	Infectious units
DNA	Deoxyribonucleic acid
dNTP	Deoxynucleotide
DTT	Dithiothreitol
<i>E.coli</i>	Escherichia coli
e.g.	exempli gratia
EDTA	Ethylenediaminetetraacetic acid
eGFP	Enhanced green fluorescent protein
EIPA	5-(N-Ethyl-N-isopropyl)amiloride
EMEM	Eagle's Minimum Essential Medium
MHC	Major histocompatibility complex

ABBREVIATIONS

ER	Endoplasmic reticulum
et al.	Et alia; and others
EtOH	Ethanol
Exoc1	Exocyst Complex Component 1
FDA	Food and Drug Administration
FAE	Follicular-associated epithelium
FBS	Fetal bovine serum
Fc	Fragment crystallizable
FCS	Fetal calf serum
FDA	Food and drug administration
Fig	Figure
Flot1	Flotillin-1
F-Primer	Forward-Primer
g	Standard gravity; gram
G	Guanine
GAPDH	Glyceraldehyde 3-phosphate dehydrogenase
GFP	Green fluorescent protein
GI tract	Gastrointestinal tract
Gln	L-glutamine
GOTERM	Gene ontology term
GSD	Ground state depletion
h	Hour
H ₂ O	Water
HBSS	Hank's Balanced Salt Solution
HeLa	Human cervix carcinoma cells
HIV-1	Human immunodeficiency virus 1
HPLC	High-performance liquid chromatography
HSA	Human serum albumin
IgG	Immunoglobulin G
kb	Kilobase
kg	Kilogram
Lamp	Lysosomal-associated membrane protein
LC-MS	Liquid-chromatography mass-spectrometry
M	Mol/l
MFI	Median fluorescence intensity
MDP	Muramyl dipeptide
Mg	Magnesium
mg	Milligram
MHC	Major histocompatibility complex
min	Minute
mL	Milliliter
Mm	Millimeter
mmol	Millimole
mRNA	Messenger ribonucleic acid

MS	Mass spectrometry
CTMA-Cl	Cetyltrimethylammonium chloride
MTT	3-(4,5-dimethylthiazol-2-yl)-2,5-diphenyltetrazolium bromide
MVB	Multivesicular body
N	Nucleotide
n. d.	not determined
MES	2-(N-morpholino)ethanesulfonic acid
n. a.	not available
n. s.	not significant
NaCl	Sodium chloride
NC	Nanocapsule
NCBI	National Center for Biotechnology Information
ng	Nanogram
NGS	Next Generation Sequencing
NH ₂	Amine group
nm	Nanometer
nm	nanometer
NP	Nanoparticle
nt	Nucleotide
HEK	Human embryonic kidney
OH	Hydroxy group
Ova-NC	Ovalbumin nanocapsules
P/S	Penicillin/Streptomycin
PBS	Phosphate-buffered saline
PC	Polycarbonate
PCR	Polymerase Chain Reaction
PEG	Polyethylene glycol
PI	Propidium iodide
MWCO	Molecular weight cut-off
PLGA	Poly(lactic-co-glycolic)
PLLA	Poly-L-Lactide
PMT	Photomultiplier
PNP	Polymeric nanoparticles
ppm	Parts per million
PS	Polystyrene
PS-NP	Polystyrene nanoparticles
qRT-PCR	Quantitative real time PCR
Rab	Ras-related in brain
Rac1	Ras-related C3 botulinum toxin substrate 1
RFP	Red fluorescent protein
RFU	Relative fluorescent units
RhoB	Ras homolog family member B
RNA	Ribonucleic acid

ABBREVIATIONS

rpm	Rounds per minute
R-Primer	Reverse-Primer
rRNA	Ribosomal ribonucleic acid
SD	Standard deviation
SDS	Sodium dodecyl sulfate
SDS-PAGE	SDS polyacrylamide gel electrophoresis
sec	Second
R848	Resiquimod
RPKM	Reads per kilobase per million mapped reads
SEM	Scanning electron microscopy
Seq	Sequencing
Exc	Excitation
Em	Emission
siRNA	Small interfering RNA
SNP	Single Nucleotide Polymorphism
SPIONs	Superparamagnetic iron oxide nanoparticles
SR	Super-resolution
T	Thymine
Tab	Table
TEER	Transepithelial electrical resistance
TEM	Transmission electron microscopy
TGN	Trans-Golgi network
T _m	Melting temperature
tRNA	Transfer ribonucleic acid
Tub	Tubulin
U	Unit
HCl	Hydrochloric acid
abs	Absolute
NaOH	Sodium hydroxide
PEI	Polyethylenimine
TAE	Tris Acetate-EDTA
UV	Ultraviolet
V	Volt
W	Watt
BMDC	Bone marrow-derived (dendritic) cell
WGA	Wheat germ agglutinin

II List of Figures

Fig. 1: Anatomy of the small intestine and the implications for orally applied nanocarriers.	6
Fig. 2: Transcytosis of 12 nm human serum albumin–gold nanoparticles across a hCMEC/D3 endothelial cell monolayer.	13
Fig. 3: Putative pathways for endo-/ trans- and exocytosis of P22NPs in Caco-2 cells. ...	17
Fig. 4: Historical sequencing cost per human genome.....	20
Fig. 5: Next Generation Sequencing via the Illumina Sequencing principle.	22
Fig. 6: Preparation of Caco-2 cells on transwell Filters.....	45
Fig. 7: Analysis of co-localization: Time Scheme.	58
Fig. 8: Caco-2 cells forming a monolayer.....	73
Fig. 9: Comparison of TEER values of Caco-2 cell layers grown on different transwell materials.	74
Fig. 10: Surface structure of a polycarbonate membrane with 3 μm pores.	75
Fig. 11: Toxicity tests of nanoparticle treated Caco-2 cells.....	76
Fig. 12: Cellular uptake of nanoparticles in Caco-2 cells determined by flow cytometry. 77	
Fig. 13: Cellular uptake of carboxylated polystyrene nanoparticles in Caco-2 cells.....	78
Fig. 14: Cellular uptake of aminated polystyrene nanoparticles in Caco-2 cells.....	79
Fig. 15: Prevention of nanoparticle aggregation in cell culture medium.	79
Fig. 16: Uptake of polystyrene nanoparticles in transwell system.....	80
Fig. 17: Development of TEER values before and after nanoparticle addition.	81
Fig. 18: Transcytosis of carboxylated polystyrene nanoparticles in different concentrations.....	82
Fig. 19: Uptake of differently charged lutensol-stabilized polystyrene nanoparticles.....	83
Fig. 20: Transcytosis of differently charged lutensol-stabilized nanoparticles.....	85
Fig. 21: Transcytosis of differently sized carboxylated SDS-stabilized polystyrene nanoparticles.....	86
Fig. 22: Transcytosis rate of polystyrene nanoparticles in different apical pH media.....	87
Fig. 23: Analysis of FC fragment adsorption on lutensol-stabilized nanoparticles via SDS-Page.	89
Fig. 24: Analysis of FC fragment adsorption on lutensol-stabilized nanoparticles via Pierce Assay.	89

Fig. 25: Transcytosis rate of FC-functionalized polystyrene nanoparticles.....	91
Fig. 26: Transcytosis rate of Vitamin B ₁₂ -functionalized polystyrene nanoparticles.	92
Fig. 27: Apical view of Caco-2 cells incubated with nanoparticles in transwell system..	94
Fig. 28: Central view of Caco-2 cells incubated with nanoparticles in transwell system..	95
Fig. 29: Basal view of Caco-2 cells incubated with nanoparticles in transwell system....	96
Fig. 30: SDS Page of nanoparticle treated Caco-2 cells and protein/nanoparticle containing basal transwell medium.	98
Fig. 31: Mass spectrometry analysis of basal cell culture medium after nanoparticle addition.....	99
Fig. 32: RNA Extraction from Caco-2 cells.....	101
Fig. 33: Amplification of putative trafficking relevant cDNAs via polymerase chain reaction.	102
Fig. 34: Test restriction of recombinant ZsGreen plasmids.	103
Fig. 35: HEK293-T cells producing lentiviral particles.....	104
Fig. 36: Lentiviral flash test.	105
Fig. 37: Determination of transgenic stability.....	106
Fig. 38: Co-Localization of polystyrene nanoparticles with different GFP-tagged proteins.	108
Fig. 39: Live Cell Imaging of nanoparticle trafficking.	109
Fig. 40: Localization of Rab3a and polystyrene nanoparticles on transwell filters.	110
Fig. 41: Visualization of polystyrene nanoparticles trapped in vesicles in Caco-2 cells.	113
Fig. 42: Polystyrene nanoparticles in undefined vesicles.....	114
Fig. 43: Kinetic uptake of nanoparticles in Rab5a-positive Caco-2 cells.	116
Fig. 44: Kinetic uptake of nanoparticles in Rab7a-positive Caco-2 cells.	117
Fig. 45: Comparison of manually counted vs Fiji Script determined NP co-localization with Rab5a.....	118
Fig. 46: Comparison of manually counted vs Fiji Script determined NP co-localization with Rab7a.....	118
Fig. 47: Co-Localization profiles of nanoparticles with different endolysosomal and putative exo- and transcytotic marker proteins.	120
Fig. 48: Co-localization of polystyrene nanoparticles with GFP- or mCherry-tagged proteins.	122
Fig. 49: Intracellular localization of Cpne1 and Rab7a.....	123

Fig. 50: Pathway hypothesis for the intracellular trafficking of polystyrene nanoparticles in Caco-2 cells.	124
Fig. 51: RNA Extraction of (Ovalbumin nanocapsule-treated) BMDCs.	126
Fig. 52: Quality control of total RNA extractions via agarose gelelectrophoresis.....	127
Fig. 53: Analysis of total RNA quality for Next Generation Sequencing.....	128
Fig. 54: Evaluation of Next Generation Sequencing reads via Geneious R8.....	129
Fig. 55: Mapping of paired end reads against the murine reference sequence.	130
Fig. 56: Expression analysis of (Adj-Ovalbumin nanocapsule-treated) BMDCs.	131
Fig. 57: Scatter plots of expression differences in BMDCs.....	133
Fig. 58: Comparison of upregulated genes determined via qPCR and NGS.	135
Fig. 59: Comparison of downregulated or housekeeping genes determined via qPCR and NGS.....	136
Fig. 60: Proposed KEGG-pathways of upregulated genes.....	138
Fig. 61: Antigen processing and presentation pathway.....	139

III List of Tables

Tab. 1: Chemicals and buffers.....	25
Tab. 2: Media and sera	28
Tab. 3: Consumables and kits.....	29
Tab. 4: Enzymes	31
Tab. 5: Pharmacological inhibitors	31
Tab. 6: Nanoparticles	32
Tab. 7: Primers	33
Tab. 8: Plasmids	36
Tab. 9: Instruments.....	37
Tab. 10: Software and bioinformatics	39
Tab. 11: Standard cDNA synthesis protocol	47
Tab. 12: Standard PCR program	49
Tab. 13: Quantitative real time polymerase chain reaction protocol	68

IV Abstract

The broad field of nanotechnology offers a lot of different materials for a sheer infinite number of applications. Since every nanomaterial is unique, interactions with eukaryotic cells need to be thoroughly evaluated. In the present thesis, polymeric nanoparticles are analyzed for their intracellular impacts and respective pathways to gain insight into the opportunities for the nanoparticle usage in the field of nanomedicine.

The first part of the thesis deals with the potential use of nanoparticles for oral drug delivery. The oral application of pharmaceuticals is unarguably the most convenient method of application. Especially for protein- or peptide-based drugs, however, the effectiveness is significantly reduced due to enzymatic digestion in the stomach as well as a poor bioavailability in the small intestine. For these difficult formulations, the encapsulation into nanocarriers would protect the sensitive drug and thus could considerably improve the efficiency of oral drug delivery. However, before the cargo can be released, the nanocarrier needs to cross multiple barriers of the human body. The mechanisms behind the process of transcytosis are up to now not fully understood. In this thesis, all kind of physicochemical parameters are scanned for their influence on the rate of nanoparticle transcytosis through Caco-2 cells. This includes different charges, sizes, pH values and functionalizations on the nanoparticle surface. In addition, a combination of mass spectrometry, confocal laser scanning microscopy and transmission electron microscopy is used to identify potential key proteins involved in transcytosis. Elaborate co-localization studies with GFP- and/or mCherry-tagged proteins give a detailed overview, where the nanoparticles exactly are trafficked at which time point of incubation. The trafficking data is finally confirmed via the use of double transgenic cell lines and a pathway hypothesis for successful transcytosis is established.

The second part of the thesis deals with question if nanomaterials can also have an impact on mRNA level after uptake. For this purpose, bone marrow derived dendritic cells are chosen as a cell type which should react rapidly and strongly to foreign material. Cells are treated with protein-based ovalbumin nanocapsules. These were either unfilled or filled with the adjuvants resiquimod and muramyl dipeptide, which are supposed to trigger an immune response from the cell. The RNA is extracted and the whole transcriptome is analyzed via Next Generation Sequencing. The mRNA expression levels of nanocapsule-treated vs. untreated cells are subsequently quantified via bioinformatic methods and finally pathways of up- and downregulated genes are investigated.

V Deutscher Abstract

Das breite Feld der Nanotechnologie bietet eine Vielzahl verschiedener Materialien für eine schier unendliche Anzahl an Verwendungsmöglichkeiten. Da jedes Nanomaterial einzigartig ist, müssen Interaktionen mit eukaryotischen Zellen jedoch sorgsam evaluiert werden. In der vorliegenden Arbeit werden polymere Nanopartikel auf ihre intrazellulären Auswirkungen und Pathways untersucht, um Erkenntnisse über die Verwendung von Nanopartikeln für das Forschungsfeld der Nanomedizin zu gewinnen.

Der erste Part der Dissertation beschäftigt sich mit der potentiellen Verwendung von polymeren Nanopartikeln für die orale Medikamentenverabreichung, welche zweifelsohne die angenehmste Applikationsmöglichkeit darstellt. Für Protein- oder Peptid-basierte Medikamente ist die Effizienz des oral applizierten Wirkstoffs aufgrund des enzymalen Abbaus im Magen-Darm-Trakt stark reduziert. Für solche Medikamente könnte die Einkapsulierung in Nanoträgern zu einem Schutz des sensiblen Wirkstoffs führen und somit die Effizienz der oralen Medikamentenverabreichung verbessern. Bevor der Wirkstoff im Blut oder in der Zielzelle freigesetzt werden kann, muss der Nanoträger jedoch mehrere Barrieren des menschlichen Körpers überwinden. Die Mechanismen der Transzytose von Nanoträgern sind bis heute nicht komplett aufgeklärt. In der vorliegenden Dissertation werden verschiedene physikochemische Parameter untersucht, welche die Transzytose von Nanoträgern beeinflussen. Zusätzlich wird eine Kombination der Massenspektrometrie, konfokaler Laserscanningmikroskopie und Transmissionselektronenmikroskopie dazu verwendet, potentielle Schlüsselproteine für die Transzytose zu detektieren. Ausführliche Kollokalisationsstudien der Nanoträger mit GFP- oder mCherry-gekoppelten Markerproteinen geben einen detaillierten Überblick darüber, wo sich die Nanoträger zu bestimmten Zeitpunkten innerhalb von Caco-2 Zellen befinden. Die Daten des intrazellulären Traffickings werden anschließend mit doppeltransgenen Caco-2 Zellen bestätigt und eine Pathway Hypothese für die Transzytose postuliert.

Der zweite Part der Dissertation beschäftigt sich mit der Frage, ob Nanoträger auch einen Einfluss auf mRNA Ebene haben können. Dazu werden dendritische Zellen verwendet, da dieser Zelltyp schnell und stark auf zellfremdes Material reagieren sollte. Die Zellen werden mit Protein-basierten Ovalbumin Nanokapseln behandelt. Diese sind entweder unbefüllt oder mit den Adjuvantien R848 und MDP beladen, welche eine Immunantwort auslösen sollen. Die RNA wird extrahiert und das Transkriptom mittels Next Generation Sequencing analysiert. Anschließend wird die mRNA Expression von Nanokapsel-behandelten und unbehandelten Zellen mittels bioinformatischer Methoden verglichen und hoch- und runterregulierte intrazelluläre Pathways untersucht.

1 Introduction¹

1.1 Introduction into nanomedicine

Nanotechnology has evolved into one of the most extensive research fields. During the last decades, research and industrial development of nanomaterials have greatly increased and improved. Due to the complexity of research subfields, many definitions of the term “nanomaterial” can be found in the literature. The Official Journal of the European Union (2011/696/EU) inter alia gives the following definition: “Nanomaterial means a natural, incidental or manufactured material containing particles, in an unbound state or as an aggregate or as an agglomerate and where, for 50 % or more of the particles in the number size distribution, one or more external dimensions is in the size range 1 nm-100 nm”[1]. One of the major research subfields of nanotechnology is nanomedicine, which certainly attracted attention in the recent years. Nanomedicines may be broadly defined as either nanoscale ($< 1 \mu\text{m}$) imaging agents or therapeutic agents that lead to a systematic enhancement, protection, controlled release, precise targeting or less cytotoxicity of a drug. After years of development, in 1995 the first nanomedicine, liposomal doxorubicin (DOXIL, Janssen Products), was approved by the FDA[2]. Since then, the range of different nanomedicines has been considerably expanded. In 2016, there were already 51 FDA-approved nanomedicines available and 77 nanomedical products in clinical trials[3]. Currently, the most clinically relevant nanomedicines are liposomes as well as protein based, polymeric/micelle-based, iron-oxid, silica and gold nanoparticle formulations[3, 4]. Although many nanoparticle therapeutics are designed for the treatment of cancer[5], this is by far not the only intended field of application. Nanobiotechnology offers the unique possibility to tailor materials specific for diverse applications by manipulating and combining physicochemical and biological properties. In this thesis, two different nanoparticle systems will be used and investigated. The first one, polystyrene nanoparticles (PS-NP), have no significant relevance for in vivo drug delivery due to the fact that they are

¹ Parts of the following chapter were already published and are republished in this thesis with permission of:

Taylor & Francis Group, *The challenges of oral drug delivery via nanocarriers*, Reinholz J, Landfester K, Mailänder V, Drug delivery, 2018, DOI: 10.1080/10717544.2018.1501119.

non-biodegradable. However, they mark an optimal nanoparticle model system since they can be rather easily synthesized, size-adjusted and decorated with different surface functionalizations[6]. The second one, ovalbumin nanocapsules (Ova-NC), are an example for nanomaterials entirely made from proteins. The advantage of such a system is the fact that proteins can be easily degraded respectively cleaved by enzymes[7] to release the encapsulated cargo. However, protein-based nanoparticles are significantly harder to reliably and reproducibly synthesize compared to the PS-NP model system. The power of nanomedicine in general is limited by cellular responses to the respective nanomaterial. Thus, it is essential to identify associated nanoparticle-cell interactions, toxicity and last but not least intracellular pathways.

1.2 Why do we need oral drug delivery via nanocarriers?

For the majority of people worldwide, the oral administration of pharmaceuticals is the preferred method of application. Despite the obvious advantage of being pain free, it also offers the feature of being noninvasive and overall convenient to handle. Taking the pharmaceutical market of Germany as an example, in 2017 120,257 of 163,478 (74%) drugs were available for the peroral application[8]. This includes several types of tablets, powders, granulates, drops and syrups.

However, the oral dosage form also has several drawbacks. Before the orally applied drug is able to reach its target, in most instances it needs to overcome multiple compartments of the human body, which is challenging for a broad spectrum of pharmaceuticals, especially for protein- or peptide-based ones. In general, the first major challenge for the drug after ingestion is surviving the harsh acidic pH-value in the stomach. In addition, the proteases pepsin and cathepsin start to digest proteins into peptides. Once the drug surpasses the stomach and enters the small intestine via the duodenum, it faces the major enzymatic digestion machinery of the human body. Oligosaccharides and maltose are degraded into glucose, fructose, galactose and mannose via sucrase, maltase and lactase. Lipids are cleaved into glycerol and fatty acids via the pancreatic triacylglycerol lipase and carboxyl ester lipase. Peptides are digested into amino acids via trypsin, chymotrypsin, carboxypeptidase, dipeptidase and aminopeptidase.

Upon surviving these two major locations of digestion in the human body, the drug needs to be absorbed primarily via enterocytes in the small intestine to reach the bloodstream. Up to now, many pharmaceuticals exhibit a fairly low resorption rate, resulting in a poor bioavailability[9], while most of the pharmaceuticals are not even considered further if they cannot cross the intestinal barrier.

Thus, preventing the drug from degradation and enhancing the absorption rate in the small intestine highly improves the impact of orally applied pharmaceuticals. Up to now, many drugs are fabricated with an enteric coating. This coating mostly consists of a polymeric layer, which is stable at low pH values and therefore protects the active ingredient from dissolving in the stomach and thereby getting degraded or inactivated in the low-pH surrounding of the stomach. Upon reaching the rather alkaline pH milieu in the small intestine, the enteric coating breaks down and the drug gets accessible. At this point, it can either have the desired effect directly in the small intestine or get absorbed via microvilli and transported into the bloodstream, from where it can reach its target cells. Nevertheless, even with such a coating many pharmaceuticals still exhibit a poor or even no bioavailability via the oral administration. A prominent example for this problem is the peptide hormone insulin, which is crucial for the glucose absorption from blood. If a patient is suffering from insulin-dependent types of diabetes mellitus, he or she needs to regulate his blood sugar levels via subcutaneous injections of insulin multiple times each day. For millions of people worldwide living with diabetes mellitus (422 million in 2014[10]), an oral dosage form of insulin would significantly increase the quality of life. Up to now, however, there is no orally applied insulin available since the majority of the peptide hormone gets degraded via proteases before it can reach the target cells.

One of the most promising approaches to overcome the aforementioned obstacles for oral drug delivery is the employment of nanomedicines. For oral drug delivery, especially the encapsulation or complexation of a drug into nanomaterials is relevant. The result, a nanocarrier, is ideally able to 1. protect the drug from the harsh conditions in stomach and intestine, 2. increase the intestinal absorption into the bloodstream, 3. target specific cells in the human body and 4. guarantee a controlled release inside the target cells.

In contrast to the fact that most of the drugs worldwide get manufactured for the oral application, nearly all of the FDA-approved nanomedicines are dependent on intravenous injection. Up to date, there is no FDA-approved nanocarrier designed specifically for oral drug delivery. There are, however, several in vivo animal studies that show an increased bio

availability of encapsulated or complexed drugs after oral administration. For example, the complexation of daidzein into lipid nanocarriers and subsequent oral administration yielded an increase of bioavailable daidzein in the blood by at least 10-fold over the oral administration of free daidzein in rat studies[11]. The encapsulation of insulin into (chitosan-coated) solid lipid nanoparticles resulted in a major boost in relative pharmacological bioavailabilities of 8% (uncoated) and 17% (chitosan-coated) of insulin in rats[12]. The oral bioavailability of probucol, a lipophilic drug, could be increased by approximately 10-fold after incorporation into a porous starch based self-assembled nano-delivery system in rat experiments[13].

Nevertheless, the discrepancy between a high number of examined nanocarriers in animal studies and the absence of FDA-approved nanocarriers for oral drug delivery indicates major difficulties in the development of such carrier systems for the human body. Thus, further research has to be carried out in order to get behind the exact intracellular mechanisms of nanocarrier transport.

1.3 Natural barriers of the human body and their implications for oral drug delivery via nanocarriers

The major obstacle for oral drug delivery via nanocarriers is the fact that the nanocarrier needs to cross several natural barriers of the human body before the incorporated drug can reach the target cell. Once being ingested, the nanomaterial will protect the drug from the acidic milieu and the proteolytic “thunderstorm” in the stomach. After leaving the stomach, the nanocarrier enters the small intestine and is transported along the duodenum, jejunum and ileum (Fig. 1). Here, either the cargo needs to be released for intestinal absorption or the nanocarrier itself needs to be taken up. Otherwise, the nanocarrier will inevitably be withdrawn from the human body, since the colon does not have the capacity to absorb solid materials. While the small intestine is adsorbing the nutrients, the colon afterwards solely reduces the amount of water in the feces. Following this uptake in the small intestine, the nanocarrier needs to traverse the layer of epithelial cells to reach the lamina propria. From there on, the next obstacle is a layer of endothelial cells, which the nanocarrier needs to transverse in order to reach the lumen of the blood vessel. Once the nanocarrier enters the bloodstream, there are two possibilities. Either the drug can be directly released into the blood stream or further transported to a target cell. However, the second possibility bears two additional barriers – the traversal through endothelial cells to exit the blood stream as well as the entering into the target cell.

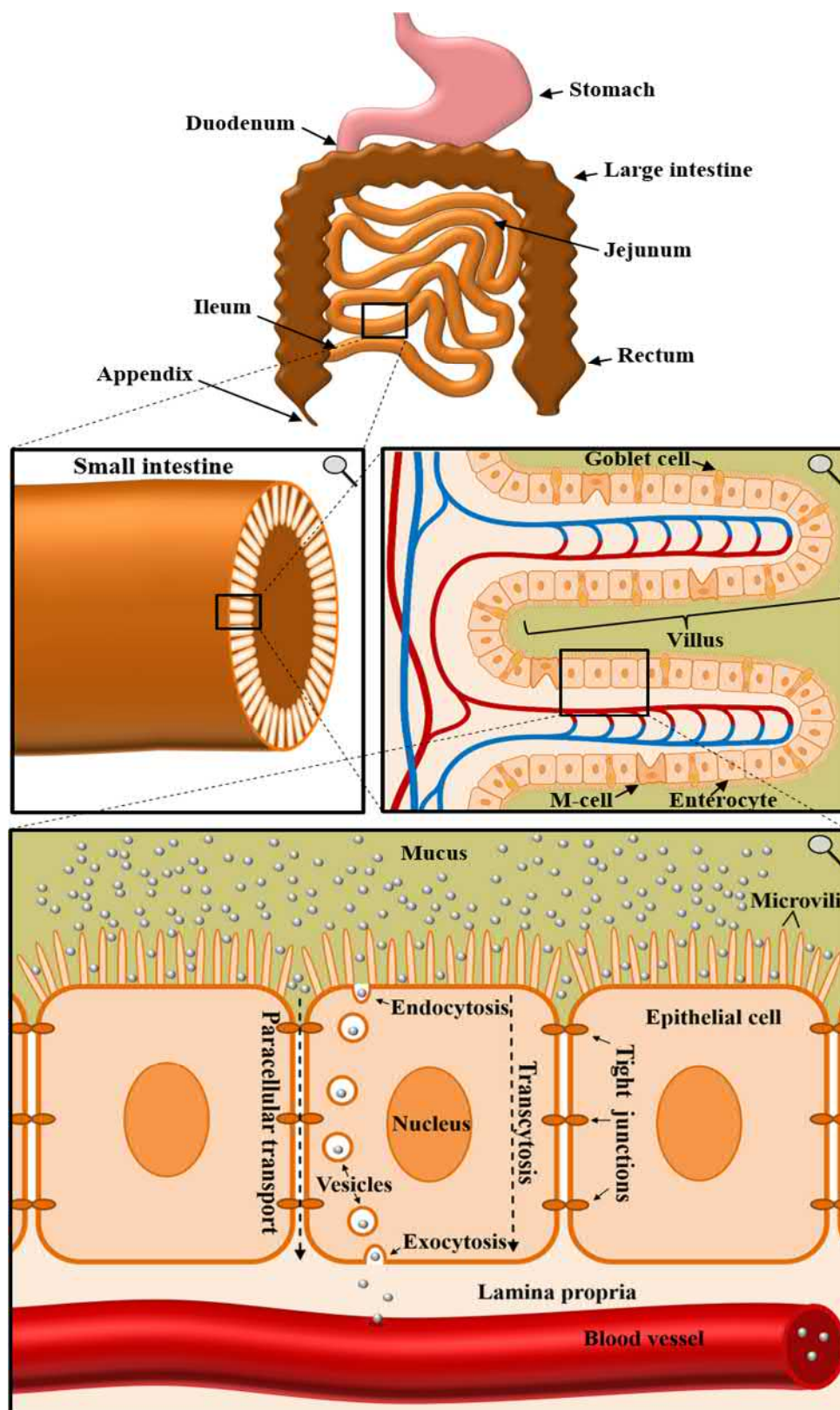


Fig. 1: Anatomy of the small intestine and the implications for orally applied nanocarriers.

Multiple consecutive close-ups are displayed. In order to enter the bloodstream, orally applied nanocarriers have to cross multiple borders of the human body. Especially the uptake and crossing of enterocytes in the small intestine marks a key challenge in oral drug delivery via nanocarriers[14]. Republished with permission of the Taylor & Francis Group, *The challenges of oral drug delivery via nanocarriers*, Reinholz J, Landfester K, Mailänder V, Drug delivery, 2018, DOI: 10.1080/10717544.2018.1501119.

As aforementioned, for a functional and reliable oral drug delivery via nanocarriers the crossing of multiple cellular borders is crucial. The barrier function of epithelial cells is achieved by a cell connection via tight junctions, adherens junctions, desmosomes and due to the fact that there is nearly no intercellular space between the cells. In endothelial cells, these properties are accomplished by tight junctions, adherens junctions and, in contrast to epithelial cells, gap junctions[15]. Epithelial cells cover all tissues towards the external side (even if the digestion tract may be seen as being inside the body), whereas endothelial cells are present on the interior surface of blood- and lymphatic vessels. The biological function of both is a protection and a regulation of metabolism of the respective tissues and vessels. Though being diverse in their morphology, virtually all endo- and epithelial cells are polarized and consist of an apical and a basal side. One of the most challenging aspects of drug delivery via nanocarriers is to overcome these barriers. Therefore, a fundamental understanding of the molecular mechanisms of entering and crossing epi- and endothelial cells is crucial for the development of nanomedicines.

The first barrier of the human body for nanocarriers to overcome is the intestinal barrier, where enterocytes, goblet cells and M (Microfold) cells, all linked via tight junctions, represent the majority of cells. The complex structure of the human gastrointestinal tract is established by villi, which increase the absorptive intestinal surface area to about 300-400 m²[16]. The small intestine, naturally responsible for the absorption of nutrients, is divided into duodenum, jejunum and ileum. In these areas, villi are covered by mucus layers with a different thickness, ranging from 120 µm to 480 µm[17]. Mucus is produced by goblet cells to protect epithelial cells from bacterial interactions as well as physical damage by ingested food[18]. However, despite being unarguably highly important for the protection of the human intestine, it marks the very first hurdle to overcome for orally applied nanocarriers. Many nanomaterials get immobilized by the mucus gel layer[19] and thus are not even able to reach the intestinal epithelial cell layer. Especially a decoration with poly ethylene glycol (PEG) chains[20, 21], the combination of anionic and cationic charges[22, 23] or the usage of self-nanoemulsifying drug delivery systems (SNEDDS)[24] are valuable approaches to penetrate the mucosal barrier[25]. A different approach is the decoration of nanoparticles with proteolytic enzymes like papain to cleave mucoglycoprotein substructures, which demonstrably increases mucosal penetration[26].

The major obstacle after penetrating the mucus layer is, however, crossing the first line of epithelial cells. Once the nanocarrier reaches the apical side of the cells, there are essentially two possibilities for the transport to the basal side. The first is a paracellular transport, which involves a loosening of tight junctions and a transport between epithelial cells without a cellular uptake. A promising material for achieving paracellular transport is chitosan, a polysaccharide, which is demonstrably able to reversibly open tight junctions[27]. Nevertheless, for most nanocarrier systems, a paracellular transport is either toxic or simply not feasible due to size restrictions. The second possibility is transcytosis, which is defined as the transport through the interior of a cell. This process consists of an uptake, preferably endocytosis, a transport within the cell as well as a withdrawal from the interior of the cell, namely exocytosis.

1.4 Endocytosis in epi- and endothelial cells

In general, endo- and epithelial cells use multiple pathways of internalization. Endocytosis mechanisms and efficiencies mainly depend on size, charge and surface properties of the nanomaterial. The major pathways for the internalization of nanomaterials in endo- and epithelial cells are clathrin-mediated, caveolin-mediated and lipid-raft-mediated endocytosis as well as macropinocytosis, phagocytosis and receptor-mediated endocytosis[28]. For the determination of endocytosis pathways, often pharmacological inhibitors are used[29, 30]. For example, chlorpromazine can inhibit clathrin-mediated uptake by inducing a reversible translocation of clathrin and adapter proteins from the plasma membrane to vesicles[31], amiloride and EIPA inhibit macropinocytosis by either lowering the submembranous pH value and preventing Rac1 and Cdc42 signaling (amiloride) or inhibiting the Na^+/H^+ -pump on plasma membranes (EIPA)[32-34], genistein can inhibit caveolae-mediated uptake via its function as a tyrosine-kinase inhibitor[35], methyl- β -cyclodextrin depletes cholesterol from the cell membrane and can therefore also be used for the inhibition of caveolae-mediated uptake[36]. However, nearly all pharmacological inhibitors induce side effects and can effect multiple pathways of internalization[29]. Many studies focus on endocytosis in Caco-2 (human colorectal adenocarcinoma) cells, since the intestine is the first barrier to overcome within the scope of oral drug delivery via nanocarriers. In general, positively charged nanoparticles tend to be taken up better than negatively charged NP, which could be shown for 50 nm and 100 nm PS-NP in Caco-2 cells[37]. The same study pointed out that positively charged NP were

endocytosed via a mixture of the clathrin-mediated pathway, a cholesterol-dependent pathway and macropinocytosis, while for negatively charged NP uptake was primarily mediated via lipid raft pathway (caveolae). Endocytosis of exogenous iron-loaded ferritin was shown to be clathrin-mediated[38], while for 80 nm PLGA nanoparticles, a co-mediation of clathrin, lipid raft, caveolin and macropinocytosis was observed[39]. Wheat germ agglutinin-functionalized polymeric nanoparticles with a size around 120 nm were also shown to be predominantly internalized via the clathrin-mediated pathway[40]. In addition, some studies examined the endocytosis pathways of natural material in Caco-2 cells. For example, pure DNA-fragments as well as human IgG are presumably internalized via macropinocytosis[41, 42], whereas for Vitamin B₁₂ the clathrin-mediated pathway is used[43]. However, by combining such natural material with nanoparticles the endocytosis mechanisms can be altered, which can subsequently be used to increase the uptake efficiency.

A second cell line widely used in the investigation of endocytosis in epithelial cells is the MDCK cell line (Madin-Darby Canine Kidney epithelial cells). Recent studies show that 100 nm PLGA-NP in these cells are internalized via caveolae/lipid raft-mediated endocytosis as well as via clathrin-mediated endocytosis, while no macropinocytosis was observed[44]. On the other hand, positively charged 20 nm and 120 nm PS-NP enter MDCK cells predominantly via clathrin-mediated endocytosis[45]. PEG-PLA nanoparticles with a size of approximately 90 nm were internalized mainly via clathrin-mediated endocytosis, while macropinocytosis was also involved[46]. Furthermore, positively charged hexanoyl-chitosan nanoparticles entered MDCK cells far more efficiently than negatively charged succinoyl-chitosan nanoparticles[47].

In contrast to epithelial cells, caveoli are believed to be the most abundant endocytotic structures in endothelial cells[48]. Thus, many studies have focused on caveolin-mediated endocytosis of nanomaterial. For example, 20-100 nm BSA-coated polymeric nanoparticles in BLMVEC (bovine lung microvascular endothelial) cells mainly get internalized via this pathway[49]. Approximately 70 nm sized Nano-Mg(OH)₂ particles are endocytosed via the same caveolin-mediated pathway in HUVEC (human umbilical vein endothelial) cells[50]. However, for 43 nm PS-NP in HUVEC cells, a clathrin-mediated uptake was shown. Interestingly, the same cells endocytosed 24 nm PS-NP via a clathrin- and caveolin-independent mechanism[51]. Similar results were shown for 20 nm and 40 nm gold nanoparticles in HMEC-1 (human microvascular endothelial) cells, although in this study also macropinocytosis was observed[52]. Moreover, like in epithelial cells, different

functionalizations of nanoparticles also lead to an altering of pathways. For example, 35 nm poly(2-hydroxypropylmethacrylamide)-coated gold nanoparticles were internalized into hCMEC/D3 (human brain endothelial) cells by a clathrin- and caveolin-independent mechanism involving flotillin[53].

On a side note, the adsorption of proteins on nanomaterial could potentially play a role in endothelial and epithelial endocytosis processes. Up to now, this is widely discussed for the intravenous route of application but not for the oral route. Once a nanocarrier comes in contact to body fluids (in case of oral drug delivery possibly already in the mouth and GI tract; in case of i.v. application in the blood stream), it gets covered with proteins[54-56]. This forms a so-called protein corona and can substantially alter endocytosis efficiencies, as described for other cell lines like HeLa cells or human mesenchymal stem cells[57] and might therefore also alter cellular pathways. The only study so far that focused on the utilization of a protein corona for transcytosis reported differences in transcytosis efficiencies after the formation of a protein corona in HUVECs, however, these effects varied widely between different sized nanoparticles[58]. The identification of protein – nanoparticle interactions in the intestine and the implications for transcytosis might therefore be one of the new and most fascinating challenges for the development of nanocarriers for oral drug delivery.

In summary, pathways of endocytosis in both endo- and epithelial cells show remarkable similarities. Recent results show that both cell types use more than one pathway for the internalization of (nano)-material. However, clathrin-mediated as well as caveolin-mediated endocytosis seem to play a key role in most of the examined nanomaterial and cell lines. The choice of nanocarriers and their respective sizes and charges therefore needs to be thoroughly evaluated.

1.5 Transcytosis of nanomaterials

For most applications nanocarriers need to enter and cross a layer of endo- and/or epithelial cells in order to successfully deliver their cargo. While there is the possibility of a paracellular transport, the key mechanism of overcoming these natural barriers is transcytosis. Transcytosis may be defined as the transport of a substance through a cell from the apical to the basolateral membrane or vice versa. Nanocarriers designed for oral drug delivery at one point need to cross the intestinal barrier before being able to reach their target cells. Intravenous applied nanocarriers on the other hand need to cross the respective endothelial cell layers, for example the blood-brain-barrier, to escape from the blood stream. However, the transcytosis efficiency of nanomaterial in these cells is fairly low, which limits the therapeutic possibilities for nanomedicine. It is thus essential to understand the molecular mechanisms behind transcytosis of nanomaterials.

The most common tool for transcytosis experiments is the so-called transwell system. Epi- or endothelial cells are grown on a porous membrane to reach confluence and final differentiation. The barrier function can be tested by measuring the electric resistance of the monolayer, which is called TEER-value ($\Omega \times \text{cm}^2$). The transwell chamber itself consists of an apical and a basal side. If nanomaterial is added into the apical medium, the subsequently transcytosed fraction can be measured in the basal medium.

While transcytosis in general is a partially energy-dependent process[39], the efficiency is largely impacted by size and charge of the examined nanomaterial. The smaller the nanoparticle, the better it is transcytosed across for example the intestine[43] or the blood brain barrier[59]. Regarding the charge of nanomaterial, most but not all studies point out that positively charged polymeric nanoparticles tend to cross epithelial cell layers with a higher efficiency compared to negatively charged NP. This could for example be shown for amidine- and carboxyl-modified 20-120 nm sized PNP in MDCK cells[45]. A significantly higher nanoparticle flux was also observed for aminated latex particles compared to their carboxylated equivalents in Caco-2 cells[60].

A successful transcytosis event potentially includes trafficking routes via apical early endosomes, common endosomes and basolateral sorting endosomes as well as sorting via the Golgi complex and basolateral sorting endosomes as shown by co-localization as well as inhibitor studies in MDCK cells[44]. In addition to sorting via the Golgi complex, the endoplasmatic reticulum might be involved in transcytosis, as postulated for Caco-2 cells[39]. On the contrary, the transcytosis of albumin coated nanoparticles in BLMVEC

(bovine lung microvascular endothelial) cells was shown to be solely reliant on caveolae and caveosomes[49]. Last but not least, the whole process of transcytosis might additionally be dependent on the regulation of cytoskeleton and motorproteins[39, 61].

Recent research additionally focused on improving the rate of transcytosis via nanoparticle bioconjugations with different proteins. For example, a functionalization of polymeric nanoparticles with the FC portion of IgG (Immunoglobulin G) significantly increased the rate of transcytosis in Calu-3 airway epithelial cells[62]. In Caco-2 cells, transcytosis efficiency could be enhanced by 2-fold via this modification[63]. The same study revealed that targeting of the FcRn receptor *in vivo* enhanced the absorption efficiency from 1,2% per hour to 13.7% per hour. In addition, such targeted nanoparticles containing insulin were able to achieve a prolonged hypoglycemic response in mice when orally administered at a clinically relevant insulin dose. The authors concluded that Fc-region modified NP essentially avoid the lysosomal pathway and are subsequently transcytosed with a higher efficiency. Similarly, a bioconjugation with Vitamin B₁₂ of 50 nm or 100 nm PS-NP increased the apical-to-basal transport by 3-fold (for 50 nm NP) and 7-fold (100 nm) in Caco-2 cells[43]. Yet another approach for oral drug delivery is a surface functionalization with folic acid to target the folate receptor. PLGA-NPs modified with folic acid highly increased the transcytosis efficiency in Caco-2 cells and might be used to enhance oral bioavailability[64].

On the contrary, nanoparticles targeted to the brain can be functionalized with transferrin to cross the blood-brain barrier more efficiently via Tf receptor-mediated transcytosis, which could be shown for 45 and 80 nm sized nanoparticles[65]. A different study revealed that coating iron oxid nanoparticles with PECAM-1 antibodies also considerably enhances the nanoparticle flux across hCMEC/D3 cells, another model for the blood-brain barrier[66]. An example for transcytosis of 12 nm gold nanoparticles across a hCMEC/D3 endothelial cell layer grown on transwells observed via TEM can be found in Fig. 2[67].

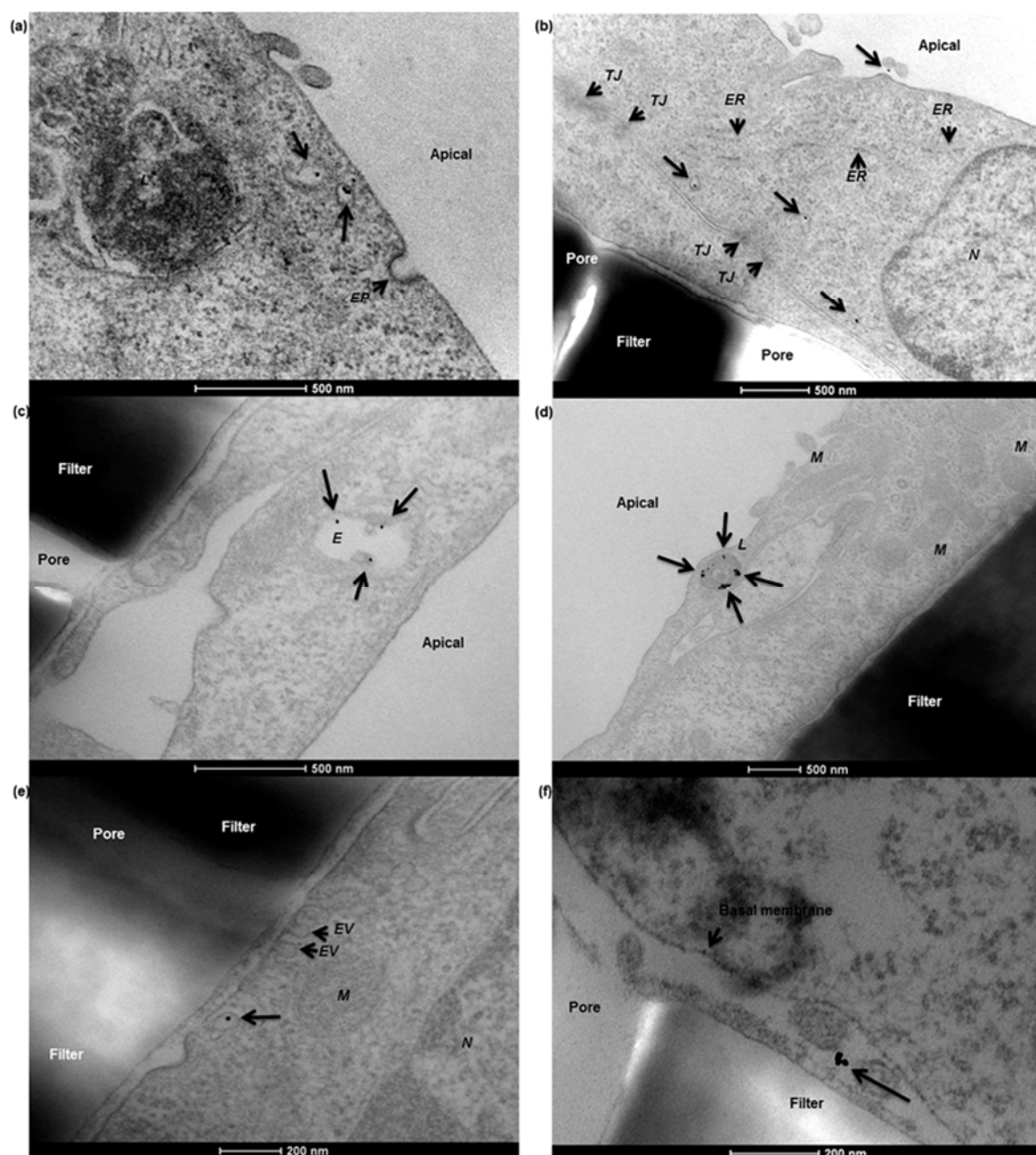


Fig. 2: Transcytosis of 12 nm human serum albumin–gold nanoparticles across a hCMEC/D3 endothelial cell monolayer.

In this study, the authors demonstrated a protocol for the in vitro determination of nanoparticle translocation across a cell monolayer using Transmission electron microscopy. (a) Nanoparticles present in apical sorting vesicles within the cytosolic space. (b) Gold nanoparticles detected in different cytoplasmic regions. (c) Nanoparticles co-localizing with endosomes. (d) Nanoparticles co-localizing with lysosomes (d). (e) A single gold nanoparticle exits the basolateral cell membrane from a vesicle. (f) The nanoparticle is finally present in the basal compartment. Abbreviations: EP, endocytic pit; ER, endoplasmic reticulum; EV, exocytic vesicle; E, endosome; L, lysosome; M, mitochondria; N, nucleus; TJ, tight junction[67]. Republished with permission of the Royal Society of Chemistry, *A TEM protocol for quality assurance of in vitro cellular barrier models and its application to the assessment of nanoparticle transport mechanisms across barriers*, Ye D, Dawson KA, Lynch I, *The Analyst* online 140 (1), 83-97, 2015; permission conveyed through Copyright Clearance Center, Inc.

Additionally, a promising candidate respectively target for the intestinal transcytosis of nanocarriers might be M cells, a cell type which is mainly localized in Peyer's patches in the small intestine[68]. Their natural function is the transcytosis of antigens across the gut epithelium[69]. One of the major advantages of this cell type is the fact that the mucus layer is considerably thinner and thus cells are easier to access[70]. M cells in general are reported to have high transcytotic activities in apical-to-basal direction[71, 72]. In addition, M cells feature a significantly reduced intracellular lysosomal activity[73]. The transcytosis of nanocarriers through M cells was already reported for several nanomaterials[74, 75] and M cells can also be targeted directly via nanocarrier surface modifications. For example, PEGylated PLGA-based nanoparticles featuring RGD peptides (tripeptide Arg-Gly-Asp) as a targeting ligand at their surface were used to successfully target the $\beta 1$ integrins on the apical side of M cells[76].

In summary, many studies have dealt with the process of transcytosis. Many different nanoparticle and cell combinations have been examined and the molecular mechanisms as well as the rate of transcytosis strongly depend on the utilized nanomaterial. However, a reliable therapeutic nanocarrier system for either oral drug delivery or for crossing the blood brain barrier still requires an improved transcytosis efficiency.

1.6 Exocytosis of nanomaterials

After nanomaterials enter animal cells via one of the endocytosis mechanisms outlined above, the cell determines the further trafficking. While it is possible that the nanocarrier gets (a) degraded in lysosomes, (b) trafficked to a specific cellular organelle or (c) releases its cargo inside the cytosol, the cell might also (d) traffic it to the extracellular space. This process is called exocytosis and is of high interest due to the fact that nanomedicines need to be released from the cell to successfully transverse a barrier.

In general, exocytosis is an energy-dependent process, which could be shown for poly(D,L-lactide-co-glycolide) nanoparticles with a size of approximately 100 nm in vascular smooth muscle cells[77]. In addition, the size of nanomaterial seems to have a keen impact on the rate of exocytosis. In Hela cells, transferrin-coated Au NP with sizes ranging from 14 to 100 nm were compared. The study revealed that smaller nanoparticles were exocytosed at (a) a faster rate and (b) at a higher overall percentage than larger nanoparticles[78]. Furthermore, the exocytosis rate of silicon particles loaded with 15 nm and 30 nm SPIONs in

macrophages was examined via iron measurement of the cell culture media 2-7 days after the nanoparticle treatment. A significantly higher amount of iron was found for 15 nm SPIONs, indicating a higher efficiency of exocytosis for the smaller nanoparticles[79]. Apparently, the surface chemistry of nanoparticles also appears to affect the exocytosis efficiency, which could be shown for macrophages treated with gold nanoparticles. While PEGylated gold nanoparticles were exocytosed rather rapidly, cationic gold nanoparticles agglomerated inside the cell, which significantly delayed their exocytosis[80]. The authors therefore concluded that exocytosis, at least for gold nanoparticles in macrophages, can be manipulated via surface modifications.

Exocytosis events of nanoparticles are rather rare, which contributes to the low efficiency of transcytosis. Primarily depending on the endocytosis mechanism, several exocytosis pathways are possible: Lysosomal escape and subsequent exocytosis, lysosomal fusion with the plasma membrane, MVB or late endosome fusion with the plasma membrane and fusion of caveolae or caveosomes with the plasma membrane[81, 82]. In accordance with the notable variability of endocytotic pathways, different nanomaterials are released to the extracellular space via different exocytosis mechanisms in different cell types.

In general, lysosomal fusion with the plasma membrane is a Ca^{2+} -regulated process which is inter alia necessary for membrane repair mechanisms[83]. An example for lysosomal fusion with the plasma membrane with subsequent exocytosis could be shown for phosphonate-modified mesoporous silica nanoparticles with an approximate size of 130 nm in various cell lines. Within 24 h, A549 (lung cancer) cells showed the highest exocytosis rate, followed by MDA-MB 231 (breast cancer), PANC-1 (pancreatic cancer), MCF-7 (breast cancer), MDA-MB 435 (melanoma cancer) and H9 (human embryonic stem cell line) cells. The lysosomal fusion and secretion was shown via cLSM co-localization studies and via measurements of the enzyme β -hexosaminidase, a marker for lysosomal exocytosis[84]. Moreover, the study revealed that the Golgi apparatus was not involved in exocytosis in any of the tested cell lines. However, pharmacological inhibitors for microtubule formation and actin polymerization both inhibited exocytosis, proposing a function of both for the lysosomal transport and plasma membrane fusion, as already stated by previous research[85]. A different study focused on 50 nm sized silica nanoparticles in H1299 (human lung carcinoma) cells. The study revealed that nanoparticle clusters in lysosomes were easily exocytosed in comparison to free nanoparticles in the cytoplasm[86].

In addition to lysosomal exocytosis, exocytosis of multivesicular bodies might play a key role in secretion of nanomaterial. TEM images of SPIONs trafficked in J774 macrophages illustrated a possible fusion of MVBs with the plasma membrane, which might be the mechanism responsible for the nanoparticle secretion[79]. Similar results proposing a possible key role for MVB in SPION secretion were observed in HMVEC (human microvascular vein endothelial) cells[87]. A study examining sub 100 nm Au-NP in HeLa cells showed that nanoparticles after uptake were trafficked towards the plasma membrane in late endosomes and lysosomes. The vesicles fused with the membrane and subsequently released the nanoparticles, which were finally secreted by the cells[78].

On the other hand, lipid rafts and especially cholesterol might also be involved in the process of nanomaterial exocytosis[88]. A study focusing on the uptake of 60 nm sized cationic polysaccharide nanoparticles in 16HBE cells observed a considerable increase of endocytosis after cholesterol depletion. To further analyze this result, they added filipin into the medium of nanoparticle treated cells, which significantly decreased the rate of exocytosis[89]. Finally, exocytosis can also be triggered by increasing the extracellular calcium concentration[90]. This phenomenon was examined for gold nanoparticles in HT-29 (human colonic adenocarcinoma) cells. It could be revealed that different Ca^{2+} concentrations in the medium (0-10 mM) influence the amount of exocytosed nanoparticles. While the physiological extracellular free calcium concentration in mammals is roughly 2 mM, even higher concentrations up to 10 mM increased the amount of exocytosed gold nanoparticles[91].

All in all, exocytosis is a very diverse and complex process with a variety of different factors involved. For many applications, especially drug delivery through natural barriers via nanocarriers, exocytosis is the crucial process. The pathways show a huge diversity, depending on the material, surface chemistry, charge, size and of course the different mammalian cell lines (an example for a postulated nanoparticle transcytosis / exocytosis pathway is depicted in Fig. 3). A deeper understanding of the exocytosis process in epi- and endothelial cells might in addition contribute to an enhancement in transcytosis efficiencies. Thus, the process of exocytosis needs to be further examined in a broader spectrum of nanomaterials and cell lines.

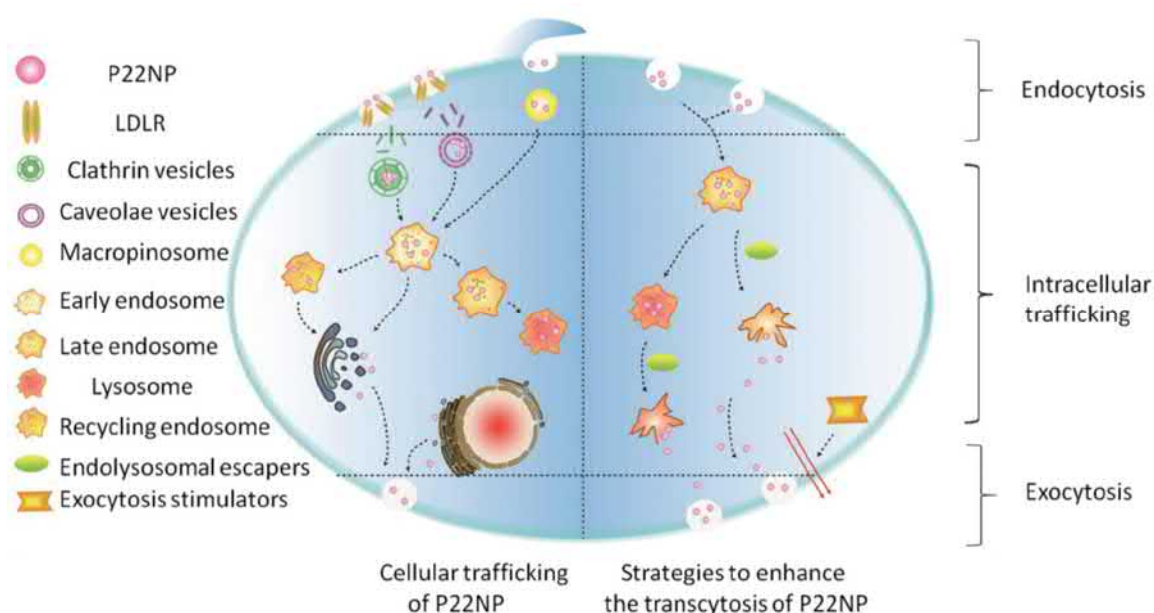


Fig. 3: Putative pathways for endo-/ trans- and exocytosis of P22NPs in Caco-2 cells.

The black arrows represent the pathways that were demonstrated by the authors. In addition, the application of hemagglutinin-2 and metformin led to an increase of endolysosomal escape and exocytosis of nanoparticles, overall resulting in an increase of transcytosis[92]. Republished with permission of the Royal Society of Chemistry, *The combination of endolysosomal escape and basolateral stimulation to overcome the difficulties of "easy uptake hard transcytosis" of ligand-modified nanoparticles in oral drug delivery*, Cui Y, Shan W, Zhou R, Liu M, Wu L, Guo Q, Zheng Y, Wu J, *Nanoscale* 10 (3), 1494-1507, 2018; permission conveyed through Copyright Clearance Center, Inc.

In the present thesis, mainly Caco-2 cells will be investigated for their interactions with nanoparticles, focusing on endo-/ trans- and exocytosis of polymeric nanoparticles, since Caco-2 cells are the worldwide most used and accepted cell line for apical-to-basal transport experiments. Nevertheless, there are potentially adequate cell types available that might show a stronger effect on a molecular level after nanoparticle treatment. For this reason, dendritic cells are chosen as a second cell type to investigate for their cell-nanoparticle-interactions, since these cells supposedly react very strong and rapidly to foreign material.

1.7 Dendritic cells and nanoparticle induced vaccination

Dendritic cells (DCs) are antigen-presenting cells[93] that were originally discovered, albeit not yet characterized per se as dendritic cells, by P. Langerhans in 1868[94]. These immune cells were further examined and described by R. Steinman and Z. Cohn in 1973/1974[95, 96]. The name “dendritic cell” derives from the cell’s branched morphology. Their main biological function is the procession of antigens and a subsequent presentation via MHC molecules on the surface for T cells, thereby inter alia initiating adaptive immunity[97]. Their natural role as the primary antigen presenting cell type[98] can be used for vaccination and is currently impetuously researched for vaccination against cancer[99, 100]. For this approach, isolated DCs are loaded ex vivo with tumor antigen and afterwards re-administered into the human body[101]. One of the newest promising approaches is the targeting of dendritic cells via nanoparticles for vaccination [102]. The general ultimate goal of a vaccination is the continuous provision of antibodies and the maintenance of memory cells for rapid cellular responses[103]. A rising number of vaccines consist of a combination of antigen and adjuvant. An adjuvant’s purpose is the enhancement of a cellular immune response[104], mainly by enhancing the expression of surface markers for cell adhesion and antigen presentation[105]. Typical adjuvants are for example aluminum salts, emulsions or lipid vesicles [106]. In order to achieve a sufficient immune response of dendritic cells, reliable adjuvants are still urgently needed and currently evaluated in pre-clinical trials[107], especially for the development of nanocarriers for vaccination.

Two promising adjuvants for the development of vaccines are the Toll-like receptor agonist resiquimod (R848)[108, 109] and the synthetic immunoreactive peptide muramyl dipeptide (MDP)[105]. However, to ensure a sufficient response of dendritic cells, all cellular reactions to the nanocarrier and particularly to the encapsulated adjuvant need to be evaluated carefully. Despite nanocarrier induced cytotoxic effects, especially uptake mechanisms and intracellular trafficking pathways as well as immunological pathways induced by nanocarriers need to be screened. One approach for the determination of cellular reactions might be the treatment of dendritic cells with nanocarriers containing adjuvants followed by an investigation of the cell’s transcriptome. By analyzing up- as well as down-regulated genes, several putative relevant and interesting immunological and intracellular transport pathways might be determined. In this thesis, the putative vaccination relevant adjuvants MDP and R848 will be monitored regarding their impact on the mRNA expression levels of dendritic cells via Next Generation Sequencing.

1.8 Next Generation Sequencing and RNA-Seq

The history of nucleic acid sequencing begins in year 1977, where A. Maxam and W. Gilbert and F. Sanger published their revolutionary methods and thereby introduced the “First Generation Sequencing”. The principle of Maxam-Gilbert sequencing, also well-known as “chemical sequencing” bears on specific chemical breaks of a terminally labeled DNA molecule and a subsequent size separation via polyacrylamide gel electrophoresis[110]. The even more groundbreaking Sanger sequencing technique, also known as “chain-termination sequencing”, relies on DNA amplification of a single-stranded DNA template via a DNA polymerase[111]. Supplementary to standard dNTPs, chain-terminating nucleotides which lack a 3' OH group (ddNTPs) are added to the reaction. Whenever such a chain-terminating nucleotide is randomly incorporated by the DNA polymerase, the reaction stops. Resulting different sized DNA fragments can be labeled with a radioactive or fluorescent tag[112] and size separated via gel electrophoresis. The Sanger method was majorly improved, automated[113] and finally used for the sequencing of the first human genome[114]. This project took nearly 20 years from planning to the 2.91-billion base pair consensus sequence and costed about \$2.7 billion[115].

In the meantime, sequencing techniques were considerably improved and were termed as Next Generation Sequencing or “Second Generation Sequencing”. The first established method used the principle of pyrosequencing[116, 117] and the first commercial sequencer (GS 20) was introduced by 454 Life Sciences and used in 2005 for the sequencing of the *Mycoplasma genitalium* genome[118]. SOLiD sequencing (Supported Oligonucleotide Ligation and Detection) depending on emulsion PCR was developed in 2005 and used for a resequencing of the *E.coli* genome[119]. Following these major breakthroughs, the Solexa/Illumina Genome Analyzer was launched in 2006 [115], marking yet another milestone in nucleic acid sequencing. Despite the newest developments around single molecule real time sequencing[120], nanopore sequencing[121] and various other promising approaches[122] (summarized as “Third Generation Sequencing”), Illumina Sequencing is up to now probably still the most relevant sequencing method available.

The introduction and worldwide adoption of Next Generation Sequencing methodologies lead to a significant drop in DNA sequencing costs. In contrast to the first human genome sequenced by the Sanger technique (\$2.7 billion), the first Next Generation sequenced genome (the genome of James D. Watson) costed around \$1 million[123]. In the meantime, sequencing cost dropped further and further (Fig. 4) and the race for a \$1,000 genome[124] was finally claimed to be “won” by Illumina in 2014[125, 126].

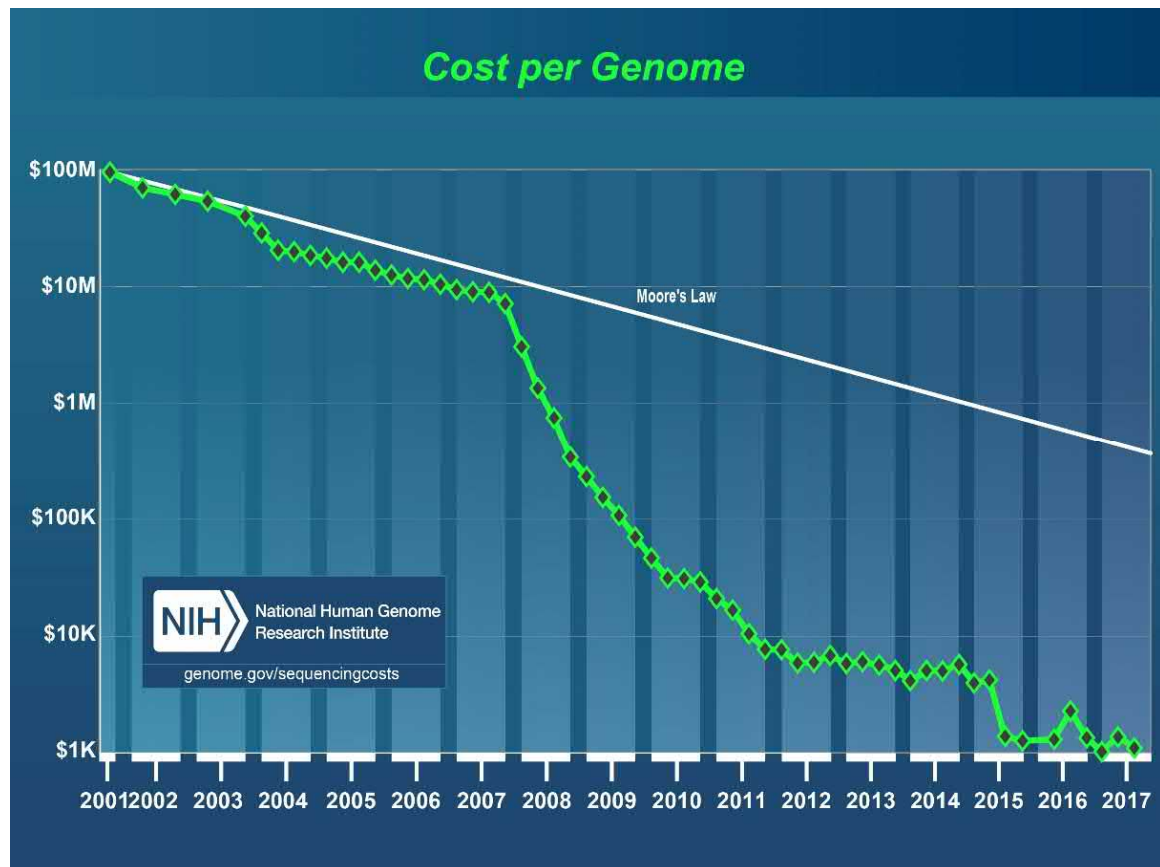


Fig. 4: Historical sequencing cost per human genome.

This figure depicts the historical average prices for the sequencing of one human genome ranging from 2001 to 2017. The graph shows that sequencing costs significantly dropped with the introduction of Next Generation Sequencing systems around 2007. Around the year 2015, the first \$1,000 genomes have become reality[127].

For Illumina Sequencing, target DNA first needs to be sheared into several hundred basepair long fragments. Then, DNA fragments are end-repaired to generate 5'-phosphorylated ends and a single adenine base is attached to the 3' end via Klenow fragment. Afterwards, DNA fragments are furnished with oligonucleotide adapters, which are complementary to adapters anchored in the flowcell. Hereupon, prepared DNA fragments are added to the flowcell and can bind to their counterpart adapters. The next step is an amplification of anchor-bound DNA via "bridge amplification", which results in the creation of DNA clusters with the identical sequence on the flowcell (approximately 50×10^6 separate clusters can be achieved per flow cell). Prior to sequencing, DNA clusters are denatured to provide single stranded DNA. Then, a primer complementary to the adapter sequence, DNA polymerase and four different reversible fluorescent dye terminator bases are added to the flow cell. The dye terminator base is incorporated by the DNA polymerase according to the complementary sequence of DNA template and at this point the reaction stops. All chemicals are washed away and high speed cameras record the fluorescence of each cluster. Afterwards, terminator moieties are cleaved off and a new badge of dye terminator bases is added. This procedure is repeated until the desired read length is achieved[115]. The principle of cluster generation and dye terminator binding and recording is displayed in Fig. 5.

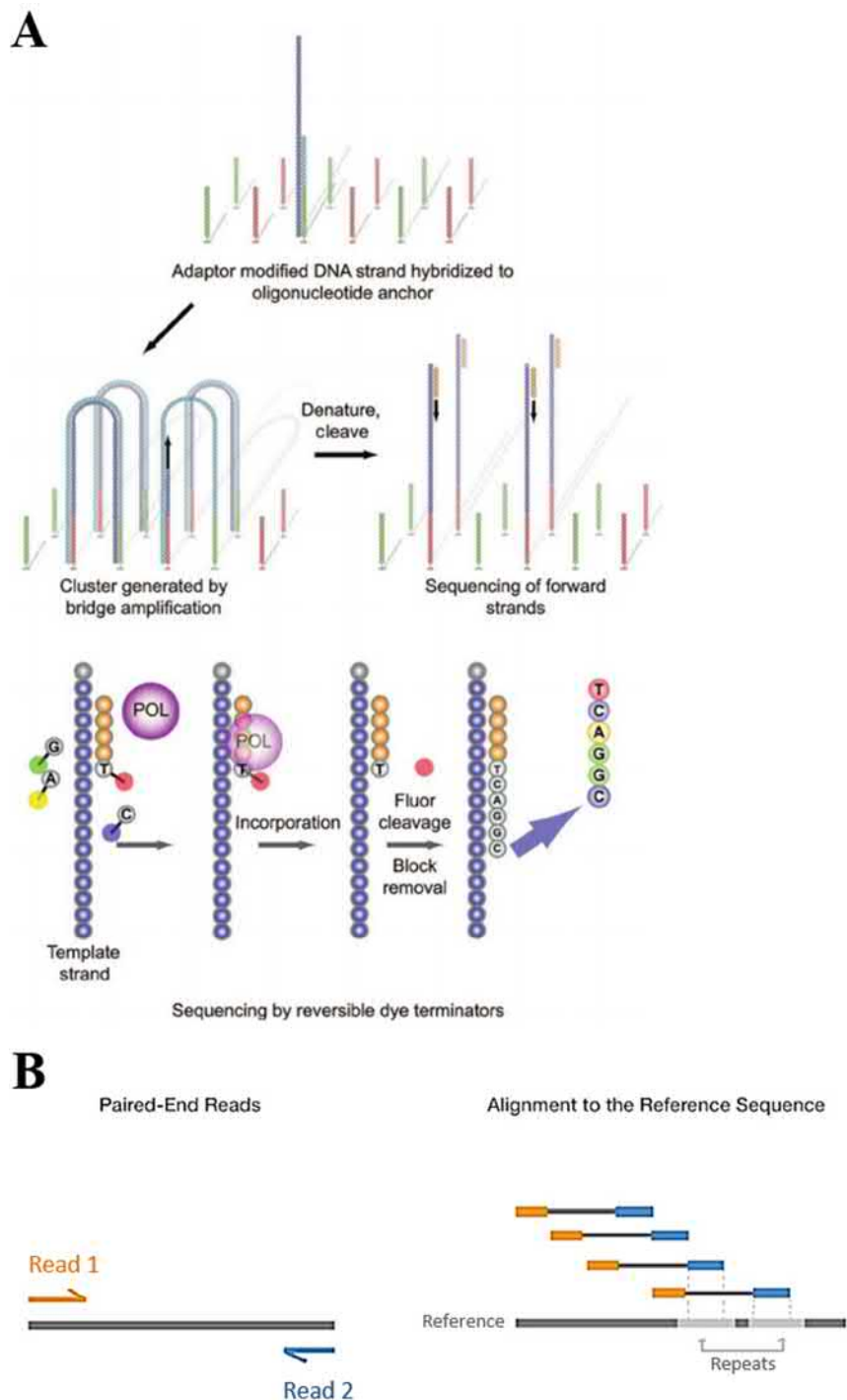


Fig. 5: Next Generation Sequencing via the Illumina Sequencing principle.

This figure depicts the principle of Illumina Sequencing. A) Adaptor modified DNA strand is hybridized to an oligo anchor and immobilized. Then, DNA clusters are created by bridge amplification. After a denaturation and cleavage, a polymerase, primers and the four reversible dye terminators are added and sequencing is started. After the incorporation of dye terminators, fluorescence is detected and recorded. After removal of the fluorophore and block, the next synthesis cycle can be initiated [115]. Republished with permission of the American Association for Clinical Chemistry Inc., *Next-Generation Sequencing: From Basic Research to Diagnostics*, Voelkerding K, Dames S, Durtschi J, Clinical chemistry 55 (4), 641-658, 2009; permission conveyed through Copyright Clearance Center, Inc. B) Paired end sequencing allows both ends of the strand to be sequenced. Since the distance between the reads is known, read mapping to a reference sequence is facilitated[128].

Despite the great opportunities for whole genome sequencing, NGS can also be used for sequencing mRNA by translating it into complementary DNA (cDNA). Such a RNA-Seq[129], also known as whole transcriptome sequencing[130], offers the possibility to detect alternative gene splicing[131], post-transcriptional modifications[132], viral influences[133], single nucleotide polymorphisms (SNPs)[134] and maybe most importantly changes in gene expression[135, 136]. RNA expression of a certain gene is calculated by quantifying the amount of reads that match to the respective gene locus in an annotated reference sequence[137]. Usually, gene expression is calculated in RPKM (reads per kilobase of exon model per million mapped reads)[129].

Via such an analysis, multiple conditions of the sequenced organism respectively sequenced cells can be analyzed. In this thesis, RNA-Seq will be used for the quantification of gene expression of BMDCs treated with ovalbumin nanocapsules (with and without encapsulated MDP and R848). This expression will be quantified against an untreated control sample to analyze if nanocapsules have an effect on the transcriptome.

1.9 Aims

While nanotechnology is a highly emergent research area, there are still relatively few nanoparticle based formulations approved by the FDA for drug delivery. The reason behind this is mainly a lack of knowledge about nanoparticle-cell interactions for an overwhelming amount of nanomaterials. This thesis aims to shed light on two different polymeric nanocarrier systems and their intracellular effects and trafficking pathways.

The first project deals with oral drug delivery via nanocarriers, which, in theory, marks one if not the most promising approach for the oral delivery of pharmaceuticals. At least for peptide based drugs, such a carrier system is urgently needed for a protection against the proteolytic environment in the stomach. However, several natural barriers of the human body impede the uptake or cellular traversal of nanocarrier systems. Especially the intestinal barrier needs to be crossed reliably to ensure a successful nanocarrier release into the bloodstream. In this thesis, the transcytotic capability of different sized and charged polystyrene nanoparticles will be screened in Caco-2 cells, a widely accepted cell model for transcytosis experiments. In addition, different nanoparticle functionalizations will be tested for their influence on transcytosis efficiencies. Putative transcytotic and intracellular trafficking relevant proteins will be examined via mass spectrometry analysis and generation of stable GFP-protein-expressing transgenic cell lines. Putative trafficking and transcytosis relevant proteins will finally be analyzed for their spatial and temporal co-localization to create protein machinery profiles.

The second project deals with the effect of nanomaterials on a transcriptomic level. For this analysis, murine bone marrow derived dendritic cells are treated with (adjuvant-filled) ovalbumin nanocapsules for different time points. RNA is extracted and prepared for RNA-Seq via Next Generation Sequencing. RNA expression of (adjuvant-filled) ovalbumin nanocapsules treated cells will be compared against each other as well as against the RNA expression of untreated control cells. Obtained Next Generation Sequencing results will be validated via quantitative real-time polymerase chain reaction. Finally, up- and downregulated genes will be determined and investigated for up- and down-regulated pathways via various bioinformatical methods.

2 Materials and Methods²

2.1 Materials

2.1.1 Chemicals and buffers

Tab. 1 lists the chemicals and buffers and the respective manufacturers used for this work.

Tab. 1: Chemicals and buffers

Chemical	Manufacturer
2-Propanol	Sigma-Aldrich, USA
3-[(3-Cholamidopropyl)dimethylammonio]-1-propanesulfonate (CHAPS)	Serva, Germany
7-Aminoactinomycin D	BioLegend, USA
Acetic acid	Sigma-Aldrich, USA
Agar	Sigma-Aldrich, USA
Agarose Standard	Sigma-Aldrich, USA
Ampicillin	Sigma-Aldrich, USA
Annexin V-Pacific Blue™	Thermo Fisher Scientific, USA
Bovine Serum Albumin	Sigma-Aldrich, USA
CellMask™ Deep Red Plasma membrane Stain	Thermo Fisher Scientific, USA
CellMask™ Orange Plasma membrane Stain	Thermo Fisher Scientific, USA
Cleaning solution for flow systems	Partec, Germany
cOmplete™ Protease Inhibitor Cocktail	Roche, Switzerland
D-(+)-Glucose	Sigma-Aldrich, USA
Decontamination solution for flow systems	Partec, Germany
Deoxynucleotide (dNTP) Solution Mix	New England Biolabs, USA

² Parts of the following chapter were already published and are republished in this thesis with permission of:

Elsevier Science and Technology Journals, *Protein machineries defining pathways of nanocarrier exocytosis and transcytosis*, Reinholz J, Diesler C, Schöttler S, Kokkinopoulou M, Ritz S, Landfester K, Mailänder V, Acta Biomaterialia 71, 2018; permission conveyed through Copyright Clearance Center, Inc.

MATERIALS & METHODS

Dimethyl Sulfoxide (DMSO)	Sigma-Aldrich, USA
DNA Gel Loading Dye	Thermo Fisher Scientific, USA
Dulbecco's Phosphate Buffered Saline	Sigma-Aldrich, USA
Ethanol abs.	VWR International, USA
Fugene HD	Promega, USA
GeneRuler 1 kb DNA Ladder	Thermo Fisher Scientific, USA
GeneRuler 100 bp Plus DNA Ladder	Thermo Fisher Scientific, USA
GlutaMAX™ Supplement	Gibco, USA
Hank's Balanced Salt Solution	Gibco, USA
Hydrochloric acid	Sigma-Aldrich, USA
Hypochloride solution for flow systems	Partec, Germany
Immunoglobulin G	Athens Research & Technology, USA
Immunoglobulin G, FC Fragment	Athens Research & Technology, USA
Leica Microsystems™ Immersion Oil for Microscopes	Leica, Germany
Lipofectamine 3000	Thermo Fisher Scientific, USA
MEM Non-Essential Amino Acids Solution	Gibco, USA
MES	Sigma-Aldrich, USA
Nuclease-Free Water	Qiagen, Netherlands
NuPAGE™ LDS Sample Buffer	Thermo Fisher Scientific, USA
NuPAGE™ MES SDS Running Buffer	Thermo Fisher Scientific, USA
NuPAGE™ Sample Reducing Agent	Thermo Fisher Scientific, USA
Paraformaldehyde	Sigma-Aldrich, USA
Penicillin/Streptomycin	Gibco, USA
Peptone	Sigma-Aldrich, USA
Pierce 660nm Protein Assay Reagent	Thermo Fisher Scientific, USA
Pierce Silver Staining Kit	Thermo Fisher Scientific, USA
Polybrene	Sigma-Aldrich, USA
Polyethyleneimine	Polysciences Incorporated, USA

Propidium Iodide	Sigma-Aldrich, USA
Puromycin	Gibco, USA
SeeBlue™ Plus2 Pre-stained Protein Standard	Thermo Fisher Scientific, USA
Sheath Fluid for flow systems	Partec, Germany
SimplyBlue SafeStain	Thermo Fisher Scientific, USA
Sodium chloride	VWR International, USA
Sodium hydroxide	Sigma-Aldrich, USA
Standard <i>Taq</i> Reaction Buffer	New England Biolabs, USA
RNase™ AWAY spray	Thermo Fisher Scientific, USA
SYBR® Safe DNA gel stain	Invitrogen, USA
TAE buffer	Thermo Fisher Scientific, USA
Thiourea	Sigma-Aldrich, USA
Trypan Blue solution	Sigma-Aldrich, USA
Tryptone	Sigma-Aldrich, USA
Trypsin-EDTA (0.25%)	Gibco, USA
Urea	Serva, Germany
Vitamin B ₁₂	Sigma-Aldrich, USA
Yeast Extract	Sigma-Aldrich, USA

2.1.2 Media and sera

Tab. 2 lists the media and sera used for this work as well as the respective manufacturers.

Tab. 2: Media and sera

Name	Manufacturer
Dulbecco's Modified Eagle's Medium (Powder)	Sigma-Aldrich, USA
Dulbecco's Modified Eagle Medium	Gibco, USA
Fast-Media® Amp Agar	Invivogen, USA
Opti-MEM™ Reduced Serum Media	Gibco, USA
Fast-Media® Amp LB	Invivogen, USA
Fetal Bovine Serum	Gibco, USA
MEM Eagle with Earle's BSS, with L-glutamine	Lonza, Switzerland
MEM Non-Essential Amino Acids Solution	Gibco, USA
SOC Outgrowth Medium	New England Biolabs, USA

2.1.3 Consumables and kits

Tab. 3 lists the Consumables and commercial kits used for this work as well as the respective manufacturers.

Tab. 3: Consumables and kits

Name	Manufacturer
μ-Dish 35 mm, low	Ibidi, Germany
μ-Slide 8 Well Glass Bottom	Ibidi, Germany
12mm Transwell® -COL Collagen-Coated 3.0μm Pore PTFE Membrane Insert, Sterile (Product #3494)	Corning, USA
12mm Transwell® with 0.4μm Pore Polyester Membrane Insert, Sterile (Product #3460)	Corning, USA
12mm Transwell® with 3.0μm Pore Polycarbonate Membrane Insert, Sterile (Product #3402)	Corning, USA
12mm Transwell® with 3.0μm Pore Polyester Membrane Insert, Sterile (Product #3462)	Corning, USA
6-, 12-, 24-, 48-, 96-well plates	Greiner, Germany
Cell counting slides	Bio-Rad Laboratories, Inc., USA
CellTiter 96® AQueous One Solution Cell Proliferation Assay (MTS)	Promega, USA
CellTiter-Glo® Luminescent Cell Viability Assay	Promega, USA
Cryo tubes	Greiner, Germany
Disposable scalpels	Feather, Japan
Eppendorf Safe-Lock Tubes 1,5 ml	Eppendorf, Germany
Eppendorf® LoBind microcentrifuge tubes 1,5 ml	Eppendorf, Germany
Falcon Centrifuge Tubes (15, 50 ml)	Greiner, Germany
Flow Cytometry tubes (3.5 ml)	Partec, Germany
In-Fusion® HD Cloning Kit	Clontech Laboratories, USA
iQ™ SYBR® Green Supermix	Bio-Rad Laboratories, Inc., USA
iScript™ cDNA Synthesis Kit	Bio-Rad Laboratories, Inc., USA
Lenti-X™ GoStix™	Clontech Laboratories, USA
NuPAGE™ 10% Bis-Tris Protein Gels	Thermo Fisher Scientific, USA

MATERIALS & METHODS

Parafilm	Bemis, USA
Pasteur glass pipettes	Brand, Germany
PCR Tubes (0.2 ml)	Bio-Rad Laboratories, Inc., USA
Pierce™ LAL Chromogenic Endotoxin Quantitation	Thermo Fisher Scientific, USA
QIAGEN Plasmid Maxi Kit	Qiagen, Netherlands
QIAGEN Plasmid Mini Kit	Qiagen, Netherlands
QIAquick Gel Extraction Kit	Qiagen, Netherlands
QIAshredder Spin Columns	Qiagen, Netherlands
RNeasy Mini Kit	Qiagen, Netherlands
Serological pipettes (5, 10, 25, 50 ml)	Greiner, Germany
Sterile cell culture flasks	Greiner, Germany
Sterile pipette tips (10, 20, 200, 1000 µl)	STARLAB International, Germany
Sterile syringes (10, 20, 50 ml)	B. Braun Melsungen AG, Germany
Syringe Filter 0.2 µm	Sartorius, Germany
Syringe Filter 0.45 µm	Sartorius, Germany

2.1.4 Enzymes

Tab. 4 lists the enzymes used for this work as well as the respective manufacturers.

Tab. 4: Enzymes

Name	Manufacturer
Antarctic Phosphatase	New England Biolabs, USA
Bam H1	New England Biolabs, USA
CloneAmp™ DNA polymerase	Clontech Laboratories, USA
DNase I	Qiagen, Netherlands
Eco R1 HF	New England Biolabs, USA
Reverse transcriptase	Bio-Rad Laboratories, Inc., USA
T4 DNA Ligase	New England Biolabs, USA
<i>Taq</i> DNA Polymerase	New England Biolabs, USA

2.1.5 Pharmacological inhibitors

Tab. 5 lists the pharmacological inhibitors used for this work as well as the respective manufacturers.

Tab. 5: Pharmacological inhibitors

Name	Manufacturer
5-(N-Ethyl-N-isopropyl) amiloride (EIPA)	Sigma-Aldrich, USA
Bafilomycin A1	Sigma-Aldrich, USA
Blebbistatin	Sigma-Aldrich, USA
Chlorpromazine	Sigma-Aldrich, USA
Colchicine	Sigma-Aldrich, USA
Cytochalasin D	Sigma-Aldrich, USA
Dynasore hydrate	Sigma-Aldrich, USA
Filipin III	Sigma-Aldrich, USA
Staurosporine	Sigma-Aldrich, USA
Wortmannin	Sigma-Aldrich, USA

2.1.6 Nanoparticles

Tab. 6 lists the polymeric nanoparticles used for this work describing size, surfactant, functionalization, dye and zeta potential.

Tab. 6: Nanoparticles

Name	Size (diameter)	Surfactant	Functionalization	Exc. /Em.	Zeta potential [in H ₂ O]
PS-Lut-120	120 nm	Lutensol	Unfunctionalized	523/536 nm	-6.67 mV
PS-Lut-COOH-116	116 nm	Lutensol	Carboxy-funct.	523/536 nm	-7.21 mV
PS-Lut-NH ₂ -126	126 nm	Lutensol	Amino-funct.	523/536 nm	7.58 mV
PS-CTMACl-NH ₂ -120	120 nm	CTMA-Cl	Amino-funct.	523/536 nm	38.5 mV
PS-SDS-COOH-91	91 nm	SDS	Carboxy-funct.	523/536 nm	-39.3 mV
PS-SDS-COOH-148	148 nm	SDS	Carboxy-funct.	523/536 nm	-37.4 mV
PS-SDS-COOH-59	59 nm	SDS	Carboxy-funct.	523/536 nm	-37.6 mV
PS-SDS-COOH-127	127 nm	SDS	Carboxy-funct.	580/605 nm	-59.1 mV
PS-SDS-COOH-208	208 nm	SDS	Carboxy-funct.	580/605 nm	-36.6 mV
PS-SDS-COOH-65	65 nm	SDS	Carboxy-funct.	580/605 nm	n. d.
PS-CTMACl-NH ₂ -109	109 nm	CTMA-Cl	Amino-funct.	580/605 nm	n. d.
PS-CTMACl-NH ₂ -59	59 nm	CTMA-Cl	Amino-funct.	580/605 nm	n. d.
PS-CTMACl-NH ₂ -144	144 nm	CTMA-Cl	Amino-funct.	580/605 nm	n. d.

2.1.7 Primers

The following primers were obtained from Sigma-Aldrich (USA) for amplification, Sanger sequencing or quantitative real time polymerase chain reactions. Bases in red are flanking homologous base pairs bases derived from the vector, bases in black are complementary to the respective cDNA, bases in blue are filler bases to preserve the open reading frame.

Tab. 7 lists the primers used for this work as well as the respective application and oligonucleotide sequence.

Tab. 7: Primers

Gene	Application	Oligonucleotide sequence (5' – 3')
Rab5a	Amplification for cloning into pLVX-mCherry-N1	F: CTCAAGCTTCGAATT ATGGCTAGTCGAGGCGCAAC R: GTCGACTGCAGAATT CC GTTACTACAACACTGATTCCTGGT
Rab7a	Amplification for cloning into pLVX-mCherry-N1	F: CTCAAGCTTCGAATT ATGACCTCTAGGAAGAAAGTGTGCT R: GTCGACTGCAGAATT CC GCAACTGCAGCTTTCTGCCG
Rab9a	Amplification for cloning into pLVX-mCherry-N1	F: CTCAAGCTTCGAATT ATGGCAGGAAAATCATCACTTTTTAAAG R: GTCGACTGCAGAATT CC ACAGCAAGATGAGCTAGGCTTG
Rab11	Amplification for cloning into pLVX-mCherry-N1	F: CTCAAGCTTCGAATT ATGGGTACCCGCGACGACGAG R: GTCGACTGCAGAATT CC GATGTTCTGACAGCACTGCAC
Lamp1	Amplification for cloning into pLVX-mCherry-N1	F: CTCAAGCTTCGAATT ATGGCGGCCCCCGGCA R: GTCGACTGCAGAATT CC GATAGTCTGGTAGCCTGCGTG
Flot1	Amplification for cloning into pLVX-mCherry-N1	F: CTCAAGCTTCGAATT ATGTTTTTCACTTGTGGCCCAAATG R: GTCGACTGCAGAATT CC AGCTGTTCTCAAAGGCTTGTGATT

Rab27a	Amplification for cloning into pLVX-ZsGreen1-N1	F: CTCAAGCTTCGAATT ATGTCTGATGGAGATTATGATTACC R: GTCGACTGCAGAATT CC ACAGCCACATGCCCCCTTTCT
Rab3a	Amplification for cloning into pLVX-ZsGreen1-N1	F: CTCAAGCTTCGAATT ATGGCATCCGCCACAGACTC R: GTCGACTGCAGAATT CC GCAGGCGCAGTCCTGGTG
Rab5c	Amplification for cloning into pLVX-ZsGreen1-N1	F: CTCAAGCTTCGAATT ATGGCGGGTCGGGGAGG R: GTCGACTGCAGAATT CC GTTGCTGCAGCACTGGCTC
Exoc1	Amplification for cloning into pLVX-ZsGreen1-N1	F: CTCAAGCTTCGAATT ATGACAGCAATCAAGCATGCATTAC R: GTCGACTGCAGAATT CC GTGGGACTGTGCAATGCTGG
Cpne1	Amplification for cloning into pLVX-ZsGreen1-N1	F: CTCAAGCTTCGAATT ATGGCCCACTGCGTGACCT R: GTCGACTGCAGAATT CC GGCCTGGGGGGCCTGT
Lamp1	Amplification for cloning into pLVX-ZsGreen1-N1	F: CTCAAGCTTCGAATT ATGGCGGCCCCCGGCA R: GTCGACTGCAGAATT CC GATAGTCTGGTAGCCTGCGTG
Cav1	Amplification for cloning into pLVX-ZsGreen1-N1	F: CTCAAGCTTCGAATT ATGTCTGGGGGCAAATACGTAG R: GTCGACTGCAGAATT CC TATTTCTTTCTGCAAGTTGATGCGG
Rab5a	Amplification for cloning into pLJM1-EGFP	F: CTCAAGCTTCGAATT CC ATGGCTAGTCGAGGCGCAAC R: TCGAGGTCGAGAATT CC TCAGTTACTACAACACTGATTCCTG
Rab7a	Amplification for cloning into pLJM1-EGFP	F: CTCAAGCTTCGAATT CC ATGACCTCTAGGAAGAAAGTGTGCT R: TCGAGGTCGAGAATT CC TCAGCAACTGCAGCTTTCTGC
Rab9a	Amplification for cloning into pLJM1-EGFP	F: CTCAAGCTTCGAATT CC ATGGCAGGAAAATCATCACTTTTAAAG R: TCGAGGTCGAGAATT CC TCAACAGCAAGATGAGCTAGGCT
Rab11	Amplification for cloning into pLJM1-EGFP	F: CTCAAGCTTCGAATT CC ATGGGTACCCGCGACGACGAG R: TCGAGGTCGAGAATT CC TTAGATGTTCTGACAGCACTGCAC

RhoB	Amplification for cloning into pLJM1-EGFP	F: CTCAAGCTTCGAATTCATGGCGGCCATCCGCAAGAA R: TCGAGGTCGAGAATTCATAGCACCTTGCAGCAGTTG
Flot1	Amplification for cloning into pLJM1-EGFP	F: CTCAAGCTTCGAATTCATGTTTTTCACTTGTGGCCCAAATG R: TCGAGGTCGAGAATTCCTAAGCTGTTCTCAAAGGCTTGTG
pLJM1-Seq	Sanger Sequencing	F: GATCACTCTCGGCATGGAC R: AATTGTGGATGAATACTGCCA
pLVX-ZsGreen1-N1-Seq	Sanger Sequencing	F: CTGGTTTAGTGAACCGTCAG R: GAAGCGCATGAACTCCTTGA
pLVX-mCherry-Seq	Sanger Sequencing	F: CATAGAAGACACCGACTCTA R: TTGATGATGGCCATGTTATC
IL12b	qRT-PCR	F: GGTGTAACCAGAAAGGTGCG R: AGGGAACACATGCCCACTTG
IRF7	qRT-PCR	F: CCAGCTCTCACCGAGCG R: GTTCTTACTGCTGGGGCCAT
Cxcl10	qRT-PCR	F: CCACGTGTTGAGATCATTGCC R: TCACTCCAGTTAAGGAGCCC
CD11c	qRT-PCR	F: TGTTTGAGTGTCAGGAGCAGG R: CGGAGGTCACCTAGTTGGG
HSAP8	qRT-PCR	F: TCACAGTGCCCGCTTACTTC R: TTCCTTTCAGCTCCGACCTTC
MMP12	qRT-PCR	F: GAACTTGCAGTCGGAGGGAA R: TCTTGACAAGTACCATTGAGCA
GAPDH	qRT-PCR	F: GGCAAATTCAACGGCACAGT R: TAGGGCCTCTCTTGCTCAGT
F2RL2	qRT-PCR	F: GCCAAAGTGGCATAAATGTTTCAG R: GCTCCTGTCCAGCCCTCTAT
Spata32	qRT-PCR	F: TCTAAAACCACGCCCCGAGAC R: GGATGCGATTGGTGTCTGGA
Nos2	qRT-PCR	F: GGTGAAGGGACTGAGCTGTT R: ACGTTCTCCGTTCTCTTGCA

2.1.8 Plasmids

Tab. 8 lists the plasmid vectors used for this work describing function, gene for fluorescent protein expression, size and supplier.

Tab. 8: Plasmids

Name	Function	Fluorescent protein	Size	Supplier
pLJM1-EGFP	HIV-1-based, lentiviral expression vector	eGFP	8083 bp	Addgene.org (UK)
pLVX-mCherry-N1	HIV-1-based, lentiviral expression vector	ZsGreen	8763 bp	Clontech Laboratories (USA)
pmCherry-N1	HIV-1-based, lentiviral expression vector	mCherry	8778 bp	Clontech Laboratories (USA)
psPAX2	Lentiviral packing vector	-	10668 bp	Addgene.org (UK)
pMD2.G	VSV-G envelope expressing vector	-	5822 bp	Addgene.org (UK)

2.1.9 Bacteria

Stellar™ Competent Cells (*E. coli* HST08 strain; Clontech Laboratories, USA) were used for In Fusion Cloning related heat shock transformation. One Shot™ TOP10 Chemically Competent *E. coli* (similar to DH10B™ strain; Thermo Fisher Scientific, USA) were used for Re-transformations.

2.1.10 Cell lines

Caco-2 cell line (ATCC® HTB-37™) and human embryonic kidney HEK293T cells (ATCC® CRL-3216™) were purchased from ATCC (USA).

2.1.11 Instruments

Tab. 9 lists the instruments used for this work as well as the respective manufacturers.

Tab. 9: Instruments

Name	Manufacturer
AE31E Inverted Microscope	Motic, Germany
Agagel Maxi	Biometra, Germany
Attune NxT Acoustic Focusing Cytometer	Thermo Fisher Scientific, USA
Autoclave Hiclave HG50	HMC Europe, Germany
Automated cell counter TC10	Bio-Rad Laboratories, Inc., USA
Bacteria incubator UM200	Memmert, Germany
Cell culture flow c-(Max Pro)3-130	Berner, Germany
Cell culture incubator C200	Labotec, Germany
Cell culture incubator Safeflow 1.2	BioAir Solutions, USA
Centrifuge 5810R, 5804R, 5702R and 5430	Eppendorf, Germany
Confocal laser scanning microscope Leica SP5 II	Leica, Germany
ENDOHEM-12 electrode	World Precision Instruments Inc., USA
Flow cytometer CyFlow ML	Partec, Germany
Fluorescence imager LAS-3000	Fujifilm, Japan
Fluorescence microscope IX81-ZDC	Olympus, Japan
Freezer -20°	Liebherr, Germany
Freezer -80°C Hera Freeze Top	Thermo Fisher Scientific, USA
Heracell™ VIOS 160i Incubator	Thermo Fisher Scientific, USA
Heraeus™ Pico™ 21 Microcentrifuge	Thermo Fisher Scientific, USA
Incubator Innova 44	New Brunswick Scientific, USA.
Innova 44 Incubator Shaker	New Brunswick Scientific, USA
Inverted microscope CKX41	Olympus, Japan
Magnetic stirring hotplate MR 3001 K	Heidolph, Germany
Microcentrifuge Minispin plus	Eppendorf, Germany

Microscale AE100	Mettler Toledo, Switzerland
Microwave NN-E2009W	Panasonic, Japan
Millicell® ERS-2 Epithelial Volt-Ohm Meter	Merck Millipore, Germany
Multipette® plus	Eppendorf, Germany
Nitrogen tank LS6000	Taylor-Wharton, Germany
PCR Mastercycler EP Gradient S	Eppendorf, Germany
Pipettes	Eppendorf, Germany
Pipetus® Akku	Hirschmann, Germany
Plate reader Infinite M1000	Tecan, Germany
PowerPac™ HC Power Supply	Bio-Rad Laboratories, Inc., USA
QIAvac 24 Plus vacuum manifold	Qiagen, Netherlands
Real time system CFX96	Bio-Rad Laboratories, Inc., USA
SDS-PAGE chamber Mini Gel Tank	Thermo Fisher Scientific, USA
Synapt G2-Si mass spectrometer	Waters, USA
Table centrifuge Minispin plus	Eppendorf, Germany
Thermo mixer MHR 23	HL by Ditabis, Germany
Transilluminator UVT-28	Herolab, Germany
Ultracentrifuge Optima™ MAX	Beckman Coulter, USA
Vacuum pump Vacusafe comfort	IBS Integra Bioscience, Germany
ViewPix 1100 scanning system	Biostep, Germany
Vortexer Reax Control	Heidolph, Germany
Water bath	Memmert, Germany
X-Cite® 120PC Q	Excelitas Technologies, Germany
Zeta Sizer Nano Series	Malvern Instruments, UK

2.1.12 Software and bioinformatics

Tab. 10 lists the software and bioinformatics used for this work as well as the respective manufacturers or website.

Tab. 10: Software and bioinformatics

Name	Manufacturer or website
Attune NxT Flow Cytometer Software	Thermo Fisher Scientific, USA
Basic Local Alignment Search Tool	https://blast.ncbi.nlm.nih.gov/Blast.cgi
Bio-Rad CFX manager	Bio-Rad Laboratories, Inc., USA
CellSens	Olympus, Japan
DAVID ontology analysis	http://david.abcc.ncifcrf.gov/
FCS Express V4.0	DeNovo Software, USA
FinchTV	Geospiza, Inc., USA
FlowMax 3	Partec, Germany
Geneious R8	Biomatters, New Zealand
ImageJ (Fiji)	http://rsbweb.nih.gov/ij/
LAS AF (Lite)	Leica, Germany
MS Office 2013/2016	Microsoft, USA
NanoDrop 8000 Spectrophotometer	Thermo Fisher Scientific, USA
NCBI Primer BLAST	https://www.ncbi.nlm.nih.gov/tools/primer-blast/
Oligo Calc: Oligonucleotide Properties Calculator	http://biotools.nubic.northwestern.edu/OligoCalc.html
OligoAnalyzer 3.1	https://eu.idtdna.com/calc/analyzer
Plate reader software i-control 1.6.19.0	Tecan, Germany
UCSF Chimera	https://www.cgl.ucsf.edu/chimera/

2.2 Methods

2.2.1 Cell culture techniques

Caco-2 cells were cultured either in MEM Eagle with Earle's BSS (EMEM) or Dulbecco's Modified Eagle Medium (DMEM) without phenol red, supplemented with 10% fetal bovine serum, 1% L-glutamin as well as 100 U/mL penicillin and 100 µg/mL streptomycin at 37 °C, 5% CO₂ in a humidified atmosphere.

Caco-2 cell vials were thawed in a 37 °C water bath and immediately transferred to 20 mL pre-warmed cell culture medium. Cells were then centrifuged at 130 x g for 5 minutes. DMSO-containing supernatant was removed and cells were reconstituted in 20 mL fresh pre-warmed cell culture medium and transferred into a sterile cell culture flask.

Cell culture medium was changed every other day and the cells were subpassaged before reaching 100% confluence. For that purpose, cells were detached using trypsin-EDTA and centrifuged at 130 x g for 5 minutes. Cells were afterwards reconstituted in fresh cell culture medium and cells were split in a ratio of 1:4. Caco-2 cells did never exceed a number of 50 subpassages.

For cell counting, 20 µl of cell suspension were added to 20 µl trypan blue and mixed thoroughly by pipetting up and down. Afterwards, the solution was added to cell counting slides and measured by automated cell counter TC10.

For long term freezing, cells were grown to nearly reach 100% confluence. Cells were then detached using trypsin-EDTA, centrifuged at 130 x g for 5 minutes and reconstituted in fresh cell culture medium. After determining the number of cells via the, cells were again centrifuged at 130 x g for 5 minutes and reconstituted in freezing medium (70% EMEM, 20% FBS, 10% DMSO). Finally, 1 million cells per mL were aliquoted into cryotubes and stored for 48 hours in an isopropanol-filled cryoblock. For long term storage, cells were then transferred to a liquid nitrogen tank.

2.2.2 Nanoparticle synthesis

Polystyrene nanoparticles were synthesized by Katja Klein (Max-Planck-Institute for Polymer Research, Mainz) using direct miniemulsion polymerization. For amino-functionalized nanoparticles, a dispersed phase was prepared using distilled styrene (Merck, Germany) (5.82441 g for PS-CTMACl-NH₂-120), hexadecane (Sigma-Aldrich, USA) (251.33 mg for PS-CTMACl-NH₂-120), 2,2'-azobis(2-methylbutyronitrile) (V59; Wako chemicals, Japan) as initiator (100.26 mg for PS-CTMACl-NH₂-120), as well as Bodipy (523/536) (5.94 mg for PS-CTMACl-NH₂-120) as fluorescence dye. The continuous phase contained 2-aminoethyl methacrylate hydrochloride (AEMG) (0.183 g for PS-CTMACl-NH₂-120), cetyltrimethylammonium chloride solution (CTMA-Cl) (0.30 g for PS-CTMACl-NH₂-120) as surfactant and deionized water (23.72 g for PS-CTMACl-NH₂-120).

For carboxyl-functionalized nanoparticles, the dispersed phase was prepared using distilled styrene (5.8521 g for PS-SDS-COOH-91; 5.7149 g for PS-SDS-COOH-148; 5.85660 g for PS-SDS-COOH-127; 5.67909 g for PS-SDS-COOH-208), hexadecane (151.44 mg for PS-SDS-COOH-91; 152.14 mg for PS-SDS-COOH-148; 150.57 mg for SDS-COOH-127; 152.29 mg for PS-SDS-COOH-208), V59 as initiator (100.91 mg for PS-SDS-COOH-91; 101.2 mg for PS-SDS-COOH-148; 101.00 mg for SDS-COOH-127; 100.98 mg for PS-SDS-COOH-208), acrylic acid (150.87 mg for PS-SDS-COOH-91; 337.0 mg for PS-SDS-COOH-148; 153.27 mg for SDS-COOH-127; 336.63 mg for PS-SDS-COOH-208) as well as either Bodipy (523/536) (6.74 mg for PS-SDS-COOH-91 and 6.12 mg for PS-SDS-COOH-148) or Bodipy (630/650) (5.63 mg for SDS-COOH-127 and 5.37 mg for PS-SDS-COOH-208) as fluorescence dye. The continuous phase contained sodium dodecyl sulfate (SDS) (100 mg for PS-SDS-COOH-91; 20 mg for PS-SDS-COOH-148; 100 mg for PS-SDS-COOH-127; 20 mg for PS-SDS-COOH-208) solved in a total volume of 24 mL deionized water. All further nanoparticles syntheses were scaled accordingly.

2.2.3 Zeta potential and size determination of nanoparticles

Zeta potentials were determined in 2 mL potassium chloride (1mM) via Zeta Sizer Nano Series. For several nanoparticles, also the zeta potential in DMEM was determined. For this purpose, PS-NP were incubated for 1 h in DMEM with FBS to mimic cell culture conditions. Hereupon, nanoparticles were centrifuged for 1 h at 20,000 x g and 4 °C and redispersed in PBS. Finally, Zeta potentials were also determined in 2 mL potassium chloride (1 mM).

Nanoparticle sizes were determined on the Nicomp 380 Submicron Particle Sizer (PSS Nicomp, USA).

2.2.4 Nanoparticle filtration

Polystyrene nanoparticles were incubated for 1 h at a concentration of 500 µg/mL in DMEM containing 10% FBS at 37 °C and 300 rpm shaking. Then, the nanoparticle suspension was filtered through 0.45 µm sterile filters. Concentration of aggregation-free flow-through was determined via fluorescence intensity scan at the plate reader Infinite M1000 (Tecan, Germany), using a calibration curve of dilution series of unfiltered PS-NPs from stock solution as a reference.

2.2.5 Cell viability assays

2.2.5.1 MTS cell proliferation assay

CellTiter 96® AQueous One Solution Cell Proliferation Assay (Promega, USA) was used according to the manufacturer's recommendations with minor modifications. Therefore, 5,000 Caco-2 cells were seeded into a transparent 96-well plate (Greiner, Germany) in a total volume of 100 µl. Cells were incubated for 48 h at 37 °C to achieve adherence. Then, nanoparticles were added in concentrations ranging from 75 µg/mL to 600 µg/mL. As a positive control, a total concentration of 20% DMSO was used. Cells were incubated for another 48 h at 37 °C. Afterwards, 20 µl of CellTiter 96® AQueous One Solution Reagent were added to each well and incubated for 1 h at 37 °C. Finally, absorbance at 490 nm was recorded at the plate reader Infinite M1000 (Tecan, Germany). Mean absorbance of medium without cells as blank was subtracted from all samples. Mean absorbance of untreated Caco-2 cells (negative control) was defined as 100% metabolic activity and all samples were afterwards normalized to this value.

2.2.5.2 CellTiter Glo proliferation assay

CellTiter-Glo® Luminescent Cell Viability Assay (Promega, USA) was used according to the manufacturer's recommendations with minor modifications. Therefore, 10,000 Caco-2 cells were seeded into a white-bottomed 96-well-plate (Greiner, Germany) in a total volume of 100 µl. Cells were incubated for 48 h at 37 °C to achieve adherence. Then, nanoparticles were added in concentrations ranging from 75 µg/mL to 600 µg/mL. As a positive control, a total concentration of 20% DMSO was used. Cells were incubated for another 48 h at 37 °C. The 96-well plate was equilibrated for 30 minutes at room temperature. Then, 100 µl of CellTiter-Glo® Reagent were added to the 100 µl of sample for each well. Cell lysis was induced by incubating for 2 minutes on an orbital shaker. After 10 minutes of further incubation at dark conditions at room temperature, luminescence was read out at the plate reader Infinite M1000 (Tecan, Germany) using OD1 attenuation, 0 ms settle time and 1000 ms integration time. Background luminescence signal (only cell culture medium as blank) was subtracted from every sample. The mean luminescence signal of the negative controls was defined as 100% metabolic activity and each sample was afterwards normalized to this value.

2.2.5.3 Propidium iodide and Annexin V staining

Caco-2 cells were seeded in a density of 2×10^5 cells/mL in 12 well plates and incubated for 48 h at 37 °C to achieve adherence. Then, nanoparticles were added in concentrations ranging from 75 µg/mL to 600 µg/mL. As a positive control, a total concentration of 20% DMSO was used. Cells were incubated for another 48 h at 37 °C. Cell culture medium was removed and cells were washed three times with DPBS. Afterwards, cells were detached using 0.25% trypsin-EDTA and centrifuged for 5 minutes at 130 x g. Each cell sample was reconstituted in 100 µl DPBS containing 2 µg/mL propidium iodide and 9 µg/mL Annexin V-Pacific Blue™ (Thermo Fisher Scientific, USA). Cells were incubated for 15 minute at room temperature and dark conditions. Next, cells were once more centrifuged at 130 x g for 5 minutes and reconstituted in 1 mL DPBS. Finally, cells were measured via Attune® Acoustic Focusing Flow Cytometer (Thermo Fisher Scientific, USA) and analyzed via FCS Express V4.0 (DeNovo Software, USA). For propidium iodide analysis of dead cells, the negative control was set to 100% and samples were afterwards normalized to this value (relative percentage). For Annexin V analysis, the absolute percentage of Annexin V-positive cells was determined, including the negative control.

2.2.6 Endotoxin determination

The Pierce™ LAL Chromogenic Endotoxin Quantitation Assay was performed according to the manufacturer's recommendations. All examined polystyrene nanoparticles were tested in a concentration of 75 µg/mL. Lipopolysaccharide levels were calculated in EU (endotoxin units) / mL by using a calibration curve of pure endotoxin.

2.2.7 In vitro Transcytosis Assay

Polycarbonate Transwells® (Corning Incorporated, USA) with a pore size of 3 μm inserts were used to measure the rate of apical-to-basal transport of nanoparticles in vitro. For this purpose, Caco-2 cells were seeded out in a density of 1.5×10^5 cells per well. The apical chamber was filled with 0.5 mL and the basal chamber with 1.5 mL fresh DMEM (Fig. 6). Both cell culture media were carefully changed every other day without disturbing the growing cell layer on the porous membrane.



Fig. 6: Preparation of Caco-2 cells on transwell Filters.

This figure depicts the Transwell® system in 12-well plates. Caco-2 cells are seeded onto the porous membrane in 0.5 mL DMEM and 1.5 mL DMEM is added into the basal part of the 12-well plate.

After exactly 14 days of differentiation, transepithelial electrical resistance (TEER) -values were determined using an ENDOHM-12 electrode (World Precision Instruments Inc., USA) in combination with the Millicell® ERS-2 Epithelial Volt-Ohm Meter (Merck Millipore, Germany). Since temperature can significantly influence TEER values[138], wells were kept on a pre-heated metal plate for electrical resistance measurements. Only cell layers that exhibited a TEER-value over $500 \Omega \times \text{cm}^2$ before and after the incubation with nanoparticles

were used for the analysis. Cells were afterwards incubated with 75 – 600 $\mu\text{g/mL}$ fluorescent nanoparticles resuspended in DMEM in the apical chamber for 24 hours.

Finally, at least 2 x 200 μl of the basal medium was transferred to a transparent 96 well plate (Greiner, Germany). Fluorescence was read out at the plate reader Infinite M1000 (Tecan, Germany) using an excitation wavelength of 523 nm (5 nm bandwidth) and an emission wavelength of 536 nm (5 nm bandwidth). Background fluorescence signal (only DMEM as blank) was subtracted from every sample. The rate of transcytosis was calculated using a dilution series calibration curve ranging from 300 $\mu\text{g/mL}$ to 0.3 $\mu\text{g/mL}$.

2.2.8 Adjustment of the pH value in DMEM

Dulbecco's Modified Eagle's Medium without sodium bicarbonate was obtained by Sigma-Aldrich (USA). The powder was transferred to a sterile 1 liter flask and supplemented with 10% FBS and 1% L-glutamine as well as 100 U/mL penicillin and 100 $\mu\text{g/mL}$ streptomycin. Then, 3.9 g MES were added and the flask was filled up to exactly 1 liter with sterile water to obtain a buffer concentration of 20 mM. Next, the cell culture medium was heated to 37 $^{\circ}\text{C}$ and the pH was adjusted to 6.5 using hydrochloric acid. Finally, medium was filtered through 0.2 μm sterile filters.

2.2.9 RNA extraction

Total RNA was extracted using the RNeasy Mini Kit (Qiagen, Netherlands) according to the manufacturer's protocol. Approximately 6×10^5 Caco-2 cells or 2×10^6 BMDCs were used. For cell lysis, QIAshredder spin columns (Qiagen, Netherlands) were used. All surfaces were cleaned with RNaseTM AWAY spray (Thermo Fisher Scientific, USA) prior to RNA extraction. For RNA extraction from BMDCs, an optional DNase digestion using DNase I (Qiagen, Netherlands) according to the manufacturer's protocol was performed. RNA extractions were stored at -20 $^{\circ}\text{C}$ until further applications.

2.2.10 cDNA synthesis

All cDNAs were synthesized with the iScript™ cDNA Synthesis Kit (Bio-Rad, USA) according to the manufacturer's protocol. A standard 20 µl cDNA synthesis consisted of the following formulation:

- 5x iScript Reaction Mix 4 µl
- iScript Reverse Transcriptase 1 µl
- RNA template 1–100 ng
- Nuclease-free water to 20 µl

All cDNA reactions were briefly mixed by pipetting up and down and transferred to the Mastercycler EP Gradient S (Eppendorf, Germany) for cDNA synthesis (Tab. 11).

Tab. 11 lists a standard cDNA synthesis protocol.

Tab. 11: Standard cDNA synthesis protocol

Step	Temperature [°C]	Length
1	25	5 minutes
2	42	30 minutes
3	85	5 minutes
4	4	∞

2.2.11 Quantification of nucleic acids

Nucleic acids were quantified using the NanoDrop 8000 Spectrophotometer (Thermo Fisher Scientific, USA) according to the manufacturer's recommendations. 1.5 µl of sample were used for each measurement. Ethanol and other solvent residues were calculated using the absorbance ratio A_{260}/A_{230} . Protein contaminations were estimated using the absorbance ratio A_{260}/A_{280} . Only samples exceeding a threshold of 1.8 were used for further experiments.

2.2.12 Primer design

The following guide lines were followed for primer design:

- The length should range from 17 to 28 nucleotides (albeit primers designed for In-Fusion® HD Cloning may exceed this due to the addition of 15 necessary homologous base pairs at 5' end).
- Primers should exhibit a GC-content between 40-60%.
- If possible, primers should exhibit a G or C at 3' end.
- Melting temperature should be between 55 °C and 65 °C, while both associated primers (Forward and reverse) should have melting temperatures within the range of < 3 °C.
- Primers should not form homo- and heterodimers as well as hairpins.
- Especially 3' ends should not be complementary to each other.
- Primers should not contain multiple (> 3) identical consecutive bases.

Primers were designed using Geneious R8 and controlled using the tools Oligo Calc and Oligo Analyzer 3.1. To determine if the respective primer is truly unique, a BLAST search was performed (<https://blast.ncbi.nlm.nih.gov/Blast.cgi>). Primers were synthesized and HPLC-purified by Sigma-Aldrich (USA) and reconstituted to a concentration of 100 µM in nuclease-free water. Primers were stored at -20 °C until further usage.

2.2.13 Polymerase chain reaction

A standard 50 μ l PCR reaction consisted of the following formulation:

- 10x Standard *Taq* Reaction Buffer 5 μ l
- 10 mM dNTPs 1 μ l
- 10 μ M Forward Primer 1 μ l
- 10 μ M Reverse Primer 1 μ l
- *Taq* Polymerase 1 μ l
- Template DNA ~ 1 ng; < 1000 ng
- Nuclease-free water to 50 μ l

Every component, with the exception of *Taq* Polymerase, was vortexed thoroughly before the addition. PCR reactions were then briefly mixed by pipetting up and down and transferred to the PCR Mastercycler EP Gradient S (Eppendorf, Germany) for cyclic amplification (Tab. 12).

Tab. 12 lists a standard PCR program for DNA amplification.

Tab. 12: Standard PCR program

Step		Temperature [°C]	Length	Count
1	Initial Denaturing	95	1 minute	1x
2	Denaturing	95	30 seconds	35x
	Annealing	Variable (58-62)	45 seconds	
	Elongation	68	1 minute per kb	
3	Final Elongation	68	10 minutes	1
4	Storage	4	∞	∞

2.2.14 Agarose gel electrophoresis

To confirm successful amplification via polymerase chain reaction and / or to purify PCR fragments as well as monitoring the quality of extracted RNAs, nucleic acids were separated via agarose gel electrophoresis. Therefore, a 1% agarose (in TAE buffer) gel was prepared and SYBR® Safe DNA gel stain (Thermo Fisher Scientific, USA) was added in a dilution of 1:10,000. Then, DNA or RNA samples were mixed with Gel Loading Dye (Thermo Fisher Scientific, USA), added into the gel pockets and electrophoresis was performed for approximately 1 h at 100 V in the horizontal gel chamber Agagel Maxi (Biometra, Germany). For size determination, either the GeneRuler 1 kb DNA Ladder or GeneRuler 100 bp Plus DNA Ladder (both by Thermo Fisher Scientific, USA) were used. Finally, agarose gels were analyzed and documented via Fluorescence imager LAS-3000 (Fujifilm, Japan).

2.2.15 DNA extraction from agarose gels

In case of PCR product purification, DNA bands were visualized using the Transilluminator UVT-28 (Herolab, Germany). Respective DNA bands were excised using a scalpel and transferred to Eppendorf tubes. Next, excised DNA agarose fragments were weighed and DNA was extracted using the QIAquick Gel Extraction Kit (Qiagen, Netherlands) according to the manufacturer's recommendations. DNA was eluted in nuclease-free water and stored at -20 °C until further usage.

2.2.16 DNA restriction

DNA restrictions were performed using the following formulation:

- | | |
|-----------------------|---------------|
| • 10x Cutsmart Buffer | 5 μ l |
| • Eco R1 HF | 1 μ l |
| • Plasmid DNA | ~1 μ g |
| • Nuclease-free water | to 50 μ l |

Enzymatic restriction was carried out for at least 1 h at 37 °C. Then, linearized vector was separated via agarose gel electrophoresis and subsequently extracted and purified via QIAquick Gel Extraction Kit (Qiagen, Netherlands). In case of insert confirmation after cloning, vector and the respective restricted insert were analyzed and documented via Fluorescence imager LAS-3000 (Fujifilm, Japan).

2.2.17 In-Fusion® HD Cloning

Recombinant plasmids were established using the In-Fusion® HD Cloning Kit (Clontech Laboratories, USA) according to the manufacturer's protocol. Therefore, primers were designed that offered 15 bases of homology with either pLJM1-eGFP, pLVX-ZsGreen1-N1 or pLVX-mCherry-N1 at their respective 5' ends. Plasmids were then linearized using the restriction enzyme Eco R1. After amplifying the target cDNAs by PCR and thereby adding the homologous bases to the amplicons, In-Fusion® HD Cloning reaction was performed. Here, reactions were scaled to half of the manufacturer's recommendations.

- | | |
|---------------------------------|---------|
| • 5x In-Fusion HD Enzyme Premix | 1 µl |
| • Linearized vector | 25 ng |
| • Purified PCR fragment | 50 ng |
| • Nuclease-free water | to 5 µl |

Reactions were incubated for 15 minutes at 50 °C, then placed on ice and finally stored at -20 °C until transformation.

2.2.18 Heat shock transformation

For each heat shock transformation, 100 µl Stellar™ Competent *E. coli* (Clontech Laboratories, USA) in a 1.5 ml microcentrifuge tube were gently thawed in an ice bath in. Then, 1 ng of DNA was added to bacteria. Tubes were placed on ice for 30 minutes for equilibration. Next, heat shock was performed for 45 seconds at 42 °C. Bacteria were once more placed on ice for 2 minutes. Afterwards, pre-warmed SOC medium was added to a final volume of 500 µl and bacteria were incubated for 1 hour at 37 °C and 300 rpm shaking. Finally, 50-100 µl were plated on ampicillin-containing agar plates and incubated overnight at 37 °C. For Re-transformations, One Shot™ TOP10 Chemically Competent *E. coli* (Thermo Fisher Scientific, USA) were used according to the manufacturer's protocol. All bacterial agar plates were stored at 4 °C.

2.2.19 Colony PCR

For colony PCR, at least 3 clones for each gene were picked from the agar plate via 10 µl pipette tips. Each pipette tip was then slewed in 10 µl nuclease-free water and finally transferred to 5 mL LB-Medium containing ampicillin (50 µg/mL). Then, a standard PCR (see 2.2.13) was performed using chunks of the respective clones in 10 µl water as DNA template. PCR reactions were analyzed via agarose gel electrophoresis and documented via Fluorescence imager LAS-3000 (Fujifilm, Japan). LB-media containing positive clones were finally incubated overnight at 37 °C and 225 rpm shaking in the Bacteria incubator UM200 (Mettler, Germany).

2.2.20 Plasmid isolation

Plasmid isolations were carried out via Plasmid Maxi Kit or Plasmid Mini Kit (both obtained by Qiagen, Netherlands) according to the manufacturer's recommendations with minor modifications. For mini preps, 5 mL of overnight bacterial cultures were used. For maxi preps, 100 mL of bacterial cultures were used. All plasmids were eluted in nuclease-free water instead of elution buffer (50 µl for mini preps and 400 µl for maxi preps). Before elution, nuclease-free water was pre-warmed to 37 °C to increase elution efficacy. All centrifugation steps were carried out in the table centrifuge Minispin plus (Eppendorf, Germany). For maxi preps, the QIAvac 24 Plus vacuum manifold (Qiagen, Netherlands) was used in combination with a vacuum pump. Plasmid concentrations were quantified by NanoDrop 8000 Spectrophotometer (Thermo Fisher Scientific, USA). Confirmation of successful insertion of target cDNA was confirmed via test restriction with Eco R1. Plasmids were stored at -20 °C until further applications.

2.2.21 Sanger Sequencing

Sanger Sequencing of plasmids was carried out by StarSeq (Germany). The following formulation was used in a 0.2 ml Eppendorf tube:

- | | |
|------------------------------|--------------|
| • Sequencing Primer (F or R) | 1 μ l |
| • Plasmid DNA | 600 – 700 ng |
| • Nuclease-free water | to 7 μ l |

Sequences were obtained in .abi and .seq format. Chromatograms were analyzed via FinchTV (Geospiza, Inc., USA) and Geneious R8 (Biomatters, New Zealand). First few bases were trimmed in each chromatogram, then forward and reverse sequence were aligned and checked against the reference sequence of the respective gene's cDNA. In addition, maintaining of the GFP-gene-of-interest or gene-of-interest-GFP open reading frame was thoroughly controlled for every construct.

2.2.22 Generation of lentiviral particles

For the establishment of stable transgenic cell lines a third generation lentiviral vector system was used. The system consisted of psPAX2 as packaging plasmid, pMD2.G as VSV-G envelope expressing plasmid as well as either pLJM1-eGFP, pLVX-ZsGreen1-N1 or pLVX-mCherry-N1 as transfer plasmid. For the production of lentiviral particles, HEK293-T cells were seeded out in a density of 2×10^5 cells/well in 2 mL fresh DMEM and incubated for 24 hours at 37 °C in a humidified atmosphere. For transfection, 2 μ g transfer plasmid, 1 μ g psPAX2 and 0.5 μ g pMD2.G (if higher concentrations were used, the ratio of 4:2:1 was maintained) were mixed with 10.5 μ l Polyethyleneimine (1 mg/mL) in 200 μ l OPTI-MEM (Gibco, USA), vortexed thoroughly and incubated for at least 15 minutes at room temperature. The suspension was added dropwise to the HEK293-T cells. After 5 hours of incubation, medium was changed to DMEM without additives to prevent any cytotoxic effects of polyethyleneimine. Cells were incubated for another 48 hours to produce lentiviral particles. Finally, lentiviral supernatant was filtered through a 0.45 μ m membrane to remove any HEK293-T cells and either directly used for transfection (see 2.2.23) or further concentrated. For concentration, total supernatant was centrifuged for 2 hours at 25,000 x g

in the Ultracentrifuge Optima™ MAX (Beckman Coulter, USA). Lentiviral particles were reconstituted in 100 µl PBS/HEPES buffer, quickly shock frosted in liquid nitrogen and long term stored at -80 °C until further applications. All experiments containing lentiviral particles were carried out in a biosafety level 2 laboratory.

2.2.23 Stable transduction of eGFP-/ ZsGreen- and mCherry-tagged proteins

2 x 10⁵ Caco-2 cells were seeded out in 2 mL DMEM. After controlling the lentiviral titer via Lenti-X™ GoStix™ (Clontech Laboratories, USA), (concentrated) lentiviral supernatant was added to the Caco-2 cells for 48 hours. To increase the efficiency of infection, polybrene was added to a final concentration of 8 µg/mL. Finally, stable transfected Caco-2 cells were actively selected using 3 µg/mL puromycin (a kill curve was established beforehand) for up to 7 days. To preserve stable transgene expression, cells were cultivated in 0.2 µg/mL puromycin during the experiments. For the establishment of double transgenic cell lines, stable transgenic cells were re-infected with lentiviral particles containing a second fluorescence-coupled protein at the same conditions. Due to the fact that the used plasmids featured the same resistance cassette for puromycin, cells could not be selected a second time.

2.2.24 Fluorescence microscopy

The microscope IX81-ZDC (Olympus, Japan) was used in combination with the X-Cite® 120PC Q light source (Excelitas Technologies, Germany) for fluorescence microscopy of human cells. UPlanFl 10x/0.30 and 20x/0.30 objectives (Olympus, Japan) were used to analyze the cells and images were recorded using the high speed camera F-View II (Olympus, Japan). Pictures were finally analyzed using the software CellSens (Olympus, Japan).

2.2.25 Transient transfection

Caco-2 cells were seeded in a density of 1×10^5 cells in DMEM in a 12-well plate and incubated at 37 °C for 24 hours until adherence was achieved. Then, plasmids containing GFP-coupled cDNA were complexed either with Fugene HD (Promega, USA) or Lipofectamine 3000 (Thermo Fisher Scientific, USA). For Fugene HD transfection, 1 µg of plasmid DNA and 3 µl of Fugene HD reagent in 50 µl OPTI-MEM were mixed carefully by pipetting up and down and incubated for 10 minutes at room temperature for complexation. For Lipofectamine 3000 transfection, 1 µg of plasmid DNA, 2 µl of P3000 reagent and 3 µl of Lipofectamine 3000 reagent in 50 µl OPTI-MEM were mixed by pipetting up and down and incubated for 10 minutes at room temperature for complexation. DNA/transfection complexations were added dropwise to Caco-2 cells and incubated at 37 °C. Transfection effects were visualized after 24 and 48 hours via fluorescence microscopy or confocal laser scanning microscopy.

2.2.26 Fluorescence spectroscopy

Fluorescence spectroscopy was performed on the plate reader Infinite M1000 (Tecan, Germany). For absorbance and fluorescence measurements, transparent bottomed 96-well plates (Greiner, Germany) were used. For luminescence measurements, white bottomed 96-well plates (Greiner, Germany) were utilized. Measurements were analyzed via i-control 1.6.19.0 (Tecan, Germany).

2.2.27 Lentiviral titer detection

Presence of lentiviral particles was determined using LentiX™ GoStix™ (Clontech Laboratories, USA). Therefore, 20 µl of lentiviral supernatant were added to the sample well and the test was performed according to the manufacturer's recommendations. A positive result indicated at least 5×10^5 IFU/ml.

2.2.28 Confocal laser scanning microscopy

All confocal laser scanning microscopy applications were performed on the LSM SP5 STED Leica Laser Scanning Confocal Microscope (Leica, Germany). The setup consisted of an inverse fluorescence microscope DMA 6000 CS and multiple laser setups in combination with five different detectors between 400 and 800 nm as well as a 37 °C live cell imaging mode with 5% CO₂ supply. A HCX PL APO 63 x 1.3 glycerol objective was used for the live cell imaging studies, while a HCX PL APO CS 63 x 1.4 oil objective was used for fixed cells. Fluorescent nanoparticles as well as GFP-, mCherry and ZsGreen-coupled proteins were excited and detected in a sequential scan mode. For excitation, a HeNe laser (~0.8 mW; λ = 488 or 514 nm) and a DPSS laser (~1.3 mW; λ = 561 nm) were used. GFP and ZsGreen were detected at 499 – 520 nm, mCherry was detected at 590 – 650 nm, fluorescent nanoparticles were detected at 546 – 551 nm or 575 – 630 nm. Pictures were analyzed and edited with the software LAS AF Lite (Leica, Germany). Either 35 mm μ -Dish or 8 Well μ -Slides (both obtained by Ibidi, Germany) were used as cell culture vessels for confocal laser scanning microscopy.

2.2.29 Cell fixation

Caco-2 cells were fixed in 4% paraformaldehyde for 15 minutes. Afterwards, cells were washed 3x with DPBS and maintained in DPBS until analysis.

2.2.30 Cell membrane staining

Cell membranes were stained with either CellMask™ Deep Red or Orange plasma membrane stain (both obtained by Thermo Fisher Scientific, USA). Therefore, Caco-2 cells were incubated in 5 μ g/mL CellMask dye in HBSS for 5 minutes. Afterwards, cells were immediately analyzed via confocal laser scanning microscope.

2.2.31 Quantification of co-localization

For co-localization kinetics, Caco-2 cells were seeded out in a density of 1×10^4 cells/mL in 8 Well μ -Slides (Ibidi, Germany) and incubated at 37 °C, 5% CO₂ in a humidified atmosphere until they reached 100% confluence. Fluorescent nanoparticles were added in a concentration of 100 μ g/mL to monitor different stages of intracellular trafficking (30 minutes till 24 hours, see Fig. 7). After a maximum incubation of 2 h, cells were washed three times with PBS to eliminate the chances of any further uptake event. Afterwards, DMEM without nanoparticles was added to allow monitoring about the further trafficking of already internalized nanoparticles. After incubation, cells were fixed with 4% paraformaldehyde and analyzed at the confocal laser scanning microscope. Here, a minimum of 10 cells were chosen for each fluorescence-dye-coupled-protein and each point of time. Z-stacks of each cell were recorded with a vertical step size of 0.2 μ m. Obtained data was analyzed thoroughly by manually counting co-localization occurrence independently by two researchers (kindly assisted by bachelor student Christopher Diesler) and pooling the data afterwards. The standard deviation resulted from the 10 (+) cells that were used to calculate the arithmetic mean.

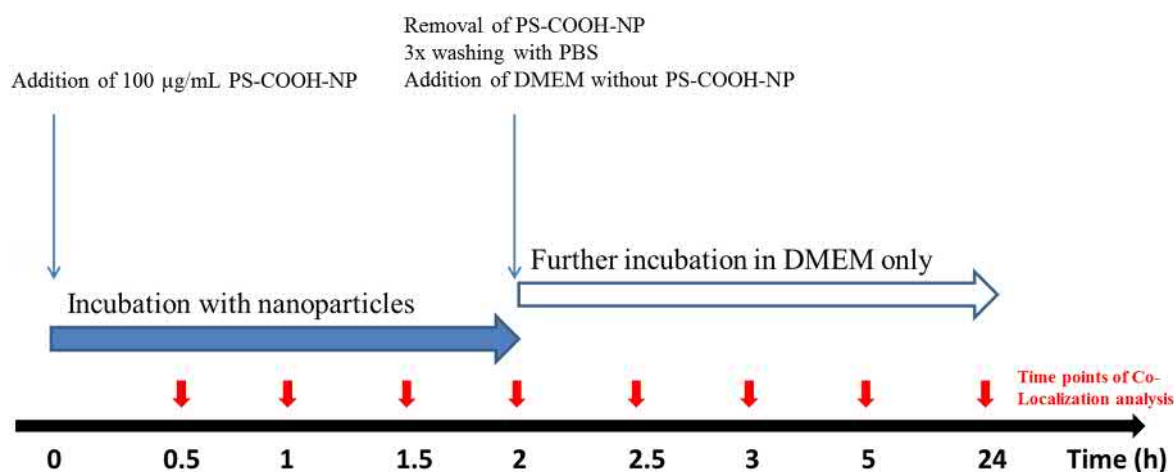


Fig. 7: Analysis of co-localization: Time Scheme.

Nanoparticles were added in a concentration of 100 μ g/mL to the Caco-2 cells growing in 8 Well μ -Slides. The time points 0.5 h until 2 h (red arrows) were measured without removing the nanoparticles from the cell culture medium. After 2 h, polystyrene nanoparticles were removed and all samples washed 3x with PBS. Fresh DMEM without polystyrene nanoparticles was added to enable further trafficking in the cells without a distortion via new endocytosed nanoparticles. Time points 2.5 h until 24 h (red arrows) were subsequently analyzed for co-localization.

2.2.32 Automatic quantification via Fiji script

To confirm and further complement our manual co-localization quantifications, we additionally used an automatic script for the quantification of our Z-stacks for the 8 different time points. This quantitative analysis of the object-based co-localization was performed with a customized macro that runs in Fiji or ImageJ[139]. The general idea is to create first a maximum z-projection of an image z-stack, containing two images: one image with vesicle staining (channel 1) and one image with nanoparticles (channel 2). Both channels are filtered to select the vesicular structures and nanoparticles, and converted into binary masks displaying selected black objects on a white background. The binary masks were multiplied with each other's to create a result mask displaying the NPs in vesicular structures. The following script was used for the analysis:

```
//get directory with lif files
dir=getDirectory("Choose directory with the lif files");
if(!File.exists(dir+"results\\")) //make directory for results
    File.makeDirectory(dir+"results\\");
print("processing directory ",dir);

run("Bio-Formats Macro Extensions");

fileList=getFileList(dir);
nFiles=lengthOf(fileList);
print(nFiles);
for(j=0;j<nFiles;j++) { //loop over all files in the directory
    if (endsWith(fileList[j],".lif")) {
        Ext.setID(dir+fileList[j]);
        Ext.getSeriesCount(seriesCount);
        print(seriesCount);
        for(i=1;i<seriesCount;i++) { //Loop over all images in .lif file, start series always with 1 {
            run("Bio-Formats Importer", "open=["+dir+fileList[j]+"] color_mode=Default
            view=Hyperstack stack_order=XYCZT series_"+i);
            current=getTitle();
            getDimensions(width, height, channels, slices, frames);
            getPixelSize(unit, pixelWidth, pixelHeight);
            print("width",width,"height",height,"channels",channels,"slices",slices,"frames",frames,"unit",unit,"
            pixelSize",pixelWidth);
            Title1=getTitle();
            print(Title1);
        }
    }
}
```

//Max z-projection and split channels

```

run("Z Project...", "projection=[Max Intensity]");
run("Make Substack...", "channels=1,3");
rename("2channels");
//run("Channels Tool...");
Stack.setDisplayMode("color");
Stack.setChannel(1);
run("Green");
Stack.setChannel(2);
run("Red");
Stack.setDisplayMode("composite");
run("Duplicate...", "title=vesicles duplicate channels=1");
selectWindow("2channels");
run("Duplicate...", "title=nanoparticles duplicate channels=2");
//run("Split Channels");

//Creation of masks for both channels
run("Set Measurements...", "area max centroid shape redirect=None decimal=2");
roiManager("Associate", "true");
//Creating masks of C0 and C1
selectWindow("vesicles");
run("FeatureJ Laplacian", "compute smoothing=2.5");
run("6_shades");
//run("Threshold...");
setAutoThreshold("Default");
run("Convert to Mask");
//run("Dilate");
run("Fill Holes");
run("Watershed");
selectWindow("nanoparticles");
run("FeatureJ Laplacian", "compute smoothing=1");
run("6_shades");
//run("Threshold...");
setAutoThreshold("Default");
run("Convert to Mask");
//run("Dilate");
run("Watershed");

//Find overlapping structures in vesicle image (C0) and nanoparticle (C1) image
imageCalculator("Multiply create 32-bit", "nanoparticles Laplacian", "vesicles Laplacian");

```

```

selectWindow("Result of nanoparticles Laplacian");
rename("co-localizing NP and vesicles");
run("8-bit");

//Analyze particles
run("Analyze Particles...", "display exclude clear summarize add");
run("Analyze Particles...", "size=0-Infinity circularity=0.00-1.00 show=Nothing display exclude clear add");
roiManager("Show None");
roiManager("Show All with labels");
roiManager("Show All");
run("Create Selection");
run("Measure");

// Visualization of overlapping structures
selectWindow("2channels");
run("Restore Selection");
run("Enlarge...", "enlarge=1");
run("Properties... ", "name=[] stroke=white width=0 fill=none");
run("Enhance Contrast", "saturated=0.35");

//Measure Vesicles
selectWindow("vesicles Laplacian");
run("8-bit");
run("Analyze Particles...", "display exclude clear summarize add");

//Measure Vesicles
selectWindow("nanoparticles Laplacian");
run("8-bit");
run("Analyze Particles...", "display exclude clear summarize add");

//Saving
selectWindow("2channels");
saveAs("tif", dir+"results/"+substring(current,lengthOf(current))+"colocalizing NPs and vesicles"+i+".tif");
selectWindow("co-localizing NP and vesicles");
saveAs("tif", dir+"results/"+substring(current,lengthOf(current))+"Coloc_NPs mask"+i+".tif");

selectWindow("Summary");
saveAs("Results", dir+"results/"+substring(current,lengthOf(current))+"Summary"+i+".xls");
selectWindow("Results");
saveAs("Results", dir+"results/"+substring(current,lengthOf(current))+"Results"+i+".xls");
run("Close All");

```

```
}  
}  
  
print("Done");  
waitForUser("Job Done", "Please check results");  
run("Close All");
```

2.2.33 Cryo high pressure freezing transmission electron microscopy

The samples were frozen under high pressure[140] (2100 bars) using a high pressure freezing machine (Engineering Office M. Wohlwend GmbH, Switzerland). Caco-2 cells grew up and were treated with polystyrene nanoparticles (500 µg/mL) on sapphire discs which were enclosed in a small volume between two specimen carriers and locked inside the specimen pressure chamber.

Dehydration of the samples at -90 °C took place inside the freeze substitution machine EM AFS 2 (Leica, Germany). The organic solvent that was used was a solution of 0.2% osmium tetroxide, 0.1% uranyl acetate and 5% water in acetone. The samples were rinsed in acetone and infiltrated in EPON 812. The polymerization took place at 60°C. Ultrathin sections were collected using a Leica ultramicrotome.

Electron micrographs were taken on the CCD camera Ultrascan 1000 (Gatan, USA) while TEM was operated at 200 kV. The Digital Micrograph software (Gatan, USA) was used to collect the images. All TEM measurements were carried out by Dr. Maria Kokkinopoulou (Max Planck Institute for Polymer Research, Germany).

2.2.34 Super-resolution Microscopy

Super-resolution (SR) images of NPs were acquired by ground-stated depletion followed by individual molecule return (GSDIM) with a commercial set up (Leica SR-GSD 3D, Leica Germany)[141]. The inverse widefield microscope DMI AF6000 (Leica, Germany) was equipped with a 160x/1.43 plan apochromatic oil objective and an EMCCD camera iXon3 ultra 897 (Andor, UK). For SR imaging, cells were seeded in 35 mm petri dishes with glass bottom (Ibidi, Germany), fixed with 4% PFA, washed and submersed in 1 mL TRIS buffer (20 mM Tris/HCl, 50 mM NaCl, pH 8). First, widefield images of the GFP-fusion proteins were acquired by excitation with a 488 nm laser (300 mW, ca. 10%) and emission was filtered by a 488 HP-T filter cube combination (Em 505-605 nm). Then fluorescence excitation and photoswitching of the NPs was induced with a 532 nm (500 mW laser, 20-30% laser power) in TIRF mode and emission was filtered by a 532 HP-T filter cube combination (Em 550 – 650 nm). Between 5,000 – 10,000 frames were collected at 100 Hz (10 msec exposure time) with an image size of 180 x 180 pixels. Fluorescence image acquisition was performed with the LAS AF 4.0 software (Leica, Germany) and image processing with Fiji and ThunderSTORM[142]. Following camera settings for the conversion of events into photons were used in ThunderSTORM: Pixel size 100 nm, photonelectrons per A/D count 12.09, base level 100, EM gain 300. The raw data were filtered with a wavelet filter and the localization of the molecules were approximated by local intensity maxima including 8 neighborhood pixels. The subpixel localization of molecules was determined by fitting the PSF with an integrated form of a symmetric 2D Gaussian function by a maximum likelihood estimation[143-145]. For the overlay of the widefield and the super-resolution image, the widefield image was resized in from 180 x 180 pixels to 900 x 900 pixels (Fiji, plugin “Resize”)[145] and smoothed by a Gaussian blur filter (sigma = 2). All super-resolution microscopy images were recorded by Dr. Sandra Ritz (Institute of Molecular Biology, Germany).

2.2.35 Nanoparticle treatment of cells

For nanoparticle treatment, Caco-2 cells were seeded either in μ -Slide 8 Well Glass Bottom dishes (Ibidi, Germany), μ -Dish 35 mm dishes (Ibidi, Germany) or onto Transwell® membrane filters. Cells were washed briefly with DPBS (with the exception of cells on transwell filters). Then, nanoparticles were added in concentrations ranging from 75 μ g/mL to 600 μ g/mL. Before analysis, cells were washed at least once with DPBS to remove free nanoparticles from the supernatant.

2.2.36 Desorption of proteins from nanoparticles

Caco-2 cells were seeded out in a density of 1.5×10^5 and cultivated for exactly 14 days at 37 °C on Polycarbonate Transwells® (Corning Incorporated, USA) with a pore size of 3 μ m. After cells were completely differentiated, polystyrene nanoparticles were added into the apical medium in a concentration of 500 μ g/mL in 0.5 mL fresh DMEM with 10% FBS and incubated for 24 hours (only cell layers exhibiting a TEER value over 500 were used). The basal part of the system was filled with 1.5 mL DMEM without FBS to minimize the bovine proteins for later mass spectrometry analysis. After 24 h, the basal medium was transferred to a 1.5 mL tube and centrifuged for 1 h and 4 °C at 20,000 x g. The supernatant was discarded and the pellet was resuspended in 300 μ l urea-thiourea buffer (7M Urea, 2 M Thiourea, 4% CHAPS). After 15 minutes of incubation at 37 °C and 300 rpm, tubes were centrifuged again for 1 h and 4 °C at 20,000 x g. The supernatant was carefully transferred to fresh 1.5 mL protease-free tubes and protein concentrations were determined using the Pierce™ 660nm Protein Assay Kit (Thermo Fisher Scientific, USA). The further protein in-solution digestion and Liquid-chromatography mass-spectrometry (LC-MS) analysis procedures were carried out by Dr. Susanne Schöttler (Max Planck Institute for Polymer Research, Germany) according to the protocol used in [54].

2.2.37 Flow cytometry

For the quantification of cellular nanoparticle uptake and cytotoxicity, flow cytometry was performed either on the CyFlow ML (Partec, Germany) or on the Attune NxT Acoustic Focusing Cytometer (Thermo Fisher Scientific, USA). Caco-2 cells were seeded in a density of 2×10^5 cells/mL in 12-well plates. After nanoparticle incubation (75 – 600 $\mu\text{g/mL}$), cells were detached using 0.25% trypsin-EDTA, washed 3x with DPBS and reconstituted in 1 mL DPBS. Nanoparticle uptake measurements at the CyFlow ML cytometer (Partec, Germany) were performed by using a 488 nm laser for excitation and a 527 nm band pass filter for emission of Bodipy 1 dye. Nanoparticle uptake measurements at the Attune NxT Acoustic Focusing Cytometer (Thermo Fisher Scientific, USA) were performed by using a 488 nm laser for excitation and a 530 nm band pass filter for emission of Bodipy 1 dye. In addition, toxicity measurements at the Attune NxT Acoustic Focusing Cytometer were performed by using a 488 nm laser for excitation and a 590 nm band pass filter for emission of propidium iodide (dead cells) as well as a 405 nm laser for excitation and a 440 nm band pass filter for emission of Pacific BlueTM-Annexin V (apoptosis). All data was analyzed via FCS Express V4 (DeNovo Software, USA). First, all cells were gated on a forward/sideward scatter plot to exclude disturbing cell debris. For the percentage calculation of dye-positive cells, a gate for dye-positive cells, which included 1% of untreated negative control cells, was used. In case median fluorescence were determined, MFIs of untreated negative control cells were subtracted from every sample. All samples were measured at least in biological duplicates.

2.2.38 SDS-PAGE

The following 30 μ l formulation was used for SDS-PAGE:

- NuPAGE™ LDS Sample Buffer 7.5 μ l
- NuPAGE™ Sample Reducing Agent 3 μ l
- Protein sample 19.5 μ l

Samples were mixed by pipetting up and down and afterwards incubated for 10 minutes at 70 °C. Then, samples were transferred to a NuPAGE™ 10% Bis-Tris Protein Gel (Thermo Fisher Scientific, USA) and SDS-PAGE was performed in a SDS-PAGE chamber Mini Gel Tank (Thermo Fisher Scientific, USA) filled with NuPAGE™ MES SDS Running Buffer (Thermo Fisher Scientific, USA). Electrophoresis was performed for 1.5 h at 150 V. 10 μ l SeeBlue™ Plus2 Pre-stained Protein Standard (Thermo Fisher Scientific, USA) were used for size determination of proteins. Finally, protein bands were visualized by using either Coomassie SimplyBlue SafeStain (Thermo Fisher Scientific, USA) or the Pierce Silver Staining Kit (Thermo Fisher Scientific, USA) according to the manufacturer's protocols. Gels were documented using the ViewPix 1100 scanning system (Biostep, Germany).

2.2.39 Determination of protein concentrations

Protein concentrations were determined using a Pierce 660nm Protein Assay (Thermo Fisher Scientific, USA). 10 μ l protein sample were mixed with 150 μ l Pierce 660nm Protein reagent in transparent 96-well plates (Greiner, Germany). After shaking for 1 minute and incubating for 5 minutes at room temperature, absorbance at 600 nm was determined via plate reader Infinite M1000 (Tecan, Germany). Protein sample concentrations were calculated by using a standard curve of bovine serum albumin ranging from 1600 μ g/mL to 25 μ g/mL as a reference. Each protein sample was measured in technical triplicates.

2.2.40 Nanoparticle functionalization

Nanoparticles were mixed with Fc region or Vitamin B₁₂ in different pH buffers (pH 2.7, 5.5, 6.1, 7.5, 9.5, 11) for 1 hour at 37 °C and constant shaking (300 rpm). Afterwards, functionalized nanoparticles were centrifuged for 1 h at 20,000 x g, washed 3 x with DPBS and a subsequent centrifugation and finally redispersed in sterile water. Concentration was determined at the plate reader Infinite M1000 (Tecan, Germany) by using a standard curve of non-functionalized nanoparticles.

2.2.41 Generation of BMDCs

Iliac crests, femora and tibiae were prepared from mice under sterile conditions, disinfected with 70% ethanol and transferred to EMEM containing 1% P/S. Bones were sliced and rinsed with a small cannula until they appeared white. Bone marrow cells were pressed through a 40 µm cell strainer and centrifuged for 10 minutes at 4 °C and 300 x g. Then, 2 x 10⁶ cells were transferred to a petri dish in 10 mL IMDM containing 2 mM L-glutamin, 1% P/S and 50 µM 2-mercaptoethanol as well as 10 ng/mL GM-CSF. After 3 and 6 days, respectively 5 mL medium containing GM-CSF were added to the petri dish. On day 7 or 8, non-adherent dendritic cells were harvested by gentle rinsing. Cells were transferred to 6-well plates for further experiment. Generation of BMDCs was carried out by David Paßlick (University Medical Center, Mainz).

2.2.42 Quantitative real time polymerase chain reaction



For quantitative real time polymerase chain reactions, specific qPCR primers were designed for the amplification of ~200 bp DNA fragments. The following formulation was used:

- | | |
|----------------------------|----------|
| • iQ™ SYBR® Green Supermix | 10 µl |
| • F-Primer | 1 µl |
| • R-Primer | 1 µl |
| • cDNA template | 3-100 ng |
| • Nuclease-free water | to 20 µl |

All ingredients were mixed gently by pipetting up and down and transferred to the Real time system CFX96 (Bio-Rad Laboratories, Inc., USA) for cyclic amplification and measurement of SYBR® Green dye. Therefore, the following protocol was used:

Tab. 13 lists a quantitative real time polymerase chain reaction protocol. SYBR® Green fluorescence was recorded after each round of amplification and after amplification for the determination of a melt curve. The Bio-Rad CFX manager (Bio-Rad Laboratories, Inc., USA) software was used.

Tab. 13: Quantitative real time polymerase chain reaction protocol

Step		Temperature [°C]	Length	Count
1	Equilibration	50	2 minutes	1x
2	Initial Denaturing	95	10 minutes	1x
3	Denaturing	95	15 seconds	 40x
	Annealing	Variable (52-62)	30 seconds	
	Elongation	72	30 seconds	
4	Final Elongation	72	10 minutes	1x
5	Equilibration	50	5 seconds	1x
6	Melt curve determination	50 - 95	-	 1x
7	Storage	4	∞	∞

Finally, gene expression was calculated by using the $\Delta\Delta C_t$ -method[146]. GAPDH was used as a reference gene. The melt curve was analyzed carefully for successful amplification of target DNA fragments.

2.2.43 Statistical analysis

All statistical analysis was carried out in MS Excel 2013/2016 (Microsoft, USA). For all experiments, mean values and standard deviations were calculated. For the comparison of two data sets, a student's t-test was carried out, at which a p-value < 0.05 was considered as significant.

2.2.44 Preparation of RNA-Seq samples

2×10^6 BMDCs/well were seeded into 6-well plates in 1 mL IMDM containing 2mM L-glutamin, 5% FBS, 1% P/S and 50 μ M 2-Mercaptoethanol as well as 10 ng/mL GM-CSF. The next day, cells were treated with 75 μ g/mL nanocapsules. Here, ovalbumin nanocapsules filled with both R848 and MDP as well as empty ovalbumin nanocapsules (synthesized by Dr. Ketil Piradashvili) were added to the cells for 1 hour, 2 hours and 4 hours, each in two biological replicates. Two biological replicates were left untreated as negative control reference. Afterwards, the different time points of nanocapsule incubation were pooled and total RNA of all samples was extracted via RNeasy Mini Kit (Qiagen, Netherlands) according to the manufacturer's recommendations. RNA quality was checked via agarose gel electrophoresis and quantity was determined via NanoDrop 8000 Spectrophotometer (Thermo Fisher Scientific, USA). Afterwards, total RNA was handed over to StarSeq (Germany) for another quality check via Bioanalyzer and subsequent Next Generation Sequencing.

2.2.45 Illumina Sequencing

Next Generation Sequencing was carried out by StarSeq (Germany). Therefore, mRNAs were sequenced via Illumina NextSeq 500™ (Illumina, Inc., USA). Overall, 25 million paired-end reads were created per sample (2 x 150 nt, 3.75 Gb) for the six data sets (two untreated samples, two samples treated with ovalbumin nanocapsules, two samples treated with MDP and R848 filled ovalbumin nanocapsules). Data were received in .fastq format.

2.2.46 Quantification of NGS data sets

Obtained NGS data sets were quantified using the software Geneious R8 (Biomatters, New Zealand). Firstly, NGS files were imported in .fastq format. Then, paired end reads were assigned to each other, whereat the distance was set to 470 bp. The genomic murine reference sequence was obtained by NCBI in .fasta format (FASTA_GCF_000001635.25_GRCm38.p5_genomic.fna) and annotated using a .gff annotation (GFF_GCF_000001635.25_GRCm38.p_genomic.gff). Finally, all data sets were mapped against the murine reference sequence containing 21 chromosomes and mitochondrial DNA using the following settings:

• Sensitivity:	Custom Sensitivity
• Fine Tuning:	Iterate 2 times
• Trim Sequences:	Do not trim
• Map multiple best matches:	Randomly
• Allow gaps:	Yes
• Maximum gaps per Read:	3%
• Maximum Gap Size:	5,000
• Minimum Overlap:	No
• Word length:	24
• Index Word Length:	14
• Ignore words repeated more than:	8 times
• Maximum Mismatches per Read:	10%
• Maximum Ambiguity:	4
• Accurately map reads with errors to repeat regions:	No
• Use paired read distances to improve assembly:	Yes
• Search more thoroughly for poor matching reads:	No
• Only map paired reads which match nearby:	No

Established contigs were quantified by using the Geneious R8 function “Calculate expression levels”. Finally, expression data was transferred to an MS Excel sheet and differences in gene expression were quantified using the “Raw transcript read” value. The ratio between the samples was subsequently used for pathway analysis.

2.2.47 Pathway analysis

Gene expression data in excel was sorted for mean enrichment scores. Therefore, mean values of untreated cells, cells treated with ovalbumin and cells treated with ovalbumin nanocapsules filled with MDP/R848 was calculated. Nanocapsule-treated mean values were then divided by the mean value to non-treated cells to determine the mean enrichment scores. A gene list comprising genes expressed at least 2 times more than the negative control was uploaded to the online software DAVID Bioinformatics Resources 6.7 into the Functional Annotation Tool with the identifier “OFFICIAL_GENE_SYMBOL”. Finally, pathways were visualized in Annotation Summery results, subchapter “KEGG_PATHWAY”.

3 Results and discussion³

3.1 Endocytosis and Transcytosis of PS-NP in Caco-2 cells

3.1.1 Caco-2 cells establishing a cellular monolayer

One of the worldwide most used cell lines for drug delivery studies across a cellular monolayer are Caco-2 (human epithelial colorectal adenocarcinoma) cells[147]. When cultivated for a longer period, these cells form a natural polarized barrier by establishing tight junctions[148]. In the present study, firstly cell growth of Caco- cells was monitored via brightfield microscopy.

After three days of cultivation, Caco-2 cells began to form first cell clusters (Fig. 8). These clusters expanded and cells almost covered the whole flask after six days. After ten days, finally, Caco-2 cells reached absolute confluence and formed a cellular monolayer. Nevertheless, an optically confluent cell layer is usually not enough for a confirmation of a sufficiently tight cell layer for transcytosis experiments.

³ Parts of the following chapter were already published and are republished in this thesis with permission of:

Elsevier Science and Technology Journals, *Protein machineries defining pathways of nanocarrier exocytosis and transcytosis*, Reinholz J, Diesler C, Schöttler S, Kokkinopoulou M, Ritz S, Landfester K, Mailänder V, Acta Biomaterialia 71, 2018; permission conveyed through Copyright Clearance Center, Inc.

Taylor & Francis Group, *The challenges of oral drug delivery via nanocarriers*, Reinholz J, Landfester K, Mailänder V, Drug delivery, 2018, DOI: 10.1080/10717544.2018.1501119.

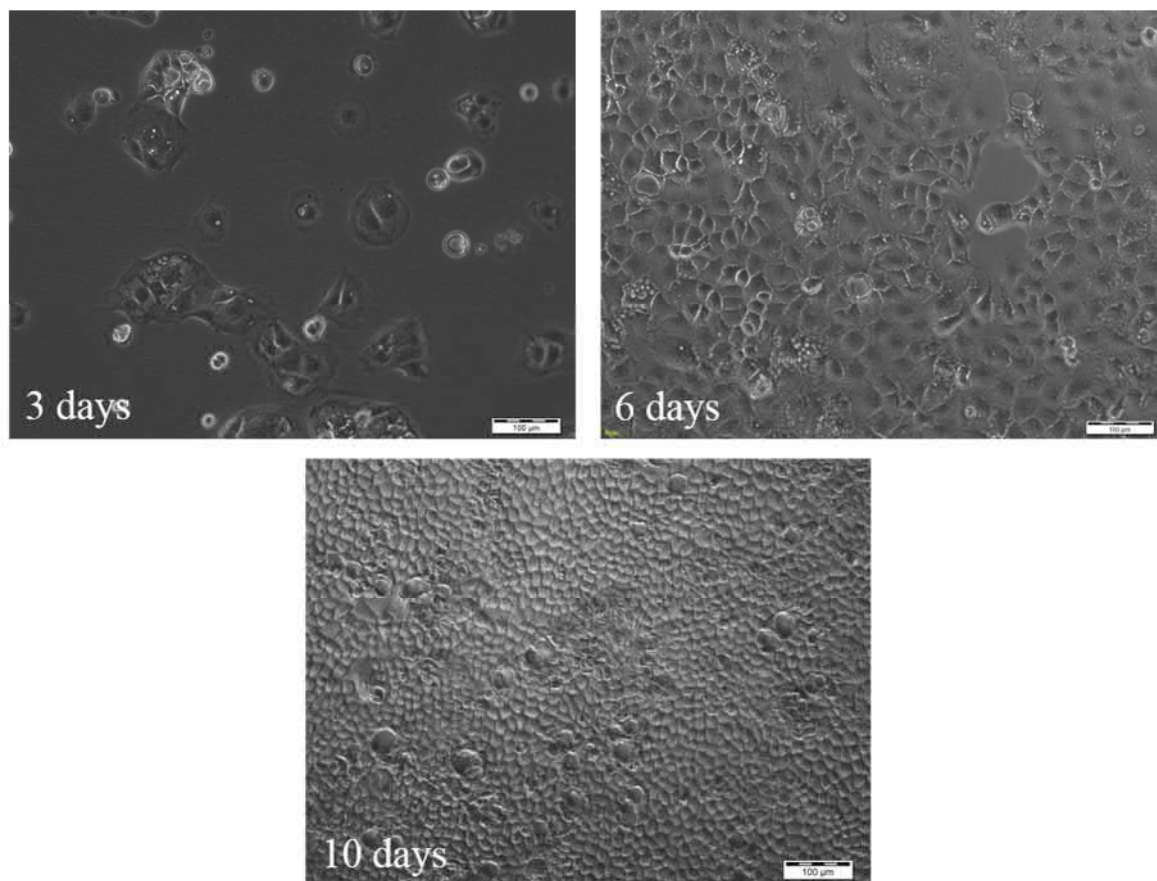


Fig. 8: Caco-2 cells forming a monolayer.

This figure depicts Caco-2 cells forming a natural monolayer. Caco-2 cells were cultured in DMEM containing 10% FBS and cell growth was monitored after 3, 6 and 10 days of cultivation. After 10 days, cells were completely confluent. Scale bar = 100 μm .

Instead of solely relying on microscopy, the TEER (Transepithelial electrical resistance) value[149] across the Caco-2 monolayer was determined. This was accomplished by seeding Caco-2 cells into various porous transwell filters. Afterwards, the TEER value was determined by measuring the electrical resistance across the Caco-2 cell layer in $\Omega \times \text{cm}^2$. Transwell filters with different properties were tested for their eligibility to facilitate a tight monolayer growth of Caco-2 cells. For this purpose, polyester membranes, collagen-coated membranes and polycarbonate membranes with a respective pore size of 0.4 μm and 3 μm were examined (Fig. 9).

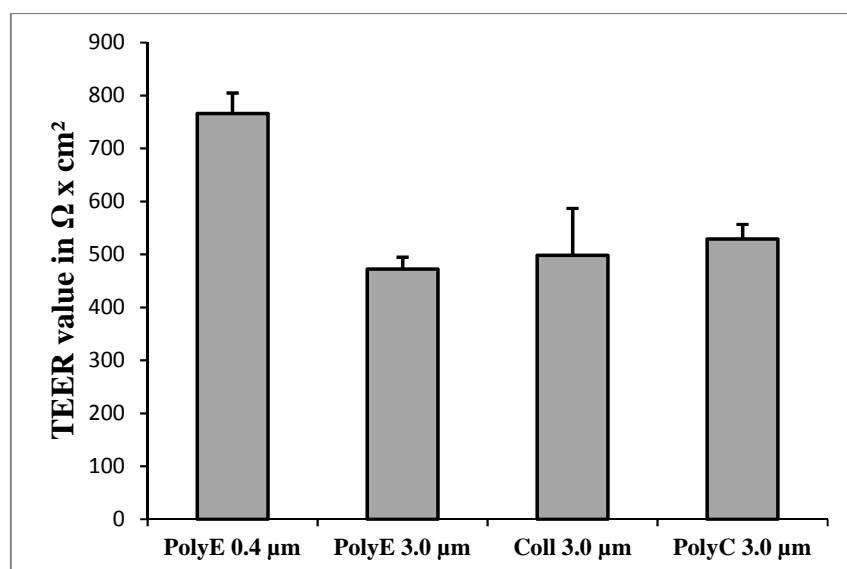


Fig. 9: Comparison of TEER values of Caco-2 cell layers grown on different transwell materials.

Caco-2 cells were cultured in DMEM containing 10% FBS and TEER values were measured after 14 days. Caco-2 grown on all materials were feasible to achieve TEER values around or over $500 \Omega \times \text{cm}^2$. PolyE = Polyester membrane, Coll = Collagen-coated membrane, PolyC = Polycarbonate membrane.

Electrical resistance measurements revealed that Caco-2 cells were feasible to achieve TEER values around or over $500 \Omega \times \text{cm}^2$ on all three tested commercially available materials. The polyester membrane with $0.4 \mu\text{m}$ pores featured the highest TEER value, speculative because of a relative increased surface area compared to the larger pore sized membranes. In the literature, comparable studies with Caco-2 cells reported TEER values ranging between 150 and $1500 \Omega \times \text{cm}^2$ [149-155]. Remarkably, later passages of Caco-2 cells are described to feature higher TEER values[156]. However, the same study pointed out that the transport capacities are not altered despite TEER value differences. Since in this study obtained TEER values were overall comparable to literature values, for the following experiments a cut-off of $500 \Omega \times \text{cm}^2$ was determined. All analyzed Caco-2 cell monolayers featured at least the above-mentioned TEER value or were discarded before performing the experiment. The intact structure of polycarbonate membranes was also confirmed via confocal laser scanning microscopy in transmission mode (Fig. 10).

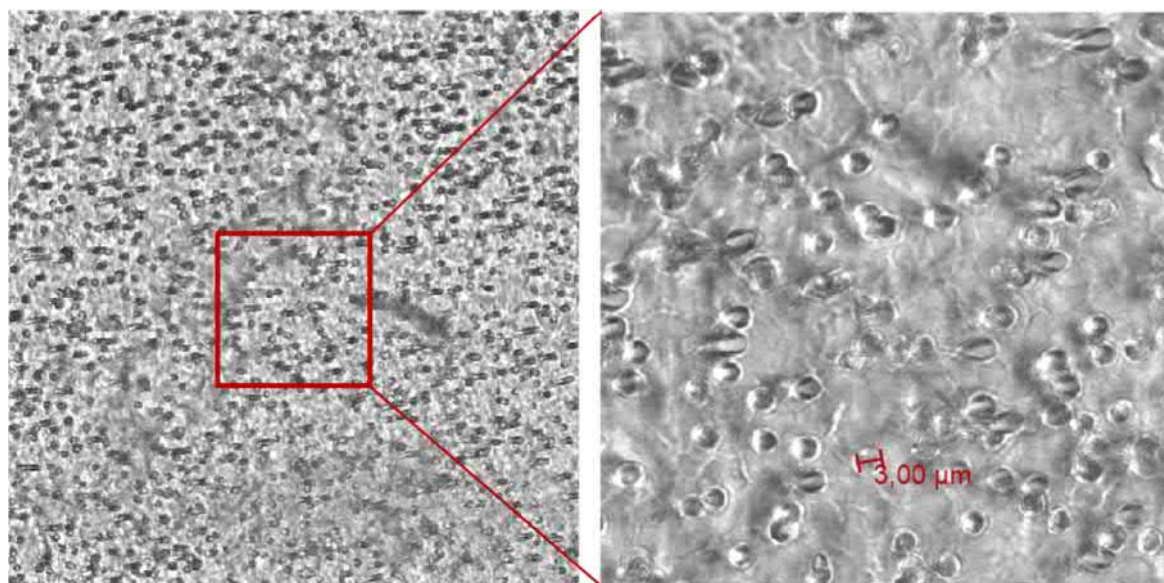


Fig. 10: Surface structure of a polycarbonate membrane with 3 μm pores.

This figure depicts a close-up of a polycarbonate transwell membrane. Images were recorded via confocal laser scanning microscopy in transmission mode. Analyzed membranes featured pores of exactly 3 μm in diameter as stated by the manufacturer.

3.1.2 Cytotoxicity of different nanoparticle systems

A lot of different nanomaterials are already shown to exhibit cytotoxic effects[157]. Naturally, to be feasible for oral drug delivery, applied nanocarriers must not induce any toxic cellular effects. In this work, polystyrene nanoparticles are used as a model nanoparticle (for size and Zeta potential analysis, see SI Fig. 1-3). Since they are non-biodegradable, their usage for oral drug delivery is non-existent. Nevertheless, to simulate experiments with these model nanoparticles, cells should not show any cytotoxic effects to mimic a natural environment and avoid artefacts in endo-/trans- and exocytosis studies. For this purpose, all used polystyrene nanoparticles were screened via different toxicity tests. For the determination of necrotic cells, propidium iodide staining was used. Apoptotic cells were measured via Annexin V-staining. The metabolic activity was determined via ATP quantification and finally cell proliferation was quantified by the reduction of MTS via NADPH and NADH. In Fig. 11, an example of a toxicity test series is displayed for a carboxylated SDS-stabilized polystyrene nanoparticle, which did not induce any cytotoxic effects in concentrations up to 600 $\mu\text{g/mL}$. Similarly, the incubation with lutensol-stabilized nanoparticles did not lead to any cytotoxic effects (SI Fig. 7). Nanoparticles stabilized with CTMA-Cl (Cetyltrimethylammonium chloride), on the other hand, were already toxic if the nanoparticle concentration exceeded 75 $\mu\text{g/mL}$ (SI Fig. 7). The toxic effects of CTMA-Cl

as a surfactant are also described in the literature, potentially caused by the quaternary ammonium groups[158, 159]. Other studies presenting results of SDS and lutensol as stabilizing surfactants causing no toxic cellular effects are also in line with the results of this thesis[160-162]. Consequently, the majority of the following experiments was conducted with SDS- or lutensol-stabilized nanoparticles. On a side note, nanoparticles were screened for endotoxin contamination (SI Fig. 8). Some nanoparticles exhibited the FDA Limit of 0.5 EU/mL slightly, which did however not have any consequences for the experiments, since the addition of fetal bovine serum already leads to a concentration of ~2 EU/mL in cell culture medium.

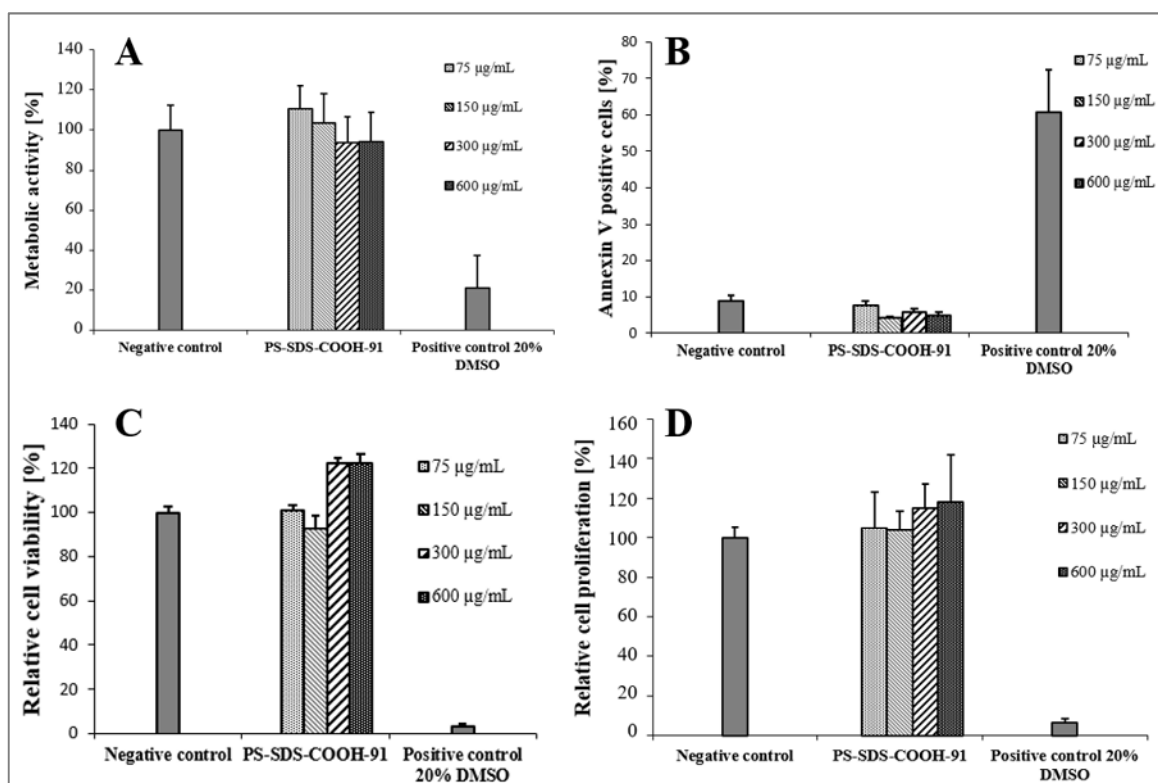


Fig. 11: Toxicity tests of nanoparticle treated Caco-2 cells.

This figure depicts different toxicity tests of nanoparticle treated Caco-2 cells. (A) Metabolic activity measured via CellTiter Glo Assay. (B) Apoptosis measured via Annexin V staining. (C) Relative cell viability measured via PI staining. (D) Relative cell proliferation measured via MTS Assay. None of the tests indicated any significant toxicity of tested polystyrene nanoparticles in concentrations up to 600 µg/mL. In contrast, the addition of 20 % DMSO as a positive control resulted in significant toxic effects in all toxicity test systems.

3.1.3 Nanoparticle uptake in Caco-2 cells

Since Caco-2 are used to mimic transcytosis across a natural monolayer, the first hurdle to overcome is entering the cell. To confirm at least a nanoparticle-cell interaction[163], nanoparticle treated cells were analyzed via flow cytometry. Polystyrene nanoparticles showed concentration-correlated binding / uptake as confirmed by an increasing median fluorescence intensity (Fig. 12). The percentage of nanoparticle-positive Caco-2 cells was nearly 100% for all tested concentrations. However, a positive fluorophore signal does not necessarily imply successful uptake by the cells.

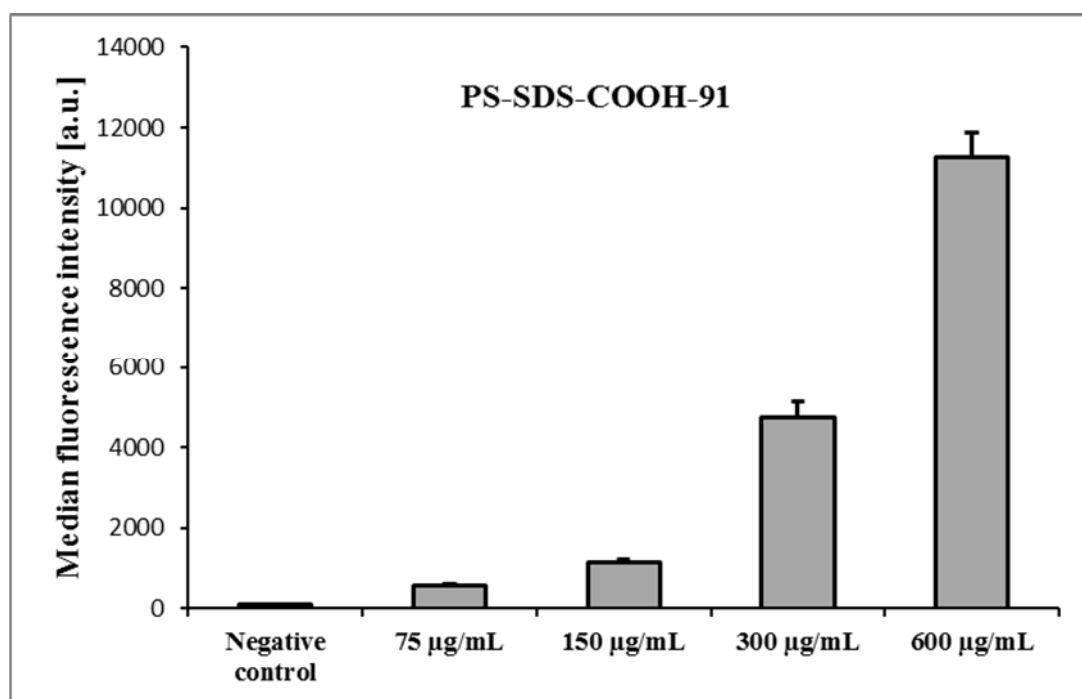


Fig. 12: Cellular uptake of nanoparticles in Caco-2 cells determined by flow cytometry.

Caco-2 cells were seeded in a density of 2×10^5 cells and treated with different concentrations of carboxylated polystyrene nanoparticles. Cells were washed 3x with DPBS and afterwards analyzed via flow cytometry. The increase in median fluorescence intensity correlated with increasing concentrations of nanoparticles.

To rule out that nanoparticles were solely adhering to the cell without being internalized, confocal laser scanning microscopy was performed. Here, Caco-2 cells treated with carboxylic (Fig. 13) and aminated (Fig. 14) SDS-stabilized polystyrene nanoparticles were compared after 4 h of nanoparticle incubation. Caco-2 cells treated with carboxylated nanoparticles showed significant cellular uptake while cells treated with aminated nanoparticles showed major nanoparticle adhesion to the cell membrane as indicated by a

yellow co-localization signal (also see SI Fig. 57-58 for SEM pictures of adhering aminated nanoparticles). This phenomenon might be explained by the electrostatic interaction of the positively charged NH_2 groups and the negative surface charge of the Caco-2 cell membrane[164-166]. Nevertheless, Caco-2 cells were also able to internalize aminated nanoparticles, albeit with a lower efficiency. However, since aminated nanoparticles tended to aggregate significantly more in cell culture medium supplemented with fetal bovine serum compared to their carboxylated counterparts, the majority of confocal laser scanning microscopy experiments was subsequently conducted with carboxylated nanoparticles.

The first confocal laser scanning microscopy studies were, even when using carboxylated SDS-stabilized nanoparticles, impeded by nanoparticle aggregates up to several micrometer in size (Fig. 15A, also see SI Fig. 59). This is putatively due to the interaction with proteins in FBS and general charged molecules in DMEM. However, in this thesis, a strategy could be employed to get rid of these aggregates. By filtering the nanoparticle containing medium through a $0.45\ \mu\text{m}$ sterile filter, aggregates were completely removed (Fig. 15B). Even when incubating this “cleansed” nanoparticle-DMEM suspension for longer time frames (up to 24 h), aggregates did not form again. Although the exact mechanisms behind this remain unclear, the strategy allowed for unhindered cLSM studies.

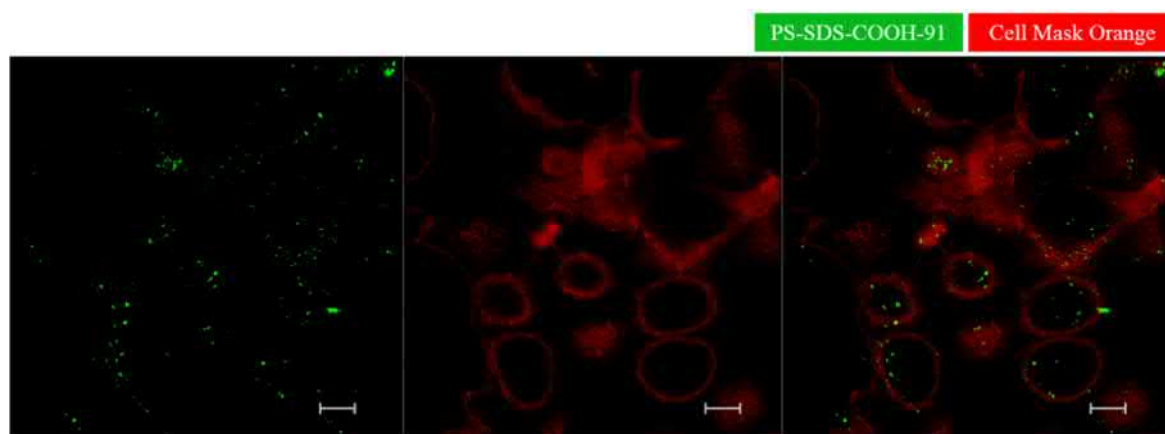


Fig. 13: Cellular uptake of carboxylated polystyrene nanoparticles in Caco-2 cells.

Caco-2 cells were seeded in a density of 1×10^4 cells and treated with $75\ \mu\text{g/mL}$ of carboxylated nanoparticles for 4 h in DMEM containing 10% FBS. Nearly all cells internalized a significant amount of nanoparticles. Scale bar = $10\ \mu\text{m}$.

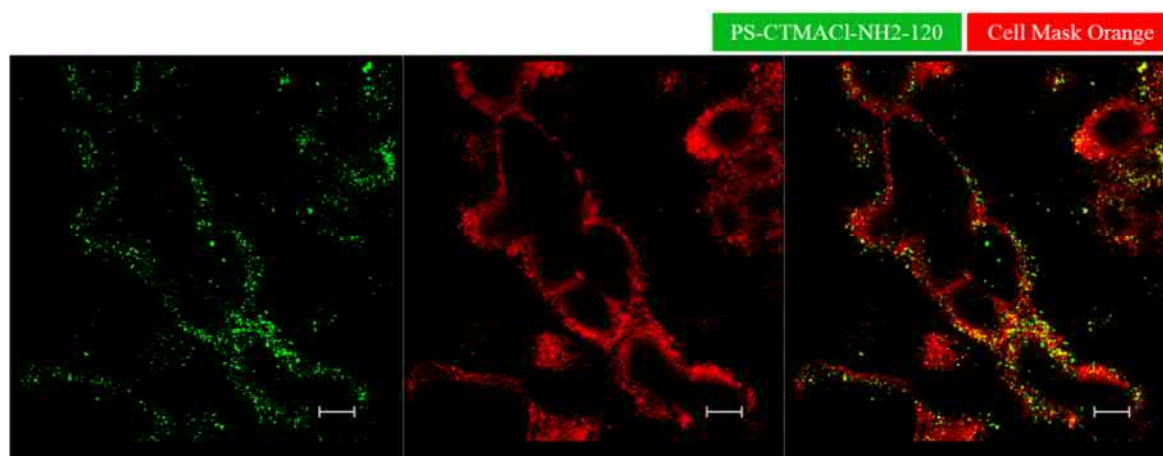


Fig. 14: Cellular uptake of aminated polystyrene nanoparticles in Caco-2 cells.

Caco-2 cells were seeded in a density of 1×10^4 cells and treated with $75 \mu\text{g/mL}$ of aminated nanoparticles for 4 h in DMEM containing 10% FBS. Cells were able to internalize PS-NH₂-NP. However, the major amount of nanoparticles adhered to the cell membrane, resulting in a yellow overlap signal. Scale bar = $10 \mu\text{m}$.

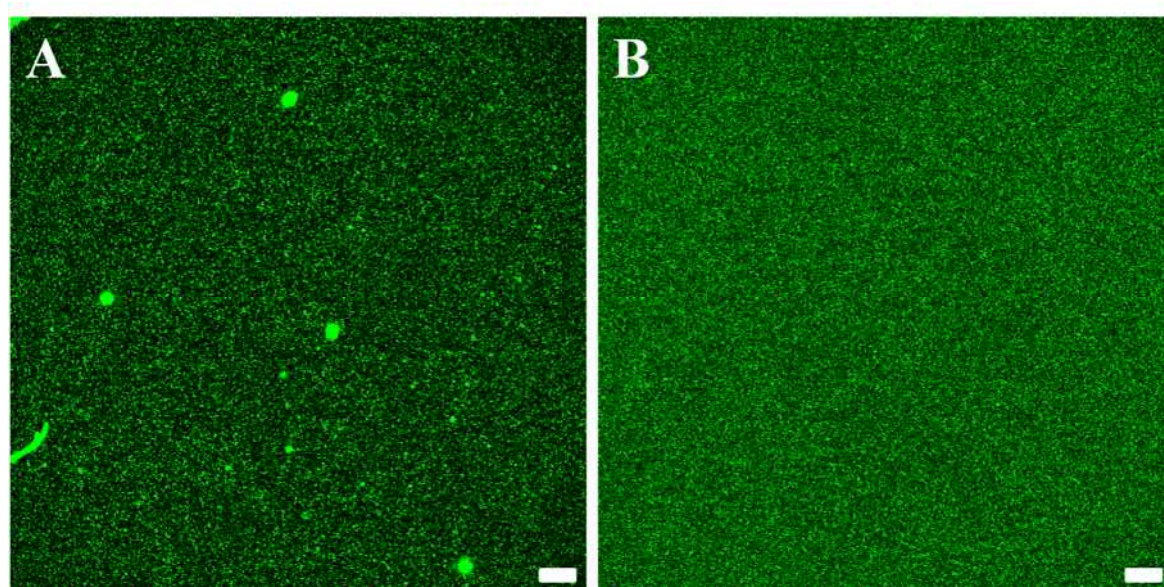


Fig. 15: Prevention of nanoparticle aggregation in cell culture medium.

This figure depicts the successful prevention of nanoparticle aggregation in DMEM containing 10% FBS. $75 \mu\text{g/mL}$ polystyrene nanoparticles were incubated for 1 h and 37°C in cell culture medium. Afterwards, the nanoparticle-DMEM-solution was filtered through a $0.45 \mu\text{m}$ sterile filter and analyzed via confocal laser scanning microscopy. (A) Unfiltered nanoparticle medium showed significant nanoparticle aggregates up to $5 \mu\text{m}$. (B) Steril-filtered nanoparticle medium was completely free of any aggregates. Scale bar = $10 \mu\text{m}$.

3.1.4 Nanoparticle uptake in transwell system

After confirming cellular uptake in well plates, nanoparticle uptake in transwell system was examined. After four hours of incubation with carboxylated polystyrene nanoparticles, about 60-70% of Caco-2 cells showed a fluorescent signal as analyzed by confocal laser scanning microscopy (Fig. 16). The percentage of uptake was slightly lower compared to nanoparticle-treated Caco-2 cells in 12-well plates. Speculatively, this might be due to the fact that Caco-2 cells grown in well plates have more physical space to internalize nanoparticles, specifically at their lateral sides, while Caco-2 cells grown in transwells can only internalize nanoparticles via their apical side. Nevertheless, the analyzed confocal laser scanning microscopy images gave a first hint that polystyrene nanoparticles were able to get internalized also in the relevant transwell system.

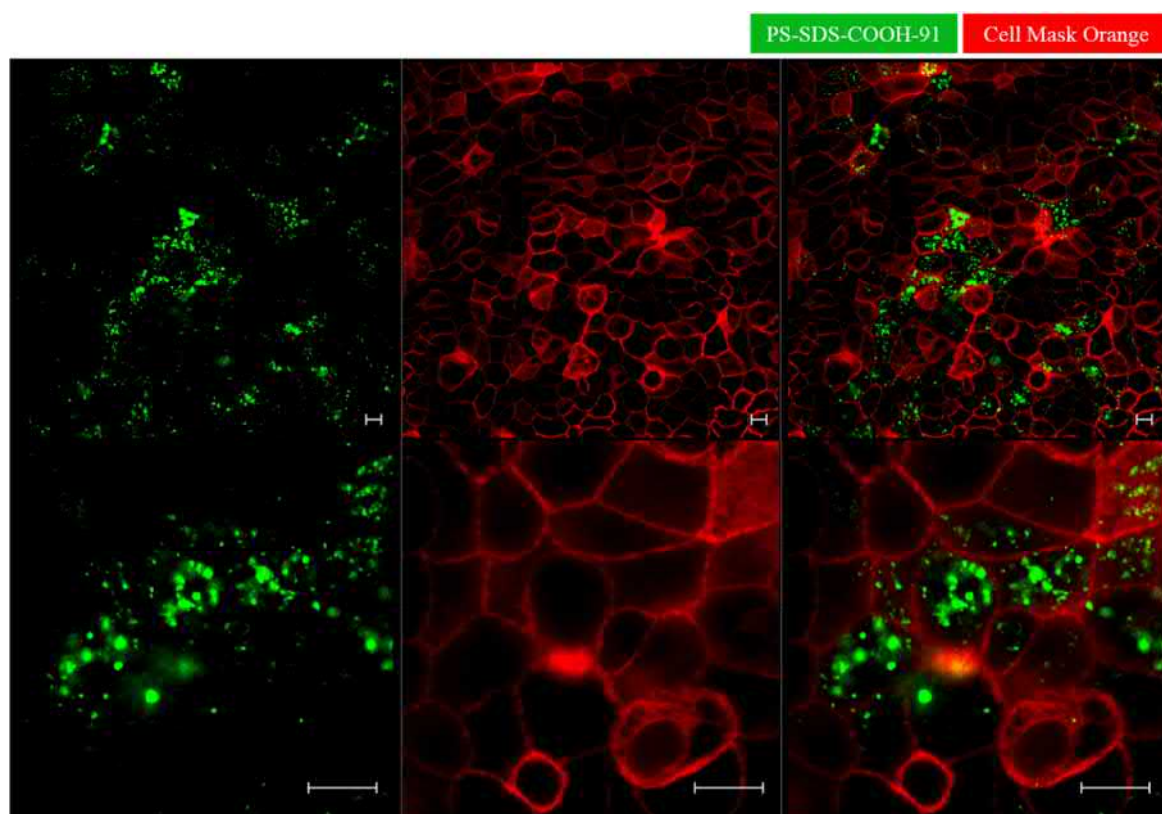


Fig. 16: Uptake of polystyrene nanoparticles in transwell system.

Caco-2 cell layers were cultivated for 14 days on polycarbonate transwell inserts. Then, carboxylated nanoparticles were added in a concentration of 300 $\mu\text{g/mL}$. After 4 h incubation, the polycarbonate membrane was cut with a scalpel and cells were analyzed via confocal laser scanning microscopy. Caco-2 cells showed sufficient internalization of nanoparticles. Scale bar = 10 μm .

3.1.5 Nanoparticle transcytosis in transwell system

After ensuring that Caco-2 cells were able to grow a confluent monolayer and internalize nanoparticles in transwell system, the system was tested for its potential to translocate nanoparticles from the apical to the basal side of the chamber. In order to exclude any leakage of nanoparticles via mechanical or nanoparticle induced disruption of the Caco-2 cell layer, the TEER value of each well was thoroughly monitored before and after nanoparticle addition (Fig. 17). The addition of 600 $\mu\text{g/mL}$ of carboxylated nanoparticles, which was the maximum concentration used for transwell experiments, did not lead to any decrease of TEER values. This indicated that the 24 h incubation with nanoparticles did not disrupt or negatively influence the integrity of the cell layer.

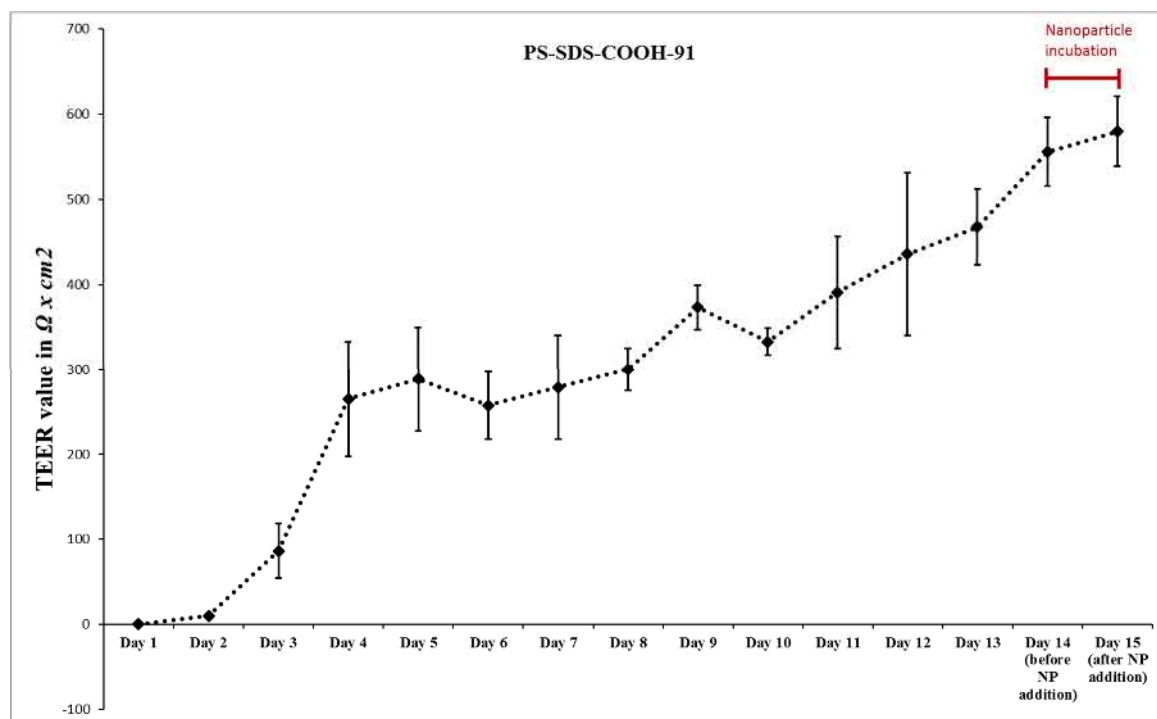


Fig. 17: Development of TEER values before and after nanoparticle addition.

Caco-2 cells were seeded out in a density of 1.5×10^5 and cultivated at 37 °C on Polycarbonate Transwells® (Corning Incorporated, USA) with a pore size of 3 μm . TEER values were determined every day using an ENDOHM-12 electrode in combination with the Millicell® ERS-2 Epithelial Volt-Ohm Meter. The first layer of cells seemed to have formed after four days. Afterwards, tight junctions were developed, resulting in an increase in epithelial resistance up to 560 $\Omega \times \text{cm}^2$. After 14 days, nanoparticles were added in a concentration of 600 $\mu\text{g/mL}$. After another 24 h, the average TEER value did not decrease, proving that polystyrene nanoparticles did not induce any damage to the cell layer. The standard deviation results from 12 tested transwell inserts.

Finally, the amount of transcytosed nanoparticles was determined by measuring the fluorescence intensity of the basal medium after 24 h of incubation with nanoparticles in apical DMEM (Fig. 18). For each used nanoparticle concentration, a standard curve (SI Fig. 9) was employed to calculate the percentage of transcytosed nanoparticles. Transcytosis efficiencies of carboxylated nanoparticles were around 0.2 % of nanoparticle stock solution for each examined concentration between 75 $\mu\text{g/mL}$ and 600 $\mu\text{g/mL}$. The fact that the percentage of transported NP was similar amongst the used concentrations indicated that nanoparticles were actively transported and did not passively diffuse from the apical to basal side of the Caco-2 cell layer. The transcytosis rate of 0.2 % was, despite being low, comparable to the results of other groups[39]. On a side note, the rate of transcytosis was also determined on different transwell plates (SI Fig. 10), with the polycarbonate membrane featuring the highest rate of transcytosis.

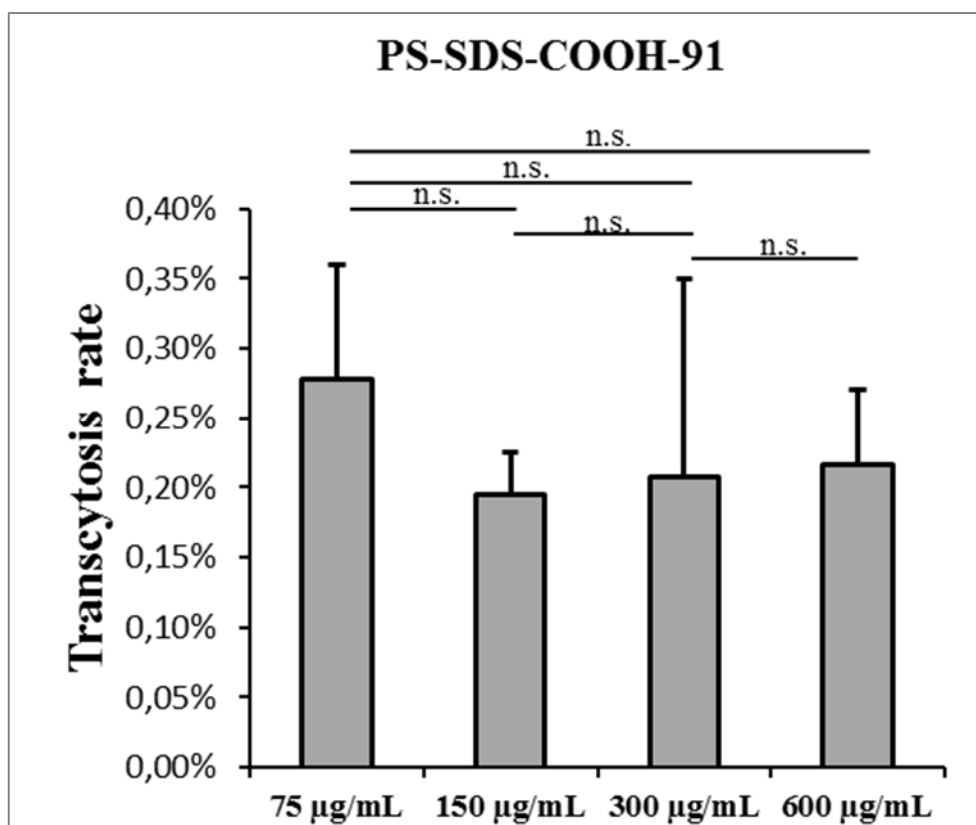


Fig. 18: Transcytosis of carboxylated polystyrene nanoparticles in different concentrations. Transcytosis of PS-SDS-COOH-91 nanoparticles was around 0.2% of nanoparticle stock solution. A Student's t-test showed no statistically significant ($p < 0.05$) differences between examined nanoparticle concentrations.

3.1.6 Uptake of differently charged nanoparticles

One concept to increase the rate of transcytosis is the increase of initially internalized nanoparticles, which can be accomplished by a functionalization with either carboxy- or aminogroups on the NP surface. The electrostatic interaction with the cell membrane should, at least in theory, permit for an increased binding and uptake of nanoparticles compared to their uncharged counterparts[167-170]. In the present thesis, binding and/or internalization of positively and negatively charged lutensol-stabilized nanoparticles were compared by flow cytometry (Fig. 19). Uptake of both charged NPs was highly significant increased, albeit the uptake of amino-functionalized NPs was even higher than the uptake of carboxy-functionalized nanoparticles. General median fluorescence intensity was rather low compared to SDS-stabilized nanoparticles (Fig. 12). This may be explained by the fact that lutensol is a PEG analog[171] and PEG is generally known to reduce protein adsorption[172, 173] and unspecific cellular uptake[174] (also described as stealth effect). The increase of uptake especially via amino-functionalization is a potential solution for nanoparticle formulations that exhibit a low transcytosis rate. By enhancing the sheer amount of endocytosed nanomaterial, the probability of successful transcytosis events might, in theory, also be increased, which is further discussed in chapter 3.1.7.

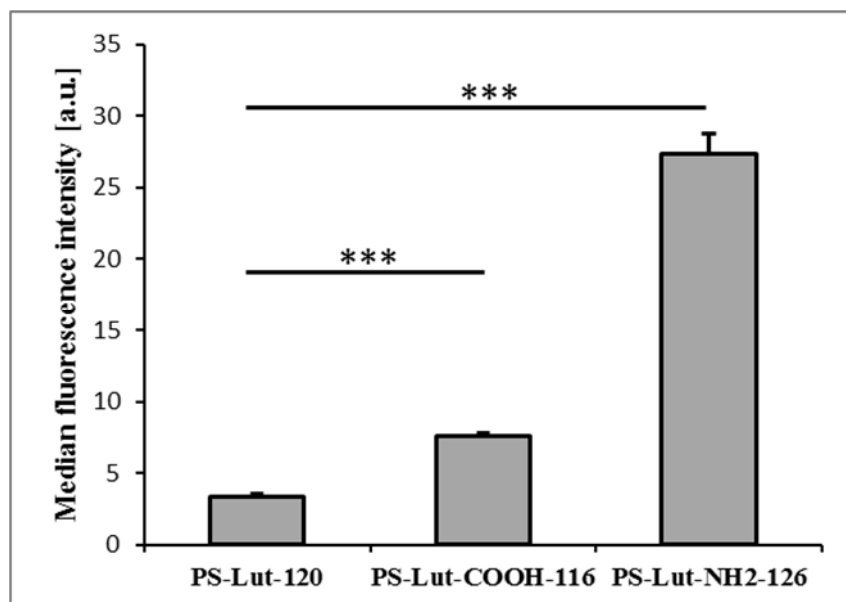


Fig. 19: Uptake of differently charged lutensol-stabilized polystyrene nanoparticles.

Caco-2 were seeded in a density of 2×10^5 cells/mL, incubated for 4 h with 75 $\mu\text{g/mL}$ lutensol-stabilized polystyrene nanoparticles with different charges and finally analyzed via flow cytometry. Positively charged nanoparticles exhibited the highest uptake, followed by negatively charged and unfunctionalized nanoparticles. A Student's t-test showed highly significant ($p < 0.001$) differences between examined nanoparticles.

3.1.7 Transcytosis of differently charged and sized nanoparticles

The increased uptake efficiency of both positively and negatively charged lutensol-stabilized nanoparticles was subsequently tested for its implications regarding transcytosis efficiencies compared to their uncharged counterparts (Fig. 20). In contrast to a highly significant increased cellular uptake, transcytosis efficiency of carboxylic lutensol-stabilized NP was surprisingly highly significantly reduced. On the other hand, amino-functionalized lutensol-stabilized nanoparticles featured a highly increased transcytosis rate, which was consistent with the increased cellular uptake measured via flow cytometry. Interestingly, it was even increased by the same factor (about 5-fold). These results indicate, that the amount of uptake directly correlates and influences the amount of transcytosed nanoparticles, at least for positively charged lutensol-stabilized nanoparticles. Contrarily, the amount of transcytosed negatively charged lutensol-stabilized nanoparticles was negatively correlated with the amount of internalized nanoparticles (3-fold increased uptake vs. 3-fold decreased transcytosis). This gives a hint that these negatively charged nanoparticles, compared to their uncharged counterparts, accumulate more inside of lysosomes in Caco-2 cells instead of being translocated to the basal side. In contrast, the increased transcytosis efficiency of positively charged nanoparticles might be explained by the fact that they were able to avoid the endolysosomal system, which is also described in the literature[46]. Similar results were obtained for charged SDS-stabilized polystyrene nanoparticles (SI Fig. 11), albeit transcytosis of positively charged SDS-stabilized nanoparticles was not as significantly increased as for lutensol-stabilized nanoparticles.

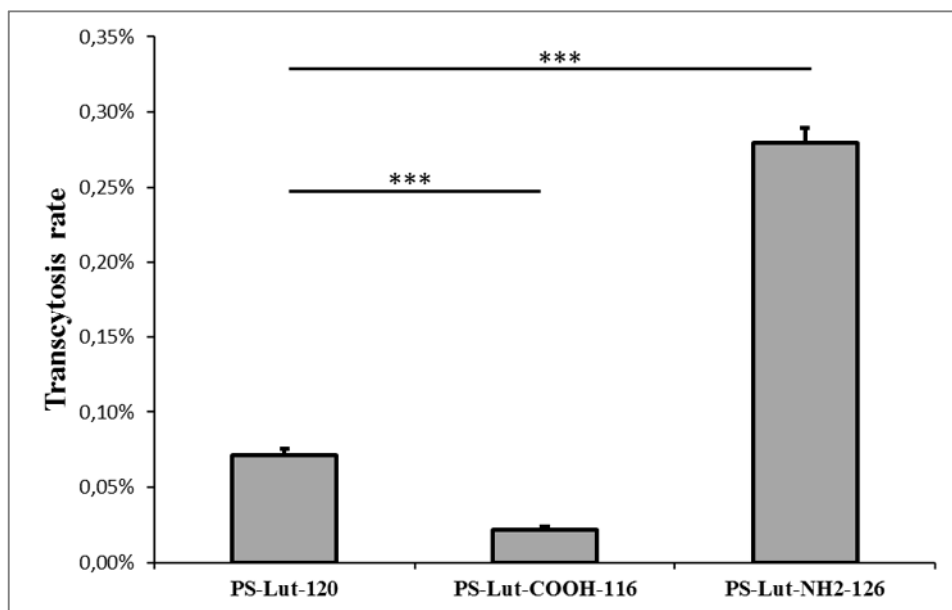


Fig. 20: Transcytosis of differently charged lutensol-stabilized nanoparticles.

This figure depicts the rate of transcytosis of differently charged lutensol polystyrene nanoparticles. Transcytosis rate was highly significant reduced for carboxylated nanoparticles while aminated nanoparticles showed highly significant increased transcytosis. A student's t-test was used to determine significance levels, where $p < 0.001$ was considered highly significant.

The size of tested polystyrene nanoparticles, however, did not have any significant influence on transcytosis rates (Fig. 21). Here, three different sized carboxylated SDS-stabilized nanoparticles were compared (59, 91 and 148 nm in diameter). Nanoparticles with a diameter of 91 exhibited a slightly higher rate of transcytosis than the respective smaller and bigger nanoparticles. These results were contradictory to previously published studies[43, 59], which reported a higher rate of transcytosis for smaller nanomaterials. A possible hypothesis for these contradictory results is an augmented aggregation of the 91 nm sized SDS-stabilized nanoparticles in cell culture medium containing 10% fetal bovine serum. Since it is already known that nanoparticle uptake can be reduced by the aggregation of nanoparticles[175, 176], the subsequent transcytosis rate may have been distorted by these macroscopic aggregates.

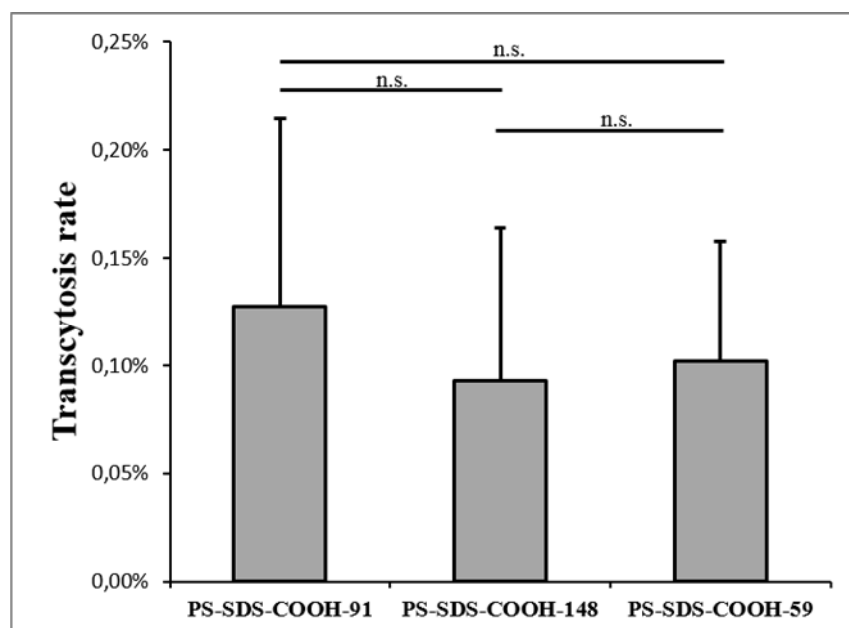


Fig. 21: Transcytosis of differently sized carboxylated SDS-stabilized polystyrene nanoparticles.

This figure depicts the rate of transcytosis of differently sized carboxylated SDS-stabilized polystyrene nanoparticles. Transcytosis rate was slightly increased for aminated nanoparticles. A student's t-test was used to determine significance levels, where $p < 0.05$ was considered significant.

3.1.8 Effect of apical pH value on transcytosis

After surviving the harsh acidic pH value in the stomach, nanoparticles need to be absorbed in the small intestine in order to be utilizable for oral drug delivery. The pH value in this part of the human digestion system gradually increases from pH 6 in the duodenum to pH 7.4 in the terminal ileum[177]. To optimize conditions for a realistic transposition of nanoparticles, nanoparticle transcytosis was monitored at different pH values (Fig. 22). Since intestinal cells are solely in contact with the intraluminal intestine via their apical side (Fig. 1), only the pH values of the apical transwell media were modified. The highest rate of transcytosis was achieved by lowering the apical pH, which resulted in a highly significant increase in transcytosis for an apical pH of 6.5 and a significant increase for an apical pH of 7.0 in comparison to standard DMEM medium (pH 7.5). In contrast, an alkaline increase in pH to 8.0 resulted in a highly significant decrease in transcytosis. Interestingly, the TEER values did not show any significant change after pH adjustment, which illustrated that the results were not caused or distorted by nanoparticle leakage. These results indicate that a slightly more acidic apical pH value can be used to optimize realistic conditions for

transcytosis experiments. This is consistent with the results from Yamashita et al., who demonstrated that an (in vitro) apical pH value of 6.0 was better for the prediction of (in vivo) drug absorption than an apical pH of 7.4[178].

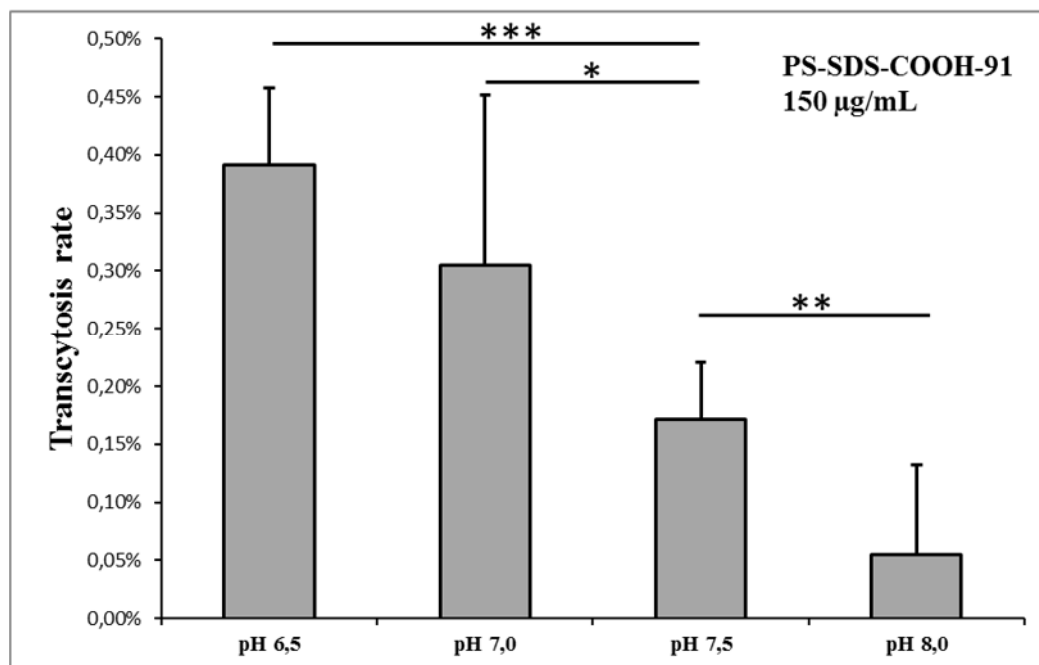


Fig. 22: Transcytosis rate of polystyrene nanoparticles in different apical pH media.

This figure depicts the rate of transcytosis of carboxylic nanoparticles in different apical pH media. The apical pH value was adjusted by acidification with HCl and buffering with MES buffer in DMEM without sodium bicarbonate. A decrease in apical pH value to 6.5 and 7.0 resulted in a (highly) significant increase in transcytosis compared to standard DMEM (pH 7.5). An increase in apical pH value to pH 8.0 resulted in a highly significant decrease in transcytosis. $P < 0.05 = *$, $p < 0.01 = **$, $p < 0.001 = ***$.

3.1.9 Nanoparticle coatings

The major obstacle of oral drug delivery via nanocarriers is the low transcytosis rate of nanocarriers through the intestine-blood-barrier (Fig.1). One possible solution to increase the translocation of nanocarriers might be the decoration on the nanocarrier surface with various agents, e.g. antibodies[66], vitamins[64], or other chemical agents. To achieve for example an antibody-coupling to nanocarriers, the usual method of choice is a chemical coupling of the respective antibody via EDC-coupling[179-181] or NCO-coupling[182]. However, in the last years, major breakthroughs were achieved to facilitate nanoparticle functionalization without chemical coupling via adsorption on the nanocarrier's surface[183]. This utilizes the phenomenon that nanoparticles, which come in contact with

proteins, immediately form a protein corona[55-57]. To some extent, especially when combining this with specific pH values for the adsorption procedure, adsorption can even outperform chemical coupling[184]. In this thesis, such an adsorption of agents on nanoparticles was tested and the transcytosis rate of functionalized nanoparticles was compared to their undecorated counterparts.

The first investigated agent was the Fragment crystallizable region (Fc region) of Immunoglobulin 1 (IgG1). This part of the antibody is responsible for the interaction with cell surface receptors[185, 186]. Coincidentally, a receptor for IgG, the neonatal Fc receptor (FcRn), is located on the surface of enterocytes. This receptor is responsible for the Immunoglobulin transfer across the neonatal intestine[187-189], however, it is also expressed in the intestine of adults[190], as detected by western blot experiments[191]. The neonatal Fc receptor is also shown to be expressed on Caco-2 cells[192, 193]. Thus, the aim was a functionalization of nanoparticles via an adsorption to decorate nanoparticles with the Fc region of IgG antibodies. These nanoparticles should then get internalized via Fc region binding to the neonatal Fc receptor, subsequently increasing the rate of transcytosis.

Firstly, parameters for a sufficient coating of polystyrene nanoparticles were determined. For this purpose, different pH buffers, ranging from pH 2.7 to pH 11, were used for the incubation with the IgG Fc region. Interestingly, the adsorption at pH 2.7 yielded the highest amount of adsorbed Fc region for all three used nanoparticle systems. In fact, it was even the only band visible on the SDS-Page (Fig. 23), which was expected around 27 kDa for reduced the Fc region. The results were finally confirmed via Pierce™ 660nm Protein Assay, where the amount of adsorbed protein was quantified via absorbance measurement (Fig. 24). For uncharged and positively charged lutensol-stabilized nanoparticles, the relative adsorbed protein amount was the highest at pH 2.7, correlating with the strong bands detected via SDS-Page.

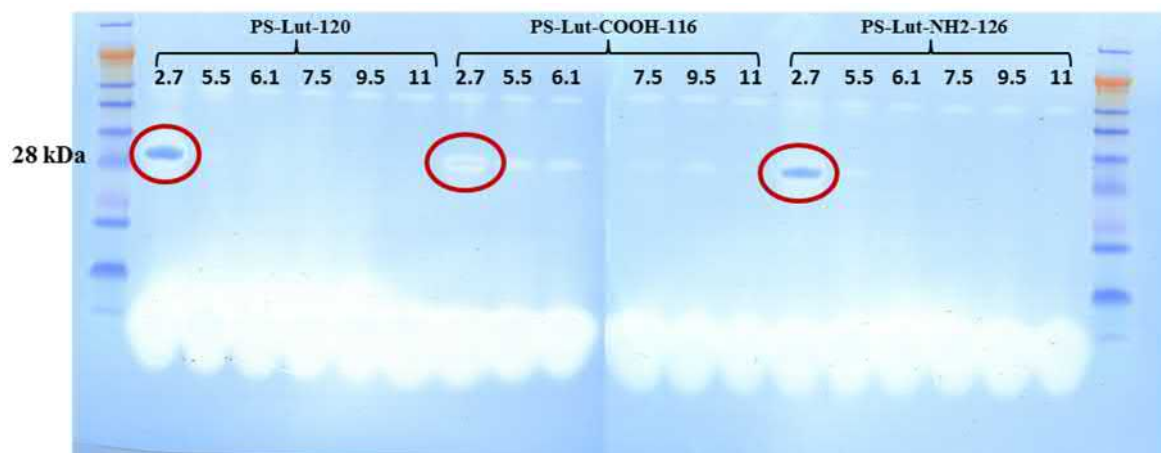


Fig. 23: Analysis of FC fragment adsorption on lutensol-stabilized nanoparticles via SDS-Page. Lutensol-stabilized nanoparticles were incubated with pure FC-fragment for 1 h and 37 °C at different pH values and constant shaking at 300 rpm. Afterwards, nanoparticles were washed 3x with DPBS and subsequently centrifuged at 20,000 x g. After reconstitution in H₂O, coated nanoparticles were analyzed via SDS-Page. Nanoparticles coated at pH 2.7 showed the highest amount of adsorbed FC fragment (red circles).

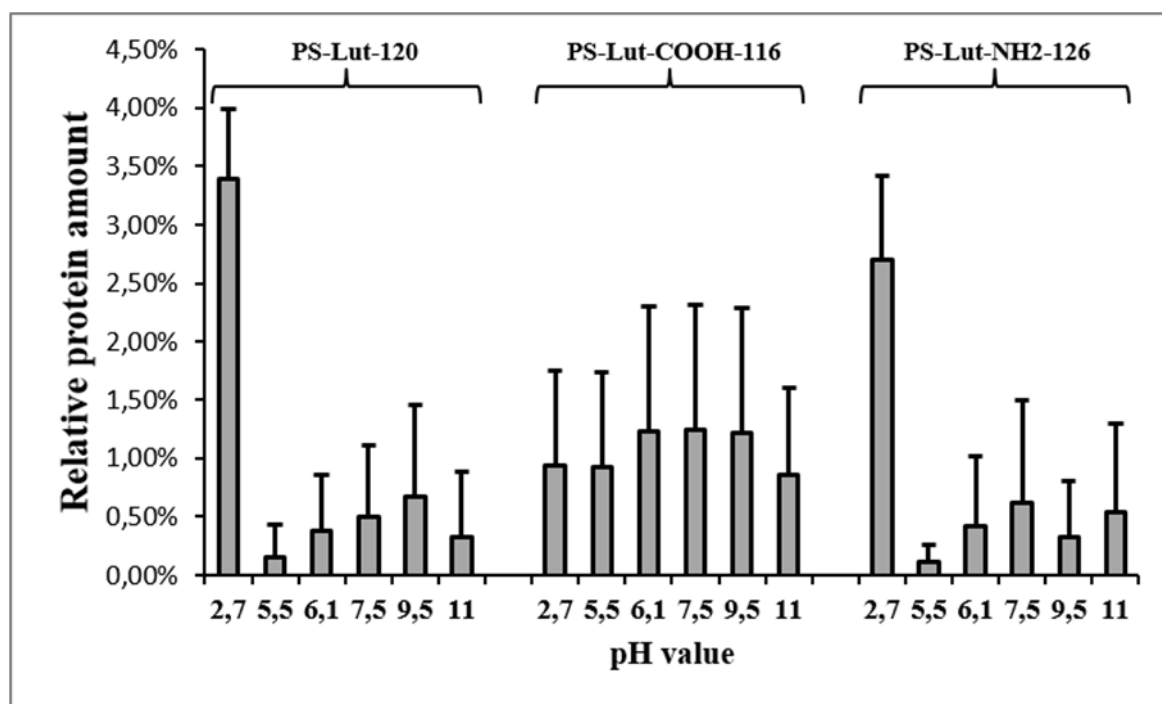


Fig. 24: Analysis of FC fragment adsorption on lutensol-stabilized nanoparticles via Pierce Assay.

Lutensol-stabilized nanoparticles were incubated with pure FC-fragment for 1 h and 37 °C at different pH values and constant shaking at 300 rpm. Afterwards, nanoparticles were washed 3x with DPBS with subsequent centrifugation at 20,000 x g. After reconstitution in H₂O, a Pierce Assay with coated nanoparticles was performed. Unfunctionalized nanoparticles as well as aminated nanoparticles coated at pH 2.7 showed the highest amount of adsorbed FC fragment. In contrast, carboxylated nanoparticles did not show a significant peak at any pH value.

3.1.10 Transcytosis efficiencies of different coated PS-NP

Finally, Fc region-decorated nanoparticles were compared to their unfunctionalized counterparts regarding their transcytosis efficiencies (Fig. 25). Since the neonatal Fc receptor is only able to bind the Fc region at a slightly acidic pH value around 6.0-6.5[194-196], experiments were conducted at an apical pH of 6.5 in customized DMEM. Transcytosis of all three lutensol-stabilized nanoparticles, which were coated with the Fc region at a pH 2.7, was increased up to a factor of 2. In contrast, transcytosis rate of nanoparticles that were prepared at a pH of 7.5 was only negligibly increased for uncharged Fc-functionalized nanoparticles and even decreased for positively charged Fc-functionalized nanoparticles. This is in line with the results of Fc-binding experiments (Fig. 23 and Fig. 24). The more Fc region was adsorbed on the nanoparticles, the more transcytosis could be measured. In the literature, it was already shown that Fc-functionalized nanoparticles can interact with the neonatal Fc receptor on the airway epithelial cell line Calu-3 and the transcytosis rate was subsequently increased[62]. This system was then transferable to Caco-2 cells[63]. However, the binding of Fc region to the nanoparticles was achieved by chemical coupling[63]. In this thesis, on the other hand, Fc region binding was solely dependent on adsorption, which is substantially easier to perform. Admittedly, the increase in transcytosis efficiency of chemical coupled Fc-functionalized nanoparticles described in the literature outperformed our adsorbing Fc-functionalized nanoparticles. Nevertheless, such a pre-adsorption might be a potential area of research to increase the up-to-now poor rates of transcytosis for nanoparticles.

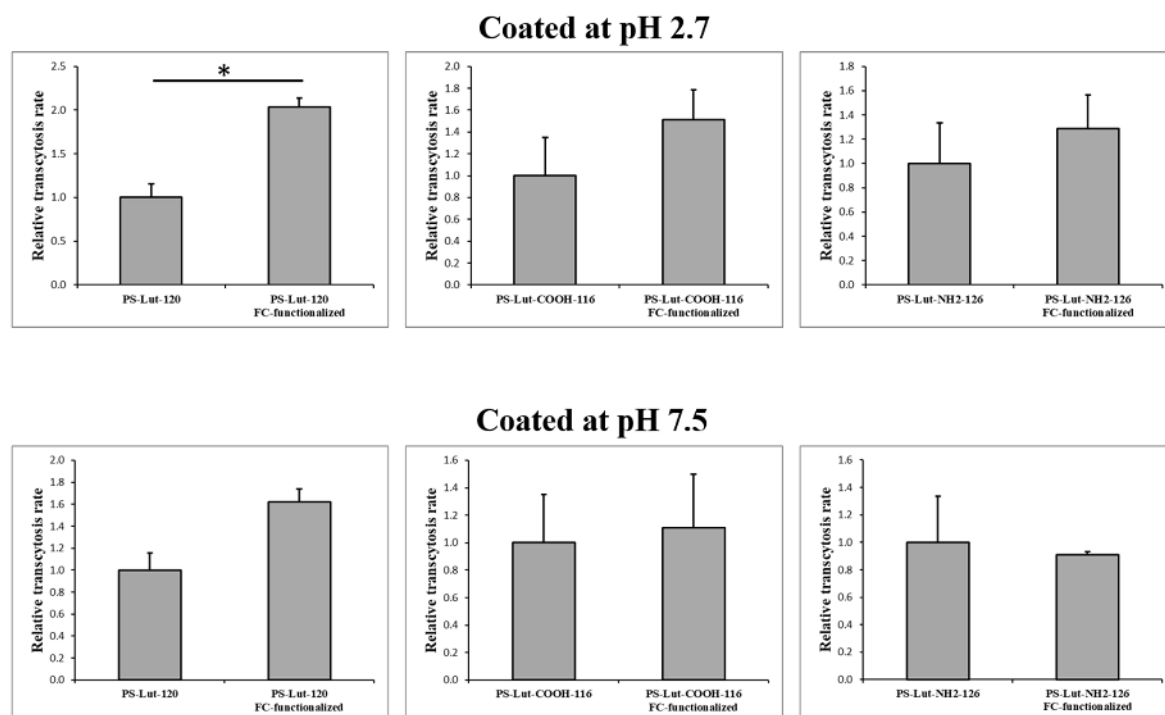


Fig. 25: Transcytosis rate of FC-functionalized polystyrene nanoparticles.

This figure depicts the transcytosis rate of FC-functionalized polystyrene nanoparticles coated at pH 2.7 and pH 7.5. All nanoparticles coated at pH 2.7 showed an increased transcytosis rate compared to nanoparticles initially coated at pH 7.5. A student's t-test was performed to determine significance levels ($p < 0.05$ was considered statistically significant).

The next step was a transfer of the established method to other agents. Therefore, Vitamin B₁₂ was analyzed for its role as another potential transcytosis-of-nanoparticles increasing agent as described in other studies[43, 197-199]. In the human intestine, Vitamin B₁₂ is internalized via receptor-mediated endocytosis. In this process, Vitamin B₁₂ firstly binds to intrinsic factor (IF) and this complex is afterwards internalized via apically expressed IF-Cbl receptor[200]. In addition, Vitamin B₁₂ can also be bound and internalized via an intrinsic factor-independent pathway via transcobalamin II receptor[201]. Both receptors can then subsequently mediate transcytosis of Vitamin B₁₂ into the bloodstream. In Caco-2 cells, the presence of both receptors was already demonstrated[202, 203]. Hence, Vitamin B₁₂ was picked as a putative agent for receptor-mediated uptake and transcytosis.

In this thesis, decoration of nanoparticles with Vitamin B₁₂ was carried out via adsorption as described in Chapter 3.1.10. Finally, nanoparticle transcytosis of functionalized nanoparticles was compared against their unfunctionalized counterparts (Fig. 26). All three tested lutensol-stabilized nanoparticles featured an increase in transcytosis efficiency after Vitamin B₁₂-functionalization. In case of positively and negatively charged nanoparticles,

this increase was highly significant. The transcytosis efficiency was enriched up to a factor of 5, which was comparable to the chemically-bound Vitamin B₁₂-conjugated nanoparticles described in the literature and might be accomplished by a pathway switch and a subsequent prevention of trafficking to lysosomes after Vitamin B₁₂-functionalization[43]. Surprisingly, the transcytosis rate was even higher than the increase for nanoparticles functionalized with the Fc region (Fig. 25). Overall, these results indicate that a functionalization of certain agents on nanoparticles via “simple” adsorption can dramatically increase the rate of transcytosis, which might be highly interesting for the development of nanocarriers for oral drug delivery.

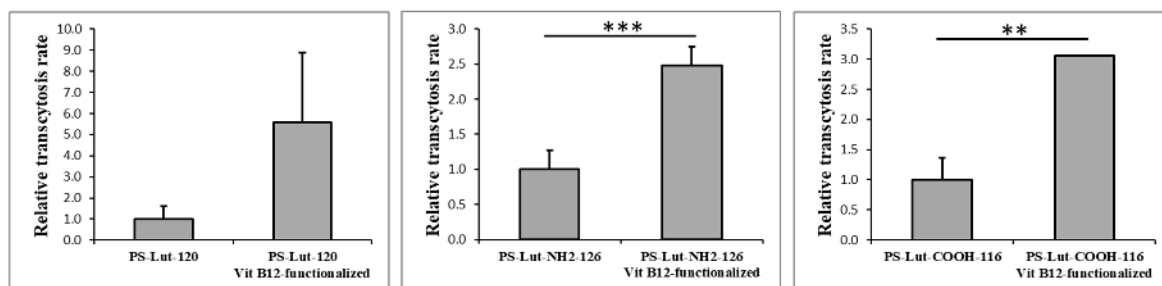


Fig. 26: Transcytosis rate of Vitamin B₁₂-functionalized polystyrene nanoparticles.

This figure depicts the transcytosis rate of Vitamin B₁₂-functionalized lutensol-stabilized polystyrene nanoparticles. Nanoparticles coated with Vitamin B₁₂ featured an up to 5-fold increase of transcytosis compared to their unfunctionalized counterparts. A student's t-test was performed to determine statistical significance levels, where $p < 0.05 = *$, $p < 0.01 = **$, $p < 0.001 = ***$.

3.1.11 Obstacles of transcytosis determination

Nanoparticle transcytosis can be determined using various strategies. These include nanoparticle translocation measurements e.g. via mass spectrometry[204], high-performance liquid chromatography[205], flow cytometry[72, 206-208], radioactivity[209], ELISA assay[210] or various fluorescence assays[211-214]. All these measurements have one thing in common: They rely on the quantification of nanoparticles in the basal transwell chamber compartment. For this process, various types of transwell membranes with different structures and pore sizes are used.

In the present thesis, the process of nanoparticle transcytosis was analyzed via confocal laser scanning microscopy. Therefore, Caco-2 cells in polycarbonate transwells with a pore size of 3 μm were incubated with 500 $\mu\text{g/mL}$ carboxylated SDS-stabilized nanoparticles for 4 h to permit for transcytotic events. Then, transwell membranes were thoroughly cut with a

scalpel. Adhered Caco-2 cells were fixed with 4% PFA and cell membranes were stained with Cell Mask Orange. Finally, Caco-2 cells were monitored via cLSM in different Z-positions (Fig. 27-29). After 4 h of nanoparticle incubation, fluorescence signal was detected in various cellular compartment when scanning through the cells in different Z-positions.

First of all, major nanoparticle clusters were detected on top of and attached to the cell membrane (Fig. 27), putatively undergoing endocytosis at the moment of fixation. Also, several nanoparticles that were already internalized could be visualized. The second Z-position snapshot displays the basal cellular compartment in contact to the transwell membrane (Fig. 28). Here, nanoparticles could be visualized being either in the process of basal cellular exocytosis or being already exocytosed and attached to the apical side of the transwell membrane. This picture also marks the first problem of the transwell system: Even though nanoparticles were clearly spatially under the cellular monolayer, it is by no means guaranteed that they will slip through the 3 μm pores and reach the basal chamber of the transwell system. The last Z-position snapshot features the basal side of the transwell membrane (Fig. 29). Here, it is clearly visible that polystyrene nanoparticles were, after being successfully transcytosed through the Caco-2 cell layer, able to slip through the 3 μm pores. However, this picture also marks one of the key problems of the transwell system. It is not guaranteed that all nanoparticles, which are transported through the monolayer, do reach the basal compartment of the transwell system. Since all methods of transcytosis measurements, however, rely on a quantification of the basal cell culture medium, it can be concluded that transcytosis measurements in general may be distorted by nanoparticles adhering on a) the apical side of the transwell membrane (not spatially reaching the pores to slip through) and b) the basal side of the transwell membrane (potentially via electrostatic forces). Nevertheless, it could be confirmed that Caco-2 cells are able to transcytose polystyrene nanoparticles in general.

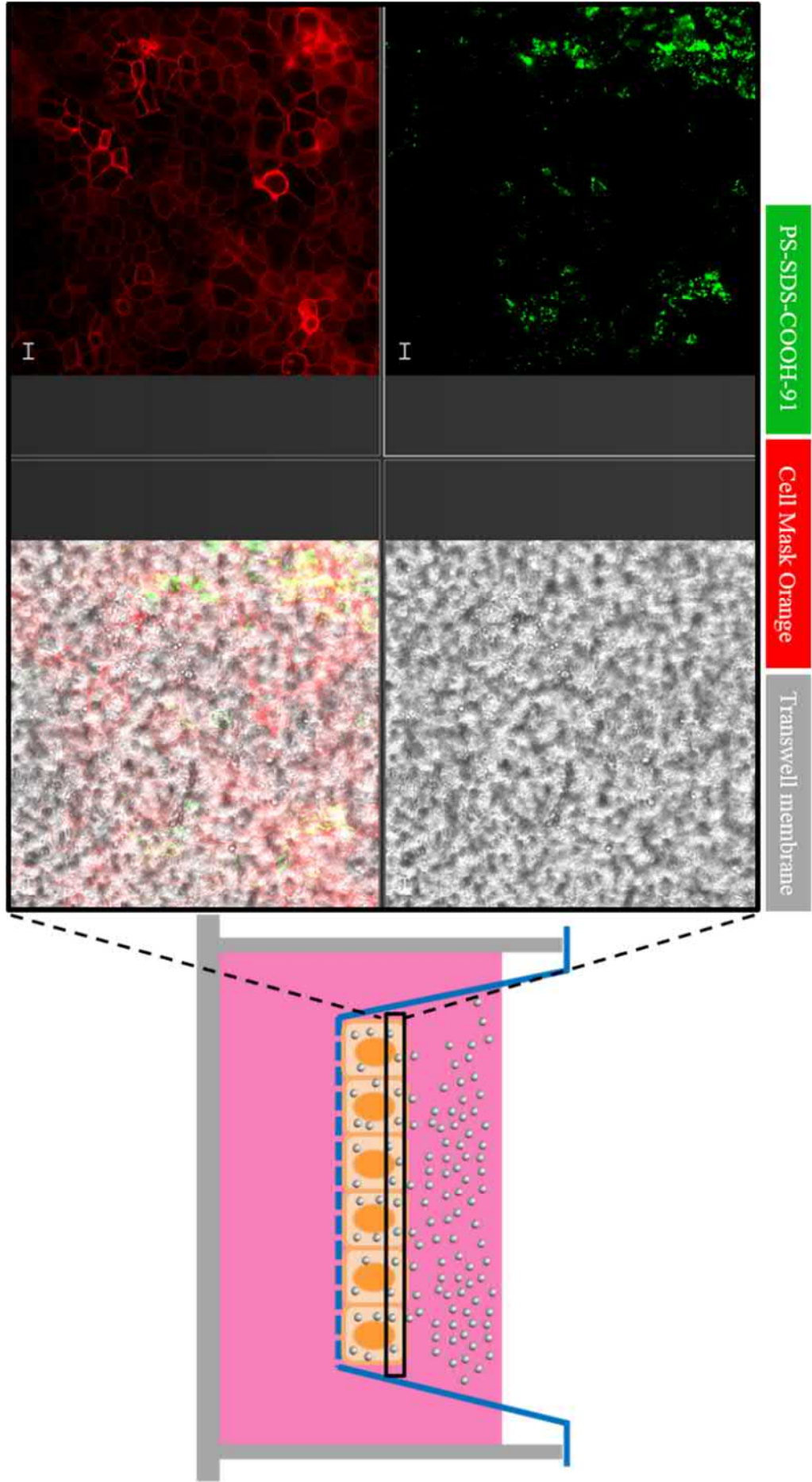


Fig. 27: Apical view of Caco-2 cells incubated with nanoparticles in transwell system.
This figure depicts the apical view of a Caco-2 cell layer on a transwell membrane incubated with 500 $\mu\text{g/mL}$ carboxylated SDS-stabilized polystyrene nanoparticles. Nanoparticles are internalized by the cells as well as adherent on the apical cell membrane. Nanoparticles are pseudocolored in green, Cell Mask Orange is pseudocolored in red, the polycarbonate transwell membrane is visualized by transmission (grey). Scale bar = 10 μm .

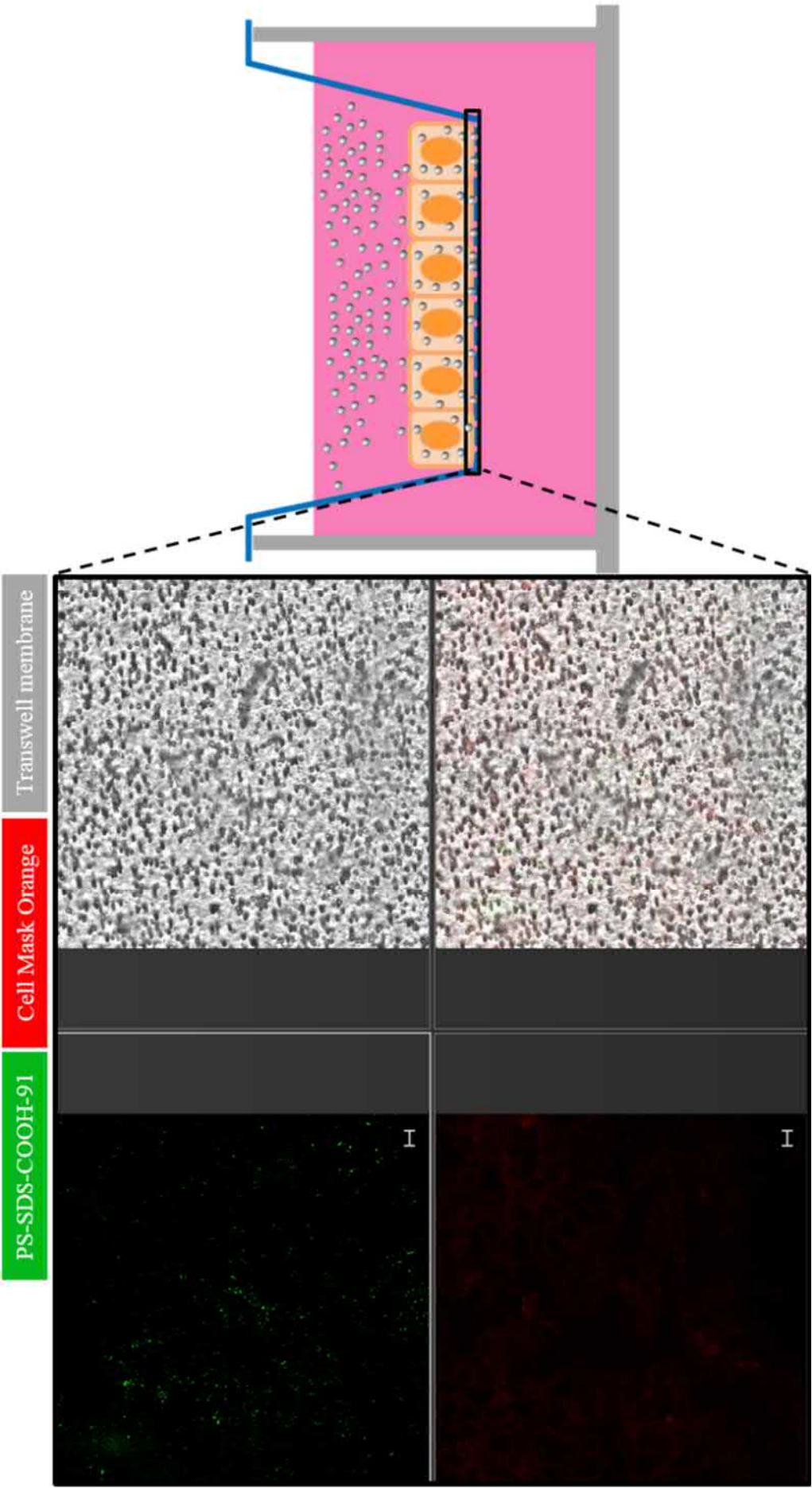


Fig. 28: Central view of Caco-2 cells incubated with nanoparticles in transwell system.

This figure depicts the central view of a Caco-2 cell layer on a transwell membrane incubated with 500 $\mu\text{g/mL}$ carboxylated SDS-stabilized polystyrene nanoparticles. Nanoparticles are localized in the basal compartment of Caco-2 cells or below the Caco-2 cell layer adhered to the polycarbonate membrane and its respective 3 μm pores. Nanoparticles are pseudocolored in green, Cell Mask Orange is pseudocolored in red, the polycarbonate transwell membrane is visualized by transmission (grey). Scale bar = 10 μm .

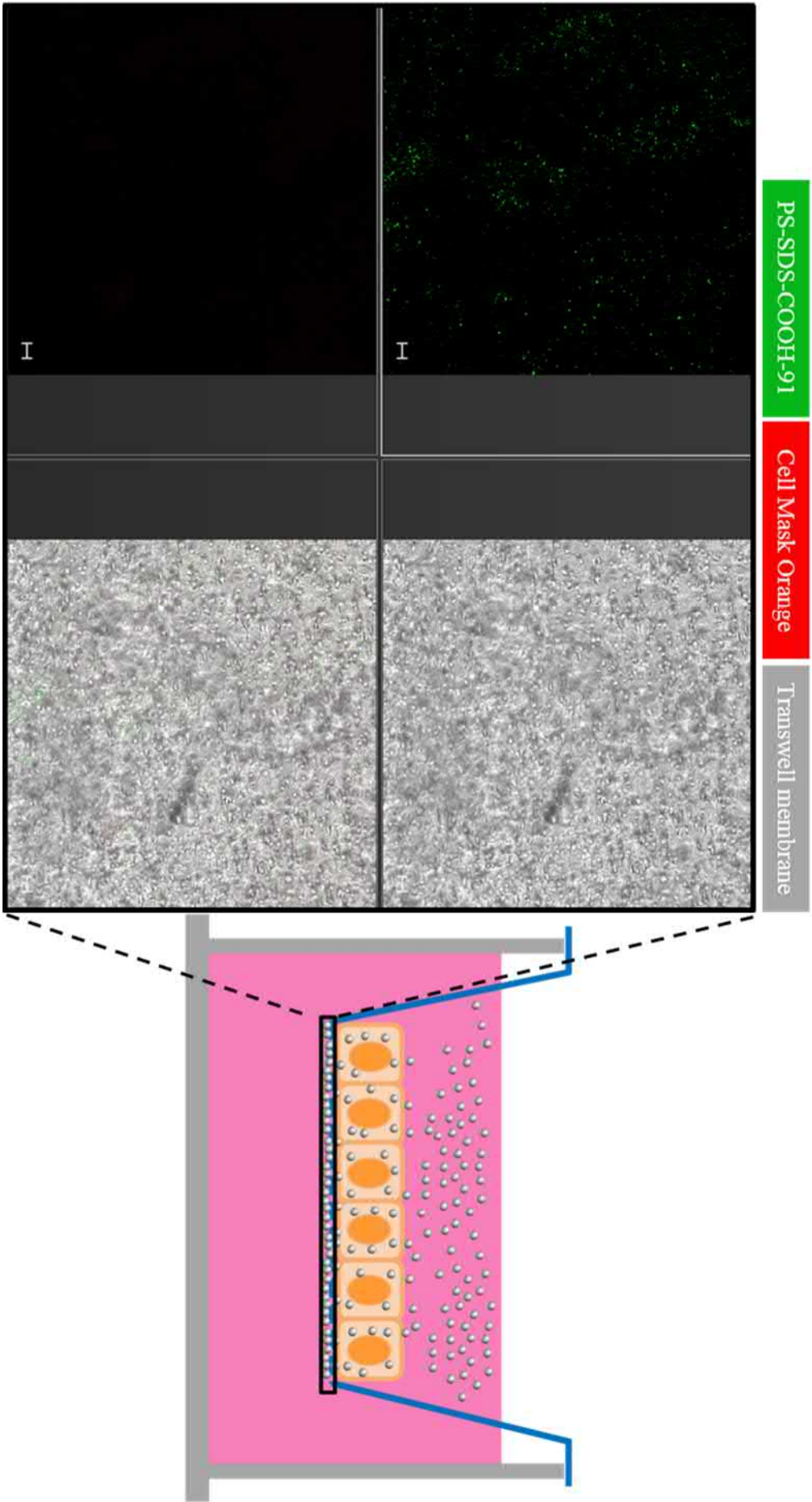


Fig. 29: Basal view of Caco-2 cells incubated with nanoparticles in transwell system. This figure depicts the basal view of a Caco-2 cell layer on a transwell membrane incubated with 500 $\mu\text{g/mL}$ carboxylated SDS-stabilized polystyrene nanoparticles. Nanoparticles are localized below the polycarbonate membrane and adherent to the basal membrane side. Nanoparticles are pseudocolored in green, Cell Mask Orange is pseudocolored in red, the polycarbonate transwell membrane is visualized by transmission (grey). Scale bar = 10 μm .

3.2 Intracellular trafficking of polystyrene nanoparticles in Caco-2 cells

In theory, drug encapsulation into nanocarriers marks one of the most promising approaches for oral drug delivery to protect the drug from digestion in the stomach and increase the bioavailability. However, up to now, the transcytosis efficiency of such carrier systems is still elusively low. This certainty goes hand in hand with the fact that nanocarrier pathways are not yet fully characterized and can be influenced by the respective material, size, charge and surface decorations. In this thesis, one of the major goals was the detection of intracellular key proteins that contribute towards successful transcytosis. For this purpose, a combination of mass spectrometry analysis and confocal laser scanning microscopy was employed.

3.2.1 Mass spectrometry analysis of transcytosed nanoparticles

Liquid chromatography/Mass spectrometry (LC/MS) is a powerful tool for the detection of organic compounds[215-217]. In the world of nanomedicine, mass spectrometry is mainly used for the investigation of the protein corona, which immediately forms after incubating a nanoparticle in any kind of protein-containing medium, e.g. blood[218-221]. In this process, peptides are identified, sequenced and the amount of each adsorbed protein can be quantified[222-224]. In this thesis, a similar approach was used for the determination of putative transcytosis relevant proteins. The idea was, that nanoparticles, that are successfully transcytosed by Caco-2 cells, adhere certain trafficking relevant proteins on their way through the cell. In addition, Caco-2 cells might segregate certain proteins in the process of (nanoparticle) exocytosis. By detecting and quantifying such proteins against a negative control, putative transcytosis relevant key players might be discovered.

Therefore, Caco-2 cells were cultivated in transwell system for 14 days until cell layers exhibited TEER values over $500 \Omega \times \text{cm}^2$. Then, different nanoparticles were added to the Caco-2 cells in a concentration of $500 \mu\text{g/mL}$ and incubated for 24 hours to facilitate transcytosis. Several transwells were left untreated and only incubated with DMEM. Next, the whole basal medium of all transwells was withdrawn and pooled for the respective fractions (nanoparticle treated vs. untreated). Proteins were extracted from the basal medium and proteins attached on transcytosed nanoparticles were detached using a protocol

from Schöttler et al.[54]. In addition, whole cellular proteins were extracted from Caco-2 cells.

Firstly, presence of proteins was determined via SDS-Page (Fig. 30). As expected, whole cell protein extracts showed a broad diversified pattern. The basal medium showed significantly less bands with some major bands between 50 and 70 kDa. In both cases, pattern did not show any major differences between nanoparticle treated and untreated cells. This was in line with our expectations, since only a fractional amount of nanoparticles is transcytosed to the basal side and only minor changes in protein patterns were expected. Thus, the method of mass spectrometry was employed to gain deeper insight into smaller changes of protein levels (Fig. 31).

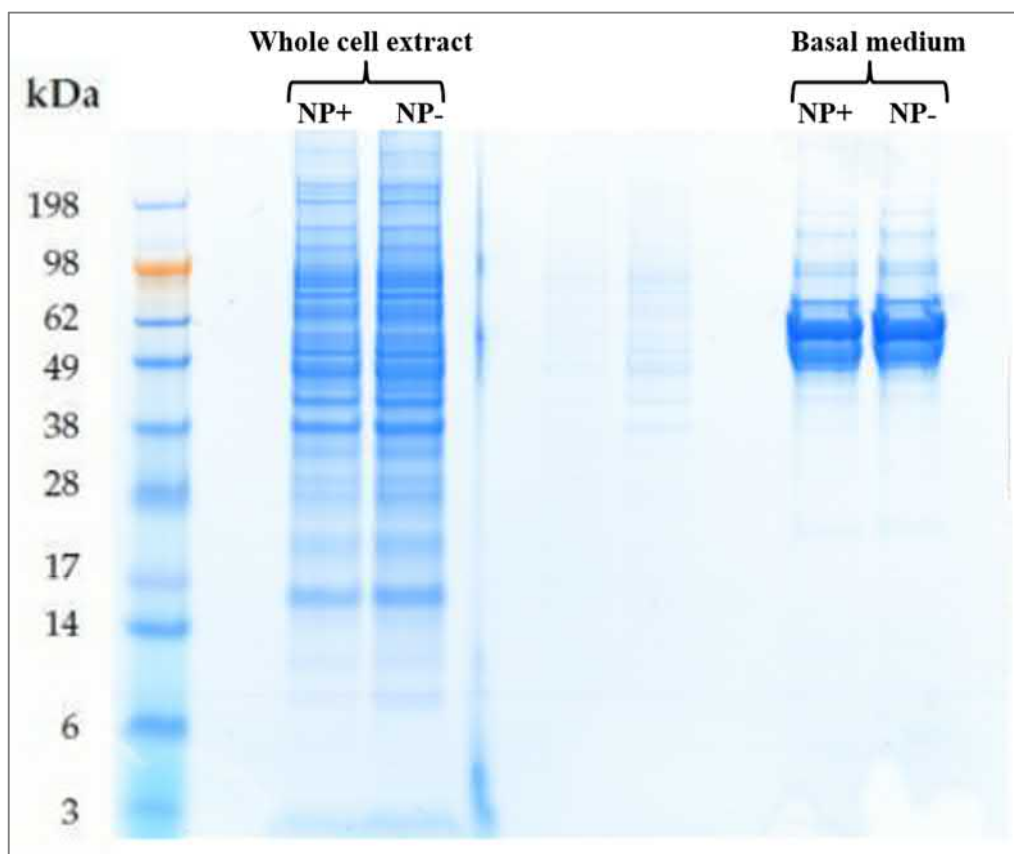


Fig. 30: SDS Page of nanoparticle treated Caco-2 cells and protein/nanoparticle containing basal transwell medium.

Caco-2 cells cultured in transwell system were treated with 500 $\mu\text{g/mL}$ polystyrene nanoparticles. After 24 hours of incubation and hence possible transcytotic activity, whole protein was extracted directly from nanoparticle treated and untreated Caco-2 cells. In addition, basal cell culture medium of nanoparticle treated and untreated wells was removed and prepared for protein (corona) analysis. Both preparations were controlled for their protein patterns via SDS-Page. In both experiments, protein patterns of nanoparticle-treated and -untreated cells were similar.

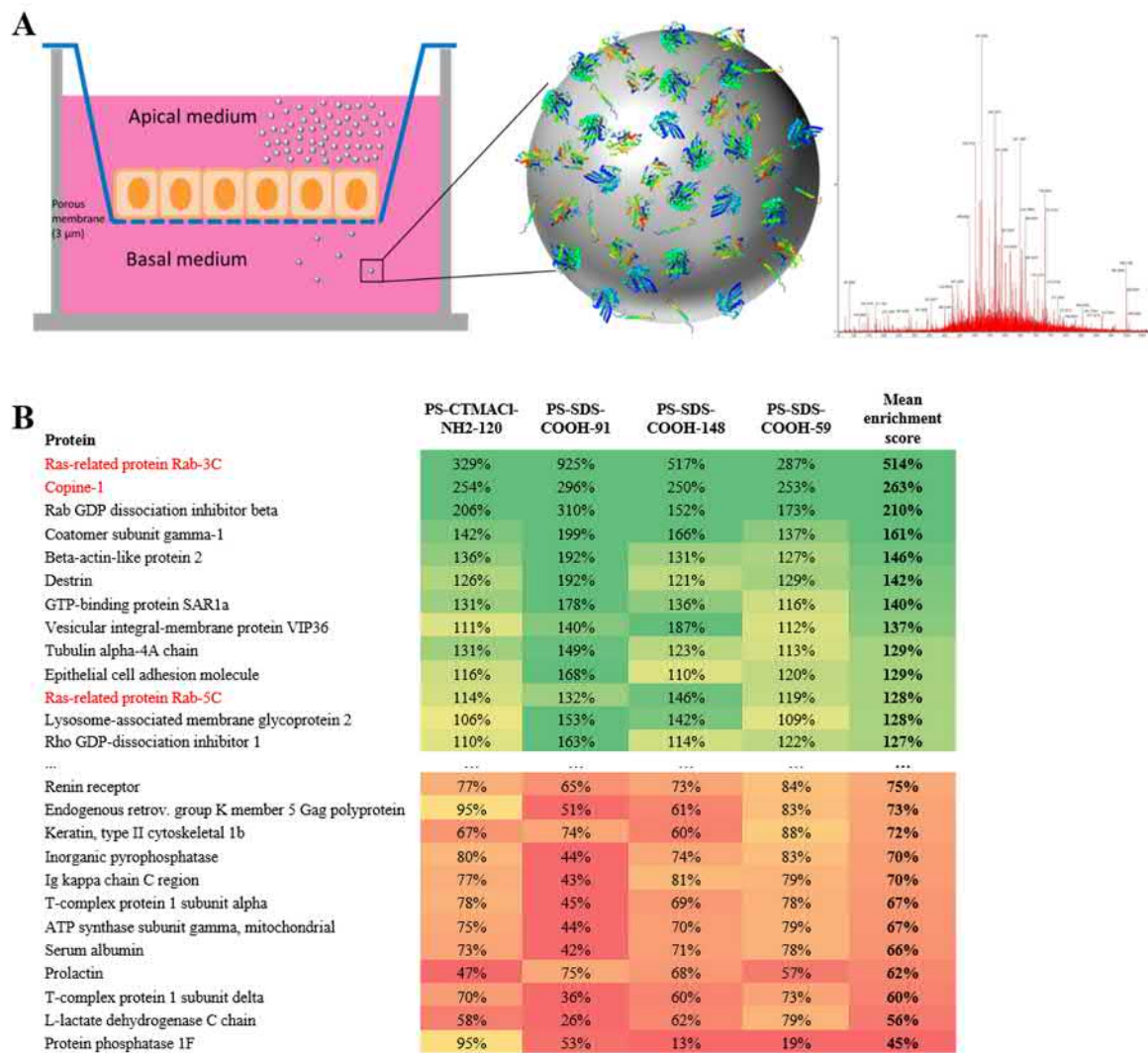


Fig. 31: Mass spectrometry analysis of basal cell culture medium after nanoparticle addition. (A) Workflow of putative transcytosis relevant protein detection. Caco-2 cells were cultivated for 14 days until polarization and four different PS-NP were added for 24 hours in DMEM containing 10% FBS at a concentration of 500 $\mu\text{g/mL}$. The protein corona of subsequent transcytosed nanoparticles as well as basal secreted proteins were analyzed and quantified via LC-MS. Protein crystal structures were obtained from the RCSB protein database[225-229](1N6H; 4UJ3; 2MOF; 2BTF; 1S8F). (B) Mass spectrometry analysis of nanoparticle positive vs. nanoparticle negative cell culture medium. Green colors symbolize a high enrichment score (here, only proteins that have a putative function in intracellular trafficking processes are displayed), while red colors indicate lower enrichment values[213].

By investigating the nanoparticles transcytosed to the basal medium 24 h after apical nanoparticle addition (Fig. 31A), a total amount of 669 proteins could be detected via mass spectrometry analysis. All proteins assigned to *Bos Taurus* as residues from the fetal bovine serum in the apical medium were removed from the data set. For the 490 remaining proteins a cutoff was set, determining that only proteins accounting for at least 0.01% of absolute proteins were displayed. The 470 remaining proteins were sorted for their mean enrichment

scores. The enrichment of the nanoparticle positive fraction over the nanoparticle negative fraction was determined as it is possible that a section of proteins from the mass spectrometry data originate from the basal secretion of proteins as well as cell debris. Interestingly, mainly proteins that have a putative function in intracellular trafficking or exocytosis were highly enriched, hinting success of the approach. Proteins that were enriched and exhibit a putative function in intracellular trafficking are listed in Fig. 31 B. Here, particularly Copine-1 (Cpne1) and Rab3 (see also 7.10) triggered our interest due their high enrichment in combination with their intracellular function. Rab3, a protein involved in many vesicular trafficking processes and especially in the regulation of exocytosis[230-232], had a mean enrichment of 514% across all used nanoparticle systems. Cpne1, which was enriched by 263%, is a Ca^{2+} -dependent protein putatively involved in trafficking towards the membrane[233] and is postulated to have a function as a secretory vesicle-binding protein and general membrane trafficking protein[234]. In addition, Rab5c, which was slightly enriched by 128%, drew attention due to the fact that the Rab5 family is reportedly involved in macropinocytosis and early trafficking of nanoparticles[235-237]. In contrast to the basal transwell medium, mass spectrometry of whole Caco-2 protein extract did not yield any interesting enrichments. After picking candidate genes from the MS data as well as other putative exocytosis relevant proteins from the literature, Caco-2 cells were transfected with GFP- or mCherry-coupled cDNAs.

3.2.2 RNA extractions from Caco-2 cells

Instead of ordering cDNAs for the creation of GFP- or mCherry-coupled transgenic Caco-2 cell lines, the mRNAs for cDNA synthesis were extracted directly from Caco-2 cells. This procedure had one major advantage. By amplifying the genes directly from Caco-2 cells, it was ensured that the gene-of-interest featured a basal expression in Caco-2 cells. After total RNA extraction, quality of RNA was controlled via spectrophotometry (Fig. 32). Extracted RNA featured a sufficient concentration of 776 ng/ μ L for cDNA synthesis. The RNA:protein ratio of 2.03, as determined by the 260/280 nm coefficient, indicated high sample purity.

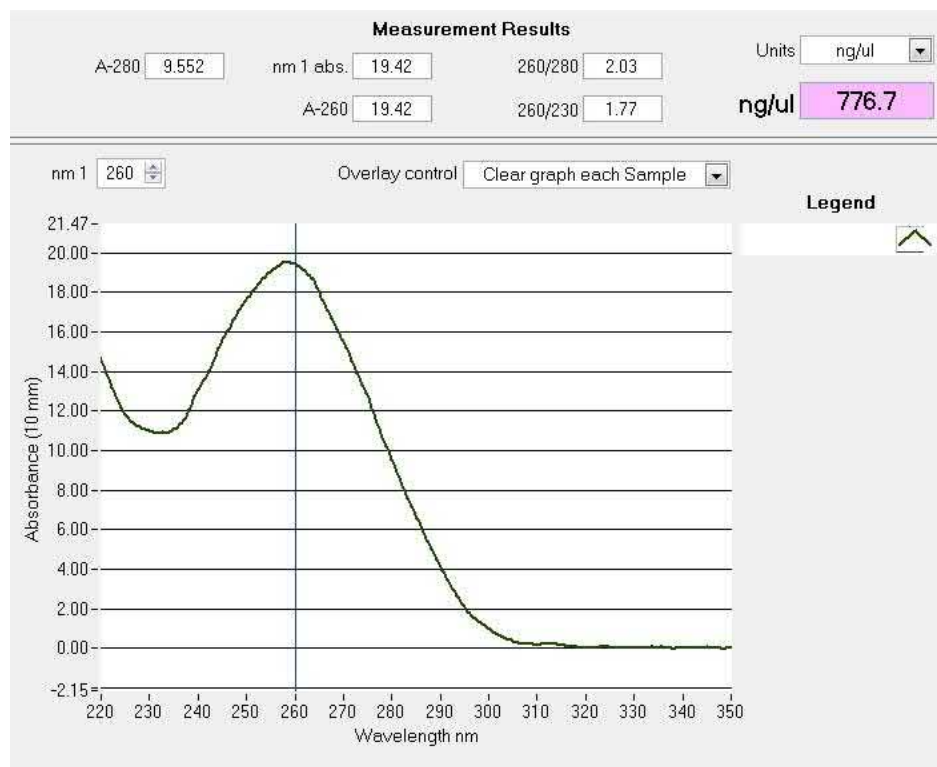


Fig. 32: RNA Extraction from Caco-2 cells.

Total RNA was extracted from Caco-2 cells using the Qiagen RNeasy Kit. Quality was controlled via Nanodrop 8000 spectrophotometric analysis. Extracted RNA showed absorbance coefficients of 2.03 (260/280 nm) and 1.77 (260/230 nm) and a total RNA amount of 776 ng/ μ L.

3.2.3 Amplification of different cDNAs

Next, total cellular cDNA was created by using a reverse transcriptase in combination with oligo(dT) and random hexamer primers. Then, the respective cDNAs were amplified via polymerase chain reaction and controlled via agarose gel electrophoresis (Fig. 33, SI Fig. 13). In total, 19 cDNAs were successfully amplified.

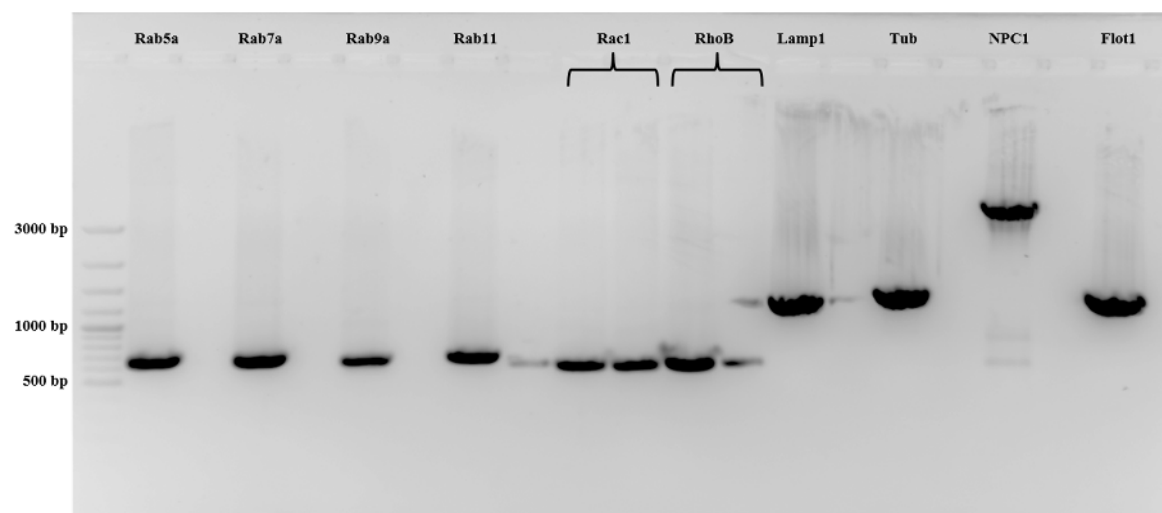


Fig. 33: Amplification of putative trafficking relevant cDNAs via polymerase chain reaction.

This figure depicts an agarose gel electrophoresis of putative transcytosis or exocytosis relevant cDNAs from total extracted Caco-2 RNA. All cDNAs could be amplified. Expected lengths: Rab5a: 645 bp, Rab7a: 621 bp, Rab9a: 603 bp, Rab11: 648 bp, Rac1: 576 bp, RhoB: 588 bp, Lamp1: 1251 bp, Tub: 1353 bp, NPC1: 3834 bp, Flot1: 1281 bp.

Within the PCR, 15 bp overlaps were added to the 5'P and 3'OH ends of cDNA fragments via specifically designed primers. These 15 bp overlaps were complementary to a part of the vector sequence (pLJM1-eGFP, pLVX-ZsGreen1-N1 or pLVX-mCherry-N1). By using the so-called In-Fusion cloning technology[238-240], cDNAs could be fused to the vector backbone via an In-Fusion enzyme, which recognizes the complementary 15 bp overlaps. Successful cloning was controlled via Eco R1 test restriction and subsequent agarose gel electrophoresis (Fig. 34). All constructs were detected at the correct band size (data for Vamp8: 300 bp, RalA: 618 bp, Rab5c: 648 bp, Rab3a: 660 bp, Rab27a: 663 bp, ACTBL2: 1128 bp, VTN: 1344 bp, Cpne1: 1611 bp, Exoc1: 2682 bp not shown in Fig. 34). RhoB and Flot1 featured additional internal restriction sites for EcoR1, hence multiple bands on the gel could be detected as expected (one extra band for Flot1, two extra bands for RhoB).

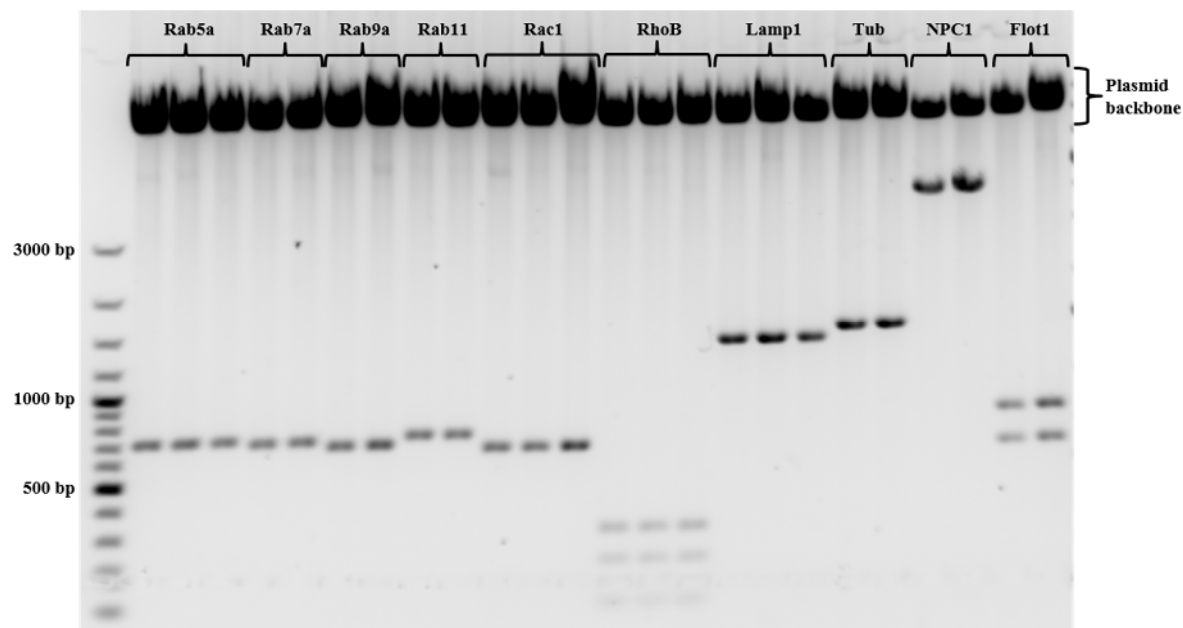


Fig. 34: Test restriction of recombinant ZsGreen plasmids.

After plasmid isolation, 2-3 potential recombinant plasmids were digested with Eco R1 for 1 h and afterwards analyzed via agarose gel electrophoresis. The plasmid backbone appeared as a major band, while inserted cDNAs were separated according to their respective sizes. RhoB and Flot1 featured double and triple bands due to additional internal restriction sites for Eco R1. Expected lengths: Rab5a: 645 bp, Rab7a: 621 bp, Rab9a: 603 bp, Rab11: 648 bp, Rac1: 576 bp, RhoB: 588 bp, Lamp1: 1251 bp, Tub: 1353 bp, NPC1: 3834 bp, Flot1: 1281 bp.

Finally, recombinant plasmids were sequenced by Sanger Sequencing to exclude a distortion of cellular experiments due to polymerase induced replication errors[241]. In some genes, minor point mutations could be detected, however, most of them were silent. In case of RalA, a miss sense mutation led to a stop codon, which made the recombinant plasmid unusable for further experiments.

3.2.4 Generation of fluorescent lentiviral vectors

The creation of artificial lentiviral vectors requires multiple lentiviral components, which are split across different vectors for safety purposes. This strategy diminishes the risk of creating a lentivirus that can replicate by itself[242]. In the present thesis, a lentiviral system consisting of three different plasmids was used, containing essentially a) the GFP-gene-of-interest-construct (SI Fig. 14-16), b) the genes for lentiviral envelope (SI Fig. 17) and c) the genes for lentiviral packaging (SI Fig. 18). To produce lentiviral particles, all three plasmids were transfected into HEK293T cells, a standard cell line for the production of lentiviruses[243-245]. Since the transfer plasmid contained the gene for eGFP (or other fluorophors), lentivirus particle-producing HEK293T cells could be detected via fluorescence microscopy (Fig. 35). After 48 hours of incubation, nearly all HEK293T cells were positive for eGFP, indicating the production of lentiviral particles.

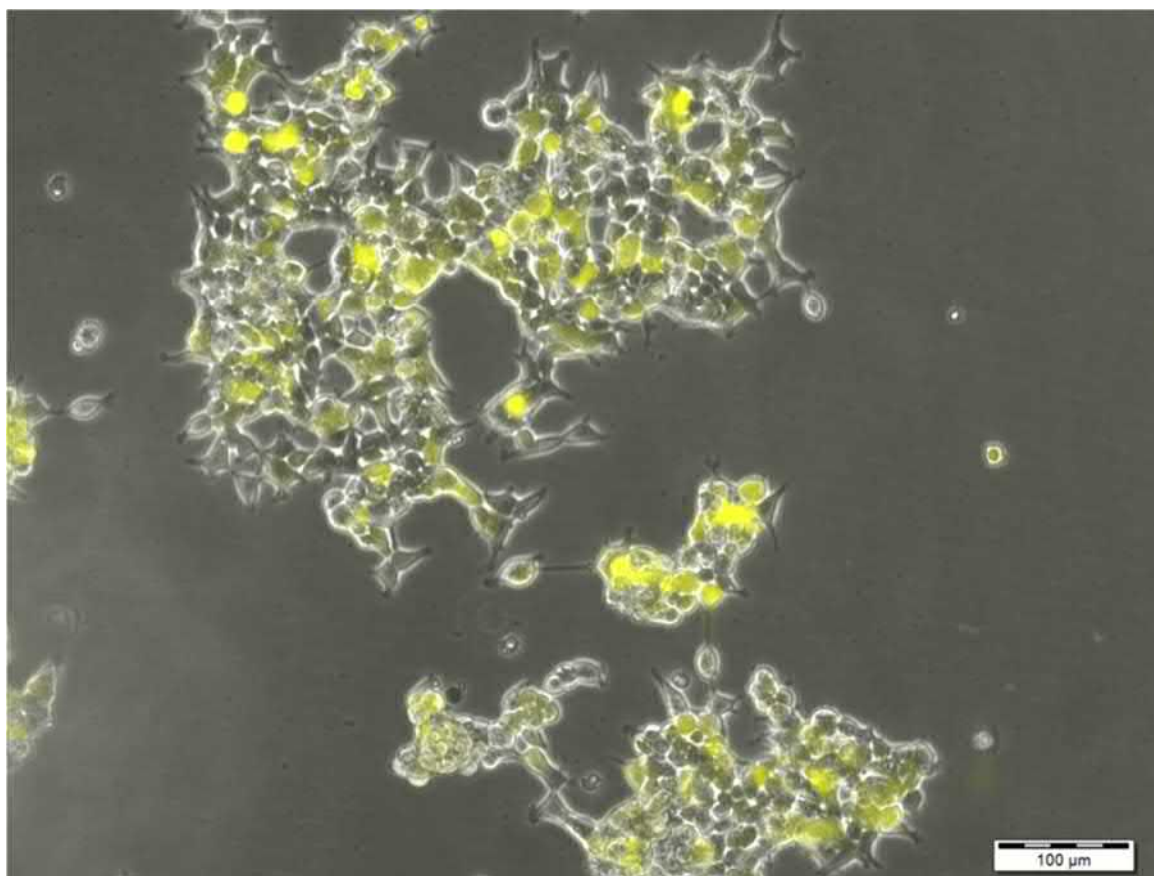


Fig. 35: HEK293-T cells producing lentiviral particles.

This figure depicts HEK293-T cells transfected with pLVX-ZsGreen1-N1, psPAX2 and pMD2.G. ZsGreen dye was excited via a 488 nm fluorescence lamp. Nearly all HEK293-T cells were positive for ZsGreen after 48 h of incubation, indicating lentivirus production.

The presence of Lentiviral particles was also monitored via lentiviral flash test (Fig. 36). After confirming a lentiviral titer of at least 5×10^5 infectious units/mL, lentiviral particles were harvested from the supernatant and concentrated by ultracentrifugation.

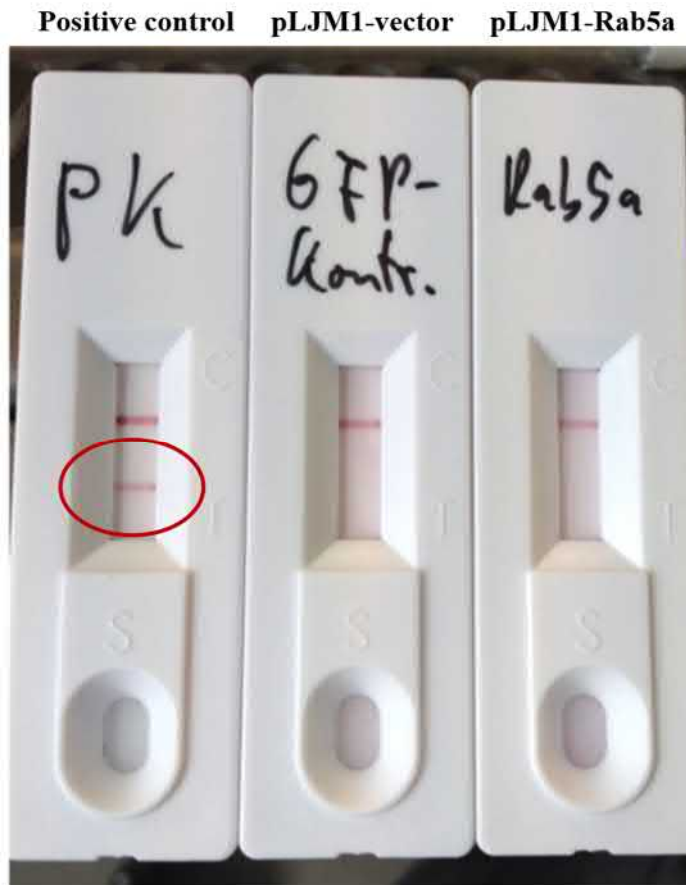


Fig. 36: Lentiviral flash test.

This figure depicts a lentiviral flash titer test. A second band (red circle) indicates a titer of at least $>5 \times 10^5$ infectious units / mL.

Afterwards, Caco-2 cells were infected for 48 h under addition of polybrene, an agent that enhances virus adsorption on cell membranes[246, 247]. Since lentiviral gene transfer results in a stable integration into the cell's genome, cells could easily be selected via puromycin, whose resistance gene was encoded on the respective transfer plasmid (see also SI Fig. 14-16). For this purpose, a puromycin kill curve was established for Caco-2 cells. This kill curve indicated that a concentration of $3 \mu\text{g/mL}$ puromycin was sufficient to kill all non-transfected cells. After approximately one week of selection pressure, Caco-2 cell lines were considered as stable transfected. All lentiviral GFP-coupled constructs with the exclusion of Vamp8, NPC1, ACTBL-2 and VTN, which neither yielded a sufficient lentiviral titer nor any fluorescence signal, could be transferred to Caco-2 cells. After

establishing transgenic cell lines, the percentage of GFP-positive cells was determined via flow cytometry analysis (Fig. 37). All cell lines, with the exception of Flot1- and Exoc1-transfected cell lines, featured over 95% GFP-positive cells. Flot1 and Exoc1 might be harder to transfect due to featuring the largest cDNA with sizes of 1281 bp and 2682 bp, respectively. In a later part of the study, another stable cell line was created, carrying the Caveolin1 gene coupled to eGFP. Caco-2 cells transfected with Cav1 were also almost 100% positive for eGFP (data not shown).

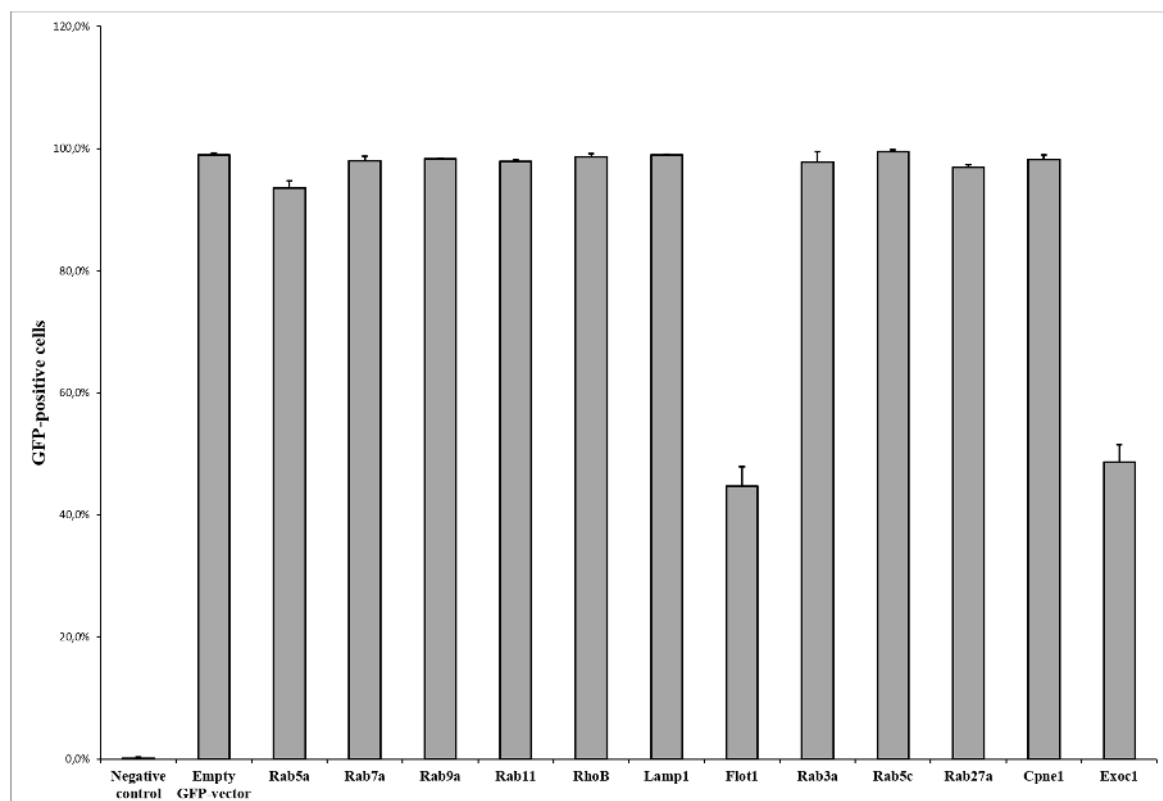


Fig. 37: Determination of transgenic stability.

Lentiviral transfected cells were controlled via flow cytometry for their GFP-signal. Flot1-GFP- and Exoc1-GFP-transfected cells featured around 40% GFP-positive cells, while other constructs were almost 100% stable transfected.

3.2.5 Co-Localization analysis of nanoparticle-treated Caco-2 cells

Markers of the endolysosomal system as well as putative exocytosis- and transcytosis-relevant proteins were analyzed by cLSM co-localization studies. After 4 hours of incubation without removal of nanoparticles in the cell culture medium, nearly all of the tested markers showed co-localization. The small GTPases Rab5a, Rab7a, Rab9a as markers for early or late endosomes[248, 249] as well as Lamp1 as marker for lysosomes were present on relatively big, well-shaped vesicles containing one or more fluorescent spots (Fig. 38A, for Rab9a also Fig. 38C as an example). Recycling endosome marker Rab11[249] manifested in smaller vesicles and did not show any co-localization to nanoparticles. RhoB as a putative marker for macropinocytosis[248] showed strong co-localization to the PS-NP and was abundant on the cell membrane as well as vesicles which presumably represent early endosomes right after macropinocytosis (Fig. 38A). In contrast, we could not detect any significant co-localization with Caveolin1 as a marker for caveolae-mediated endocytosis[49, 250]. Flotillin1 as marker for a caveolin- and clathrin-independent pathway[251] also showed only minor co-localization. Interestingly, all of the tested putative markers for the exo- and transcytotic system showed co-localization (Fig. 38B). Rab5c, a protein abundant in our mass spectrometry transcytosis data (with a mean enrichment score of enriched by 128%; Fig. 31), showed a similar co-localization pattern as early endosome marker Rab5a. Copine1, a protein enriched by 263% in our MS data, manifested in vesicular structures exhibiting co-localization to the polystyrene nanoparticles (Fig. 38C). Furthermore, Rab3a, a protein putatively involved in the regulation of exocytosis[232] showed minor co-localization (Fig. 38B). This is of particular interest, since Rab3 was the most enriched protein in our MS data comparing the nanoparticle positive and negative fraction. Additionally, Rab27a and Exoc1 (also known as Sec3) as other putative markers for the exocytosis machinery found in the literature[252-254], also showed minor co-localization. On a side note, endocytosis inhibitors were tested on Caco-2 cells (SI Fig. 12). Nearly all tested inhibitors reduced cellular uptake, indicating that uptake might not solely be dependent on macropinocytosis. However, all inhibitors were reducing cell viability, so the results were at least questionable. One of the major problems of confocal laser scanning microscopy is the so-called “bleed through”, which means that a fluorescent dye gets detected in multiple channels. To avoid any false signals, all dyes were controlled for their fluorescence spectra (SI Fig. 4-6) and potential overlaps. Also, single cLSM channels were controlled thoroughly (SI Fig. 19-20). No events of bleed through could be detected.

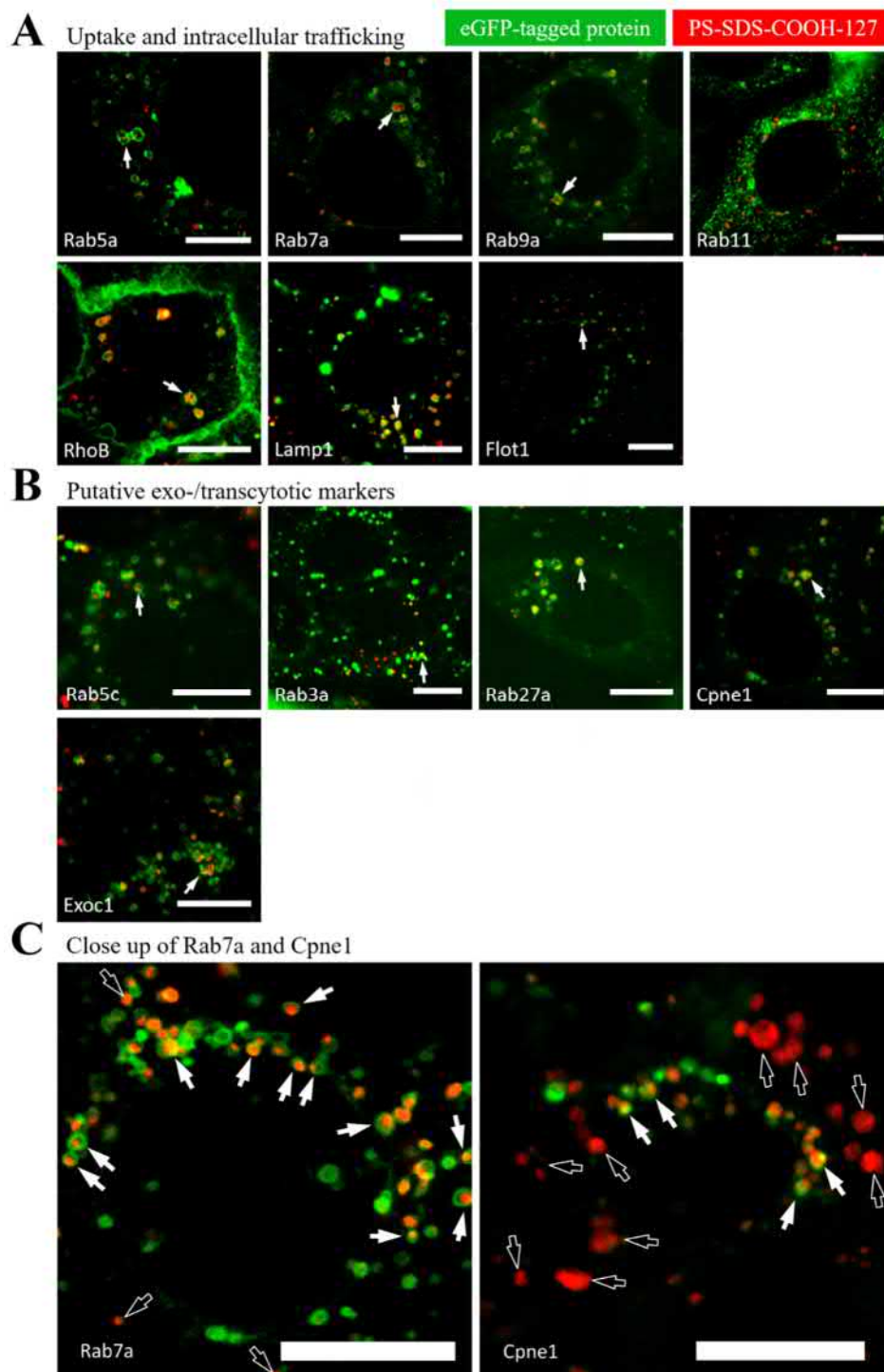


Fig. 38: Co-Localization of polystyrene nanoparticles with different GFP-tagged proteins.

Caco-2 cells were incubated in DMEM with FBS and 75 $\mu\text{g/mL}$ nanoparticles. Cells were washed three times with DPBS and fixed in 4% paraformaldehyde for 15 minutes. EGFP- or mCherry-tagged proteins are pseudocolored in green, while nanoparticles are pseudocolored in red. Co-localization resulted either in an orange overlay or nanoparticles being visualized in vesicles. (A) Co-localization of nanoparticles with different markers of the endolysosomal system. (B) Co-localization of nanoparticles with different putative markers of the exo- and transcytotic system. (C) Close up of Rab7a- and Cpne1-positive vesicles and their co-localization with polystyrene nanoparticles. \rightarrow = NP in Co-Localization with the marker protein. \nrightarrow = NP not co-localizing with the marker protein. A magnified version for each cLSM picture is available in the supplemental information (SI Figures 21-33). Scale bar = 10 μm .

To enhance the resolution and visualize nanoparticles in vesicles, another microscopy technique was employed. Ground-state-depletion (GSD) microscopy is based on depleting the ground-state energy of molecules outside of the focus, accomplishing lateral resolutions up to 15 nm in theory[255, 256]. With this super-resolution technique, nanoparticle co-localizations could be visualized, however, it was also not possible to separate huge nanoparticle clusters (SI Fig. 36-38).

Additionally, spatial co-localizations were confirmed via live cell imaging (for an example see Fig. 39) to exclude the possibility of coincidental co-localization events. Nanoparticles maintained co-localization for the whole observed time and were trafficked through the cell, as indicated by the movement line (bottom right corner; Fig. 39).

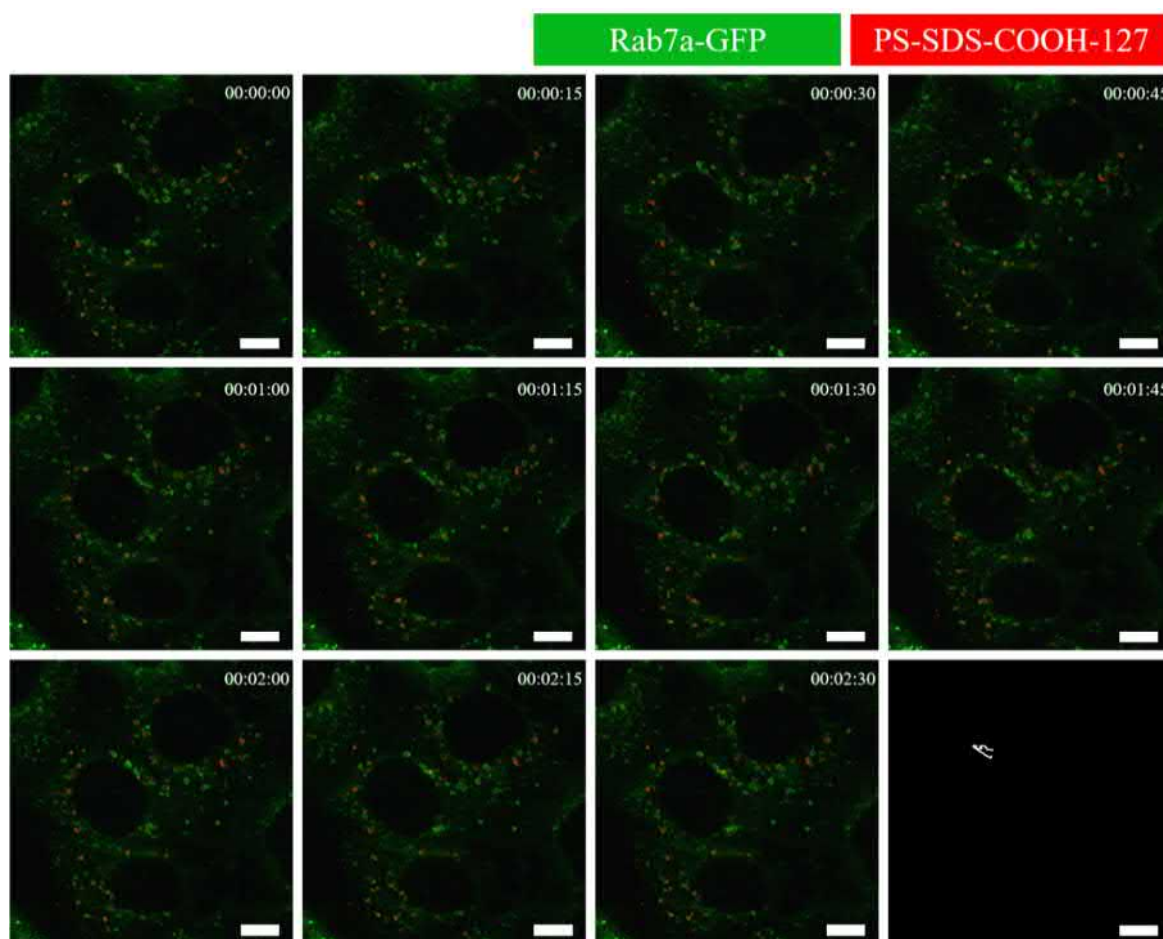


Fig. 39: Live Cell Imaging of nanoparticle trafficking.

To minimize the chance of artefacts as well as random occurring co-localization, live cell imaging experiments were performed for every transgenic construct. In the present example, nanoparticles were trapped in Rab7a positive vesicles for the whole length of live cell imaging and maintained co-localization. The movement of one nanoparticle trapped in a vesicle is indicated by the white line. Scale bar = 10 μ m.

Since Caco-2 cells in transwells are completely differentiated and polarized after around 14 days[257] and might therefore behave differently compared to Caco-2 cells grown in normal plates, trafficking experiments were also performed in transwells. Albeit pictures were substantially more difficult to obtain and analyze due to the structure of the polycarbonate membrane, the same co-localization patterns could be observed (Fig. 40, SI Fig. 34-35).

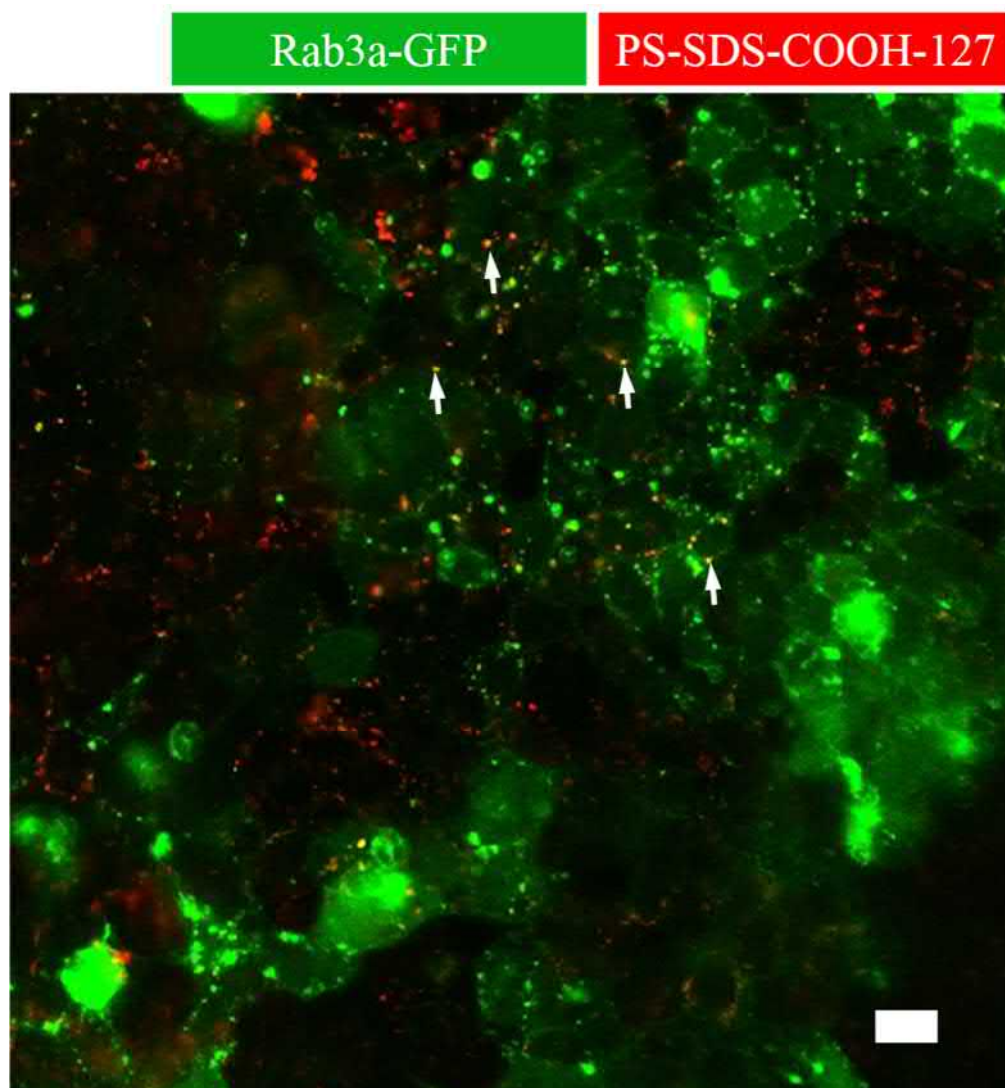


Fig. 40: Localization of Rab3a and polystyrene nanoparticles on transwell filters.

500 $\mu\text{g/mL}$ PS-SDS-COOH-127 were added for 24 hours into the apical medium. Afterwards, transwell filters were cut out with a scalpel and fixed on microscope slides. Rab3a was mostly localized on smaller vesicles and cytoplasm. Nanoparticles exhibited minor co-localization to Rab3a after 24 hours incubation on transwells, as indicated by white arrows. Scale bar = 10 μm .

3.2.6 Lysosomes as final fate for nanocarriers

Lysosomes are spherical, ovoid or tubular intracellular vesicles with an acidic pH value (pH 4.5 – 5)[258]. Their size varies between $<1\ \mu\text{m}$ and several microns, depending on the cell type[259]. The physiologic purpose is mainly an enzymatic degradation or a respective recycling of either foreign molecules or cellular compounds[260]. In addition, lysosomes are demonstrably involved in secretion, plasma membrane repair, signaling and energy metabolism processes[261]. Despite being an absolute necessity for eukaryotic cells, the lysosomal system marks one of the biggest hurdles for the transcytosis of nanocarriers. Once nanoparticles get taken up by cells, many materials get trafficked along the endolysosomal pathway. This typically involves a transport from early to late endosomes and their maturation into or fusion with lysosomes[248, 262-264]. This means the nanocarrier either gets degraded via enzymes or is, depending on the material, accumulated.

By increasing the nanoparticle concentration from $75\ \mu\text{g/mL}$ up to $600\ \mu\text{g/mL}$, it was demonstrated in this thesis that the percentage of nanoparticle transcytosis does not change significantly (Fig. 18). This phenomenon was further observed via confocal laser scanning microscopy and transmission electron microscopy – the more nanoparticles were added the bigger late endosomal respectively lysosomal structures appeared. When adding nanoparticles in a concentration of $400\ \mu\text{g/mL}$, late endosomes / lysosomes with sizes up to more than $2\ \mu\text{m}$ in diameter could be detected using Rab9a as a marker (Fig. 41). This marks one of the key problems for overcoming epithelial barriers: the lysosome as final destination for nanoparticles. In order to avoid such an accumulation or degradation, major development in the field of nanocarrier synthesis has to be done. The endolysosomal route either needs to (1) be avoided completely or (2) endosomes or lysosomes need to be triggered to fuse with the cell membrane and release the nanocarriers or (3) nanocarriers need to escape the endolysosomal system to be able to get released from the cell again.

A promising approach for the future might a combination of such in-depth nanoparticle co-localization studies with chemical agents that potentially trigger an endolysosomal escape. For example, most recently, a study shed light into endolysosomal escape and the resulting positive increase for exocytosis and a hereby associated increased transcytosis efficiency (Fig. 3). In their experiments, the addition of hemagglutinin-2 and / or metformin resulted in an increase of endolysosomal escape and subsequent exocytosis of P22NPs (NH₂-C6-[cMPRLRGC]c-NH₂ nanoparticles). By simultaneously adding these two chemicals, the combination of endolysosomal escape and exocytosis triggered an increase of transcytosis

efficiency of encapsulated insulin vs. free insulin by a factor up to 5.1[92]. Combining the within this thesis established in-depth knowledge about nanoparticle co-localizations with such chemical agents might further expedite research about the prevention of nanoparticle trafficking along the endolysosomal pathway.

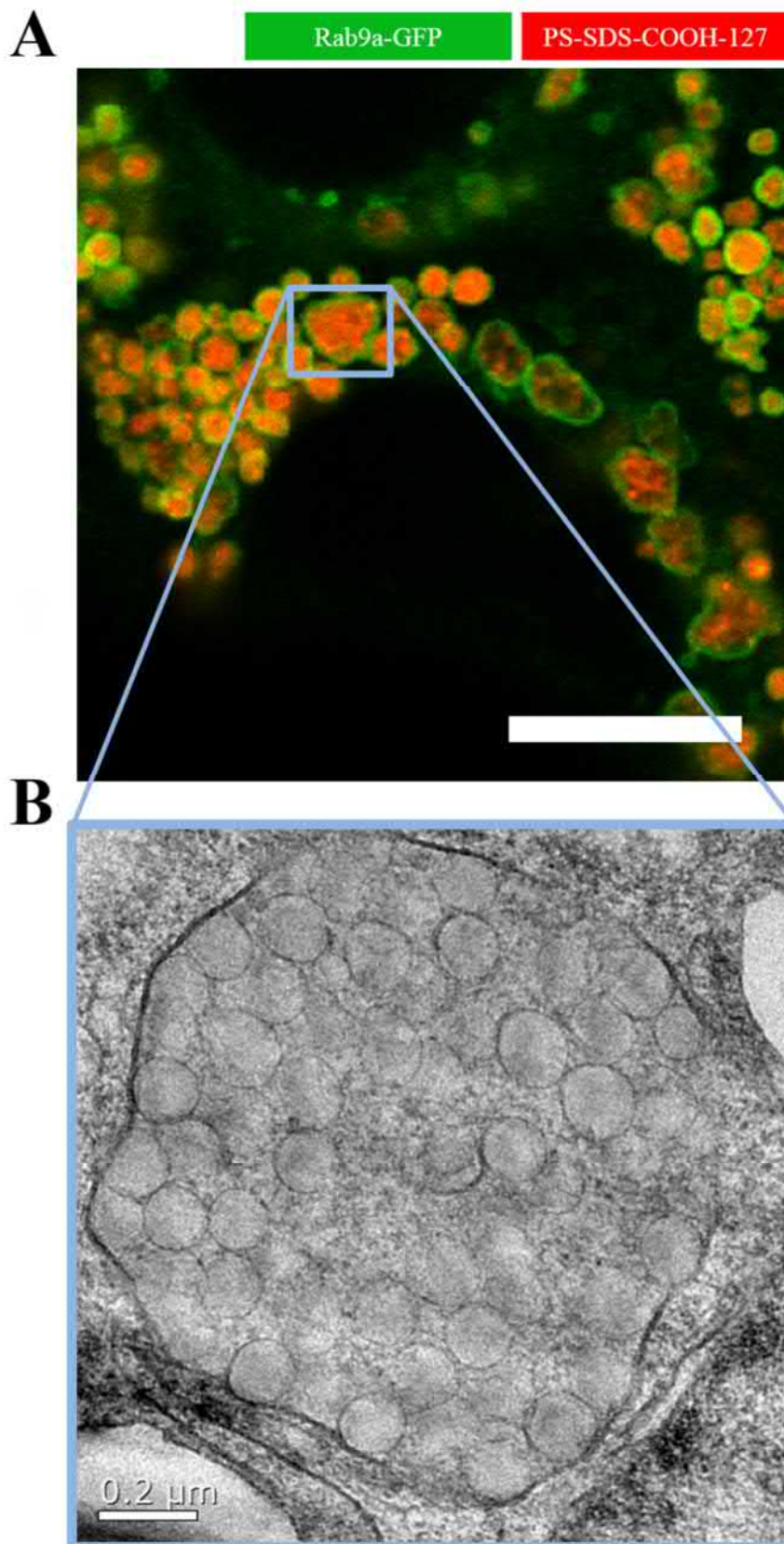


Fig. 41: Visualization of polystyrene nanoparticles trapped in vesicles in Caco-2 cells.

Caco-2 cells were incubated for 24 h in DMEM with FBS and 400 μg/mL nanoparticles. (A) Confocal laser scanning microscopy of nanoparticles heavily accumulated in Rab9a positive vesicles. Scale bar = 10 μm. (B) Transmission electron microscopy of nanoparticles trapped in vesicles. Both methods showed vesicles up to 2 μm containing polystyrene nanoparticles.

In addition, different types of vesicles could be detected by transmission electron microscopy (Fig. 42). These ranged from perfectly round vesicles to wrinkled round vesicles as well as spherical vesicles. There are multiple possible interpretations for this. Either these were simple maturing vesicles (early endosomes to late endosomes to lysosomes) or nanoparticles were transported in different types of vesicles, potentially even vesicles specifically for transcytosis. Naturally, this is hard to prove via transmission electron microscopy, but it was an interesting observation nevertheless.

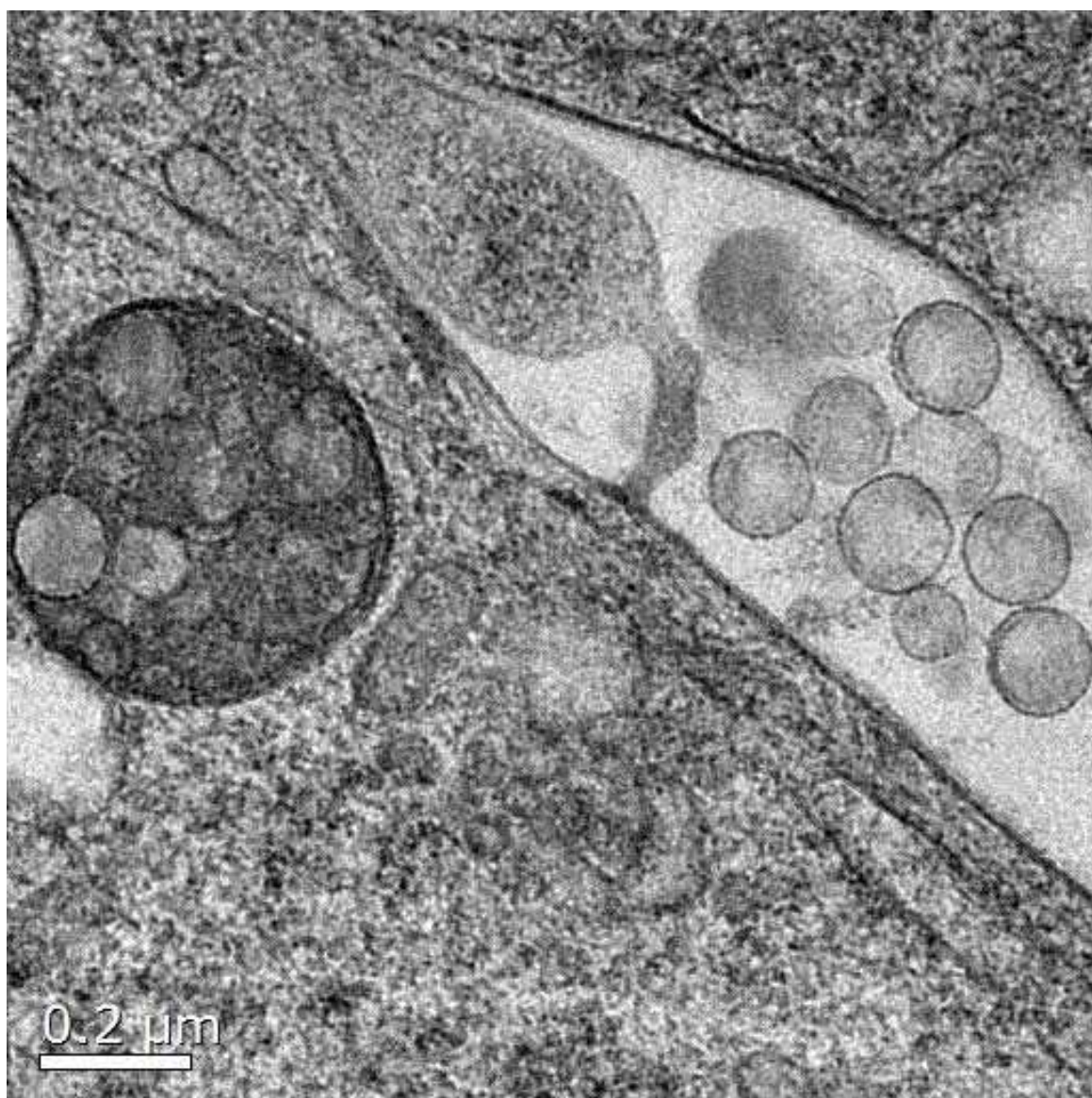


Fig. 42: Polystyrene nanoparticles in undefined vesicles.

Caco-2 cells were treated with 600 $\mu\text{g/mL}$ PS-SDS-COOH-127 for 24 h and subsequently analyzed via transmission electron microscopy. Nanoparticles were detected in different sized and shaped vesicles.

3.2.7 Trafficking profiles were established

To get a deeper insight into nanoparticle trafficking in Caco-2 cells, quantitative co-localization studies were performed. Therefore, the amount of co-localization after different time points (0,5 h; 1 h; 1.5 h; 2 h; 2,5 h; 3 h; 5 h and 24 h) was determined. After two hours of incubation with 100 $\mu\text{g/mL}$ carboxylated SDS-stabilized NP, nanoparticle containing medium was changed to DMEM to prevent any further nanoparticle uptake (also see Fig. 7 for a time scheme), which would distort co-localization values. Afterwards, nanoparticle-trafficking Caco-2 cells were recorded via confocal laser scanning microscopy by scanning through the cells in multiple Z-positions. For the quantification, two different methods were employed. The first method consisted of a manual counting of fluorescent spots inside of the cell and was conducted by two independent researchers. The second method was an automatic analysis of recorded Z-stacks via a Fiji Script[139], kindly provided by Dr. Sandra Ritz (Institute of Molecular Biology, Mainz). Two examples, how the software detected nanoparticles inside the cell and in co-localization, can be seen in Fig. 43 and Fig. 44. Nanoparticles surrounded by a white circle were counted as co-localized to the protein-of-interest by the software. In contrast, manual counting exhibited the possibility to thoroughly analyze each “critical” nanoparticle for co-localization.

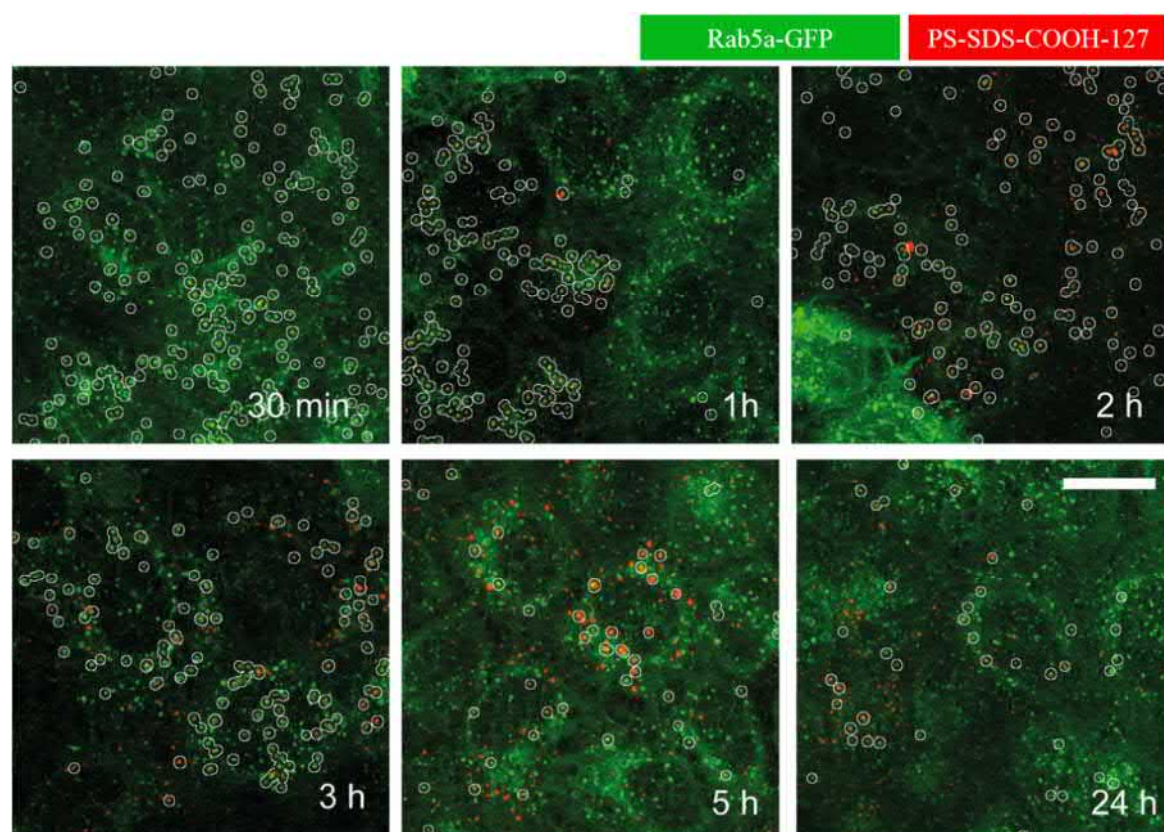


Fig. 43: Kinetic uptake of nanoparticles in Rab5a-positive Caco-2 cells.

The co-localization between nanoparticles and Rab5a-EGFP (green) stained early endosomes is indicated by white circles. Fluorescence microscope images represented as maximum z-projection. Image stacks were obtained with a confocal laser scanning microscope. The object based co-localization was automatically analyzed by a custom written Fiji macro. Scale bar = 20 μm .

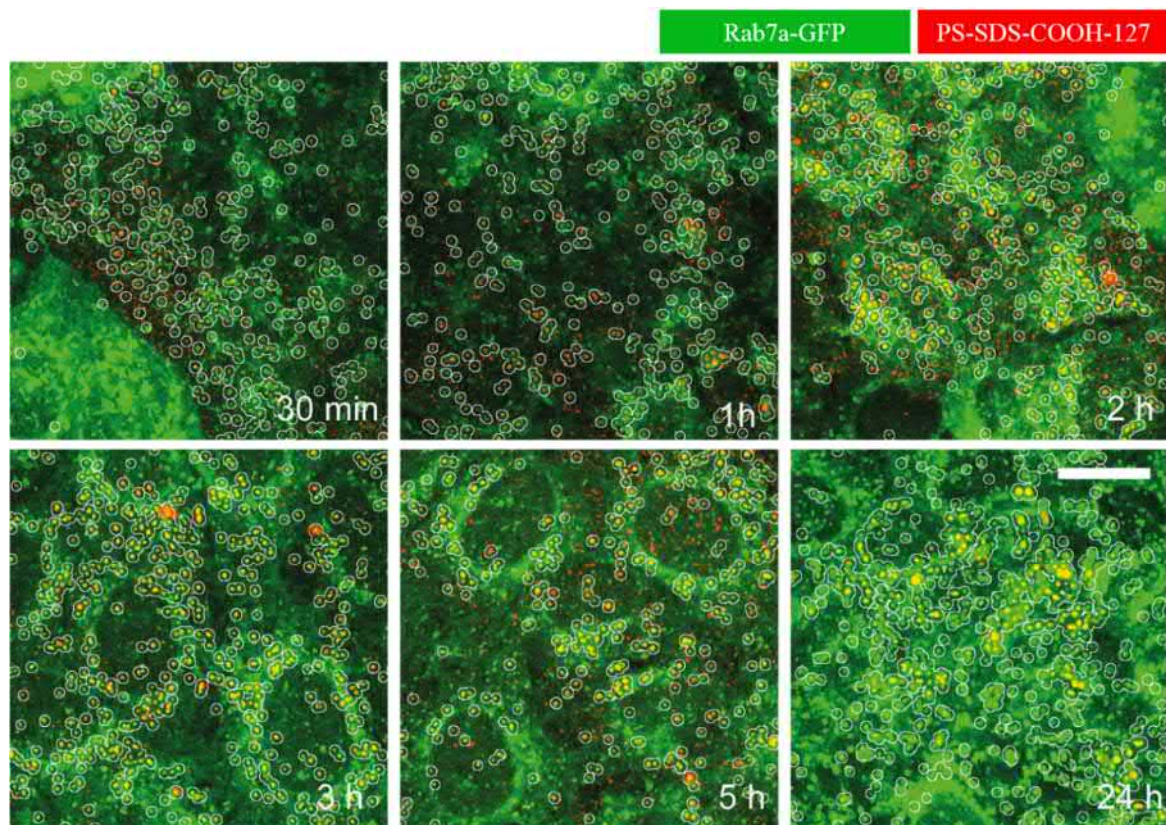


Fig. 44: Kinetic uptake of nanoparticles in Rab7a-positive Caco-2 cells.

The co-localization between nanoparticles and Rab7a-EGFP (green) stained late endosomes is indicated by white circles. Fluorescence microscope images represented as maximum z-projection. Image stacks were obtained with a confocal laser scanning microscope. The object based co-localization was automatically analyzed by a custom written Fiji macro. Scale bar = 20 μm .

The macro confirmed nearly all of the manually counted co-localization tendencies (Fig. 45, Fig. 46, SI Fig. 42-49). The quantification of Exoc1 co-localization was not possible with this script due to a low GFP signal. In addition, Rab5c showed a slightly different co-localization pattern compared to manual counting. The main difference, however, was that the script also counted nanoparticles that were a) between and b) on top of the Caco-2 cells because of the Z-stack projection. Overall, this accounted for a lower degree of co-localization.

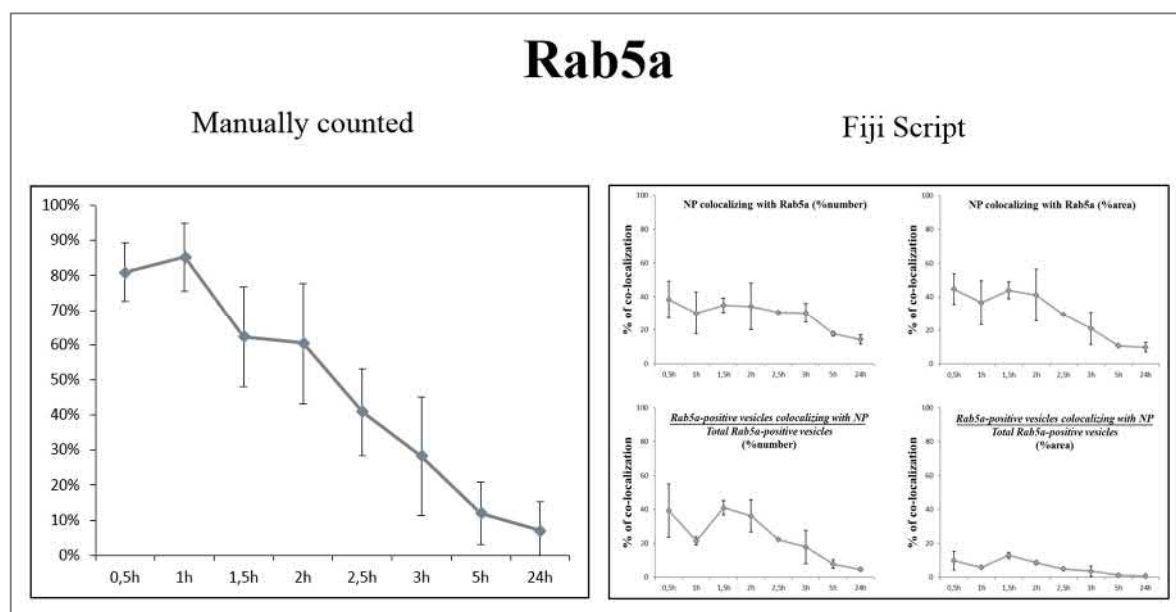


Fig. 45: Comparison of manually counted vs Fiji Script determined NP co-localization with Rab5a.

Tendency of Rab5a starting with a high level of co-localization which decreased over time was confirmed via automatic counting using a Fiji Script. Automatic calculated relative percentages are possibly lower due to the fact that the script also counted nanoparticles on top and between cells which were not internalized.

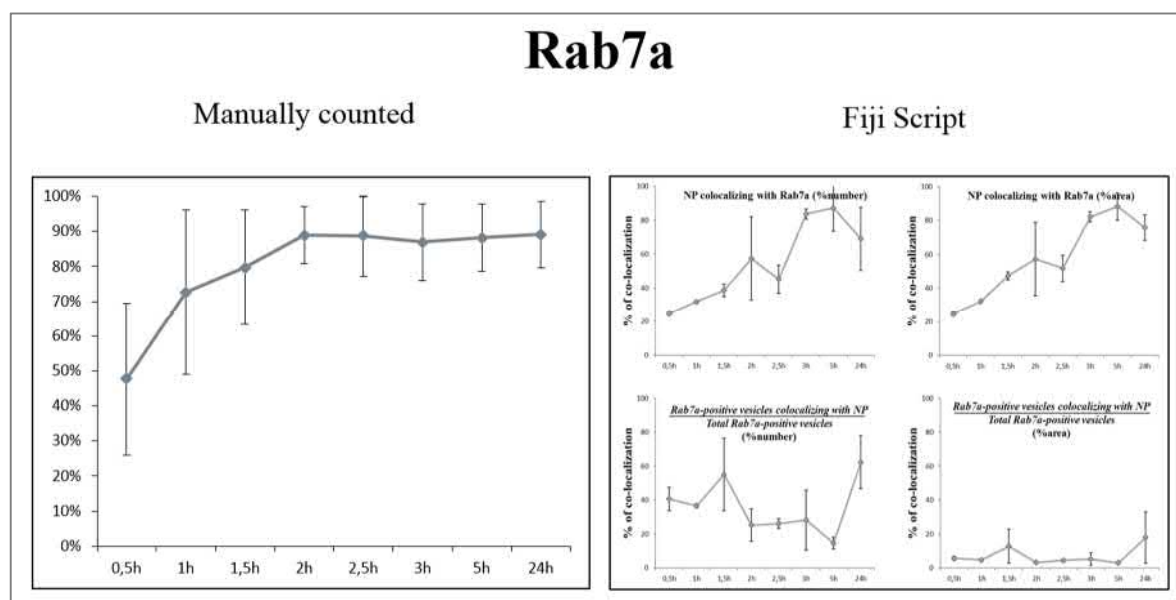


Fig. 46: Comparison of manually counted vs Fiji Script determined NP co-localization with Rab7a.

Tendency of Rab7a starting with a low level of co-localization which increased over time was confirmed via automatic counting using a Fiji Script. Automatic calculated relative percentages are possibly lower due to the fact that the script also counted nanoparticles on top and between cells which were not internalized.

Via these quantifications, trafficking profiles for polystyrene nanoparticles could be established (Fig. 47). Known markers for macropinocytosis and early endosomes Rab5a and RhoB[248] showed similar co-localization patterns, starting with a high percentage of co-localization that strongly decreased over time. Proteins abundant on late endosomes like Rab7a and Rab9a showed a medium degree of co-localization after 30 minutes, rapidly increasing and peaking at nearly 100% after two hours. Interestingly, the co-localization persisted until the end of the time lapse. In contrast, lysosomal marker Lamp1 started with nearly no co-localization and increased very slowly, but also spiked at nearly 100% after 24 hours. All markers linked to the exo- or transcytotic system either from our MS data (Rab3, Cpn1) as well as from other research groups (Rab27a[252], Exoc1[253]) started with very few co-localization occurrences, and were slowly increasing up to a maximum co-localization of 40-50%. Outliers in the present study were the proteins Rab5c (also enriched in the MS data), which started with a medium co-localization and peaked at 2 h before decreasing slowly, as well as Flot1, which showed an overall low co-localization with a minor spike at 5 hours of incubation.

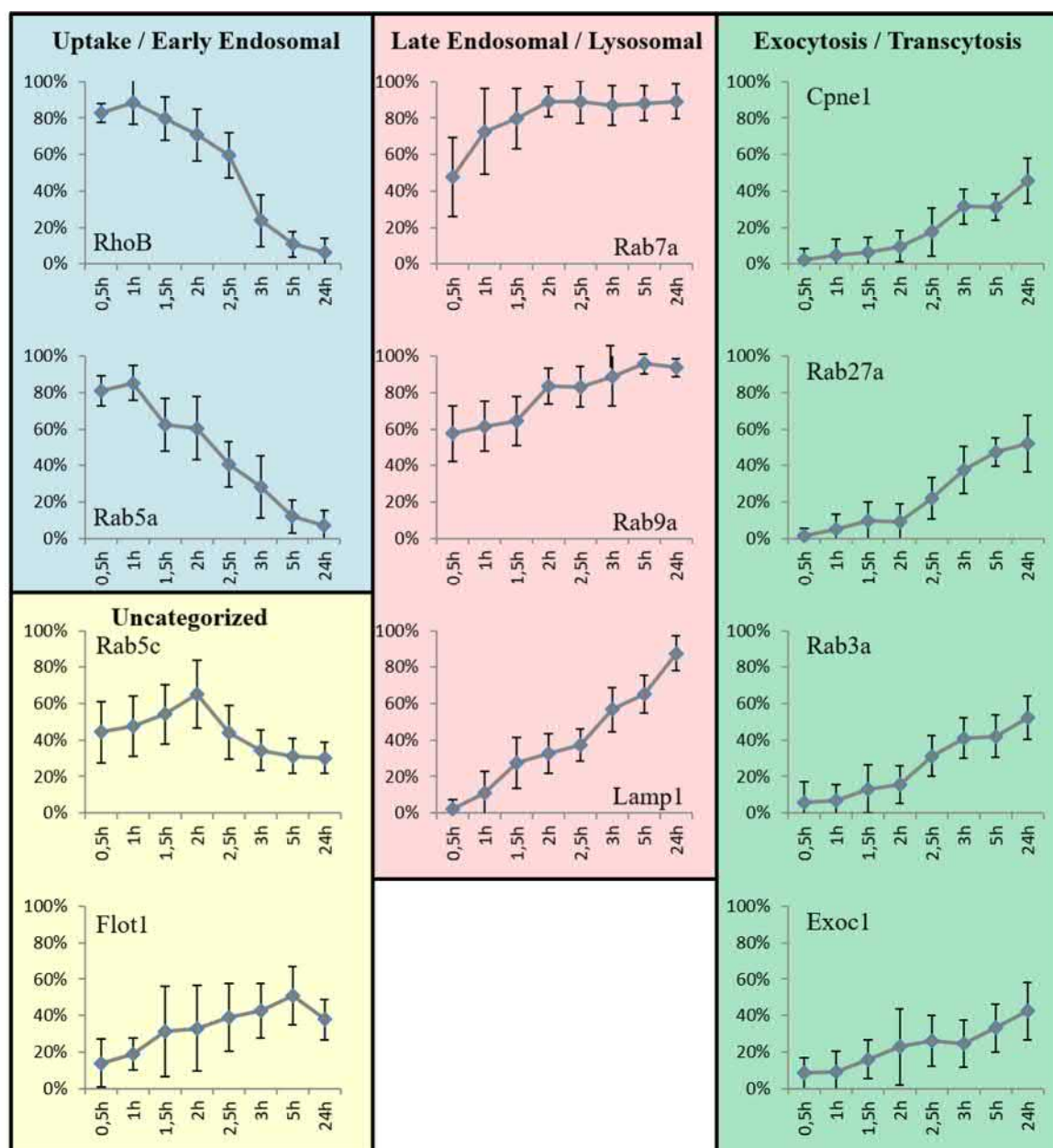


Fig. 47: Co-Localization profiles of nanoparticles with different endolysosomal and putative exo- and transcytotic marker proteins.

Caco-2 cells were cultivated until they reached 100% confluence. 100 μ g/mL PS-SDS-COOH-127 were added to DMEM containing 10% FBS and different stages of intracellular trafficking were monitored (0.5 h – 24 h). After a maximum incubation time of 2 hours, cells were washed with PBS to eliminate any further nanoparticle uptake. For statistical analysis, at least 10 cells per time point for each protein were manually counted out by two researchers independently. Co-Localization of nanoparticles with marker proteins (y-axis) was subsequently plotted against the time points (x-axis). The percentages represent $\frac{\text{Nanoparticles in Marker protein-positive vesicles}}{\text{Total nanoparticles in cell}}$. Error bars represent the standard deviation of the arithmetic mean of pooled cells for each timepoint.

3.2.8 Double transgenic cell lines confirm trafficking profiles

To confirm the data from the in-depth trafficking analysis, stable GFP-expressing Caco-2 cell lines were re-transfected with mCherry-coupled proteins via a second lentiviral gene transfer. Since a second antibiotic selection could not be performed, naturally not every Caco-2 cell was positive for both fluorescence-coupled proteins. However, up to 50% double transgenic cells could be achieved. We added the same amount of polystyrene nanoparticles to the cells and monitored them for another 24 hours. Despite not performing a quantitative analysis, cells showed similar co-localization patterns as shown before (Fig. 48). For example, Rab5a was used as an early endosome marker in combination with either late endosome marker Rab7a (SI Fig. 39), Rab9a (Fig. 48) or lysosomal marker Lamp1 (SI Fig. 40). From the quantitative analysis, a high percentage of co-localization with Rab5a positive vesicles at the early stages of trafficking was expected, changing first towards Rab7a/Rab9a positive vesicles and finally towards Lamp1 positive vesicles. Via monitoring the switch of “orange” to “violet” co-localization, we were able to confirm the quantitative co-localization data. Similar data could be obtained by the combination of macropinocytosis marker RhoB in combination with Rab7a (SI Fig. 41). Moreover, we could show that Rab7a and Rab9a are present on virtually the same vesicles (SI Fig. 50), explaining their similar co-localization patterns in Fig. 47. Interestingly, the co-localization of PS-NP with Rab7a and Rab9a was also maintained for the whole time of trafficking, suggesting not only a function on late endosomes but also in the beginning as well as in later stages of the endolysosomal pathway, e.g. the degradation in lysosomes. This theory is in accordance with the fact that the majority of Lamp1-positive vesicles was also positive for Rab9a (SI Fig. 51) as well as Rab7a (data not shown). Despite being normally strictly separated, we also found hybrid vesicles positive for Rab5a and Rab9a (SI Fig. 52) as well as Rab5a and Lamp1 (SI Fig. 53) after an incubation time of around 2 hours, where we also measured the “switch” of co-localization between the different compartments. Last but not least, Rab3a, Rab27 and Cpn1 all seemed to be more or less abundant on either Rab9, Rab7 and/or Lamp1 positive late endosomal compartments (Fig. 49, SI Fig. 54-56). We observed that for each of these proteins also certain vesicles exist that are only positive for the putative transcytosis relevant protein, but not for late endosomal compartments.

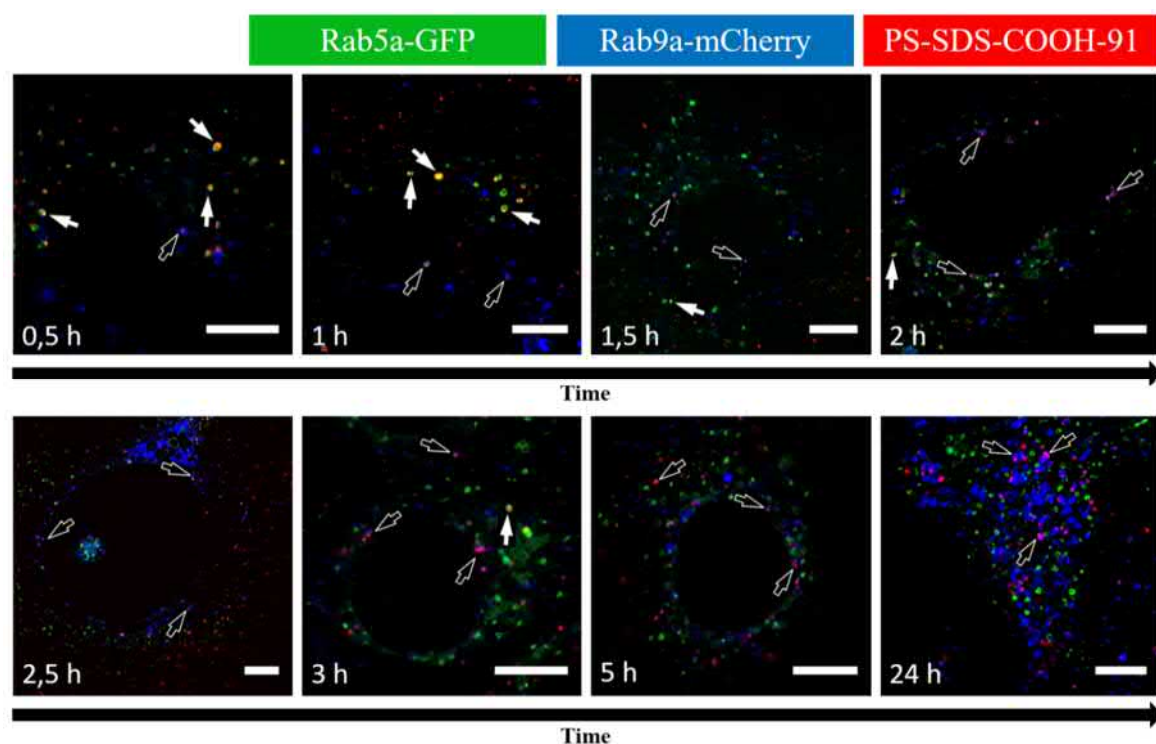

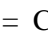


Fig. 48: Co-localization of polystyrene nanoparticles with GFP- or mCherry-tagged proteins. Caco-2 cells were cultivated until they reached 100% confluence. 100 $\mu\text{g/mL}$ PS-SDS-COOH-91 were added into DMEM containing 10% FBS and cells were monitored for 0.5 – 24 h. After a maximum incubation time of 2 hours, cells were washed with PBS to eliminate any further nanoparticle uptake. EGFP-tagged proteins are pseudocolored in green, mCherry-tagged proteins are pseudocolored in blue and polystyrene nanoparticles are pseudocolored in red. Co-Localization of GFP and nanoparticles resulted in an orange color, while co-localization of mCherry and nanoparticles resulted in violet spots.  = Co-Localization of Rab5a-GFP and polystyrene nanoparticles.  = Co-Localization of Lamp1-mCherry and polystyrene nanoparticles. Rare co-localization between GFP and mCherry resulted in light blue color. Scale bar = 10 μm .

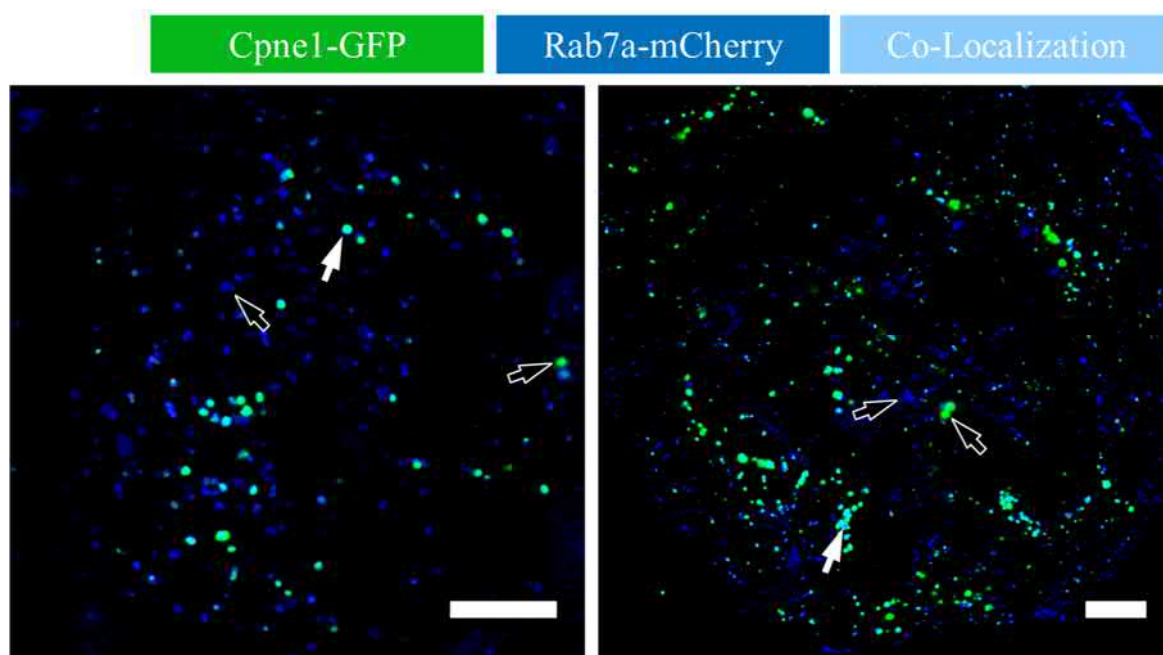

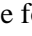


Fig. 49: Intracellular localization of Cpne1 and Rab7a.

This figure depicts the intracellular localization of Cpne1 and Rab7a. Approximately 50% of Copine1 positive vesicles were also positive for late endosome marker Rab7a.  = Vesicles featuring co-localization between both marker proteins.  = Vesicles only positive for one of the marker proteins. Scale bar = 10 μ m.

Combining all this data we hypothesize that the transcytosis of nanomaterials might be dependent on the protein composition (protein machineries) of endosomal compartments in a dynamic, time overlapping intracellular process. The “correct” composition, which might contain Rab3 or Cpne1 as suggested by our MS data as well as Rab27 or Exoc1 as exocytotic markers from the literature, might trigger the cell to fuse the vesicle with the membrane and subsequently release it (Fig. 50).

Identifying all the proteins involved in a successful transcytosis event will help to get a molecular understanding of the process, subsequently leading to an increase of the transcytosis rate which is crucial for oral drug delivery via nanocarriers. This molecular understanding could furthermore be used to define physico-chemical characteristics (e.g. size, surface charge) for certain classes of nanoparticles. In this context, applying the described methodology to other nanocarriers and cell systems might give additional insights about the intracellular nanoparticle trafficking, since the material and especially the charge can effect intracellular trafficking[46] and transcytosis efficiencies[45] in epithelial cells.

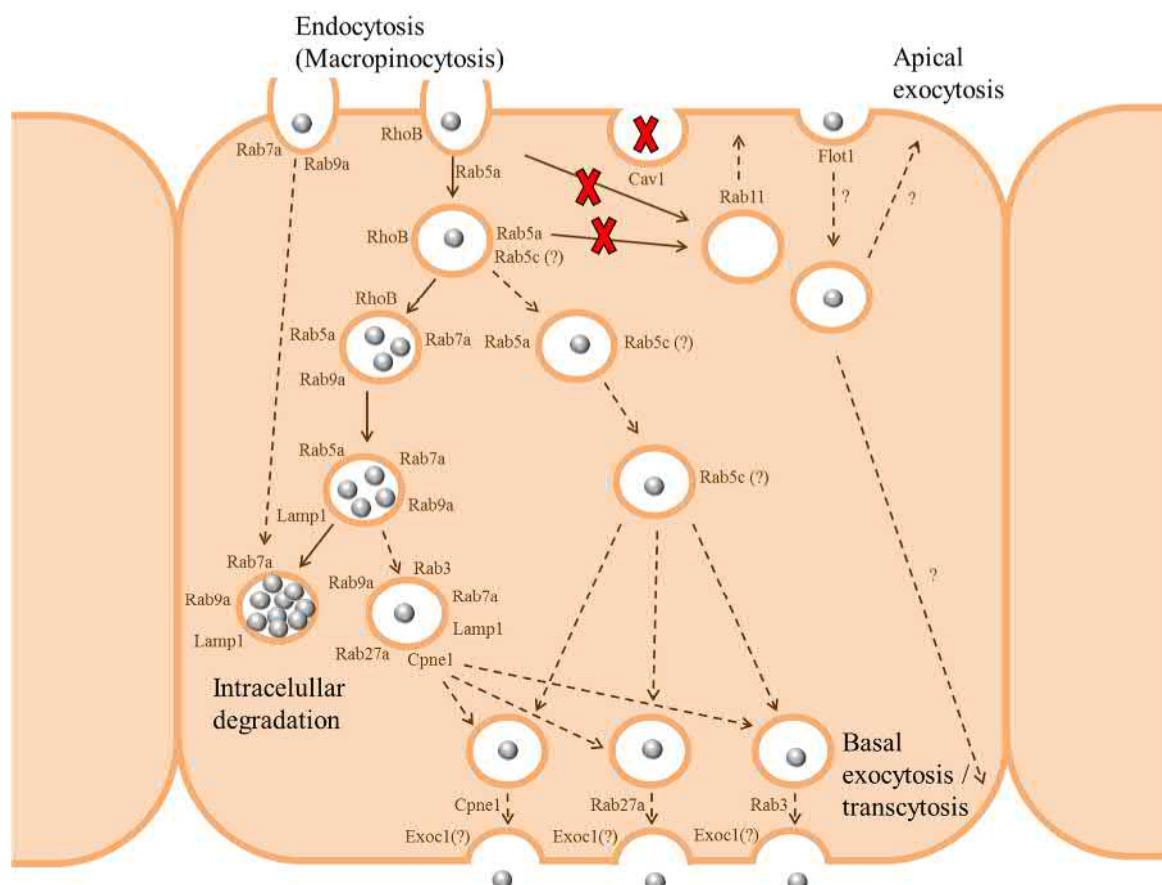


Fig. 50: Pathway hypothesis for the intracellular trafficking of polystyrene nanoparticles in Caco-2 cells.

We combined the data from our elaborate quantitative co-localization studies with the results from our mass spectrometry analysis. We did not observe any internalization via caveolae-mediated endocytosis. Nanoparticles were internalized presumably via RhoB and Rab5a mediated macropinocytosis. We hypothesize the existence of at least two different main pathways for intracellular storage and/ or degradation of nanoparticles as well as several possible pathways for nanoparticle transcytosis. We postulate a function or participation of the proteins Cpn1, Rab27, Rab3 and Exoc1 or a combination of them all for a successful nanoparticle transcytosis event.

We also attempted to determine if a simple overexpression of the putative transcytosis relevant proteins will trigger an increase in transcytosis. However, none of our tested overexpressing cell lines exhibited a significantly higher rate of transcytosis (data not shown). We believe this is due to the fact that the process of exocytosis relies on multiple complex protein machineries. Nevertheless, coating the nanoparticle with the correct “mixture” of proteins could be a very promising and interesting approach.

The hereby established in-depth knowledge about the putative localization of nanoparticles after a defined period of time might be of high interest for other research groups. However, there are certain limitations for these experiments that need to be considered. Although the Caco-2 model is widely used as the model of choice for transcytosis experiments, different nanomaterials can be transported via a variety of cell types and various mechanisms.

Nevertheless, the established methodology kinetically combines the biochemical and visual fingerprint of nanomaterial inside the cell. This could be used to analyze a broader spectrum of nanomaterials as well as transcytosis in multilayer cellular systems and in vivo systems, which will be essential for the development of nanocarriers for oral drug delivery.

3.3 Transcriptomic analysis of dendritic cells after nanoparticle addition

A lot of research in the broad spectrum of nanobiology / nanomedicine is focused on nanoparticle interactions with proteins. However, cells also seem to give a response on a transcriptomic level when treated with nanoparticles[265-268]. Most of the research using the technique of Next Generation Sequencing is focusing on potential stress induced cellular responses after nanoparticle treatment. In this thesis, a slightly different approach for a transcriptomic analysis after nanoparticle treatment was chosen. The aim was to investigate, if an uptake of nanoparticles or rather nanocapsules has any effects on 1) trafficking relevant genes and 2) genes relevant for immune responses. For this reason, dendritic cells were chosen since they potentially feature a quick and strong cellular response to foreign material. This is explained by their natural function as a part of the immune system: processing of antigens and subsequent presentation via MHC molecules[97]. For this purpose, ovalbumin nanocapsules were synthesized by Dr. Ketil Piradashvili. These were either left unloaded for control purposes or filled with resiquimod (R848) and muramyl dipeptide (MDP). These two adjuvants are described in the literature as immune boosting agents[105, 108, 109]. By comparing the transcriptomic data of murine bone marrow derived dendritic cells (BMDCs) treated with those nanocapsules vs. untreated BMDCs, insights into nanocapsule trafficking and immune activation pathways were obtained.

3.3.1 RNA extractions of bone marrow derived dendritic cells

Firstly, bone marrow derived dendritic cells were isolated by David Paßlick (University Medical Center, Mainz). Since there was understandably no information available at which point of time BMDCs react to nanocapsules on a transcriptomic level, cells were treated for 1 h, 2 h as well as 4 h with 75 $\mu\text{g/mL}$ (adjuvant-filled) ovalbumin nanocapsules. Cells incubated at the different time points were afterwards pooled. The idea behind this pooling procedure was to ensure to not miss the best time point of transcriptomic changes after the nanocapsule addition. Afterwards, total RNA was extracted. Since it is tremendously important for Next Generation Sequencing that the RNA is of a high quality, all samples were thoroughly controlled.

Total extracted RNA was around 200-300 $\text{ng}/\mu\text{L}$ as determined via spectrophotometry (Fig. 51). The RNA : protein ratio of > 2.0 , as calculated by the 260/280 nm coefficient, indicated high sample purity.

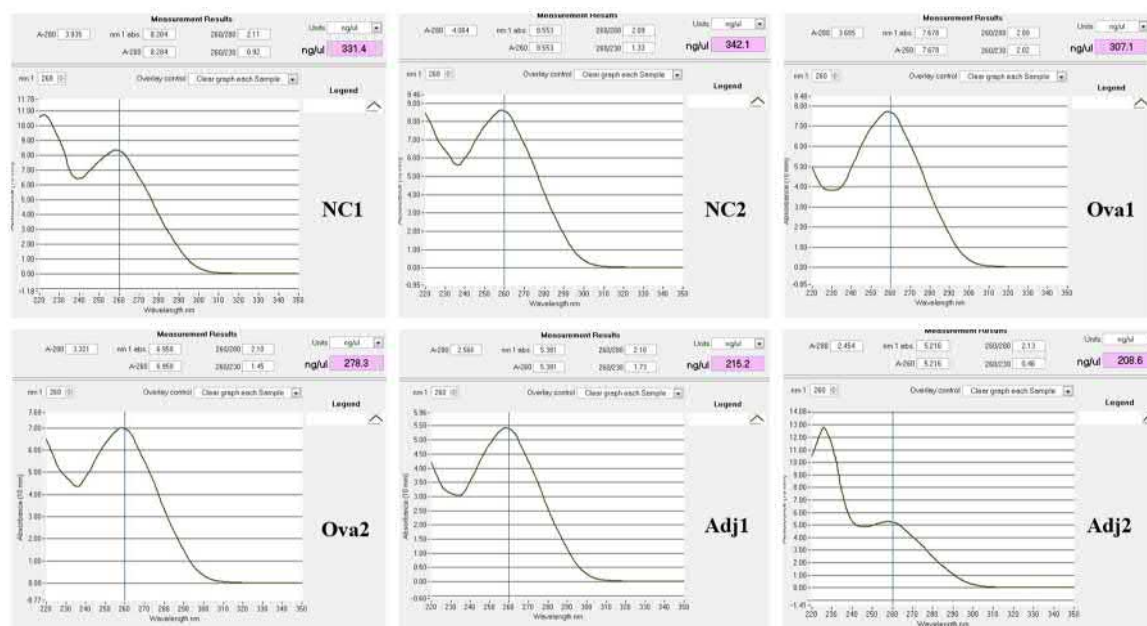


Fig. 51: RNA Extraction of (Ovalbumin nanocapsule-treated) BMDCs.

Total RNA was extracted from BMDCs using the Qiagen RNeasy Kit. Quality was controlled via Nanodrop 8000 spectrophotometric analysis. Extracted RNA showed absorbance coefficients over 2.0 (260/280 nm) and 0.4 (260/230 nm) and a total RNA amount of over 200 $\text{ng}/\mu\text{L}$.

To analyze the RNA samples for disturbing DNA contamination, agarose gel electrophoresis was performed (Fig. 52). None of the samples featured any DNA smear on the gel. Additionally, 28S rRNA and 18S rRNA bands were clearly visible. The desired ratio of 2:1 (28S : 18S) was at least partially detectable by eye.

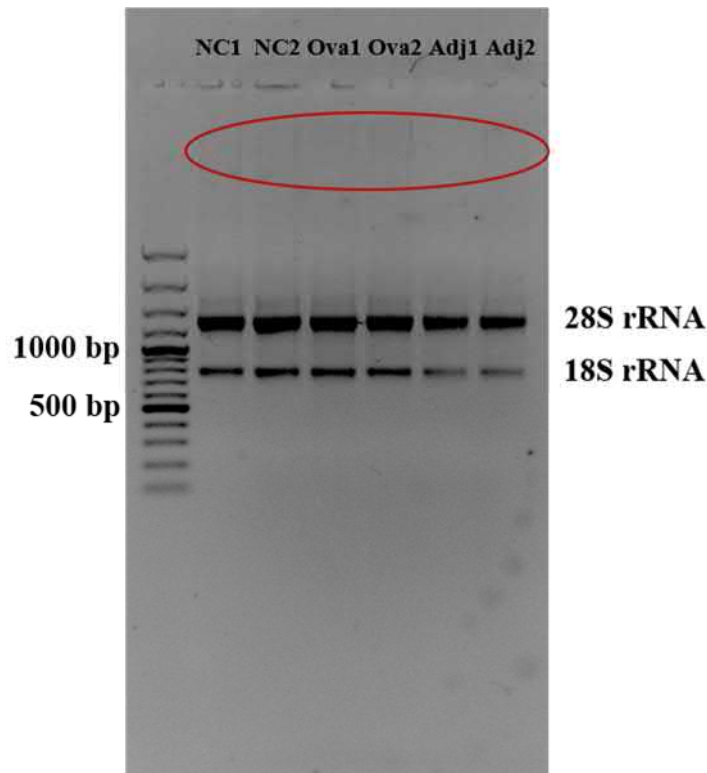


Fig. 52: Quality control of total RNA extractions via agarose gelelectrophoresis.

Total RNA extractions from (nanocapsule-treated) murine bone marrow derived dendritic cells were size separated on a 1% agarose gel. 28S rRNA and 18S rRNA bands were articulately visible. In contrast, no genomic DNA contamination was observed (red oval circle).

Last but not least, RNA was controlled via Bioanalyzer, a device that provides automatic electrophoretic separations (Fig. 53). The Bioanalyzer software calculates the so-called RNA Integrity Number (RIN), which is based on the intensity ratios of 28S rRNA, 18S rRNA and background signal[269]. This value ranges from 1 (totally degraded) to 10 (completely intact). All RNA samples featured RIN-values of at least 9.40, indicating perfect quality. After confirming sufficient quality, RNA samples were handed over to StarSeq (Mainz, Germany) for mRNA extraction, cDNA library creation and Illumina Sequencing.

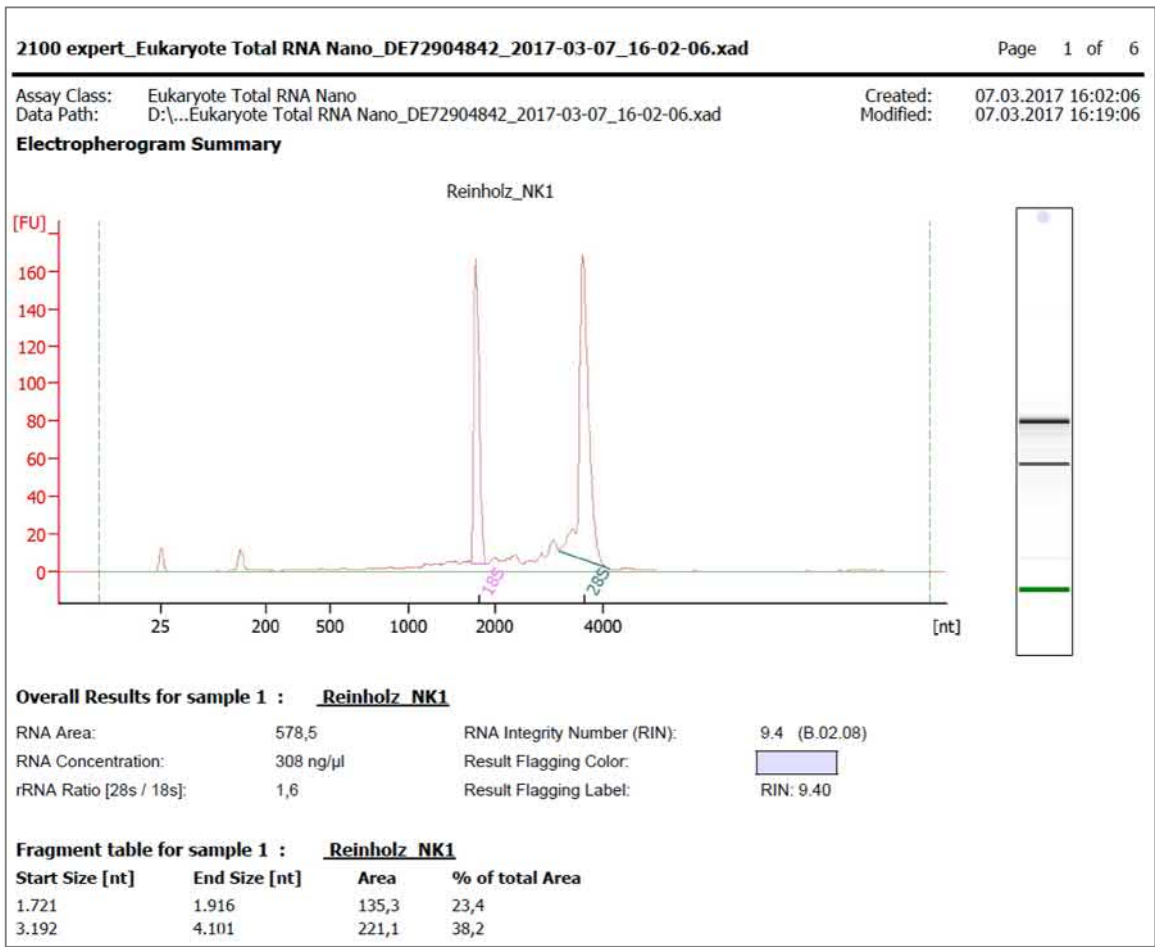


Fig. 53: Analysis of total RNA quality for Next Generation Sequencing.
Quality of total extracted RNA was analyzed via Bioanalyzer by StarSEQ (Mainz, Germany). RNA Integrity Number (RIN) was above 9.40 for all tested samples.

3.3.2 Next Generation Sequencing of ovalbumin nanocapsule-treated dendritic cells

Analysis of Next Generation Sequencing data was performed with the software Geneious R8. After Illumina sequencing, a total of 25 million reads à 150 nucleotides per sample were obtained in .fastq format. This marks an overall genetic information of > 3.7 gigabases of DNA per sample. To facilitate later mapping, DNA-Strands were sequenced in paired ends (also see Fig. 5B). Firstly, read quality was evaluated and reads were processed in the software (Fig. 54). Only a minority of reads featured ambiguous nucleotides and thus were discarded. Then, paired end reads were assigned to each other.

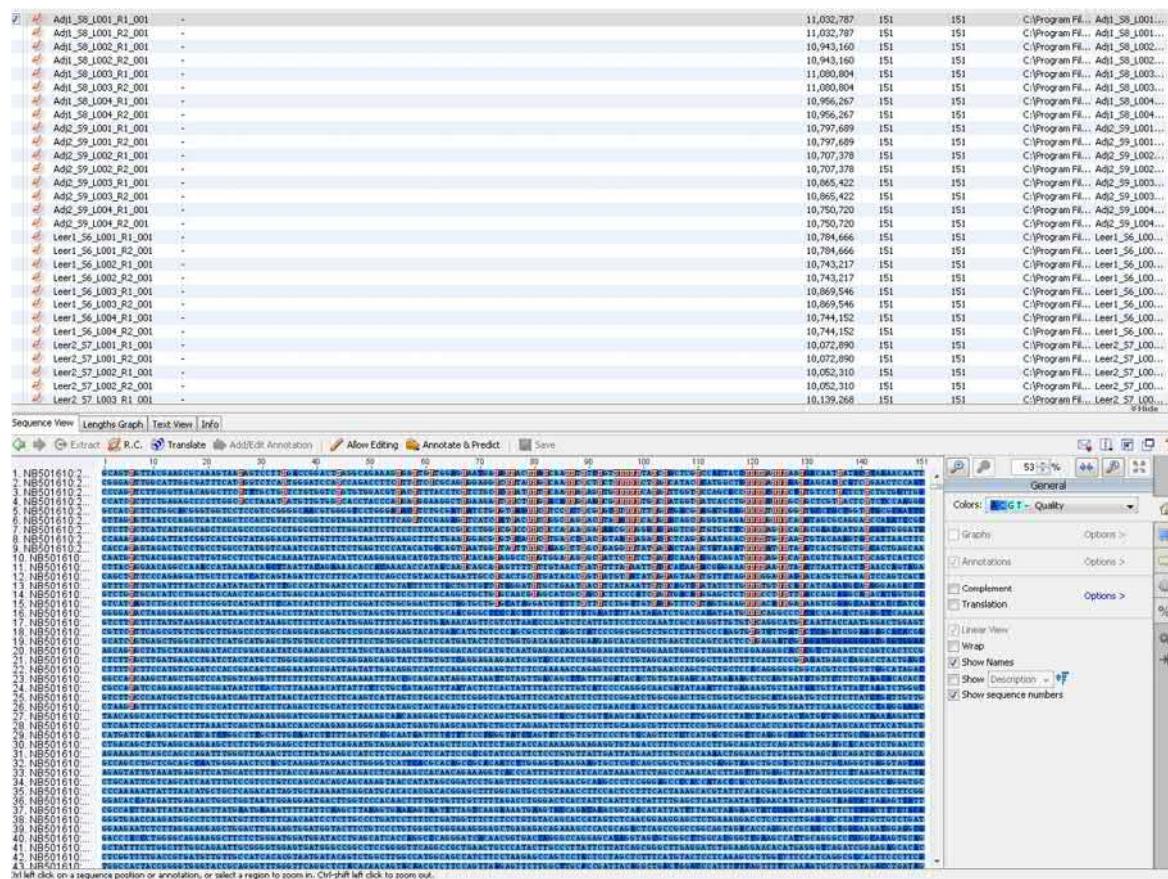


Fig. 54: Evaluation of Next Generation Sequencing reads via Geneious R8.

This figure depicts an example of the Geneious R8 interface. All reads were imported into the software, checked for their quality and paired end reads were assigned to each other. One column marks one read with a length of 150 nucleotides.

Next, the murine genomic reference sequence was added into the software and all 21 chromosomes as well as the mitochondrial DNA were annotated, respectively. Then, the six different samples were mapped against this reference sequence (Fig. 55) with the parameters described in chapter 2.2.46.

A total number of 55.810 transcripts could be detected for all six samples, corresponding to 14.840 genes. In the literature, the number of murine protein-coding genes is numbered as around ~22,000[270, 271]. The minor discrepancy can potentially be explained by the fact that not every gene is transcribed at every time point and different cells overall can transcribe different sets of RNAs[272, 273].

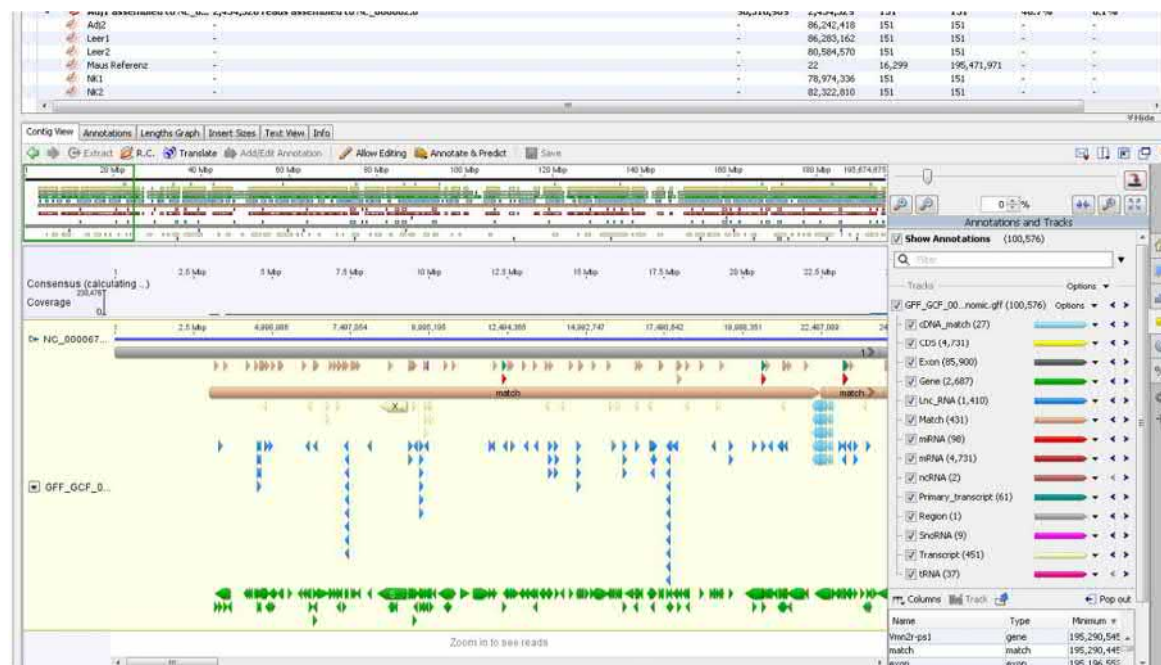


Fig. 55: Mapping of paired end reads against the murine reference sequence.

The murine reference sequence was obtained by NCBI and all 21 chromosomes and mitochondrial DNA were annotated respectively. Obtained paired end reads were mapped to the reference sequence and finally expression levels were calculated.

Afterwards, all expression data was transferred to an Excel sheet (Fig. 56). To analyze the differences between nanocapsule-treated BMDCs and untreated BMDCs, the amount of raw transcripts mapping to the gene-of-interest were compared. Therefore, firstly, the mean value of biological replicates was calculated (Fig. 56, single values for negative control in green, empty ovalbumin nanocapsule-treated cell values in yellow, adjuvant-nanocapsule-treated cell values in red). Then, the ratios of mean values (Fig. 56, blue column) were compared against each other (Fig. 56, white columns on the right side). We compared the

expression differences between untreated and empty ovalbumin nanocapsules-treated cells (Ova:NC), adjuvant-filled ovalbumin nanocapsules vs. empty ovalbumin nanocapsules (Adj:Ova) and adjuvant-filled ovalbumin nanocapsules vs. untreated cells (Adj:NC) for all 14,840 genes. An example for the calculation is presented for IL23a (Fig. 56, red square), which featured a 10.8-fold increase in expression after ovalbumin nanocapsule treatment and a 55.3-fold increase after adjuvant-filled ovalbumin nanocapsule treatment.

NC Ova Adj																		
#	A	B	C	D	E	F	G	H	I	J	K	L	M	N	O	P	Q	R
	Name	gene	Minimum	Maximum	Length	Direction	NC1	NC5	Ova1	Ova2	Adj1	Adj2	Mean NC	Mean Ova	Mean Adj	Ova-NC	Adj-Ova	Adj-NC
1	NP_01401-1	Csf3	98,701,380	98,702,960	627	forward	0.0	0.5	3.3	3.4	38.1	37.8	0.3	3.4	27.0	13.4	8.0	107.8
3	NP_032625.2	Cxcr9	92,823,799	92,828,023	381	reverse	0.0	0.8	3.2	3.6	12.0	10.7	0.4	3.4	11.7	8.5	9.3	79.3
4	NP_033775.1	Aicda	122,553,902	122,564,473	597	forward	0.3	0.0	1.5	1.8	12.1	12.1	0.2	0.8	10.4	5.0	13.8	69.0
5	NP_004646.1	H23a	128,266,696	128,268,372	511	forward	2.0	1.3	15.4	15.9	120.6	120.6	1.6	17.9	113.2	114.2	8.4	24.4
6	NP_112542.1	H23b	128,266,796	128,269,772	591	reverse	2.0	1.3	15.8	15.9	120.4	120.4	1.7	17.9	113.1	113.8	5.1	55.3
7	NP_000507075.1	H1f101	95,937,373	95,940,743	2,413	reverse	0.7	0.8	2.9	3.0	14.9	14.9	0.2	2.9	12.0	7.4	35.9	120.0
8	NP_067499.1	Cxcl10	92,847,367	92,848,814	297	reverse	21.9	17.3	171.8	120.5	2480.1	2480.1	15.8	146.2	1079.5	7.5	7.2	54.0
9	XP_00533945.1	Pxata32	103,208,156	103,210,982	1,041	reverse	0.4	1.1	12.6	14.4	11.1	10.9	0.8	13.5	16.8	18.0	2.7	49.0
10	XP_00527327.1	H1f13b	34,607,684	34,612,637	1,287	forward	1.1	1.1	8.2	5.5	15.6	16.1	1.1	6.9	52.6	6.2	7.7	47.8
12	NP_035328.2	Ptgs2	150,100,224	150,105,782	1,815	forward	5.8	2.7	30.0	30.3	151.1	151.1	4.3	30.2	176.7	7.1	5.9	42.2
14	XP_00602548.1	Ifi44	151,732,513	151,749,586	1,035	reverse	1.6	0.9	4.1	4.1	14.2	14.2	1.3	4.1	30.2	3.3	12.2	40.1
15	NP_035057.1	Nes2	78,922,268	78,939,752	3,435	forward	1.0	0.4	0.9	0.9	18.4	18.0	0.4	0.8	13.7	2.6	15.2	39.0
16	NP_062323.1	Ifi16	24,215,847	24,224,597	483	forward	3.8	1.9	21.9	20.0	114.4	113.7	2.9	23.0	105.6	7.4	5.1	37.1
17	NP_032581.1	Ifi62	34,579,366	34,579,474	1,413	forward	1.3	0.9	24.3	17.9	3.2	3.2	1.3	14.9	12.6	4.4	3.8	25.0
19	NP_032157.2	Ifi1	34,640,983	34,648,807	1,392	forward	11.8	15.3	80.3	68.7	105.9	105.9	1.4	70.3	120.4	5.1	6.8	34.5
20	CDS	Igfb2	113,304,314	113,307,933	1,222	reverse	0.5	2.1	3.0	2.2	17.8	16.7	1.3	2.6	43.3	2.0	16.6	33.3
21	NP_067559.2	H2a	26,445,406	26,456,419	1,089	reverse	24.4	14.0	99.8	76.3	166.1	166.1	13.2	81.1	525.1	4.6	7.1	32.8
22	NP_036109.3	Vmn3	23,851,584	23,869,657	1,503	forward	2.6	2.6	6.9	6.1	43.6	43.6	0.6	6.3	70.6	2.5	12.1	30.2
23	XP_011237031.1	Pycd1	173,677,686	173,695,953	1,788	forward	0.6	0.3	0.9	1.3	14.1	13.2	0.5	1.1	13.2	2.4	12.0	29.3
24	NP_736345.3	Tnfrsf15	63,729,589	63,745,004	813	reverse	32.4	4.8	37.9	32.1	278.8	278.8	8.6	35.6	233.4	4.1	7.2	29.2
25	NP_060596.2	H2gmp	156,199,524	156,200,708	486	reverse	94.1	103.2	355.2	334.9	1018.4	1018.4	96.7	365.1	2794.3	3.7	7.7	28.3
26	NP_111618.1	H2ap1	30,942,477	30,943,983	232	reverse	0.0	1.2	1.9	2.2	10.7	10.7	0.7	1.4	14.6	14.6	6.1	25.0
28	NP_032898.2	Plat	22,767,105	22,782,106	1,680	forward	1.7	2.2	9.4	6.7	32.9	32.9	2.0	6.1	48.9	4.1	6.1	25.1
29	NP_032202.1	Cxcl1	90,891,311	90,892,523	291	forward	27.5	11.9	110.5	93.9	499.9	499.9	13.7	102.2	487.8	5.2	4.8	34.8
30	NP_006530358.1	Oas1	114,923,412	114,936,031	756	forward	7.3	8.5	41.2	35.2	175.1	176.5	7.9	34.2	186.6	4.8	4.9	23.6
31	NP_002190173.1	H12b	44,404,037	44,413,236	1,008	forward	173.0	140.3	527.8	455.1	3895.3	3209.0	106.7	491.4	3616.5	3.1	7.4	12.1
32	XP_000497341.1	LOC102695943	173,468,691	173,468,872	2,766	reverse	2.3	1.3	6.1	5.5	40.1	37.4	1.6	8.8	38.8	3.2	6.7	21.6
34	CDS	Igfb1-75	113,353,950	113,354,243	294	reverse	1.0	0.0	3.1	3.6	10.0	10.1	0.5	3.4	10.6	6.7	3.1	21.1
35	NP_01718095.1	Mnda	173,896,599	173,907,861	1,371	reverse	10.2	11.8	37.0	32.3	339.6	339.1	13.0	34.7	228.2	3.2	6.5	20.7
36	NP_005456.1	Hf7	141,305,225	141,305,616	1,374	reverse	9.5	9.2	34.1	32.5	162.7	162.7	9.2	30.8	160.7	3.2	3.2	26.7
38	CDS	Igfb1-8	114,682,632	114,682,925	294	reverse	0.0	1.0	0.0	4.3	11.3	18.0	0.8	3.4	4.9	2.7	7.0	19.1
43	NP_760236.2	Hf205	174,012,244	174,018,462	1,215	reverse	16.9	26.0	81.8	62.5	356.0	356.0	23.3	73.2	403.9	3.4	5.6	18.8
44	NP_112445.1	If6	30,613,192	30,619,548	636	forward	59.0	67.4	192.1	159.4	1123.0	968.7	63.2	175.9	1102.1	2.8	6.3	17.4
45	NP_002341653.1	170023F08Iik	103,198,961	103,208,515	1,149	reverse	1.7	2.2	13.8	13.5	40.0	39.0	2.0	13.7	33.6	7.0	2.5	17.2
53	NP_00128948.1	Sifn4	83,185,103	83,189,294	1,809	forward	4.6	4.0	11.3	11.1	48.3	47.2	4.1	11.2	70.9	2.6	6.3	16.5
54	NP_035445.1	Saa3	46,712,126	46,715,100	369	reverse	279.1	356.4	751.3	559.4	3703.0	4782.1	117.8	655.4	5180.5	2.1	7.9	16.3
55	NP_033167.2	Cxcl45	90,759,443	90,760,533	399	forward	4.5	9.1	23.4	11.7	134.0	130.9	8.6	17.8	107.9	2.6	6.1	15.9
56	NP_00640648.1	If15	129,365,028	129,366,818	828	reverse	356.3	364.0	1204.8	1014.3	1132.0	1086.1	272.2	1159.8	4844.6	3.5	4.3	18.6
57	NP_034684.2	If14	129,350,711	129,359,103	813	reverse	104.7	107.9	568.7	475.8	388.7	388.7	32.8	187.8	187.8	3.8	3.8	14.1
65	CDS	Igkb1-35	70,406,469	70,406,992	347	reverse	0.0	1.7	3.9	0.9	18.4	18.1	0.9	3.4	12.0	2.8	5.0	14.6
66	NP_035984.2	Oas12	114,897,665	114,921,367	1,527	forward	18.2	17.0	53.1	48.4	283.3	310.4	17.9	50.8	241.9	2.9	4.8	13.7
70	NP_005582.3	Cmpk2	26,469,352	26,478,129	1,344	forward	12.5	9.2	34.2	25.7	180.0	170.2	10.8	30.0	149.9	2.8	5.0	13.7

Fig. 56: Expression analysis of (Adj-Ovalbumin nanocapsule-treated) BMDCs.

Overall, over 14,000 genes were detected and sorted in MS Excel for their expression ratios. Afterwards, the ratio of “Ova : Negative control”, “Adj : Ova” and “Adj : Negative control” were determined. Columns were sorted for their respective enrichment scores. The red square marks and example of an upregulated gene (IL23A), which was 10.8-fold upregulated after treatment with empty Ova-nanocapsules and 55.3-fold upregulated after treatment with Adj-Ova nanocapsules. Green columns mark the transcript counts of negative control cells, yellow columns mark the transcript counts of Ova nanocapsule-treated cells and red columns mark the transcript counts of Adj-Ova nanocapsule-treated cells (each column representing one biological replicate).

Overall, the expression of 260 genes was at least increased by a factor of 2 after empty ovalbumin nanocapsule treatment. In contrast, only 7 genes were downregulated by at least a factor of 2. For adjuvant-filled ovalbumin nanocapsule-treated cells, results were by far more significant. Here, the expression of 1590 genes was at least increased by a factor of 2 compared to the negative control, while 230 genes were downregulated by at least a factor

of 2. Interestingly, the expression of 91 genes was even upregulated by at least a factor of 10, with a few genes that exhibited upregulation factors over 50. These results already indicate, that the adjuvants were successfully released from the nanocapsules inside of the cells, triggering a cellular response.

An overview of expression changes was also given via scatter plots (Fig. 57, kindly provided by StarSeq, Mainz, Germany). Here, the FPKM (fragments per kilobase of exon per million fragments mapped[274]) values of the different samples were compared against each other. Each dot marks the expression of one single gene. Significantly up- or downregulated genes are represented as red dots, while non-significantly up- or downregulated genes are marked in green. As expected, the comparison between adjuvant-filled ovalbumin nanocapsule-treated cells and untreated cells yielded the highest amount of regulation differences (Fig. 57C). In comparison, the treatment with empty ovalbumin nanocapsules resulted in significantly fewer up- or downregulated genes (Fig. 57A). The logical divergence is indicated in the significant expression differences between empty ovalbumin nanocapsules treated cells and adjuvant-filled ovalbumin nanocapsule-treated cells (Fig. 57B).

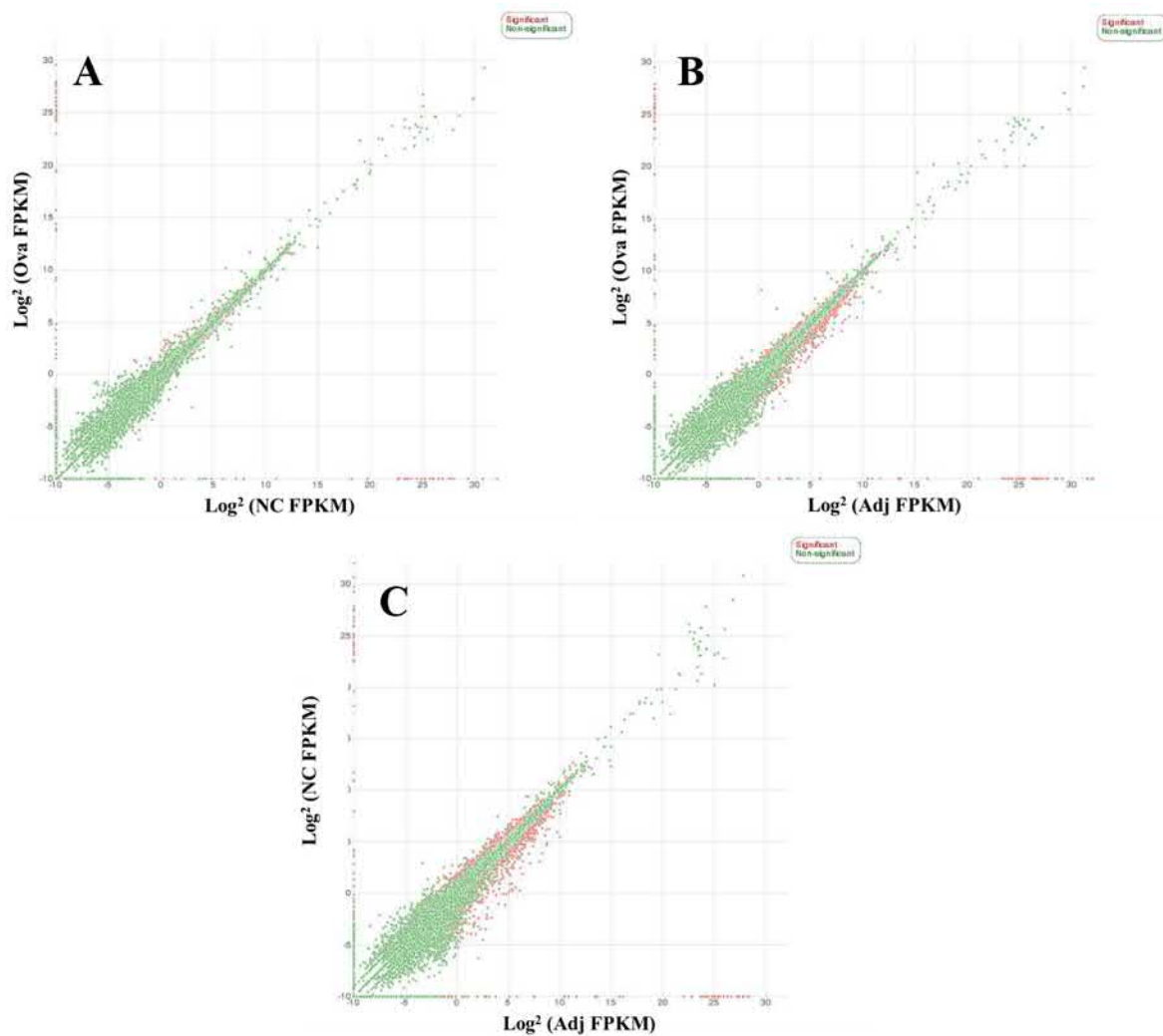


Fig. 57: Scatter plots of expression differences in BMDCs.

This figure depicts the logarithmic expression differences of all detected genes between (A) Ova nanocapsule-treated cells and Negative control cells, (B) Ova nanocapsule-treated cells and Adj-Ova nanocapsule-treated cells, (C) Adj-Ova nanocapsule-treated cells and negative control cells. Significantly up- or downregulated genes are represented by a red dot, while non-significantly up- or downregulated genes are represented by a green dot. Scatter plots were kindly provided by StarSeq, Mainz.

3.3.3 NGS results were partially confirmed via qPCR

The next step was a confirmation of the established NGS data via qPCR (Fig. 58 and Fig. 59). Here, a sample size of seven genes was chosen to compare gene expression levels. Four genes that were highly upregulated as shown by the Next Generation Sequencing data (IL12B, IRF7, CXCL10 and NOS2) were also demonstrated by qPCR to be highly upregulated (Fig. 58). The calculated relative copy number (where the negative control was set as 1), was highly comparable between the two different methodologies. In addition, the expression of genes that were demonstrated by the NGS data to either be almost unaffected (housekeeping gene HSAP8 and dendritic cell marker CD11c) or downregulated (F2RL2) after ovalbumin nanocapsule treatment was determined via qPCR (Fig. 59). Here, also all qPCR results showed the same tendency as their NGS counterparts. The only small divergence occurred for the gene CD11c, which appeared slightly more downregulated in the NGS data. However, the difference compared to the relative copy number was almost negligible. All in all, the tendencies of NGS results could be strongly confirmed via qPCR.

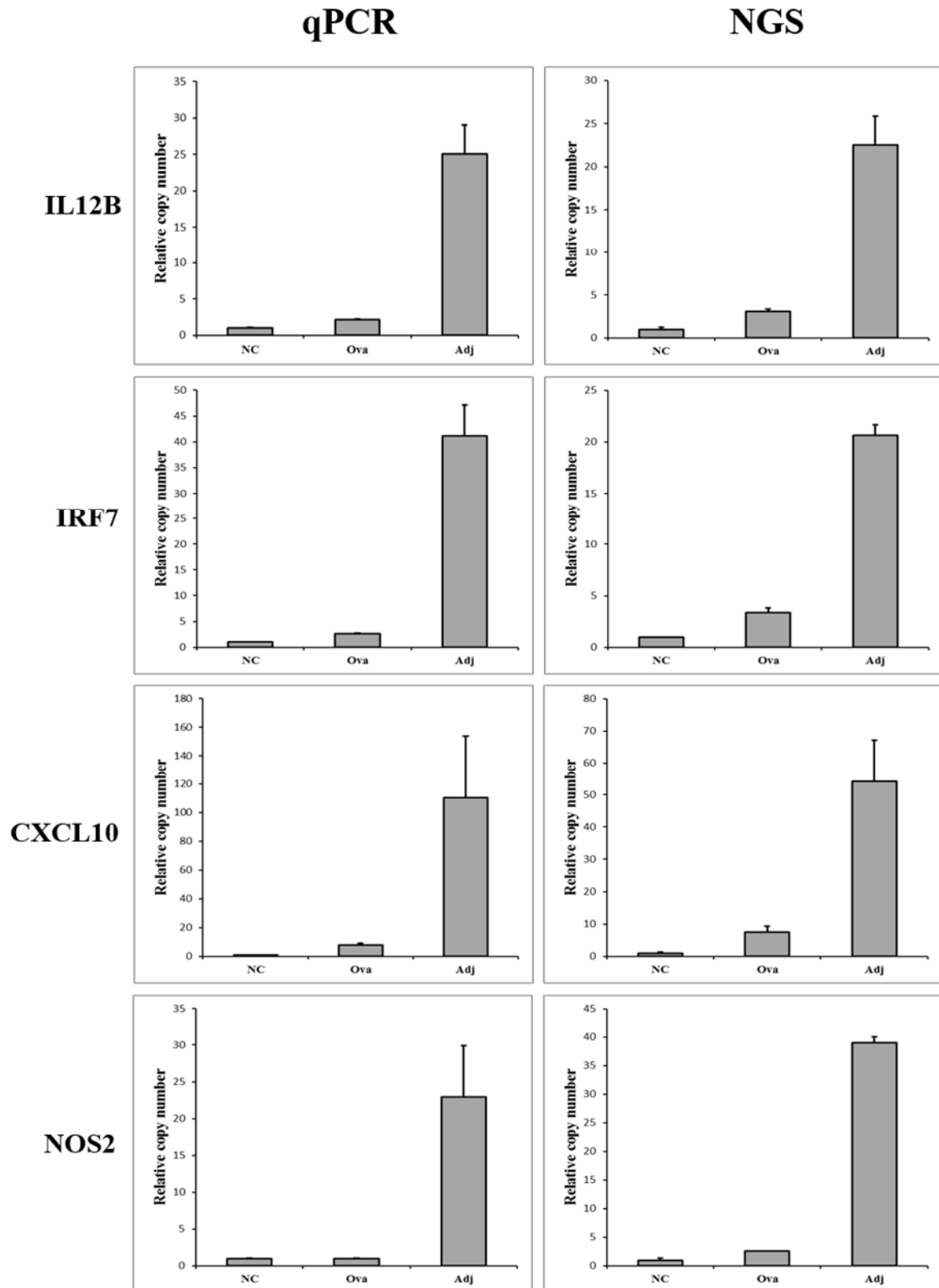


Fig. 58: Comparison of upregulated genes determined via qPCR and NGS.

This figure depicts a comparison between expression results obtained by qPCR (left) and NGS (right) for the genes IL12B, IRF7, CXCL10 and NOS2, which were upregulated in BMDCs after nanocapsule treatment. The determined relative copy number was similar comparing the two different methods.

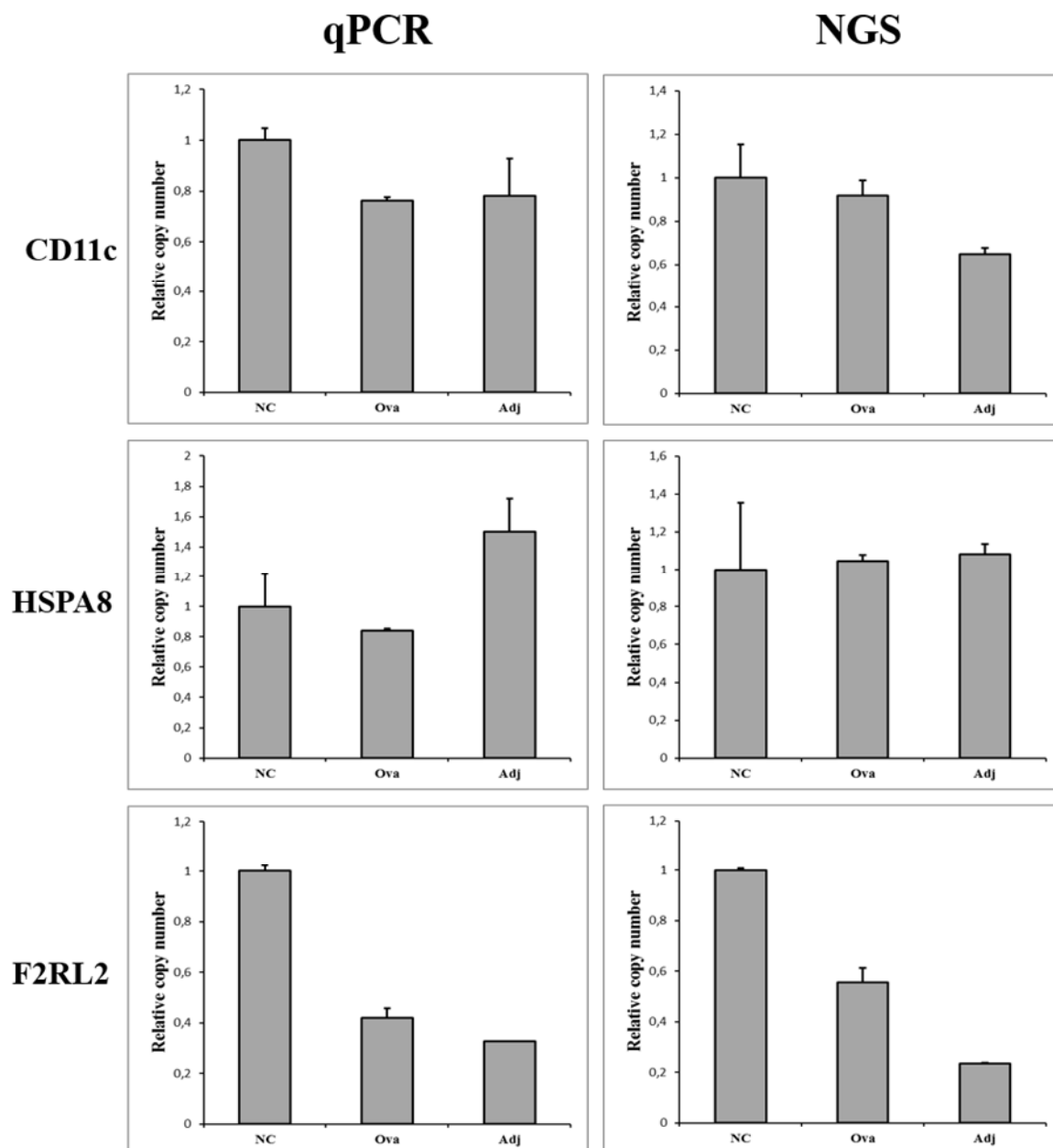


Fig. 59: Comparison of downregulated or housekeeping genes determined via qPCR and NGS. This figure depicts a comparison between expression results obtained by qPCR (left) and NGS (right) for the genes CD11c, HSPA8 and F2RL2 which were either downregulated or unaffected in BMDCs after nanocapsule treatment. The determined relative copy number was similar comparing the two different methods.

3.3.4 Pathway reconstruction after ovalbumin nanocapsule treatment

One of our goals was the determination of putative endocytotic and trafficking-relevant genes. For the determination of nanocapsule-induced trafficking pathways, all genes, that were at least 2-fold upregulated after empty ovalbumin nanocapsule treatment, were copied into the online software DAVID 6.7. However, the software did not signal any uptake- or trafficking relevant genes, which was disappointing. Speculatively, this may be due to the prolonged incubation duration of 1 – 4 hours. Ovalbumin nanocapsules get internalized rather quickly (after 15 minutes), so we might have missed this effect on mRNA levels.

Nevertheless, interesting immune-relevant pathways induced by the ovalbumin nanocapsules could be revealed. For this purpose, genes that were at least 2-fold upregulated after treatment with ovalbumin nanocapsules were used for the DAVID 6.7 analysis. The software detected 27 KEGG pathways[275] (Kyoto Encyclopedia of Genes and Genomes) that contained upregulated genes (Fig. 60). Interestingly, nearly all of these pathways were linked to immune activation. This included the cytokine-cytokine receptor interaction pathway, the Toll-like receptor signaling pathway, the chemokine signaling pathway, the Jak-STAT signaling pathway, the T-cell receptor signaling pathway as well as the antigen processing and presentation pathway (Fig. 60). The activation of these pathways gave a first hint that the nanocapsule cargo, resiquimod and muramyl dipeptide, was released inside of the cell and was able to activate the dendritic cells, at least on mRNA level.

On a side note, we also analyzed the pathways for genes that were downregulated at least 2-fold after (adjuvant-filled) ovalbumin nanocapsule addition. No immune-relevant pathways could be detected (SI Fig. 60). In addition, counts of genes matching the pathways were low, indicating unspecific matches. Consequently, down-regulated genes were not further analyzed.

27 chart records [Download File](#)

Sublist	Category	Term	RT	Genes	Count	%	P-Value	Benjamini
	KEGG_PATHWAY	Cytokine-cytokine receptor interaction	RT		43	9,5	5,3E-22	5,7E-20
	KEGG_PATHWAY	Toll-like receptor signaling pathway	RT		21	4,6	4,0E-12	2,2E-10
	KEGG_PATHWAY	Jak-STAT signaling pathway	RT		25	5,5	6,8E-12	2,5E-10
	KEGG_PATHWAY	Cytosolic DNA-sensing pathway	RT		12	2,6	3,8E-7	1,0E-5
	KEGG_PATHWAY	Allograft rejection	RT		12	2,6	6,7E-7	1,5E-5
	KEGG_PATHWAY	Type I diabetes mellitus	RT		12	2,6	1,6E-6	2,9E-5
	KEGG_PATHWAY	Intestinal immune network for IgA production	RT		11	2,4	2,8E-6	4,3E-5
	KEGG_PATHWAY	TLR-T-like receptor signaling pathway	RT		12	2,6	3,5E-6	4,8E-5
	KEGG_PATHWAY	Hematopoietic cell lineage	RT		12	2,6	2,8E-5	3,4E-4
	KEGG_PATHWAY	Graft-versus-host disease	RT		10	2,2	4,0E-5	4,3E-4
	KEGG_PATHWAY	Chemokine signaling pathway	RT		17	3,7	7,3E-5	7,2E-4
	KEGG_PATHWAY	Cell adhesion molecules (CAMs)	RT		14	3,1	5,3E-4	4,7E-3
	KEGG_PATHWAY	Apoptosis	RT		10	2,2	9,2E-4	7,6E-3
	KEGG_PATHWAY	Autoimmune thyroid disease	RT		9	2,0	1,1E-3	8,5E-3
	KEGG_PATHWAY	NOD-like receptor signaling pathway	RT		8	1,8	2,1E-3	1,5E-2
	KEGG_PATHWAY	Primary immunodeficiency	RT		6	1,3	3,7E-3	2,4E-2
	KEGG_PATHWAY	Small cell lung cancer	RT		8	1,8	1,2E-2	7,3E-2
	KEGG_PATHWAY	Asthma	RT		5	1,1	1,5E-2	8,6E-2
	KEGG_PATHWAY	Antigen processing and presentation	RT		8	1,8	1,7E-2	9,2E-2
	KEGG_PATHWAY	Prion diseases	RT		5	1,1	1,8E-2	9,5E-2
	KEGG_PATHWAY	Viral myocarditis	RT		8	1,8	2,0E-2	9,7E-2
	KEGG_PATHWAY	T cell receptor signaling pathway	RT		9	2,0	2,2E-2	1,0E-1
	KEGG_PATHWAY	MAPK signaling pathway	RT		15	3,3	2,3E-2	1,0E-1
	KEGG_PATHWAY	Acute myeloid leukemia	RT		6	1,3	2,5E-2	1,1E-1
	KEGG_PATHWAY	B cell receptor signaling pathway	RT		7	1,5	2,9E-2	1,2E-1
	KEGG_PATHWAY	Adipocytokine signaling pathway	RT		6	1,3	4,6E-2	1,8E-1
	KEGG_PATHWAY	Riboflavin metabolism	RT		3	0,7	7,0E-2	2,5E-1

Fig. 60: Proposed KEGG-pathways of upregulated genes.

This figure depicts the KEGG (Kyoto Encyclopedia of Genes and Genomes)-pathways that were upregulated for murine BMDCs after (Adj)-Ova nanocapsule treatment. Only genes that were at least upregulated by a factor of 2 were inserted into the analysis. The “count” column symbolizes the number of genes represented in the respective pathway. Analysis was performed with DAVID 6.7[276, 277].

One of the most interesting pathways for dendritic cells is the antigen processing and presentation pathway, since interaction and activation with T-cells is one of the prominent functions of dendritic cells. In the present thesis, the activation of this pathway via adjuvant-filled ovalbumin nanocapsules could be revealed (Fig. 61). Genes marked with a red star (TNF- α , PA28, HSP70, TAP 1/2 and MHC I) were at least 2-fold upregulated. This pathway finishes with an activation of CD8⁺- T cells as well as natural killer cells. Interestingly, most of the immune response pathways were also partially activated by the uptake of empty ovalbumin nanocapsules, albeit the level of upregulation was slightly lower compared to the adjuvant-filled ovalbumin nanocapsules. Since the typical purpose of an adjuvant is the enhancement of a cellular immune response[104], carrier systems made out of ovalbumin might provide functional support of this immune boost.

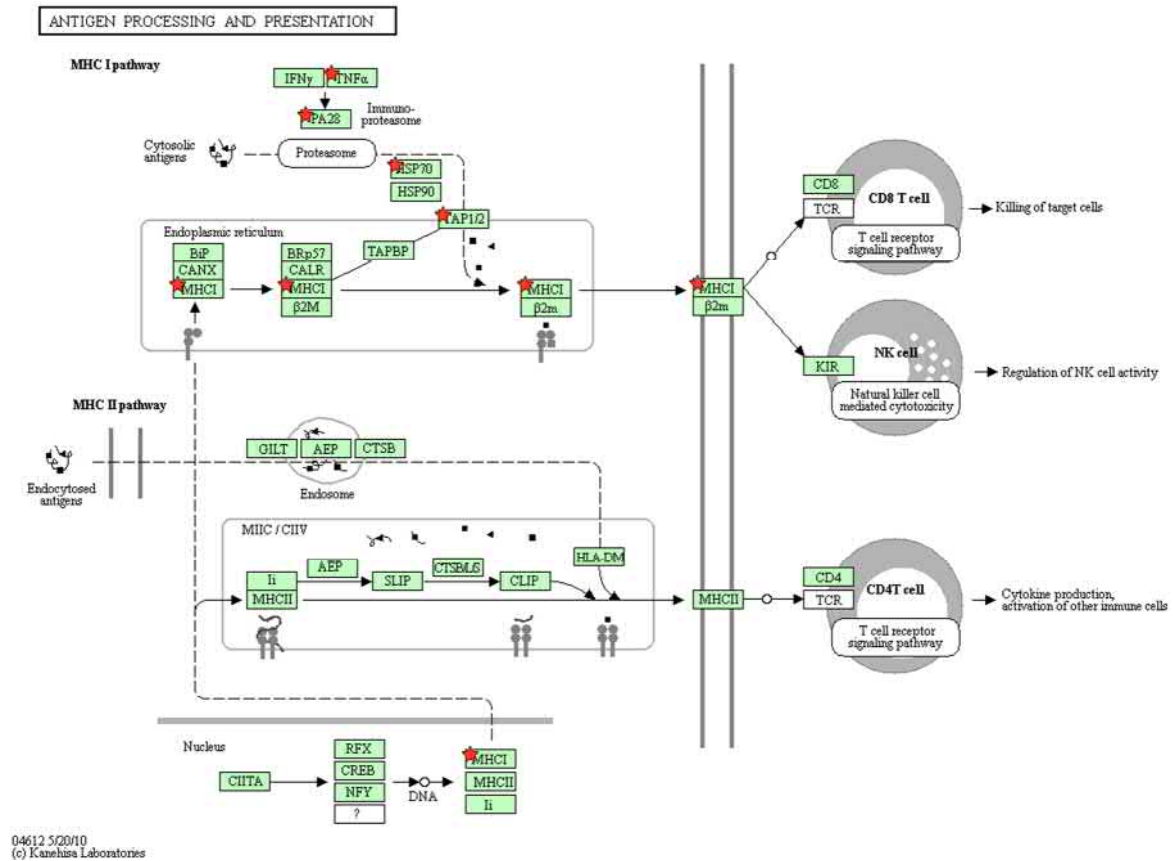


Fig. 61: Antigen processing and presentation pathway.

This figure depicts the KEGG-annotated antigen processing and presentation pathway as referenced in DAVID 6.7[276, 277]. Genes marked with a red star were highly upregulated after treatment with adjuvant-ova nanocapsules. Only genes that were at least upregulated by a factor of 2.0 were inserted into the DAVID pathway analysis. The KEGG-annotated antigen processing and presentation pathway (map04612) is republished with permission of Kanehisa Laboratories[278-280].

4 Summary and conclusion

In the present thesis, nanoparticle-cell interactions were explored via various molecular biological methods to gain insight into intracellular nanoparticle trafficking and the respective opportunities for the field of nanomedicine.

In the first chapter, nanoparticle uptake and transcytosis of different polystyrene nanoparticles were examined. First of all, basic requirements for endocytosis and transcytosis experiments were investigated by testing different transwell plates and establishing a tight Caco-2 monolayer with TEER values over $500 \Omega \times \text{cm}^2$. Twelve different polystyrene nanoparticles were tested for their cellular toxicity after incubation with Caco-2 cells. Nanoparticles stabilized with lutensol or SDS featured no significant signs of toxicity, while nanoparticles stabilized with CTMA-Cl induced grave toxic effects. Nanoparticle uptake was confirmed via flow cytometry and confocal laser scanning microscopy. The percentage of nanoparticle-positive Caco-2 cells was nearly 100% and the MFI increased directly correlated with the used concentration. Since nanoparticles were aggregating in cell culture medium, a strategy was developed to remove nanoparticle aggregates via filtration through $0.45 \mu\text{m}$ sterile filters. In cLSM studies, negatively charged nanoparticles were shown to be internalized, while positively charged nanoparticles were mainly adsorbing on the cell membrane. After confirming similar nanoparticle uptake behavior in transwell system via cLSM studies, nanoparticle transcytosis efficiency of different polystyrene nanoparticles was determined in polycarbonate transwell system. Transcytosis rate of negatively charged SDS-stabilized NP was around 0.2% of NP stock solution, regardless of the used concentration. Nanoparticle size did not influence the rate of transcytosis significantly when comparing 59 nm vs. 91 nm vs. 148 nm sized NP. Regarding lutensol-stabilized nanoparticles, positively charged NP featured highly significantly increased transcytosis compared to their uncharged counterparts, while transcytosis of negatively charged NP was highly significantly decreased. The apical pH of transwell medium also influenced the amount of transported nanoparticles. The more acidic the medium (pH 6 – 8), the more transcytosis could be detected. In addition, two potential candidates for nanoparticle coatings via adsorption were evaluated. The adsorption of Fc region on lutensol-stabilized NP featured an increase in transcytosis by a factor up to 2, while the adsorption of Vitamin B₁₂ lead to an increase in transcytosis by a factor up to 5. Last but not least, a major obstacle for the determination of transcytosis efficiencies could be revealed via confocal laser scanning microscopy. While Caco-2 cells were able to

transport the nanoparticles to their basal side, the polycarbonate membrane acted as a second barrier. The fact that nanoparticles absorbed on the polycarbonate membrane (on the apical as well as on the basal side) might distort measured transcytosis values to be slightly more negative than the actual amount of transcytosed nanoparticles. Nevertheless, actual visual proof for translocating nanoparticles was obtained by this confocal laser scanning microscopy Z-position study.

In the second chapter, a combination of mass spectrometry analysis and cLSM studies was employed to monitor intracellular trafficking of polystyrene nanoparticles in Caco-2 cells. After incubating Caco-2 cells in transwell system with nanoparticles for 24 h, the basal cell culture medium was collected and analyzed by mass spectrometry. By comparing the protein composition with the protein composition of nanoparticle-untreated control medium, putative trafficking-, transcytosis- and exocytosis-relevant genes could be discovered. Candidate genes as well as putative exocytosis-relevant genes described in the literature were amplified and coupled to GFP and/or mCherry as fluorescent marker proteins. Caco-2 cells were subsequently transfected via lentiviral gene transfer and selected until cell lines were stable. Then, elaborate co-localization studies with polystyrene nanoparticles were performed. Markers for macropinocytosis showed strong co-localization during the first hours of nanoparticle incubation, which greatly reduced over time. Markers for late endosomal and lysosomal compartments started with no significant co-localization, greatly increasing over time until nearly 100% after 24 hours. Interestingly, co-localization with putative exo- and transcytosis-relevant proteins showed a slowly and steady increasing pattern until 24 hours of incubation. The addition of more nanoparticles resulted in huge endosomes / lysosomes as shown by cLSM and transmission electron microscopy. Via this analysis, the biggest obstacle for the transcytosis of nanocarriers was determined: the lysosome as final destination. Furthermore, double transgenic cell lines were used to confirm and extend the nanoparticle trafficking profiles. It was shown via cLSM as well as TEM that certain different types of vesicles exist which can transport nanoparticles. It was hypothesized, that the protein composition of these vesicles influences whether a nanoparticle is transported to the basal side of Caco-2 cells and whether the vesicle is triggered to fuse with the basal cell membrane, resulting in exo- and transcytosis.

In the third chapter, the impact of (adjuvant-filled) ovalbumin nanocapsules on mRNA expression levels of murine bone marrow derived dendritic cells was determined. For that purpose, ovalbumin nanocapsules filled with the potential adjuvants resiquimod and muramyl dipeptide were added to the cells for 1 hour, 2 hours as well as 4 hours to ensure

cellular uptake. The mRNA of nanocapsule-treated and untreated cells was extracted and sequenced by Illumina Next Generation Sequencing, which yielded a genetic information of > 3.7 gigabases of DNA. Overall, around 14,000 genes and 55,000 transcription variants were detected via bioinformatics methods. The data was subsequently used to quantify the mRNA expression differences between nanocapsule-treated and untreated cells. The cellular uptake of empty ovalbumin nanocapsules resulted in an upregulation of 260 genes by at least a factor of 2, while adjuvant-filled ovalbumin nanocapsules triggered an upregulation of over 1500 genes by at least a factor of 2. Additionally, the expression of 91 genes was upregulated by a factor of at least 10, and a few genes even exhibited upregulation factors over 50, indicating a successful release of adjuvants inside of BMDCs. Expression data was subsequently used to determine upregulated pathways via DAVID 6.7. Disappointingly, no pathways for endocytosis and intracellular trafficking were upregulated after nanocapsule-treatment. However, a broad spectrum of immune-relevant pathways was upregulated, including the cytokine-cytokine receptor interaction pathway, the Toll-like receptor signaling pathway, the chemokine signaling pathway, the Jak-STAT signaling pathway, the T-cell receptor signaling pathway as well as the antigen processing and presentation pathway. Interestingly, many of the related genes were also upregulated by the addition of empty nanocapsules, which leads to the conclusion that ovalbumin might provide additional functional support to an adjuvant's immune boost.

Concluding, it is obvious that the area of nanomedicine and nanobiology offer great potential for the revolution of medicine. Despite offering sheer limitless applications, each nanomaterial features its own difficulties and needs to be carefully evaluated. Inter- and intracellular correlations and pathways as well as potential cytotoxic effects need to be researched thoroughly for every new material. In the present thesis, several methodologies were demonstrated to get an insight into nanoparticle-cell interactions. The future will show if those methods and insights will be transferable to other nanomaterials.

5 Deutsche Zusammenfassung

In der vorliegenden Arbeit wurden Nanopartikel-Zell-Interaktionen mittels verschiedener molekularbiologischer Methoden analysiert, um Erkenntnisse über das intrazelluläre Trafficking von polymeren Nanopartikeln und den damit einhergehenden Möglichkeiten für das Forschungsfeld der Nanomedizin zu gewinnen.

Im ersten Kapitel wurden die Aufnahme und Transzytose von verschiedenen Polystyrol Nanopartikeln untersucht. Zunächst wurden dafür die entsprechenden Voraussetzungen geschaffen, indem verschiedene Transwell Platten getestet wurden um einen dichten Caco-2 Monolayer mit einem TEER-Wert über $500 \Omega \times \text{cm}^2$ zu etablieren. Daraufhin wurden zwölf verschiedene polymere Nanopartikel auf ihre zelluläre Toxizität nach der Inkubation mit Caco-2 Zellen überprüft. Nanopartikel, die mit Lutensol oder SDS stabilisiert waren, zeigten keinerlei toxische Effekte, während mit CTMA-Cl stabilisierte Nanopartikel zu gravierenden toxischen Effekten führten. Die Aufnahme von polymeren Nanopartikeln wurde mittels Durchflusszytometrie und konfokaler Laser Scanning Mikroskopie demonstriert. Der Prozentsatz von Nanopartikel-positiven Caco-2 Zellen lag bei fast 100% und die Mediane Fluoreszenz Intensität (MFI) erhöhte sich direkt korreliert mit steigender Nanopartikelkonzentration. Da die verwendeten Nanopartikel stark im Zellkulturmedium aggregierten, wurde ein System entwickelt, um die Aggregate zu entfernen. Hierfür wurde das Nanopartikel-haltige Zellkulturmedium durch $0,45 \mu\text{m}$ Sterilfilter gepresst. In konfokalen Laser Scanning Mikroskopie Studien konnte gezeigt werden, dass negativ geladene Polystyrol Nanopartikel gut von den Caco-2 Zellen aufgenommen werden, während positiv geladene Polystyrol Nanopartikel vorwiegend an der Zellmembran adhärten. Nachdem eine ähnliche Zellaufnahme im Transwellsystem auf einer Polycarbonat Membran demonstriert wurde, wurde die Transzytose Effizienz im Transwell System bestimmt. Diese lag bei ungefähr 0,2% für negativ geladene Polystyrol Nanopartikel, unabhängig von der eingesetzten Konzentration. Die Größe von polymeren Nanopartikeln hatte keinen signifikanten Einfluss beim Vergleich von 59 nm, 91 nm und 148 nm großen NP. Bei Lutensol-stabilisierten Nanopartikeln zeigten positiv geladene NP eine signifikant höhere Transzytoserate als ungeladene NP, während negativ geladene NP eine signifikant geringere Transzytoserate aufwiesen. Auch der apikale pH-Wert hatte einen Einfluss auf die Menge der transzytierten Nanopartikel: Je saurer das apikale Zellkulturmedium (pH 6 - 8), desto höher war die Transzytoserate. Zusätzlich wurden zwei Agentien für ein Nanopartikel „Coating“ mittels Adsorption ermittelt. Die Adsorption der

Fc Region von IgG Antikörpern führte zu einer Verdopplung der Transzytoserate, während die Adsorption von Vitamin B₁₂ in einer fünffachen Erhöhung der Transzytoserate resultierte. Zu guter Letzt wurde ein großes Hindernis für die korrekte Messung der Transzytoserate entdeckt. Bei der Messung mittels konfokaler Laser Scanning Mikroskopie wurde festgestellt, dass, obwohl die Caco-2 Zellen Nanopartikel erfolgreich von ihrer apikalen zur basalen Seite transportieren, diese auf der Polycarbonat Membran adhärten (sowohl auf deren apikalen als auch basalen Seite). Dieses Phänomen könnte zu einer Verzerrung in der gemessenen Transzytoserate beitragen und dazu führen, dass die gemessenen Werte zu niedrig sind. Nichtsdestotrotz konnte mit der konfokalen Laser Scanning Mikroskopie ein bildlicher Beweis des Transzytose-Prozesses gezeigt werden.

Im zweiten Kapitel wurde eine Kombination aus der Massenspektrometrie und konfokaler Laser Scanning Mikroskopie verwendet, um das intrazelluläre Trafficking von Nanopartikeln in Caco-2 Zellen zu untersuchen. Nachdem die Caco-2 Zellen für 24 Stunden im Transwell System mit Nanopartikeln inkubiert wurden, wurde das basale Zellkulturmedium gesammelt und mittels Massenspektrometrie analysiert. Durch einen Vergleich der Proteinkomposition mit der von Nanopartikel unbehandeltem Medium konnten putativ Transzytose und Exozytose relevante Proteine entdeckt werden. Die Gene dieser, sowie weiterer in der Literatur beschriebener Proteine, wurden amplifiziert und an GFP bzw. mCherry als Fluoreszenzmarker gekoppelt. Die Caco-2 Zellen wurden anschließend mittels lentiviralem Gentransfer transfiziert und selektiert. Daraufhin wurden ausführliche Co-Lokalisationsstudien mit Polystyrol Nanopartikeln durchgeführt. Marker für Makropinozytose zeigten eine starke Kolokalisation während der ersten Stunden nach Nanopartikel Zugabe, die sich über die Zeit schnell reduzierte. Marker für späte Endosomen und lysosomale Kompartimente zeigten anfangs keinerlei bis schwache Co-Lokalisation, welche sich im Laufe der Inkubationszeit auf bis zu fast 100% erhöhte. Interessanterweise zeigten die Kolokalisations-Experimente mit putativ Trans- und Exozytose relevanten Markern eine langsam aber stetig wachsende Kolokalisation. Eine deutliche Erhöhung der Nanopartikel Konzentration resultierte in riesigen Endosomen / Lysosomen, was mittels cLSM und Transmissionselektronenmikroskopie demonstriert wurde. Mit Hilfe dieser Studie ließ sich auch das größte Hindernis der Transzytose von Nanopartikeln aufzeigen: Das Lysosom als Endstation für Nanopartikel. Zusätzlich wurden mittels doppeltransgener Caco-2 Zelllinien die Ergebnisse der Co-Lokalisationsstudien bestätigt und erweitert. Eine Analyse mittels cLSM und TEM ergab, dass sich die polymeren Nanopartikeln in vielen verschiedenen Vesikeltypen befinden können. Dies führte zur Hypothese, dass die

Proteinkomposition auf und in diesen Vesikeln darüber entscheidet, ob ein Nanopartikel zur basalen Zellmembran transportiert und dort ausgeschleust wird, mit dem Resultat eines abgeschlossenen Transzytose-Vorgangs.

Im dritten Kapitel wurde der Einfluss von (Adjuvans-gefüllten) Ovalbumin-Nanokapseln auf die mRNA Transkription in murinen dendritischen Zellen überprüft. Dafür wurden Ovalbumin-Nanokapseln mit den Adjuvantien Resiquimod und Muramyldipeptid befüllt und für 1, 2 und 4 Stunden mit den dendritischen Zellen inkubiert. Daraufhin wurde die mRNA von Nanokapsel-behandelten und unbehandelten Zellen extrahiert und mittels der Illumina Next Generation Sequencing Technologie sequenziert, was eine genetische Information von über 3,7 Gigabasen DNA einbrachte. Insgesamt konnten ungefähr 14.000 Gene und 55.000 verschiedene Transkriptvarianten mittels bioinformatischer Methoden detektiert werden. Diese Daten wurden folglich benutzt, um Unterschiede in der mRNA Expression zwischen unbehandelten und Nanokapsel-behandelten Zellen zu quantifizieren. Die Aufnahme von unbefüllten Ovalbumin-Nanokapseln resultierte in einer Hochregulation von 260 Genen um mindestens den Faktor 2, während die Aufnahme von Adjuvans-befüllten Nanokapseln zu einer Hochregulation von über 1500 Genen um mindestens den Faktor 2 führte. Zusätzlich wurden im Falle von Adjuvans-befüllten Nanokapseln 91 Gene um mindestens den Faktor 10 und einige Gene sogar um den Faktor 50 hochreguliert, was auf eine erfolgreiche Freisetzung der Adjuvantien im Zellinneren der dendritischen Zellen schließen ließ. Die mRNA Expressionsdaten wurden im weiteren Verlauf dazu benutzt, hochregulierte Pathways nach Nanokapsel-Zugabe mittels der Software DAVID 6.7 zu detektieren. Leider konnten im Zuge dessen keine Pathways der Endozytose und für das intrazelluläre Nanopartikel Trafficking detektiert werden. Nichtsdestotrotz war ein breites Spektrum an immun-relevanten Pathways hochreguliert. Dies beinhaltete unter anderem den Cytokine-Cytokine Receptor Interaction Pathway, den Toll-like Receptor Pathway, den Chemokine Signaling Pathway, den Jak-STAT signaling Pathway, den T-cell Receptor signaling Pathway und den Antigen Processing and Presentation Pathway. Interessanterweise wurden viele der immun-relevanten Gene bereits durch die Zugabe von unbefüllten Ovalbumin-Kapseln hochreguliert, was die Vermutung zulässt, dass Ovalbumin-Nanokapseln zusätzliche Unterstützung zur Immunaktivierung durch Adjuvantien beitragen könnten.

Zusammenfassend lässt sich sagen, dass das Feld der Nanomedizin bzw. der Nanobiologie großes Potential für eine Revolution der klassischen Medizin bietet. Trotz der schier unendlichen Möglichkeiten beinhaltet jedes Nanomaterial jedoch seine eigenen

Schwierigkeiten und Hindernisse und muss daher sorgsam evaluiert werden. Inter- und intrazelluläre Korrelationen und Pathways sowie potentielle zytotoxische Effekte müssen für jedes neu entwickelte Material weiter erforscht werden. In der vorliegenden Arbeit wurden einige Methoden vorgestellt, die einen Einblick in Nanopartikel-Zell-Interaktionen geben. Die Zukunft wird zeigen, ob diese Methoden und Einblicke auch auf andere Nanomaterialien übertragen werden können.

6 Bibliography

- [1] E.E. Commission, Commission Recommendation of 18 October 2011 on the definition of nanomaterial, Off. J. Eur. Union 275 (2011) 38.
- [2] Y. Min, J.M. Caster, M.J. Eblan, A.Z. Wang, Clinical translation of nanomedicine, *Chemical reviews* 115(19) (2015) 11147-11190.
- [3] D. Bobo, K.J. Robinson, J. Islam, K.J. Thurecht, S.R. Corrie, Nanoparticle-based medicines: a review of FDA-approved materials and clinical trials to date, *Pharmaceutical research* 33(10) (2016) 2373-2387.
- [4] A.C. Anselmo, S. Mitragotri, Nanoparticles in the clinic, *Bioengineering & Translational Medicine* 1(1) (2016) 10-29.
- [5] M.E. Davis, D.M. Shin, Nanoparticle therapeutics: an emerging treatment modality for cancer, *Nature reviews Drug discovery* 7(9) (2008) 771.
- [6] C. Loos, T. Syrovets, A. Musyanovych, V. Mailänder, K. Landfester, G.U. Nienhaus, T. Simmet, Functionalized polystyrene nanoparticles as a platform for studying bio-nano interactions, *Beilstein journal of nanotechnology* 5 (2014) 2403.
- [7] J. Wen, S.M. Anderson, J. Du, M. Yan, J. Wang, M. Shen, Y. Lu, T. Segura, Controlled Protein Delivery Based on Enzyme-Responsive Nanocapsules, *Advanced materials* 23(39) (2011) 4549-4553.
- [8] Abdata.de, (2017).
- [9] L. Mei, Z. Zhang, L. Zhao, L. Huang, X.-L. Yang, J. Tang, S.-S. Feng, Pharmaceutical nanotechnology for oral delivery of anticancer drugs, *Advanced drug delivery reviews* 65(6) (2013) 880-890.
- [10] W.H. Organization, Global report on diabetes, World Health Organization 2016.

- [11] Z. Zhang, Y. Huang, F. Gao, H. Bu, W. Gu, Y. Li, Daidzein–phospholipid complex loaded lipid nanocarriers improved oral absorption: in vitro characteristics and in vivo behavior in rats, *Nanoscale* 3(4) (2011) 1780-1787.
- [12] P. Fonte, T. Nogueira, C. Gehm, D. Ferreira, B. Sarmento, Chitosan-coated solid lipid nanoparticles enhance the oral absorption of insulin, *Drug delivery and translational research* 1(4) (2011) 299-308.
- [13] Z. Zhang, J. Huang, S. Jiang, Z. Liu, W. Gu, H. Yu, Y. Li, Porous starch based self-assembled nano-delivery system improves the oral absorption of lipophilic drug, *International journal of pharmaceutics* 444(1-2) (2013) 162-168.
- [14] J. Reinholz, K. Landfester, V. Mailänder, The challenges of oral drug delivery via nanocarriers, *Drug Delivery* (2018) DOI: 10.1080/10717544.2018.1501119.
- [15] G. Bazzoni, E. Dejana, Endothelial cell-to-cell junctions: molecular organization and role in vascular homeostasis, *Physiological reviews* 84(3) (2004) 869-901.
- [16] M. Schenk, C. Mueller, The mucosal immune system at the gastrointestinal barrier, *Best Practice & Research Clinical Gastroenterology* 22(3) (2008) 391-409.
- [17] L.M. Ensign, R. Cone, J. Hanes, Oral drug delivery with polymeric nanoparticles: the gastrointestinal mucus barriers, *Advanced drug delivery reviews* 64(6) (2012) 557-570.
- [18] Y.S. Kim, S.B. Ho, Intestinal goblet cells and mucins in health and disease: recent insights and progress, *Current gastroenterology reports* 12(5) (2010) 319-330.
- [19] S.S. Olmsted, J.L. Padgett, A.I. Yudin, K.J. Whaley, T.R. Moench, R.A. Cone, Diffusion of macromolecules and virus-like particles in human cervical mucus, *Biophysical journal* 81(4) (2001) 1930-1937.
- [20] S.K. Lai, D.E. O'Hanlon, S. Harrold, S.T. Man, Y.-Y. Wang, R. Cone, J. Hanes, Rapid transport of large polymeric nanoparticles in fresh undiluted human mucus, *Proceedings of the National Academy of Sciences* 104(5) (2007) 1482-1487.

- [21] Y.Y. Wang, S.K. Lai, J.S. Suk, A. Pace, R. Cone, J. Hanes, Addressing the PEG mucoadhesivity paradox to engineer nanoparticles that “slip” through the human mucus barrier, *Angewandte Chemie International Edition* 47(50) (2008) 9726-9729.
- [22] I.P. de Sousa, C. Steiner, M. Schmutzler, M.D. Wilcox, G.J. Veldhuis, J.P. Pearson, C.W. Huck, W. Salvenmoser, A. Bernkop-Schnürch, Mucus permeating carriers: formulation and characterization of highly densely charged nanoparticles, *European Journal of Pharmaceutics and Biopharmaceutics* 97 (2015) 273-279.
- [23] S.K. Lai, Y.-Y. Wang, J. Hanes, Mucus-penetrating nanoparticles for drug and gene delivery to mucosal tissues, *Advanced drug delivery reviews* 61(2) (2009) 158-171.
- [24] F. Hintzen, G. Perera, S. Hauptstein, C. Müller, F. Laffleur, A. Bernkop-Schnürch, In vivo evaluation of an oral self-microemulsifying drug delivery system (SMEDDS) for leuporelin, *International journal of pharmaceutics* 472(1-2) (2014) 20-26.
- [25] S. Dünnhaupt, O. Kammona, C. Waldner, C. Kiparissides, A. Bernkop-Schnürch, Nano-carrier systems: strategies to overcome the mucus gel barrier, *European Journal of Pharmaceutics and Biopharmaceutics* 96 (2015) 447-453.
- [26] C. Müller, K. Leithner, S. Hauptstein, F. Hintzen, W. Salvenmoser, A. Bernkop-Schnürch, Preparation and characterization of mucus-penetrating papain/poly (acrylic acid) nanoparticles for oral drug delivery applications, *Journal of nanoparticle research* 15(1) (2013) 1353.
- [27] R. Rosenthal, D. Günzel, C. Finger, S.M. Krug, J.F. Richter, J.-D. Schulzke, M. Fromm, S. Amasheh, The effect of chitosan on transcellular and paracellular mechanisms in the intestinal epithelial barrier, *Biomaterials* 33(9) (2012) 2791-2800.
- [28] G. Sahay, D.Y. Alakhova, A.V. Kabanov, Endocytosis of nanomedicines, *Journal of controlled release* 145(3) (2010) 182-195.
- [29] T.-G. Iversen, T. Skotland, K. Sandvig, Endocytosis and intracellular transport of nanoparticles: present knowledge and need for future studies, *Nano Today* 6(2) (2011) 176-185.

- [30] D. Dutta, J.G. Donaldson, Search for inhibitors of endocytosis: Intended specificity and unintended consequences, *Cellular logistics* 2(4) (2012) 203-208.
- [31] L.-H. Wang, K.G. Rothberg, R. Anderson, Mis-assembly of clathrin lattices on endosomes reveals a regulatory switch for coated pit formation, *The Journal of cell biology* 123(5) (1993) 1107-1117.
- [32] M. Koivusalo, C. Welch, H. Hayashi, C.C. Scott, M. Kim, T. Alexander, N. Touret, K.M. Hahn, S. Grinstein, Amiloride inhibits macropinocytosis by lowering submembranous pH and preventing Rac1 and Cdc42 signaling, *The Journal of cell biology* 188(4) (2010) 547-563.
- [33] M.C. Kerr, R.D. Teasdale, Defining macropinocytosis, *Traffic* 10(4) (2009) 364-371.
- [34] G.B. Ozdener, M.V. Bais, P.C. Trackman, Determination of cell uptake pathways for tumor inhibitor lysyl oxidase propeptide, *Molecular oncology* 10(1) (2016) 1-23.
- [35] L. Pelkmans, D. Püntener, A. Helenius, Local actin polymerization and dynamin recruitment in SV40-induced internalization of caveolae, *Science* 296(5567) (2002) 535-539.
- [36] S. Mahammad, I. Parmryd, Cholesterol depletion using methyl- β -cyclodextrin, *Methods in Membrane Lipids*, Springer2015, pp. 91-102.
- [37] A.M. Bannunah, D. Vllasaliu, J. Lord, S. Stolnik, Mechanisms of nanoparticle internalization and transport across an intestinal epithelial cell model: effect of size and surface charge, *Mol Pharm* 11(12) (2014) 4363-73.
- [38] E. Antileo, C. Garri, V. Tapia, J.P. Munoz, M. Chiong, F. Nualart, S. Lavandero, J. Fernandez, M.T. Nunez, Endocytic pathway of exogenous iron-loaded ferritin in intestinal epithelial (Caco-2) cells, *Am J Physiol Gastrointest Liver Physiol* 304(7) (2013) G655-61.
- [39] B. He, P. Lin, Z. Jia, W. Du, W. Qu, L. Yuan, W. Dai, H. Zhang, X. Wang, J. Wang, X. Zhang, Q. Zhang, The transport mechanisms of polymer nanoparticles in Caco-2 epithelial cells, *Biomaterials* 34(25) (2013) 6082-98.

- [40] Q. Song, L. Yao, M. Huang, Q. Hu, Q. Lu, B. Wu, H. Qi, Z. Rong, X. Jiang, X. Gao, J. Chen, H. Chen, Mechanisms of transcellular transport of wheat germ agglutinin-functionalized polymeric nanoparticles in Caco-2 cells, *Biomaterials* 33(28) (2012) 6769-82.
- [41] K. Sato, J. Nagai, N. Mitsui, Y. Ryoko, M. Takano, Effects of endocytosis inhibitors on internalization of human IgG by Caco-2 human intestinal epithelial cells, *Life Sci* 85(23-26) (2009) 800-7.
- [42] L.E. Johannessen, B. Spilsberg, C.R. Wiik-Nielsen, A.B. Kristoffersen, A. Holst-Jensen, K.G. Berdal, DNA-fragments are transcytosed across CaCo-2 cells by adsorptive endocytosis and vesicular mediated transport, *PLoS One* 8(2) (2013) e56671.
- [43] R. Fowler, D. Vllasaliu, F.F. Trillo, M. Garnett, C. Alexander, H. Horsley, B. Smith, I. Whitcombe, M. Eaton, S. Stolnik, Nanoparticle transport in epithelial cells: pathway switching through bioconjugation, *Small* 9(19) (2013) 3282-94.
- [44] B. He, Z. Jia, W. Du, C. Yu, Y. Fan, W. Dai, L. Yuan, H. Zhang, X. Wang, J. Wang, X. Zhang, Q. Zhang, The transport pathways of polymer nanoparticles in MDCK epithelial cells, *Biomaterials* 34(17) (2013) 4309-26.
- [45] F. Fazlollahi, S. Angelow, N.R. Yacobi, R. Marchelletta, A.S. Yu, S.F. Hamm-Alvarez, Z. Borok, K.J. Kim, E.D. Crandall, Polystyrene nanoparticle trafficking across MDCK-II, *Nanomedicine* 7(5) (2011) 588-94.
- [46] O. Harush-Frenkel, E. Rozentur, S. Benita, Y. Altschuler, Surface charge of nanoparticles determines their endocytic and transcytotic pathway in polarized MDCK cells, *Biomacromolecules* 9(2) (2008) 435-43.
- [47] A.A. Zubareva, T.S. Shcherbinina, V.P. Varlamov, E.V. Svirshchevskaya, Intracellular sorting of differently charged chitosan derivatives and chitosan-based nanoparticles, *Nanoscale* 7(17) (2015) 7942-52.

- [48] M.S. Ehrenberg, A.E. Friedman, J.N. Finkelstein, G. Oberdorster, J.L. McGrath, The influence of protein adsorption on nanoparticle association with cultured endothelial cells, *Biomaterials* 30(4) (2009) 603-10.
- [49] Z. Wang, C. Tiruppathi, R.D. Minshall, A.B. Malik, Size and dynamics of caveolae studied using nanoparticles in living endothelial cells, *ACS nano* 3(12) (2009) 4110-4116.
- [50] N. Meng, L. Han, X. Pan, L. Su, Z. Jiang, Z. Lin, J. Zhao, S. Zhang, Y. Zhang, B. Zhao, J. Miao, Nano-Mg(OH)₂-induced proliferation inhibition and dysfunction of human umbilical vein vascular endothelial cells through caveolin-1-mediated endocytosis, *Cell Biol Toxicol* 31(1) (2015) 15-27.
- [51] S.K. Lai, K. Hida, S.T. Man, C. Chen, C. Machamer, T.A. Schroer, J. Hanes, Privileged delivery of polymer nanoparticles to the perinuclear region of live cells via a non-clathrin, non-degradative pathway, *Biomaterials* 28(18) (2007) 2876-84.
- [52] L. Landgraf, I. Muller, P. Ernst, M. Schafer, C. Rosman, I. Schick, O. Kohler, H. Oehring, V.V. Breus, T. Basche, C. Sonnichsen, W. Tremel, I. Hilger, Comparative evaluation of the impact on endothelial cells induced by different nanoparticle structures and functionalization, *Beilstein J Nanotechnol* 6 (2015) 300-12.
- [53] C. Freese, R.E. Unger, R.C. Deller, M.I. Gibson, C. Brochhausen, H.-A. Klok, C.J. Kirkpatrick, Uptake of poly(2-hydroxypropylmethacrylamide)-coated gold nanoparticles in microvascular endothelial cells and transport across the blood–brain barrier, *Biomaterials Science* 1(8) (2013) 824.
- [54] S. Schöttler, G. Becker, S. Winzen, T. Steinbach, K. Mohr, K. Landfester, V. Mailänder, F.R. Wurm, Protein adsorption is required for stealth effect of poly (ethylene glycol)-and poly (phosphoester)-coated nanocarriers, *Nature nanotechnology* 11(4) (2016) 372-377.
- [55] T. Cedervall, I. Lynch, S. Lindman, T. Berggård, E. Thulin, H. Nilsson, K.A. Dawson, S. Linse, Understanding the nanoparticle–protein corona using methods to quantify exchange rates and affinities of proteins for nanoparticles, *Proceedings of the National Academy of Sciences* 104(7) (2007) 2050-2055.

- [56] D. Walczyk, F.B. Bombelli, M.P. Monopoli, I. Lynch, K.A. Dawson, What the cell “sees” in bionanoscience, *Journal of the American Chemical Society* 132(16) (2010) 5761-5768.
- [57] S. Ritz, S. Schöttler, N. Kotman, G. Baier, A. Musyanovych, J.r. Kuharev, K. Landfester, H.r. Schild, O. Jahn, S. Tenzer, Protein corona of nanoparticles: distinct proteins regulate the cellular uptake, *Biomacromolecules* 16(4) (2015) 1311-1321.
- [58] Y.T. Ho, R.D. Kamm, J.C.Y. Kah, Influence of Protein Corona and Caveolae-Mediated Endocytosis on Nanoparticle Uptake and Transcytosis, *Nanoscale* 10 (2018) 12386-12397.
- [59] D. Liu, B. Lin, W. Shao, Z. Zhu, T. Ji, C. Yang, In vitro and in vivo studies on the transport of PEGylated silica nanoparticles across the blood-brain barrier, *ACS Appl Mater Interfaces* 6(3) (2014) 2131-6.
- [60] A. des Rieux, E.G. Ragnarsson, E. Gullberg, V. Preat, Y.J. Schneider, P. Artursson, Transport of nanoparticles across an in vitro model of the human intestinal follicle associated epithelium, *Eur J Pharm Sci* 25(4-5) (2005) 455-65.
- [61] J.A. Wang, T.F. Meyer, T. Rudel, Cytoskeleton and motor proteins are required for the transcytosis of *Neisseria gonorrhoeae* through polarized epithelial cells, *Int J Med Microbiol* 298(3-4) (2008) 209-21.
- [62] D. Vllasaliu, C. Alexander, M. Garnett, M. Eaton, S. Stolnik, Fc-mediated transport of nanoparticles across airway epithelial cell layers, *J Control Release* 158(3) (2012) 479-86.
- [63] E.M. Pridgen, F. Alexis, T.T. Kuo, E. Levy-Nissenbaum, R. Karnik, R.S. Blumberg, R. Langer, O.C. Farokhzad, Transepithelial transport of Fc-targeted nanoparticles by the neonatal fc receptor for oral delivery, *Sci Transl Med* 5(213) (2013) 213ra167.
- [64] E. Roger, S. Kalscheuer, A. Kirtane, B.R. Guru, A.E. Grill, J. Whittum-Hudson, J. Panyam, Folic acid functionalized nanoparticles for enhanced oral drug delivery, *Mol Pharm* 9(7) (2012) 2103-10.

- [65] D.T. Wiley, P. Webster, A. Gale, M.E. Davis, Transcytosis and brain uptake of transferrin-containing nanoparticles by tuning avidity to transferrin receptor, *Proc Natl Acad Sci U S A* 110(21) (2013) 8662-7.
- [66] M. Dan, D.B. Cochran, R.A. Yokel, T.D. Dziubla, Binding, transcytosis and biodistribution of anti-PECAM-1 iron oxide nanoparticles for brain-targeted delivery, *PLoS One* 8(11) (2013) e81051.
- [67] D. Ye, K.A. Dawson, I. Lynch, A TEM protocol for quality assurance of in vitro cellular barrier models and its application to the assessment of nanoparticle transport mechanisms across barriers, *Analyst* 140(1) (2015) 83-97.
- [68] A. Gebert, H.-J. Rothkötter, R. Pabst, M cells in Peyer's patches of the intestine, *International review of cytology*, Elsevier 1996, pp. 91-159.
- [69] N.A. Mabbott, D.S. Donaldson, H. Ohno, I.R. Williams, A. Mahajan, Microfold (M) cells: important immunosurveillance posts in the intestinal epithelium, *Mucosal immunology* 6(4) (2013) 666.
- [70] A. Frey, K.T. Giannasca, R. Weltzin, P.J. Giannasca, H. Reggio, W.I. Lencer, M.R. Neutra, Role of the glycocalyx in regulating access of microparticles to apical plasma membranes of intestinal epithelial cells: implications for microbial attachment and oral vaccine targeting, *Journal of Experimental Medicine* 184(3) (1996) 1045-1059.
- [71] A. Gebert, I. Steinmetz, S. Fassbender, K.-H. Wendlandt, Antigen transport into Peyer's patches: increased uptake by constant numbers of M cells, *The American journal of pathology* 164(1) (2004) 65-72.
- [72] V. Fievez, L. Plapied, A. des Rieux, V. Pourcelle, H. Freichels, V. Wascotte, M.-L. Vanderhaeghen, C. Jérôme, A. Vanderplasschen, J. Marchand-Brynaert, Targeting nanoparticles to M cells with non-peptidic ligands for oral vaccination, *European Journal of Pharmaceutics and Biopharmaceutics* 73(1) (2009) 16-24.
- [73] J. Kunisawa, Y. Kurashima, H. Kiyono, Gut-associated lymphoid tissues for the development of oral vaccines, *Advanced drug delivery reviews* 64(6) (2012) 523-530.

- [74] N.N. Parayath, H. Nehoff, P. Müller, S. Taurin, K. Greish, Styrene maleic acid micelles as a nanocarrier system for oral anticancer drug delivery—dual uptake through enterocytes and M-cells, *International journal of nanomedicine* 10 (2015) 4653.
- [75] M.A. Clark, B.H. Hirst, M.A. Jepson, Lectin-mediated mucosal delivery of drugs and microparticles, *Advanced drug delivery reviews* 43(2-3) (2000) 207-223.
- [76] M. Garinot, V. Fiévez, V. Pourcelle, F. Stoffelbach, A. des Rieux, L. Plapied, I. Theate, H. Freichels, C. Jérôme, J. Marchand-Brynaert, PEGylated PLGA-based nanoparticles targeting M cells for oral vaccination, *Journal of Controlled Release* 120(3) (2007) 195-204.
- [77] J. Panyam, V. Labhasetwar, Dynamics of endocytosis and exocytosis of poly(D,L-lactide-co-glycolide) nanoparticles in vascular smooth muscle cells, *Pharm Res* 20(2) (2003) 212-20.
- [78] B.D. Chithrani, W.C. Chan, Elucidating the mechanism of cellular uptake and removal of protein-coated gold nanoparticles of different sizes and shapes, *Nano Lett* 7(6) (2007) 1542-50.
- [79] R.E. Serda, A. Mack, A.L. van de Ven, S. Ferrati, K. Dunner, Jr., B. Godin, C. Chiappini, M. Landry, L. Brousseau, X. Liu, A.J. Bean, M. Ferrari, Logic-embedded vectors for intracellular partitioning, endosomal escape, and exocytosis of nanoparticles, *Small* 6(23) (2010) 2691-700.
- [80] N. Oh, J.H. Park, Surface chemistry of gold nanoparticles mediates their exocytosis in macrophages, *ACS Nano* 8(6) (2014) 6232-41.
- [81] Z. Wang, C. Tiruppathi, J. Cho, R.D. Minshall, A.B. Malik, Delivery of nanoparticle: complexed drugs across the vascular endothelial barrier via caveolae, *IUBMB Life* 63(8) (2011) 659-67.
- [82] R. Sakhtianchi, R.F. Minchin, K.B. Lee, A.M. Alkilany, V. Serpooshan, M. Mahmoudi, Exocytosis of nanoparticles from cells: role in cellular retention and toxicity, *Adv Colloid Interface Sci* 201-202 (2013) 18-29.

- [83] J.V. Gerasimenko, O.V. Gerasimenko, O.H. Petersen, Membrane repair: Ca(2+)-elicited lysosomal exocytosis, *Curr Biol* 11(23) (2001) R971-4.
- [84] R.E. Yanes, D. Tarn, A.A. Hwang, D.P. Ferris, S.P. Sherman, C.R. Thomas, J. Lu, A.D. Pyle, J.I. Zink, F. Tamanoi, Involvement of lysosomal exocytosis in the excretion of mesoporous silica nanoparticles and enhancement of the drug delivery effect by exocytosis inhibition, *Small* 9(5) (2013) 697-704.
- [85] M.N. Cordonnier, D. Dauzonne, D. Louvard, E. Coudrier, Actin filaments and myosin I alpha cooperate with microtubules for the movement of lysosomes, *Mol Biol Cell* 12(12) (2001) 4013-29.
- [86] Z. Chu, Y. Huang, Q. Tao, Q. Li, Cellular uptake, evolution, and excretion of silica nanoparticles in human cells, *Nanoscale* 3(8) (2011) 3291-9.
- [87] S. Ferrati, A. Mack, C. Chiappini, X. Liu, A.J. Bean, M. Ferrari, R.E. Serda, Intracellular trafficking of silicon particles and logic-embedded vectors, *Nanoscale* 2(8) (2010) 1512-20.
- [88] C. Salaun, D.J. James, L.H. Chamberlain, Lipid rafts and the regulation of exocytosis, *Traffic* 5(4) (2004) 255-64.
- [89] C.Y. Dombu, M. Kroubi, R. Zibouche, R. Matran, D. Betbeder, Characterization of endocytosis and exocytosis of cationic nanoparticles in airway epithelium cells, *Nanotechnology* 21(35) (2010) 355102.
- [90] M. Oheim, F. Kirchhoff, W. Stuhmer, Calcium microdomains in regulated exocytosis, *Cell Calcium* 40(5-6) (2006) 423-39.
- [91] R. Chen, G. Huang, P.C. Ke, Calcium-enhanced exocytosis of gold nanoparticles, *Applied Physics Letters* 97(9) (2010) 093706.
- [92] Y. Cui, W. Shan, R. Zhou, M. Liu, L. Wu, Q. Guo, Y. Zheng, J. Wu, Y. Huang, The combination of endolysosomal escape and basolateral stimulation to overcome the

difficulties of “easy uptake hard transcytosis” of ligand-modified nanoparticles in oral drug delivery, *Nanoscale* (2018).

[93] C. Qian, X. Cao, Dendritic cells in the regulation of immunity and inflammation, *Seminars in immunology*, Elsevier, 2017.

[94] P. Langerhans, Über die Nerven der menschlichen Haut, *Archiv für pathologische Anatomie und Physiologie und für klinische Medizin* 44(2-3) (1868) 325-337.

[95] R.M. Steinman, Z.A. Cohn, Identification of a novel cell type in peripheral lymphoid organs of mice: I. Morphology, quantitation, tissue distribution, *Journal of Experimental Medicine* 137(5) (1973) 1142-1162.

[96] R.M. Steinman, Z.A. Cohn, Identification of a novel cell type in peripheral lymphoid organs of mice: II. Functional properties in vitro, *Journal of Experimental Medicine* 139(2) (1974) 380-397.

[97] B.U. Schraml, C.R. e Sousa, Defining dendritic cells, *Current opinion in immunology* 32 (2015) 13-20.

[98] C.R. e Sousa, Harnessing dendritic cells, *Seminars in Immunology*, Academic Press, 2011, p. 1.

[99] K. Palucka, J. Banchereau, Cancer immunotherapy via dendritic cells, *Nature Reviews Cancer* 12(4) (2012) 265.

[100] R.L. Sabado, N. Bhardwaj, Cancer immunotherapy: dendritic-cell vaccines on the move, *Nature* 519(7543) (2015) 300.

[101] M. Timmerman, John M, M. Levy, Ronald, Dendritic cell vaccines for cancer immunotherapy, *Annual review of medicine* 50(1) (1999) 507-529.

[102] L.J. Cruz, P.J. Tacken, F. Rueda, J.C. Domingo, F. Albericio, C.G. Figdor, Targeting nanoparticles to dendritic cells for immunotherapy, *Methods in enzymology*, Elsevier 2012, pp. 143-163.

- [103] J. Sarkander, S. Hojyo, K. Tokoyoda, Vaccination to gain humoral immune memory, *Clinical & translational immunology* 5(12) (2016).
- [104] B. Pulendran, R. Ahmed, Immunological mechanisms of vaccination, *Nature immunology* 12(6) (2011) 509.
- [105] C. Ogawa, Y.-J. Liu, K. S Kobayashi, Muramyl dipeptide and its derivatives: peptide adjuvant in immunological disorders and cancer therapy, *Current bioactive compounds* 7(3) (2011) 180-197.
- [106] C.B. Fox, R.M. Kramer, L. Barnes V, Q.M. Dowling, T.S. Vedvick, Working together: interactions between vaccine antigens and adjuvants, *Therapeutic advances in vaccines* 1(1) (2013) 7-20.
- [107] L. Yang, W. Li, M. Kirberger, W. Liao, J. Ren, Design of nanomaterial based systems for novel vaccine development, *Biomaterials science* 4(5) (2016) 785-802.
- [108] M. Igartua, J.L. Pedraz, Topical resiquimod: a promising adjuvant for vaccine development?, *Expert review of vaccines* 9(1) (2010) 23-27.
- [109] J.J. Wu, D.B. Huang, S.K. Tying, Resiquimod: a new immune response modifier with potential as a vaccine adjuvant for Th1 immune responses, *Antiviral research* 64(2) (2004) 79-83.
- [110] A.M. Maxam, W. Gilbert, A new method for sequencing DNA, *Proceedings of the National Academy of Sciences* 74(2) (1977) 560-564.
- [111] F. Sanger, S. Nicklen, A.R. Coulson, DNA sequencing with chain-terminating inhibitors, *Proceedings of the national academy of sciences* 74(12) (1977) 5463-5467.
- [112] E.C. Strauss, J.A. Kabori, G. Siu, L.E. Hood, Specific-primer-directed DNA sequencing, *Analytical biochemistry* 154(1) (1986) 353-360.
- [113] T. Hunkapiller, R. Kaiser, B. Koop, L. Hood, Large-scale and automated DNA sequence determination, *Science* 254(5028) (1991) 59-67.

- [114] J.C. Venter, M.D. Adams, E.W. Myers, P.W. Li, R.J. Mural, G.G. Sutton, H.O. Smith, M. Yandell, C.A. Evans, R.A. Holt, The sequence of the human genome, *science* 291(5507) (2001) 1304-1351.
- [115] K.V. Voelkerding, S.A. Dames, J.D. Durtschi, Next-generation sequencing: from basic research to diagnostics, *Clinical chemistry* 55(4) (2009) 641-658.
- [116] E.D. Hyman, A new method of sequencing DNA, *Analytical biochemistry* 174(2) (1988) 423-436.
- [117] P. Nyrén, Enzymatic method for continuous monitoring of DNA polymerase activity, *Analytical biochemistry* 167(2) (1987) 235-238.
- [118] M. Margulies, M. Egholm, W.E. Altman, S. Attiya, J.S. Bader, L.A. Bemben, J. Berka, M.S. Braverman, Y.-J. Chen, Z. Chen, Genome sequencing in microfabricated high-density picolitre reactors, *Nature* 437(7057) (2005) 376.
- [119] J. Shendure, G.J. Porreca, N.B. Reppas, X. Lin, J.P. McCutcheon, A.M. Rosenbaum, M.D. Wang, K. Zhang, R.D. Mitra, G.M. Church, Accurate multiplex polony sequencing of an evolved bacterial genome, *Science* 309(5741) (2005) 1728-1732.
- [120] J. Eid, A. Fehr, J. Gray, K. Luong, J. Lyle, G. Otto, P. Peluso, D. Rank, P. Baybayan, B. Bettman, Real-time DNA sequencing from single polymerase molecules, *Science* 323(5910) (2009) 133-138.
- [121] D. Branton, D.W. Deamer, A. Marziali, H. Bayley, S.A. Benner, T. Butler, M. Di Ventra, S. Garaj, A. Hibbs, X. Huang, The potential and challenges of nanopore sequencing, *Nature biotechnology* 26(10) (2008) 1146.
- [122] F. Ozsolak, Third-generation sequencing techniques and applications to drug discovery, *Expert opinion on drug discovery* 7(3) (2012) 231-243.
- [123] D.A. Wheeler, M. Srinivasan, M. Egholm, Y. Shen, L. Chen, A. McGuire, W. He, Y.-J. Chen, V. Makhijani, G.T. Roth, The complete genome of an individual by massively parallel DNA sequencing, *nature* 452(7189) (2008) 872.

- [124] E.R. Mardis, Anticipating the \$1,000 genome, *Genome biology* 7(7) (2006) 112.
- [125] C. Sheridan, Illumina claims \$1,000 genome win, Nature Publishing Group, 2014.
- [126] M. Watson, Illuminating the future of DNA sequencing, *Genome biology* 15(2) (2014) 108.
- [127] <https://www.genome.gov/sequencingcostsdata/>, (2017).
- [128] <https://www.illumina.com/science/technology/next-generation-sequencing/paired-end-vs-single-read-sequencing.html>.
- [129] A. Mortazavi, B.A. Williams, K. McCue, L. Schaeffer, B. Wold, Mapping and quantifying mammalian transcriptomes by RNA-Seq, *Nature methods* 5(7) (2008) 621.
- [130] R.D. Morin, M. Bainbridge, A. Fejes, M. Hirst, M. Krzywinski, T.J. Pugh, H. McDonald, R. Varhol, S.J. Jones, M.A. Marra, Profiling the HeLa S3 transcriptome using randomly primed cDNA and massively parallel short-read sequencing, *Biotechniques* 45(1) (2008) 81.
- [131] E.T. Wang, R. Sandberg, S. Luo, I. Khrebtkova, L. Zhang, C. Mayr, S.F. Kingsmore, G.P. Schroth, C.B. Burge, Alternative isoform regulation in human tissue transcriptomes, *Nature* 456(7221) (2008) 470.
- [132] J.H. Bahn, J.-H. Lee, G. Li, C. Greer, G. Peng, X. Xiao, Accurate identification of A-to-I RNA editing in human by transcriptome sequencing, *Genome research* 22(1) (2012) 142-150.
- [133] A.D. Radford, D. Chapman, L. Dixon, J. Chantrey, A.C. Darby, N. Hall, Application of next-generation sequencing technologies in virology, *Journal of General Virology* 93(9) (2012) 1853-1868.
- [134] E.M. Quinn, P. Cormican, E.M. Kenny, M. Hill, R. Anney, M. Gill, A.P. Corvin, D.W. Morris, Development of strategies for SNP detection in RNA-seq data: application to lymphoblastoid cell lines and evaluation using 1000 Genomes data, *PloS one* 8(3) (2013) e58815.

-
- [135] A. Oshlack, M.D. Robinson, M.D. Young, From RNA-seq reads to differential expression results, *Genome biology* 11(12) (2010) 220.
- [136] C. Trapnell, A. Roberts, L. Goff, G. Pertea, D. Kim, D.R. Kelley, H. Pimentel, S.L. Salzberg, J.L. Rinn, L. Pachter, Differential gene and transcript expression analysis of RNA-seq experiments with TopHat and Cufflinks, *Nature protocols* 7(3) (2012) 562.
- [137] M. Griffith, J.R. Walker, N.C. Spies, B.J. Ainscough, O.L. Griffith, Informatics for RNA sequencing: a web resource for analysis on the cloud, *PLoS computational biology* 11(8) (2015) e1004393.
- [138] L.-F. Blume, M. Denker, F. Gieseler, T. Kunze, Temperature corrected transepithelial electrical resistance (TEER) measurement to quantify rapid changes in paracellular permeability, *Die Pharmazie-An International Journal of Pharmaceutical Sciences* 65(1) (2010) 19-24.
- [139] J. Schindelin, I. Arganda-Carreras, E. Frise, V. Kaynig, M. Longair, T. Pietzsch, S. Preibisch, C. Rueden, S. Saalfeld, B. Schmid, Fiji: an open-source platform for biological-image analysis, *Nature methods* 9(7) (2012) 676-682.
- [140] K. McDonald, B.M. Cavalier, *Handbook of Cryo-Preparation Methods for Electron Microscopy*, *Microscopy and Microanalysis* 15(5) (2009) 469.
- [141] J. Fölling, M. Bossi, H. Bock, R. Medda, C.A. Wurm, B. Hein, S. Jakobs, C. Eggeling, S.W. Hell, Fluorescence nanoscopy by ground-state depletion and single-molecule return, *Nature methods* 5(11) (2008) 943-945.
- [142] M. Ovesný, P. Křížek, J. Borkovec, Z. Švindrych, G.M. Hagen, ThunderSTORM: a comprehensive ImageJ plug-in for PALM and STORM data analysis and super-resolution imaging, *Bioinformatics* 30(16) (2014) 2389-2390.
- [143] F. Huang, S.L. Schwartz, J.M. Byars, K.A. Lidke, Simultaneous multiple-emitter fitting for single molecule super-resolution imaging, *Biomedical optics express* 2(5) (2011) 1377-1393.

- [144] C.S. Smith, N. Joseph, B. Rieger, K.A. Lidke, Fast, single-molecule localization that achieves theoretically minimum uncertainty, *Nature methods* 7(5) (2010) 373-375.
- [145] A. Muñoz, T. Blu, M. Unser, Least-squares image resizing using finite differences, *IEEE Transactions on Image Processing* 10(9) (2001) 1365-1378.
- [146] K.J. Livak, T.D. Schmittgen, Analysis of relative gene expression data using real-time quantitative PCR and the $2^{-\Delta\Delta CT}$ method, *methods* 25(4) (2001) 402-408.
- [147] P. Artursson, K. Palm, K. Luthman, Caco-2 monolayers in experimental and theoretical predictions of drug transport¹, *Advanced drug delivery reviews* 46(1-3) (2001) 27-43.
- [148] I.J. Hidalgo, T.J. Raub, R.T. Borchardt, Characterization of the human colon carcinoma cell line (Caco-2) as a model system for intestinal epithelial permeability, *Gastroenterology* 96(3) (1989) 736-749.
- [149] B. Srinivasan, A.R. Kolli, M.B. Esch, H.E. Abaci, M.L. Shuler, J.J. Hickman, TEER measurement techniques for in vitro barrier model systems, *Journal of laboratory automation* 20(2) (2015) 107-126.
- [150] A.F. Kotzé, H.L. Lueßen, B.J. de Leeuw, J.C. Verhoef, H.E. Junginger, Comparison of the effect of different chitosan salts and N-trimethyl chitosan chloride on the permeability of intestinal epithelial cells (Caco-2), *Journal of controlled release* 51(1) (1998) 35-46.
- [151] B. Wahlang, Y.B. Pawar, A.K. Bansal, Identification of permeability-related hurdles in oral delivery of curcumin using the Caco-2 cell model, *European Journal of Pharmaceutics and Biopharmaceutics* 77(2) (2011) 275-282.
- [152] F. Ingels, B. Beck, M. Oth, P. Augustijns, Effect of simulated intestinal fluid on drug permeability estimation across Caco-2 monolayers, *International journal of pharmaceutics* 274(1-2) (2004) 221-232.

- [153] K. Yunomae, H. Arima, F. Hirayama, K. Uekama, Involvement of cholesterol in the inhibitory effect of dimethyl- β -cyclodextrin on P-glycoprotein and MRP2 function in Caco-2 cells, *FEBS letters* 536(1-3) (2003) 225-231.
- [154] I.J. Hidalgo, R.T. Borchardt, Transport of bile acids in a human intestinal epithelial cell line, Caco-2, *Biochimica et Biophysica Acta (BBA)-General Subjects* 1035(1) (1990) 97-103.
- [155] Y. Mine, J.W. Zhang, Surfactants enhance the tight-junction permeability of food allergens in human intestinal epithelial Caco-2 cells, *International archives of allergy and immunology* 130(2) (2003) 135-142.
- [156] S. Lu, A.W. Gough, W.F. Bobrowski, B.H. Stewart, Transport properties are not altered across Caco-2 cells with heightened TEER despite underlying physiological and ultrastructural changes, *Journal of pharmaceutical sciences* 85(3) (1996) 270-273.
- [157] S.W. Shin, I.H. Song, S.H. Um, Role of physicochemical properties in nanoparticle toxicity, *Nanomaterials* 5(3) (2015) 1351-1365.
- [158] J.M. Siebert, D. Baumann, A. Zeller, V. Mailänder, K. Landfester, Synthesis of Polyester Nanoparticles in Miniemulsion Obtained by Radical Ring-Opening of BMDO and Their Potential as Biodegradable Drug Carriers, *Macromolecular bioscience* 12(2) (2012) 165-175.
- [159] S. Lerch, Uptake mechanism, intracellular trafficking and endo-isosomal pH monitoring of polystyrene nanoparticles, Johannes Gutenberg-Universität Mainz, 2011.
- [160] A. Musyanovych, J. Schmitz-Wienke, V. Mailänder, P. Walther, K. Landfester, Preparation of biodegradable polymer nanoparticles by miniemulsion technique and their cell interactions, *Macromolecular bioscience* 8(2) (2008) 127-139.
- [161] V. Mailänder, K. Landfester, Interaction of nanoparticles with cells, *Biomacromolecules* 10(9) (2009) 2379-2400.

- [162] G. Baier, A. Baki, S. Tomcin, V. Mailänder, E. Alexandrino, F. Wurm, K. Landfester, Stabilization of Nanoparticles Synthesized by Miniemulsion Polymerization Using “Green” Amino-Acid Based Surfactants, *Macromolecular Symposia*, Wiley Online Library, 2014, pp. 9-17.
- [163] A. Salvati, I. Nelissen, A. Haase, C. Åberg, S. Moya, A. Jacobs, F. Alnasser, T. Bewersdorff, S. Deville, A. Luch, Quantitative measurement of nanoparticle uptake by flow cytometry illustrated by an interlaboratory comparison of the uptake of labelled polystyrene nanoparticles, *NanoImpact* 9 (2018) 42-50.
- [164] M. Pekker, M. Shneider, The surface charge of a cell lipid membrane, *arXiv preprint arXiv:1401.4707* (2014).
- [165] N.M. Goldenberg, B.E. Steinberg, Surface charge: a key determinant of protein localization and function, *Cancer research* 70(4) (2010) 1277-1280.
- [166] H. Chang, A. Ikram, F. Kosari, G. Vasmatzis, A. Bhunia, R. Bashir, Electrical characterization of micro-organisms using microfabricated devices, *Journal of Vacuum Science & Technology B: Microelectronics and Nanometer Structures Processing, Measurement, and Phenomena* 20(5) (2002) 2058-2064.
- [167] E. Fröhlich, The role of surface charge in cellular uptake and cytotoxicity of medical nanoparticles, *International journal of nanomedicine* 7 (2012) 5577.
- [168] X. Jiang, A. Musyanovych, C. Röcker, K. Landfester, V. Mailänder, G.U. Nienhaus, Specific effects of surface carboxyl groups on anionic polystyrene particles in their interactions with mesenchymal stem cells, *Nanoscale* 3(5) (2011) 2028-2035.
- [169] D.L. Thorek, A. Tsourkas, Size, charge and concentration dependent uptake of iron oxide particles by non-phagocytic cells, *Biomaterials* 29(26) (2008) 3583-3590.
- [170] A. Villanueva, M. Canete, A.G. Roca, M. Calero, S. Veintemillas-Verdaguer, C.J. Serna, M. del Puerto Morales, R. Miranda, The influence of surface functionalization on the enhanced internalization of magnetic nanoparticles in cancer cells, *Nanotechnology* 20(11) (2009) 115103.

- [171] M. Kokkinopoulou, J. Simon, K. Landfester, V. Mailänder, I. Lieberwirth, Visualization of the protein corona: towards a biomolecular understanding of nanoparticle-cell-interactions, *Nanoscale* 9(25) (2017) 8858-8870.
- [172] H. Otsuka, Y. Nagasaki, K. Kataoka, PEGylated nanoparticles for biological and pharmaceutical applications, *Advanced drug delivery reviews* 64 (2012) 246-255.
- [173] S. Schöttler, K. Landfester, V. Mailänder, Controlling the stealth effect of nanocarriers through understanding the protein corona, *Angewandte Chemie International Edition* 55(31) (2016) 8806-8815.
- [174] Z. Amoozgar, Y. Yeo, Recent advances in stealth coating of nanoparticle drug delivery systems, *Wiley Interdisciplinary Reviews: Nanomedicine and Nanobiotechnology* 4(2) (2012) 219-233.
- [175] S. Behzadi, V. Serpooshan, W. Tao, M.A. Hamaly, M.Y. Alkawareek, E.C. Dreaden, D. Brown, A.M. Alkilany, O.C. Farokhzad, M. Mahmoudi, Cellular uptake of nanoparticles: journey inside the cell, *Chemical Society Reviews* 46(14) (2017) 4218-4244.
- [176] A. Albanese, W.C. Chan, Effect of gold nanoparticle aggregation on cell uptake and toxicity, *ACS nano* 5(7) (2011) 5478-5489.
- [177] J. Fallingborg, Intraluminal pH of the human gastrointestinal tract, *Danish medical bulletin* 46(3) (1999) 183-196.
- [178] S. Yamashita, T. Furubayashi, M. Kataoka, T. Sakane, H. Sezaki, H. Tokuda, Optimized conditions for prediction of intestinal drug permeability using Caco-2 cells, *European journal of pharmaceutical sciences* 10(3) (2000) 195-204.
- [179] D. Bartczak, A.G. Kanaras, Preparation of peptide-functionalized gold nanoparticles using one pot EDC/sulfo-NHS coupling, *Langmuir* 27(16) (2011) 10119-10123.
- [180] A. Salvati, A.S. Pitek, M.P. Monopoli, K. Prapainop, F.B. Bombelli, D.R. Hristov, P.M. Kelly, C. Åberg, E. Mahon, K.A. Dawson, Transferrin-functionalized nanoparticles

lose their targeting capabilities when a biomolecule corona adsorbs on the surface, *Nature nanotechnology* 8(2) (2013) 137.

[181] A. Aires, S.M. Ocampo, B.M. Simões, M.J. Rodríguez, J.F. Cadenas, P. Couleaud, K. Spence, A. Latorre, R. Miranda, Á. Somoza, Multifunctionalized iron oxide nanoparticles for selective drug delivery to CD44-positive cancer cells, *Nanotechnology* 27(6) (2016) 065103.

[182] B. Kang, P. Okwieka, S. Schöttler, S. Winzen, J. Langhanki, K. Mohr, T. Opatz, V. Mailänder, K. Landfester, F.R. Wurm, Carbohydrate-based nanocarriers exhibiting specific cell targeting with minimum influence from the protein corona, *Angewandte Chemie International Edition* 54(25) (2015) 7436-7440.

[183] P. Kocbek, N. Obermajer, M. Cegnar, J. Kos, J. Kristl, Targeting cancer cells using PLGA nanoparticles surface modified with monoclonal antibody, *Journal of controlled release* 120(1-2) (2007) 18-26.

[184] M. Tonigold, J. Simon, D. Estupinan, M. Kokkinopoulou, J. Reinholz, U. Kintzel, A. Kaltbeitzel, P. Renz, M. Domogalla, K. Steinbrink, I. Lieberwirth, D. Crespy, K. Landfester, V. Mailänder, Preadsorption of antibodies enables targeting of nanocarriers despite a biomolecular corona, *Nature Nanotechnology* (2018) DOI: 10.1038/s41565-018-0171-6.

[185] W. Choe, T.A. Durgannavar, S.J. Chung, Fc-binding ligands of immunoglobulin G: an overview of high affinity proteins and peptides, *Materials* 9(12) (2016) 994.

[186] G. Raychaudhuri, D. McCool, R. Painter, Human IgG1 and its Fc fragment bind with different affinities to the Fc receptors on the human U937, HL-60 and ML-1 cell lines, *Molecular immunology* 22(9) (1985) 1009-1019.

[187] M.J. Day, R.D. Schultz, *Veterinary immunology: principles and practice*, CRC Press 2014.

[188] R.S. Blumberg, T. Koss, C.M. Story, D. Barisani, J. Polischuk, A. Lipin, L. Pablo, R. Green, N.E. Simister, A major histocompatibility complex class I-related Fc receptor for IgG on rat hepatocytes, *The Journal of clinical investigation* 95(5) (1995) 2397-2402.

-
- [189] U. Shah, B.L. Dickinson, R.S. Blumberg, N.E. Simister, W.I. Lencer, A.W. Walker, Distribution of the IgG Fc receptor, FcRn, in the human fetal intestine, *Pediatric research* 53(2) (2003) 295.
- [190] D.C. Roopenian, S. Akilesh, FcRn: the neonatal Fc receptor comes of age, *Nature reviews immunology* 7(9) (2007) 715.
- [191] E. Israel, S. Taylor, Z. Wu, E. Mizoguchi, R. Blumberg, A. Bhan, N. Simister, Expression of the neonatal Fc receptor, FcRn, on human intestinal epithelial cells, *Immunology* 92(1) (1997) 69-74.
- [192] P.J. Hornby, P.R. Cooper, C. Kliwinski, E. Ragwan, J.R. Mabus, B. Harman, S. Thompson, A.L. Kauffman, Z. Yan, S.H. Tam, Human and non-human primate intestinal FcRn expression and immunoglobulin G transcytosis, *Pharmaceutical research* 31(4) (2014) 908-922.
- [193] B.L. Dickinson, K. Badizadegan, Z. Wu, J.C. Ahouse, X. Zhu, N.E. Simister, R.S. Blumberg, W.I. Lencer, Bidirectional FcRn-dependent IgG transport in a polarized human intestinal epithelial cell line, *The Journal of clinical investigation* 104(7) (1999) 903-911.
- [194] N.E. Simister, A.R. Rees, Isolation and characterization of an Fc receptor from neonatal rat small intestine, *European journal of immunology* 15(7) (1985) 733-738.
- [195] E.A. Jones, T.A. Waldmann, The mechanism of intestinal uptake and transcellular transport of IgG in the neonatal rat, *The Journal of clinical investigation* 51(11) (1972) 2916-2927.
- [196] R. Rodewald, pH-dependent binding of immunoglobulins to intestinal cells of the neonatal rat, *The Journal of cell biology* 71(2) (1976) 666-669.
- [197] G. Russell-Jones, L. Arthur, H. Walker, Vitamin B12-mediated transport of nanoparticles across Caco-2 cells, *International journal of pharmaceutics* 179(2) (1999) 247-255.

- [198] R. Fowler, D. Vllasaliu, F.H. Falcone, M. Garnett, B. Smith, H. Horsley, C. Alexander, S. Stolnik, Uptake and transport of B12-conjugated nanoparticles in airway epithelium, *Journal of controlled release* 172(1) (2013) 374-381.
- [199] K.B. Chalasani, G.J. Russell-Jones, A.K. Jain, P.V. Diwan, S.K. Jain, Effective oral delivery of insulin in animal models using vitamin B12-coated dextran nanoparticles, *Journal of Controlled Release* 122(2) (2007) 141-150.
- [200] B. Seetharam, Receptor-mediated endocytosis of cobalamin (vitamin B12), *Annual review of nutrition* 19(1) (1999) 173-195.
- [201] S. Bose, S. Seetharam, N.M. Dahms, B. Seetharam, Bipolar functional expression of transcobalamin II receptor in human intestinal epithelial Caco-2 cells, *Journal of Biological Chemistry* 272(6) (1997) 3538-3543.
- [202] N. Dan, D.F. Cutler, Transcytosis and processing of intrinsic factor-cobalamin in Caco-2 cells, *Journal of Biological Chemistry* 269(29) (1994) 18849-18855.
- [203] C. Dix, I. Hassan, H. O Bray, R. Shah, G. Wilson, The transport of vitamin B12 through polarized monolayers of Caco-2 cells, *Gastroenterology* 98(5) (1990) 1272-1279.
- [204] A.J. Clark, M.E. Davis, Increased brain uptake of targeted nanoparticles by adding an acid-cleavable linkage between transferrin and the nanoparticle core, *Proceedings of the National Academy of Sciences* 112(40) (2015) 12486-12491.
- [205] W. Lu, Y.-Z. Tan, K.-L. Hu, X.-G. Jiang, Cationic albumin conjugated pegylated nanoparticle with its transcytosis ability and little toxicity against blood–brain barrier, *International journal of pharmaceutics* 295(1-2) (2005) 247-260.
- [206] I. Kadiyala, Y. Loo, K. Roy, J. Rice, K.W. Leong, Transport of chitosan–DNA nanoparticles in human intestinal M-cell model versus normal intestinal enterocytes, *European Journal of Pharmaceutical Sciences* 39(1-3) (2010) 103-109.

- [207] A. des Rieux, V. Fievez, I. Théate, J. Mast, V. Pr  at, Y.-J. Schneider, An improved in vitro model of human intestinal follicle-associated epithelium to study nanoparticle transport by M cells, *European journal of pharmaceutical sciences* 30(5) (2007) 380-391.
- [208] E.G. Ragnarsson, I. Schoultz, E. Gullberg, A.H. Carlsson, F. Tafazoli, M. Lerm, K.-E. Magnusson, J.D. S  derholm, P. Artursson, *Yersinia pseudotuberculosis* induces transcytosis of nanoparticles across human intestinal villus epithelium via invasin-dependent macropinocytosis, *Laboratory Investigation* 88(11) (2008) 1215.
- [209] I. Kratzer, K. Wernig, U. Panzenboeck, E. Bernhart, H. Reicher, R. Wronski, M. Windisch, A. Hammer, E. Malle, A. Zimmer, Apolipoprotein AI coating of protamine–oligonucleotide nanoparticles increases particle uptake and transcytosis in an in vitro model of the blood–brain barrier, *Journal of Controlled Release* 117(3) (2007) 301-311.
- [210] Y.-C. Kuo, C.-Y. Chung, Transcytosis of CRM197-grafted polybutylcyanoacrylate nanoparticles for delivering zidovudine across human brain-microvascular endothelial cells, *Colloids and Surfaces B: Biointerfaces* 91 (2012) 242-249.
- [211] F. Chen, Z.-R. Zhang, F. Yuan, X. Qin, M. Wang, Y. Huang, In vitro and in vivo study of N-trimethyl chitosan nanoparticles for oral protein delivery, *International Journal of Pharmaceutics* 349(1-2) (2008) 226-233.
- [212] M.-K. Yoo, S.-K. Kang, J.-H. Choi, I.-K. Park, H.-S. Na, H.-C. Lee, E.-B. Kim, N.-K. Lee, J.-W. Nah, Y.-J. Choi, Targeted delivery of chitosan nanoparticles to Peyer’s patch using M cell-homing peptide selected by phage display technique, *Biomaterials* 31(30) (2010) 7738-7747.
- [213] J. Reinholz, C. Diesler, S. Sch  ttler, M. Kokkinopoulou, S. Ritz, K. Landfester, V. Mail  nder, Protein Machineries defining Pathways of Nanocarrier Exocytosis and Transcytosis, *Acta biomaterialia* 71 (2018) 432-443.
- [214] Y. Jallouli, A. Paillard, J. Chang, E. Sevin, D. Betbeder, Influence of surface charge and inner composition of porous nanoparticles to cross blood–brain barrier in vitro, *International journal of pharmaceutics* 344(1-2) (2007) 103-109.

- [215] T.R. Covey, E.D. Lee, A.P. Bruins, J.D. Henion, Liquid chromatography/mass spectrometry, *Analytical chemistry* 58(14) (1986) 1451A-1461A.
- [216] W.M. Niessen, *Liquid chromatography-mass spectrometry*, CRC Press 2006.
- [217] G.A. Schultz, R.R.Q. De Almeida, M.H. Allen, *Liquid chromatography-mass spectrometry*, Google Patents, 2010.
- [218] M. Lundqvist, C. Augustsson, M. Lilja, K. Lundkvist, B. Dahlbäck, S. Linse, T. Cedervall, The nanoparticle protein corona formed in human blood or human blood fractions, *PloS one* 12(4) (2017) e0175871.
- [219] B.-J.L. Van Hong Nguyen, Protein corona: A new approach for nanomedicine design, *International journal of nanomedicine* 12 (2017) 3137.
- [220] F. Pederzoli, G. Tosi, M.A. Vandelli, D. Belletti, F. Forni, B. Ruozi, Protein corona and nanoparticles: how can we investigate on?, *Wiley Interdisciplinary Reviews: Nanomedicine and Nanobiotechnology* 9(6) (2017).
- [221] B. Kharazian, N. Hadipour, M. Ejtehad, Understanding the nanoparticle–protein corona complexes using computational and experimental methods, *The international journal of biochemistry & cell biology* 75 (2016) 162-174.
- [222] K. Biemann, Mass spectrometry of peptides and proteins, *Annual review of biochemistry* 61(1) (1992) 977-1010.
- [223] V.H. Wysocki, K.A. Resing, Q. Zhang, G. Cheng, Mass spectrometry of peptides and proteins, *Methods* 35(3) (2005) 211-222.
- [224] K. Biemann, S.A. Martin, Mass spectrometric determination of the amino acid sequence of peptides and proteins, *Mass Spectrometry Reviews* 6(1) (1987) 1-75.
- [225] M. Vetter, R. Stehle, C. Basquin, E. Lorentzen, Structure of Rab11-FIP3-Rabin8 reveals simultaneous binding of FIP3 and Rabin8 effectors to Rab11, *Nature structural & molecular biology* (2015).

- [226] A.K. Rout, M.-P. Strub, G. Piszczek, N. Tjandra, Structure of transmembrane domain of lysosome-associated membrane protein type 2a (LAMP-2A) reveals key features for substrate specificity in chaperone-mediated autophagy, *Journal of Biological Chemistry* 289(51) (2014) 35111-35123.
- [227] J.G. Wittmann, M.G. Rudolph, Crystal structure of Rab9 complexed to GDP reveals a dimer with an active conformation of switch II, *FEBS Lett* 568(1-3) (2004) 23-9.
- [228] G. Zhu, J. Liu, S. Terzyan, P. Zhai, G. Li, X.C. Zhang, High resolution crystal structures of human Rab5a and five mutants with substitutions in the catalytically important phosphate-binding loop, *Journal of Biological Chemistry* 278(4) (2003) 2452-2460.
- [229] C.E. Schutt, J.C. Myslik, M.D. Rozycki, N.C. Goonesekere, U. Lindberg, The structure of crystalline profilin-beta-actin, *Nature* 365(6449) (1993) 810-6.
- [230] G.F. Von Mollard, B. Stahl, A. Khokhlatchev, T. Südhof, R. Jahn, Rab3C is a synaptic vesicle protein that dissociates from synaptic vesicles after stimulation of exocytosis, *Journal of Biological Chemistry* 269(15) (1994) 10971-10974.
- [231] P.-M. Lledo, L. Johannes, P. Vernier, R. Zorec, F. Darchen, J. Vincent, J. Henry, W.T. Mason, Rab3 proteins: key players in the control of exocytosis, *Trends in neurosciences* 17(10) (1994) 426-432.
- [232] G.F. von Mollard, B. Stahl, C. Li, T.C. Südhof, R. Jahn, Rab proteins in regulated exocytosis, *Trends in biochemical sciences* 19(4) (1994) 164-168.
- [233] Y. Zhang, Q. Gao, S. Duan, Y. He, X. Sun, R. Jiang, Y. Duan, X. Zhong, J. Ge, Upregulation of Copine1 in trabecular meshwork cells of POAG patients: a membrane proteomics approach, *Mol Vis* 14 (2008) 1028-36.
- [234] C.E. Creutz, J.L. Tomsig, S.L. Snyder, M.C. Gautier, F. Skouri, J. Beisson, J. Cohen, The copines, a novel class of C2 domain-containing, calcium-dependent, phospholipid-binding proteins conserved from Paramecium to humans, *J Biol Chem* 273(3) (1998) 1393-402.

- [235] E.M. Plummer, M. Manchester, Endocytic uptake pathways utilized by CPMV nanoparticles, *Molecular pharmaceutics* 10(1) (2012) 26-32.
- [236] L. Kou, J. Sun, Y. Zhai, Z. He, The endocytosis and intracellular fate of nanomedicines: Implication for rational design, *Asian Journal of Pharmaceutical Sciences* 8(1) (2013) 1-10.
- [237] L. Treuel, X. Jiang, G.U. Nienhaus, New views on cellular uptake and trafficking of manufactured nanoparticles, *Journal of The Royal Society Interface* 10(82) (2013) 20120939.
- [238] A. Laganowsky, E. Reading, T.M. Allison, M.B. Ulmschneider, M.T. Degiacomi, A.J. Baldwin, C.V. Robinson, Membrane proteins bind lipids selectively to modulate their structure and function, *Nature* 510(7503) (2014) 172.
- [239] N.S. Berrow, D. Alderton, R.J. Owens, The precise engineering of expression vectors using high-throughput in-fusion™ PCR cloning, *High Throughput Protein Expression and Purification*, Springer2009, pp. 75-90.
- [240] C.R. Irwin, A. Farmer, D.O. Willer, D.H. Evans, In-fusion® cloning with vaccinia virus DNA polymerase, *Vaccinia Virus and Poxvirology*, Springer2012, pp. 23-35.
- [241] J. Cline, J.C. Braman, H.H. Hogrefe, PCR fidelity of Pfu DNA polymerase and other thermostable DNA polymerases, *Nucleic acids research* 24(18) (1996) 3546-3551.
- [242] X. Wang, M. McManus, Lentivirus production, *Journal of visualized experiments: JoVE* (32) (2009).
- [243] U. Blömer, I. Gruh, H. Witschel, A. Haverich, U. Martin, Shuttle of lentiviral vectors via transplanted cells in vivo, *Gene Therapy* 12(1) (2005) 67.
- [244] K. Hrecka, M. Gierszewska, S. Srivastava, L. Kozackiewicz, S.K. Swanson, L. Florens, M.P. Washburn, J. Skowronski, Lentiviral Vpr usurps Cul4–DDB1 [VprBP] E3 ubiquitin ligase to modulate cell cycle, *Proceedings of the National Academy of Sciences* 104(28) (2007) 11778-11783.

- [245] T.I. Cornu, T. Cathomen, Targeted Genome Modifications Using Integrase-deficient Lentiviral Vectors, *Molecular Therapy* 15(12) (2007) 2107-2113.
- [246] H.E. Davis, J.R. Morgan, M.L. Yarmush, Polybrene increases retrovirus gene transfer efficiency by enhancing receptor-independent virus adsorption on target cell membranes, *Biophysical chemistry* 97(2-3) (2002) 159-172.
- [247] R. Coelen, D. Jose, J. May, The effect of hexadimethrine bromide (polybrene) on the infection of the primate retroviruses SSV 1/SSAV 1 and BaEV, *Archives of virology* 75(4) (1983) 307-311.
- [248] D. Hofmann, S. Tenzer, M.B. Bannwarth, C. Messerschmidt, S.-F. Glaser, H.r. Schild, K. Landfester, V. Mailänder, Mass spectrometry and imaging analysis of nanoparticle-containing vesicles provide a mechanistic insight into cellular trafficking, *ACS nano* 8(10) (2014) 10077-10088.
- [249] H. Stenmark, Rab GTPases as coordinators of vesicle traffic, *Nature reviews Molecular cell biology* 10(8) (2009) 513-525.
- [250] N. Oh, J.H. Park, Endocytosis and exocytosis of nanoparticles in mammalian cells, *Int J Nanomedicine* 9 Suppl 1 (2014) 51-63.
- [251] O.O. Glebov, N.A. Bright, B.J. Nichols, Flotillin-1 defines a clathrin-independent endocytic pathway in mammalian cells, *Nature cell biology* 8(1) (2006) 46-54.
- [252] M. Fukuda, Rab27 and its effectors in secretory granule exocytosis: a novel docking machinery composed of a Rab27· effector complex, *Biochemical Society Transactions* 34(5) (2006) 691-695.
- [253] B. He, W. Guo, The exocyst complex in polarized exocytosis, *Current opinion in cell biology* 21(4) (2009) 537-542.
- [254] G. Raposo, W. Stoorvogel, Extracellular vesicles: exosomes, microvesicles, and friends, *The Journal of cell biology* 200(4) (2013) 373-383.

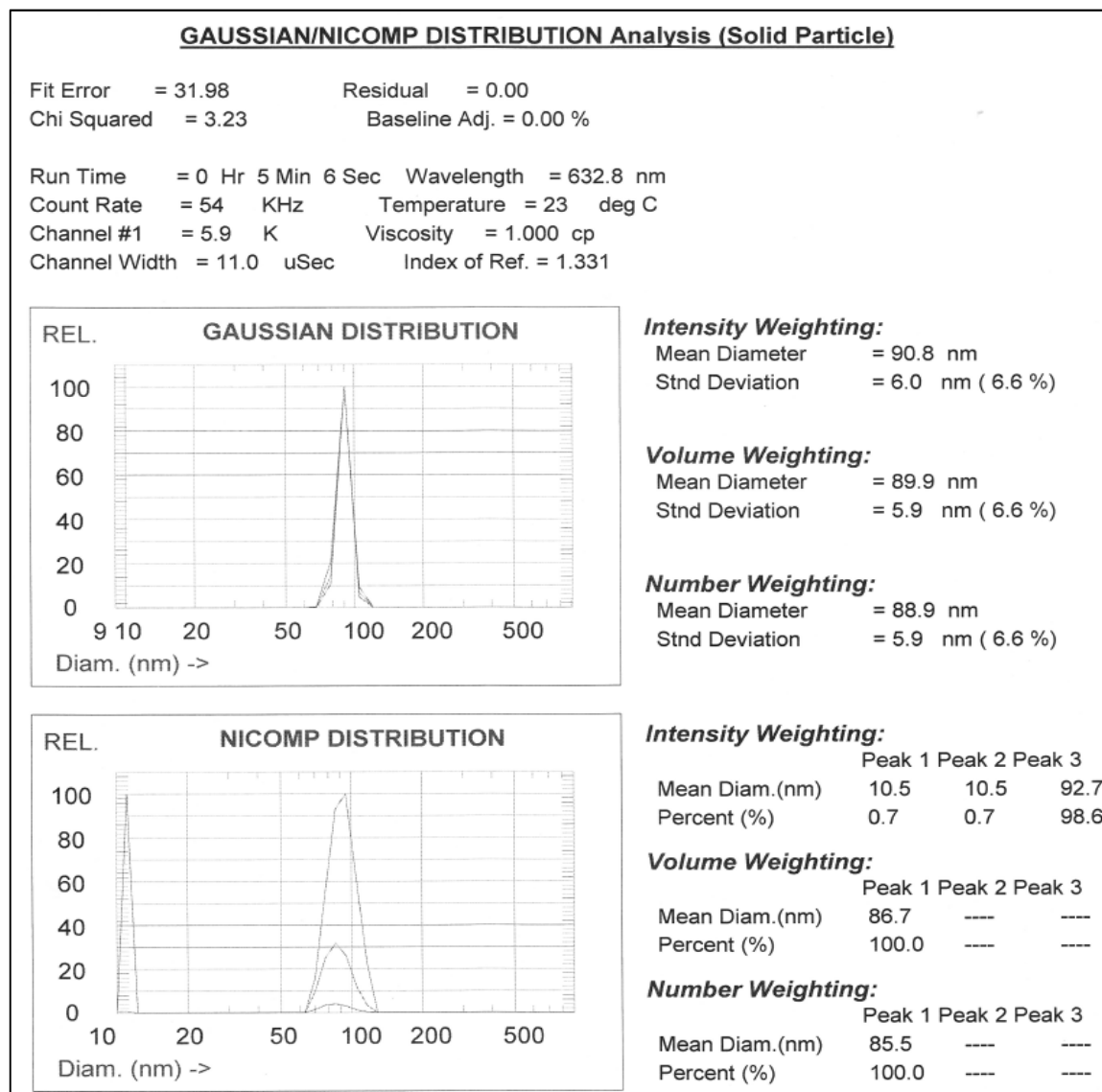
- [255] S.W. Hell, M. Kroug, Ground-state-depletion fluorescence microscopy: A concept for breaking the diffraction resolution limit, *Applied Physics B* 60(5) (1995) 495-497.
- [256] S. Chong, W. Min, X.S. Xie, Ground-state depletion microscopy: detection sensitivity of single-molecule optical absorption at room temperature, *The Journal of Physical Chemistry Letters* 1(23) (2010) 3316-3322.
- [257] S. Ferruzza, C. Rossi, M.L. Scarino, Y. Sambuy, A protocol for differentiation of human intestinal Caco-2 cells in asymmetric serum-containing medium, *Toxicology in Vitro* 26(8) (2012) 1252-1255.
- [258] J.A. Mindell, Lysosomal acidification mechanisms, *Annual review of physiology* 74 (2012) 69-86.
- [259] P. Saftig, *Lysosomes*, Springer 2005.
- [260] P. Saftig, J. Klumperman, Lysosome biogenesis and lysosomal membrane proteins: trafficking meets function, *Nature reviews Molecular cell biology* 10(9) (2009) 623-635.
- [261] C. Settembre, A. Fraldi, D.L. Medina, A. Ballabio, Signals from the lysosome: a control centre for cellular clearance and energy metabolism, *Nature reviews Molecular cell biology* 14(5) (2013) 283-296.
- [262] Y.-B. Hu, E.B. Dammer, R.-J. Ren, G. Wang, The endosomal-lysosomal system: from acidification and cargo sorting to neurodegeneration, *Translational neurodegeneration* 4(1) (2015) 18.
- [263] S. Lerch, S. Ritz, K. Bley, C. Messerschmidt, C.K. Weiss, A. Musyanovych, K. Landfester, V. Mailänder, Nanoprobng the acidification process during intracellular uptake and trafficking, *Nanomedicine: Nanotechnology, Biology and Medicine* 11(6) (2015) 1585-1596.
- [264] D. Ye, M.N. Raghnaill, M. Bramini, E. Mahon, C. Aberg, A. Salvati, K.A. Dawson, Nanoparticle accumulation and transcytosis in brain endothelial cell layers, *Nanoscale* 5(22) (2013) 11153-65.

- [265] D.F. Simon, R.F. Domingos, C. Hauser, C.M. Hutchins, W. Zerges, K.J. Wilkinson, Transcriptome sequencing (RNA-seq) analysis of the effects of metal nanoparticle exposure on the transcriptome of *Chlamydomonas reinhardtii*, *Applied and environmental microbiology* 79(16) (2013) 4774-4785.
- [266] J.K. Carrow, L.M. Cross, R.W. Reese, M.K. Jaiswal, C.A. Gregory, R. Kaunas, I. Singh, A.K. Gaharwar, Widespread changes in transcriptome profile of human mesenchymal stem cells induced by two-dimensional nanosilicates, *Proceedings of the National Academy of Sciences* 115(17) (2018) E3905-E3913.
- [267] E. Bajak, M. Fabbri, J. Ponti, S. Gioria, I. Ojea-Jiménez, A. Collotta, V. Mariani, D. Gilliland, F. Rossi, L. Gribaldo, Changes in Caco-2 cells transcriptome profiles upon exposure to gold nanoparticles, *Toxicology letters* 233(2) (2015) 187-199.
- [268] S. García-Sánchez, I. Bernales, S. Cristobal, Early response to nanoparticles in the *Arabidopsis* transcriptome compromises plant defence and root-hair development through salicylic acid signalling, *BMC genomics* 16(1) (2015) 341.
- [269] A. Schroeder, O. Mueller, S. Stocker, R. Salowsky, M. Leiber, M. Gassmann, S. Lightfoot, W. Menzel, M. Granzow, T. Ragg, The RIN: an RNA integrity number for assigning integrity values to RNA measurements, *BMC molecular biology* 7(1) (2006) 3.
- [270] https://www.genome.jp/dbget-bin/www_bget?gn:T01002.
- [271] https://www.gencodegenes.org/mouse_stats.html.
- [272] B. Alberts, A. Johnson, J. Lewis, M. Raff, K. Roberts, P. Walter, *An Overview of Gene Control*, (2002).
- [273] A. Ralston, K. Shaw, Gene expression regulates cell differentiation, *Nature education* 1(1) (2008) 127.
- [274] M. McCabe, S. Waters, D. Morris, D. Kenny, D. Lynn, C. Creevey, RNA-seq analysis of differential gene expression in liver from lactating dairy cows divergent in negative energy balance, *BMC genomics* 13(1) (2012) 193.

- [275] M. Kanehisa, The KEGG database, 'In Silico' Simulation of Biological Processes: Novartis Foundation Symposium 247, Wiley Online Library, 2008, pp. 91-103.
- [276] D.W. Huang, B.T. Sherman, R.A. Lempicki, Bioinformatics enrichment tools: paths toward the comprehensive functional analysis of large gene lists, *Nucleic acids research* 37(1) (2008) 1-13.
- [277] D.W. Huang, B.T. Sherman, R.A. Lempicki, Systematic and integrative analysis of large gene lists using DAVID bioinformatics resources, *Nature protocols* 4(1) (2008) 44.
- [278] M. Kanehisa, M. Furumichi, M. Tanabe, Y. Sato, K. Morishima, KEGG: new perspectives on genomes, pathways, diseases and drugs, *Nucleic acids research* 45(D1) (2016) D353-D361.
- [279] M. Kanehisa, Y. Sato, M. Kawashima, M. Furumichi, M. Tanabe, KEGG as a reference resource for gene and protein annotation, *Nucleic acids research* 44(D1) (2015) D457-D462.
- [280] M. Kanehisa, S. Goto, KEGG: kyoto encyclopedia of genes and genomes, *Nucleic acids research* 28(1) (2000) 27-30.

7 Supplementary data⁴

7.1 NICOMP Distribution

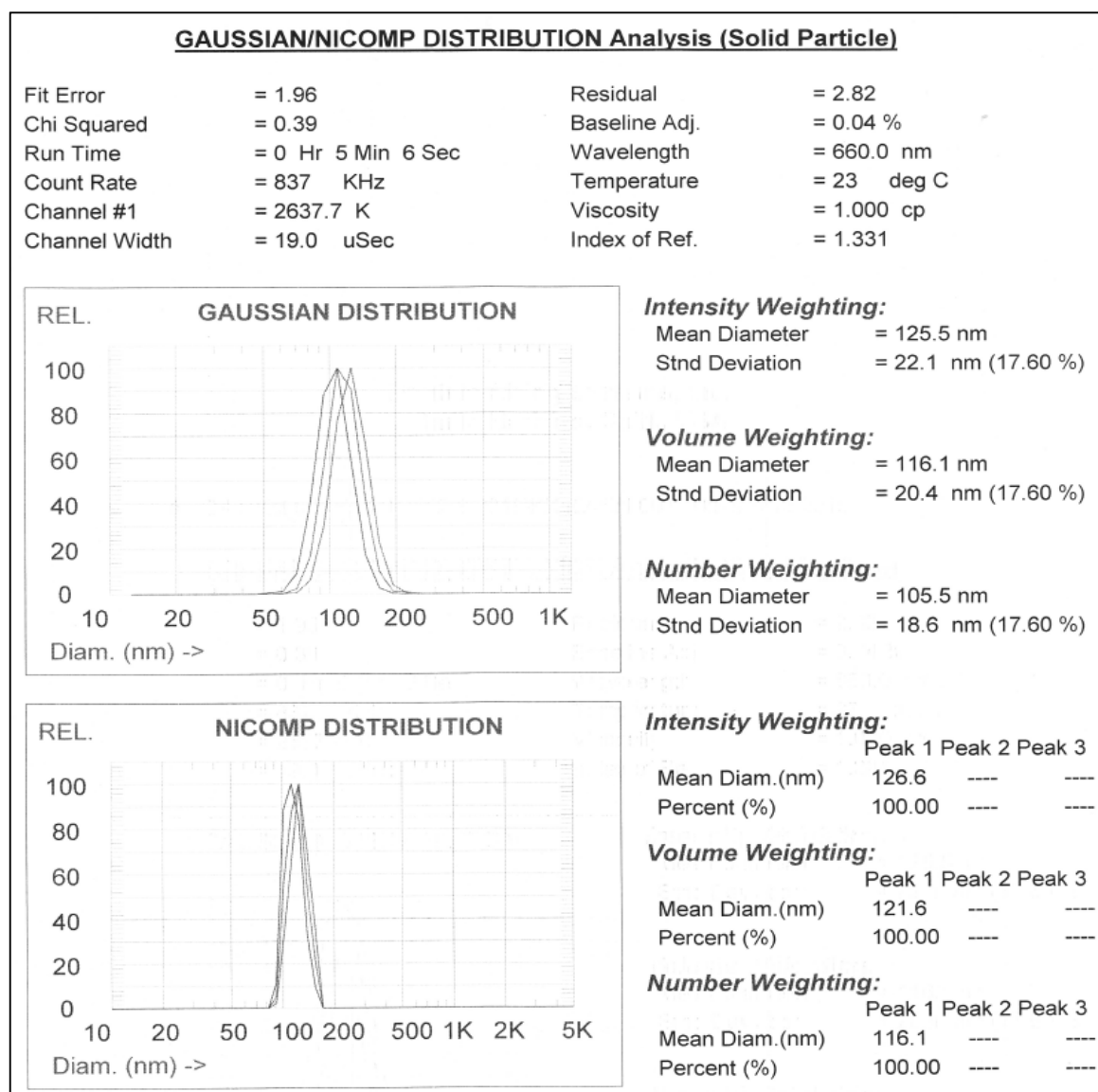


SI Fig. 1: Size distribution of PS-SDS-COOH-91.

This SDS-stabilized polystyrene nanoparticle featured a mean diameter of 91 nm (± 6) and a PDI of 0.004. Size was determined on the Nicomp 380 Submicron Particle Sizer (PSS Nicomp, USA).

⁴ Parts of the following chapter were already published and are republished in this thesis with permission of:

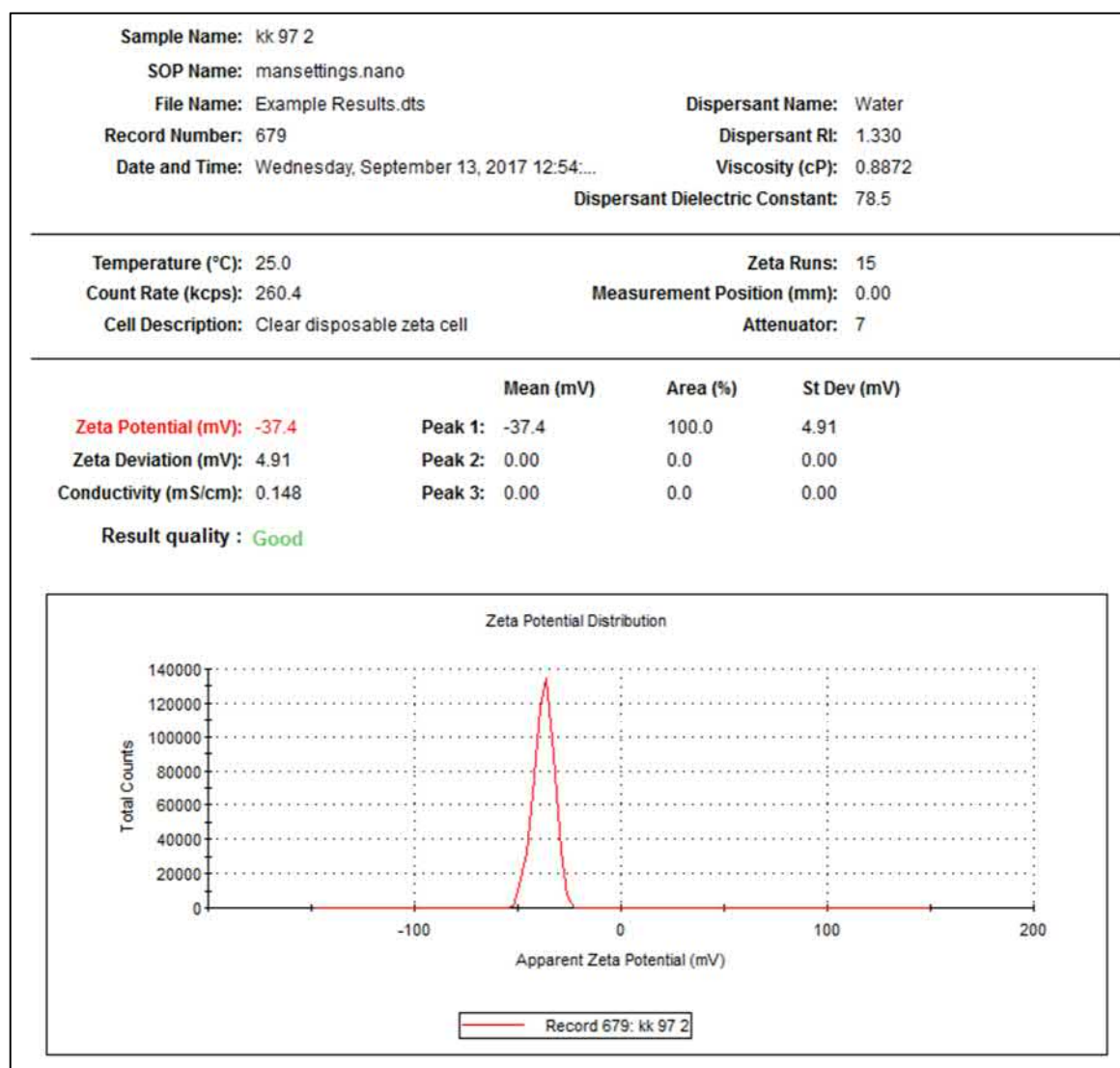
Elsevier Science and Technology Journals, *Protein machineries defining pathways of nanocarrier exocytosis and transcytosis*, Reinholz J, Diesler C, Schöttler S, Kokkinopoulou M, Ritz S, Landfester K, Mailänder V, Acta Biomaterialia 71, 2018; permission conveyed through Copyright Clearance Center, Inc.



SI Fig. 2: Size distribution of PS-SDS-COOH-127.

This SDS-stabilized polystyrene nanoparticle featured a mean diameter of 126 nm (± 22) and a PDI of 0.031. Size was determined on the Nicomp 380 Submicron Particle Sizer (PSS Nicomp, USA).

7.2 Zeta potential analysis

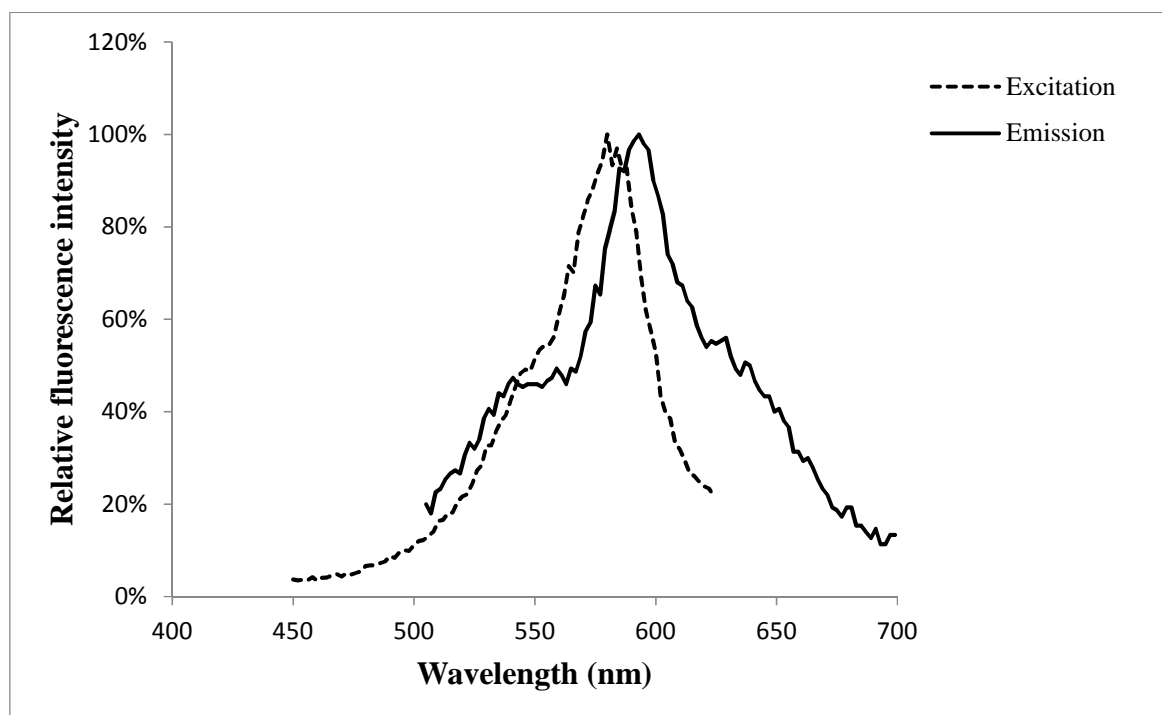


SI Fig. 3: Zeta potential of PS-SDS-COOH-148.

This figure depicts an example for a zeta potential analysis of a polystyrene nanoparticle. The zeta potential of the nanoparticle PS-SDS-COOH-148 was around -25 ± 4 , exhibiting only one major peak.

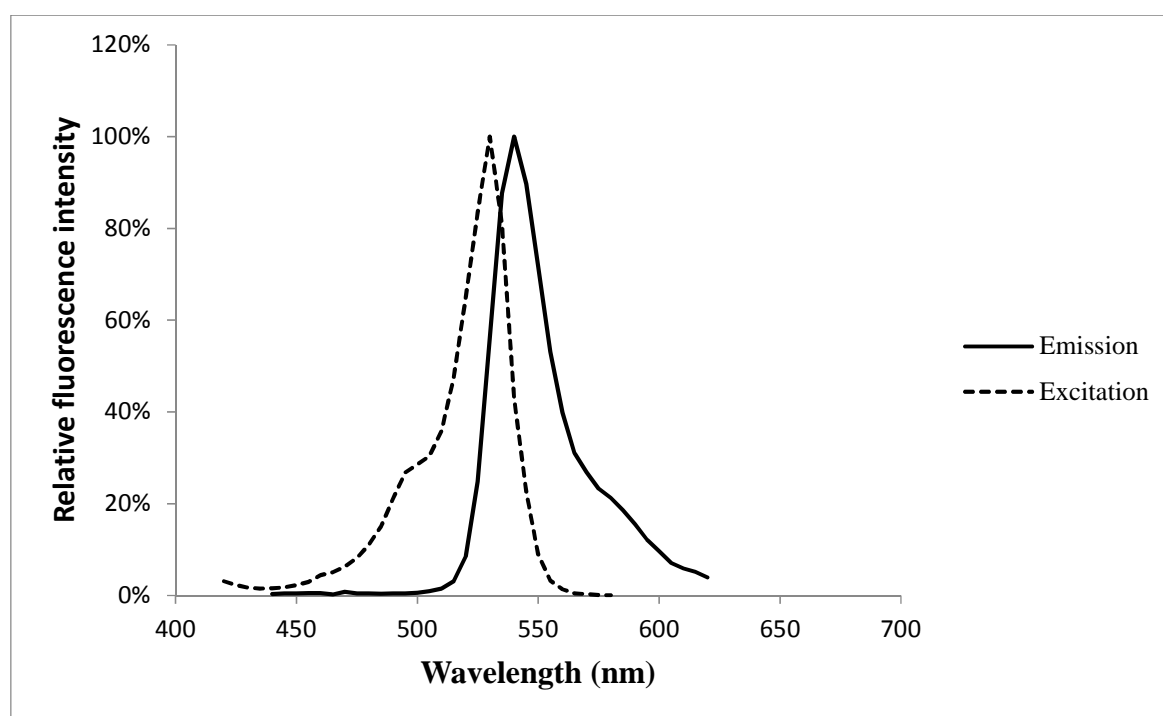
7.3 Fluorescent dyes

The fluorescence of both Bodipy dyes was determined via platereader measurement to rule out any difficulties for confocal imaging. The spectra were compared to respective spectra of eGFP and mCherry, which were obtained from the ThermoFisher Scientific Fluorescence SpectraViewer (<https://www.thermofisher.com/de/de/home/life-science/cell-analysis/labeling-chemistry/fluorescence-spectraviewer.html>).



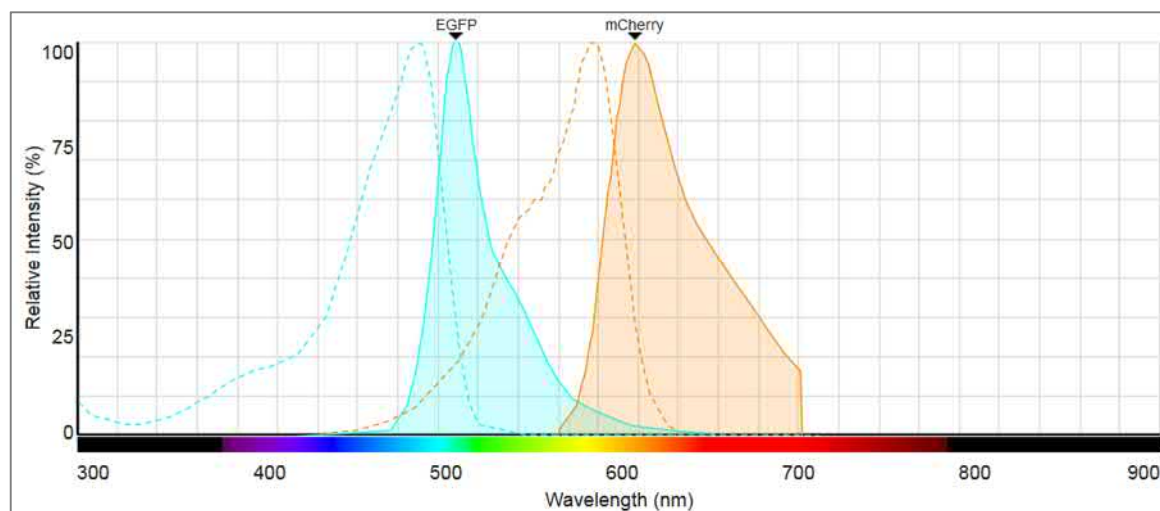
SI Fig. 4: Excitation and Emission of PS-SDS-COOH-127 (580/600).

These polystyrene nanoparticles were used for co-localization studies with GFP-tagged proteins. Fluorescence spectra were recorded via plate reader measurement.



SI Fig. 5: Excitation and Emission of PS-SDS-COOH-91 (523/536).

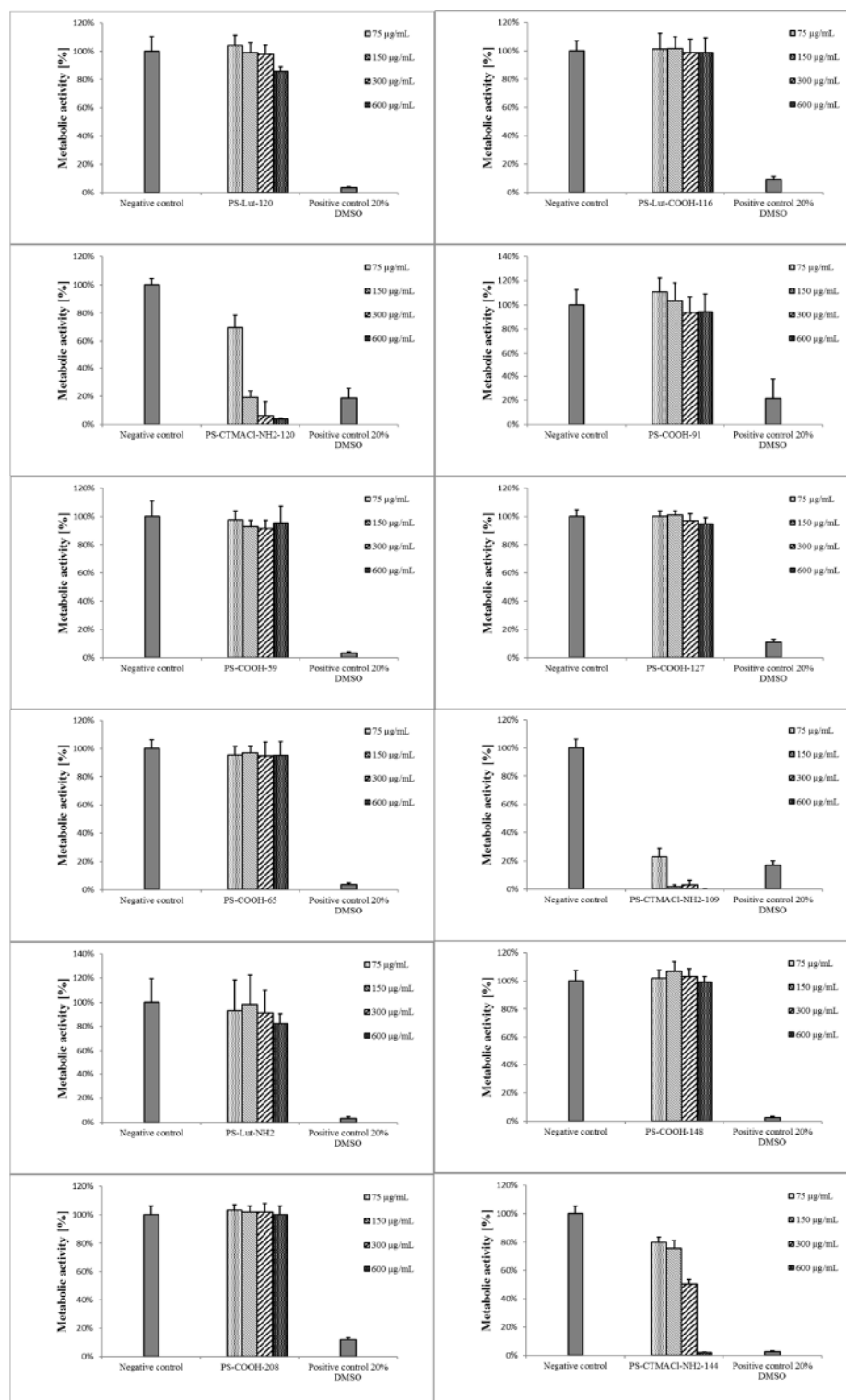
These polystyrene nanoparticles were used as a substitute nanoparticle for co-localization with double transgenic cells, since PS-SDS-COOH-127 (580/600) overlapped with the mCherry signal. Fluorescence spectra were recorded via plate reader measurement.



SI Fig. 6: Excitation and Emission of eGFP and mCherry.

Both fluorescent dyes were used for co-localization studies. Fluorescence spectra were obtained by ThermoFisher Scientific Fluorescence SpectraViewer (<https://www.thermofisher.com/de/de/home/life-science/cell-analysis/labeling-chemistry/fluorescence-spectraviewer.html>).

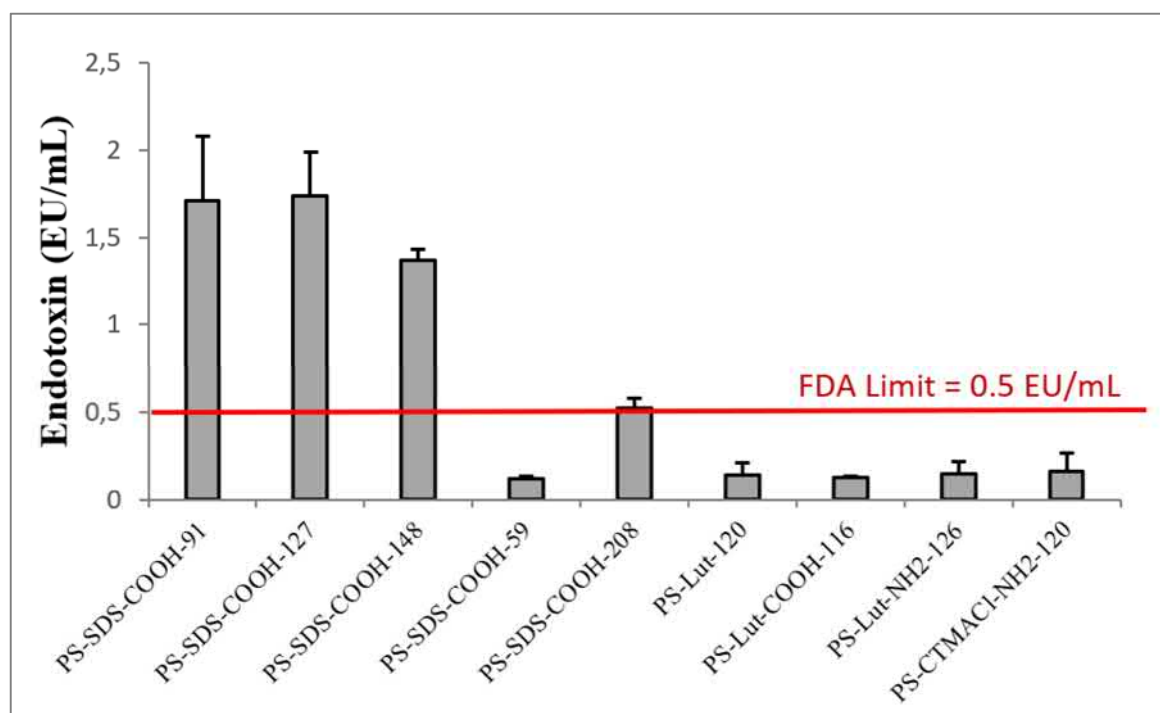
7.4 Toxicity tests



SI Fig. 7: Toxicity of different polystyrene nanoparticles.

The CellTiter 96® AQueous One Solution Cell Proliferation Assay was used according to the manufacturer's recommendations with minor modifications. Different polystyrene nanoparticles were added in concentrations ranging from 75 µg/mL to 600 µg/mL. As a positive control, a total concentration of 20% DMSO was used. Mean absorbance of untreated Caco-2 cells (negative control) was defined as 100% metabolic activity and all samples were afterwards normalized to this value.

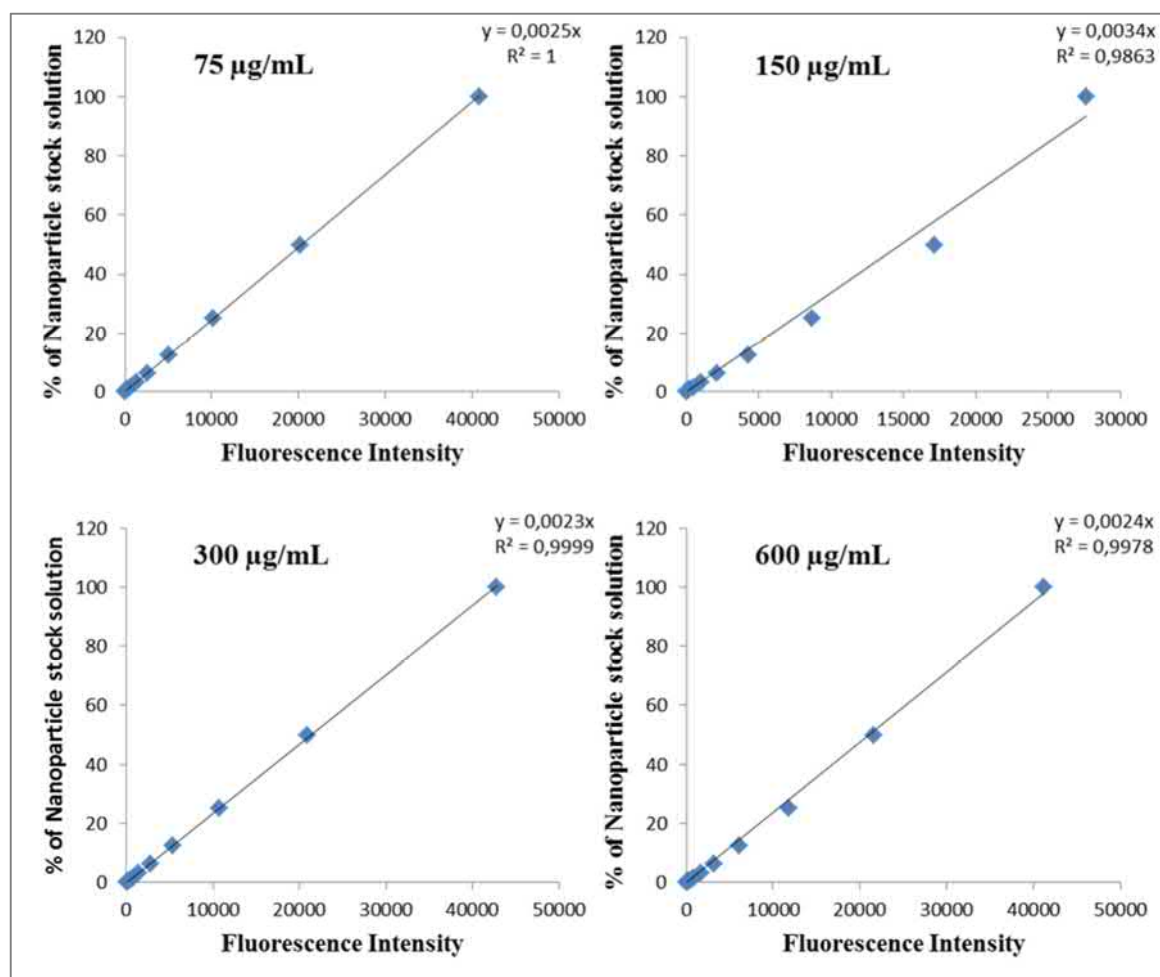
7.5 Determination of endotoxin contaminations



SI Fig. 8: Endotoxin test of different polystyrene nanoparticles.

The Pierce™ LAL Chromogenic Endotoxin Quantitation Assay was performed according to the manufacturer's recommendations. All examined polystyrene nanoparticles were tested in a concentration of 75 µg/mL. Lipopolysaccharide levels were calculated in EU (endotoxin units) / mL by using a calibration curve of pure endotoxin. The limit of 0.5 EU/mL as proposed by the FDA is marked with a red line.

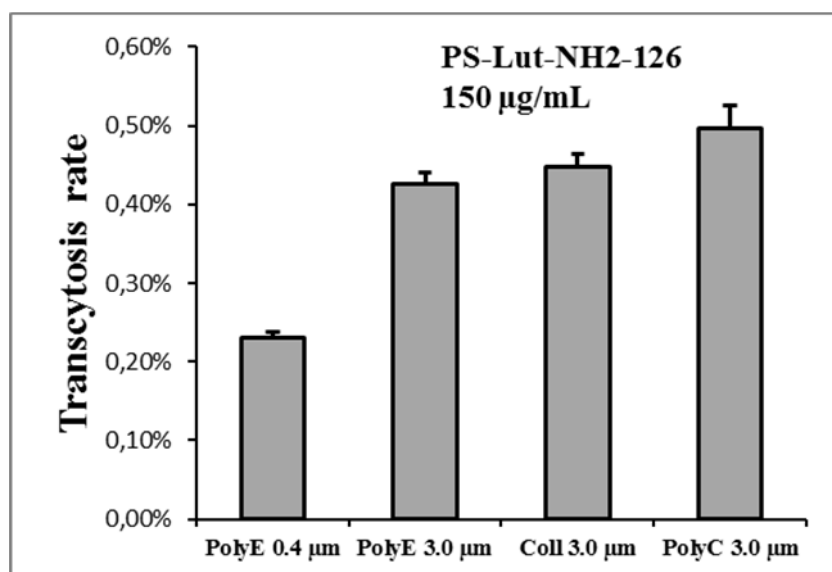
7.6 Calibration curves



SI Fig. 9: Transcytosis calibration curves for different nanoparticle concentrations.

Polystyrene nanoparticles were diluted in 1:1 steps, starting from 300 µg/mL down to 0,3 µg/mL. The resulting equation was subsequently used for the determination of transcytosis efficiencies.

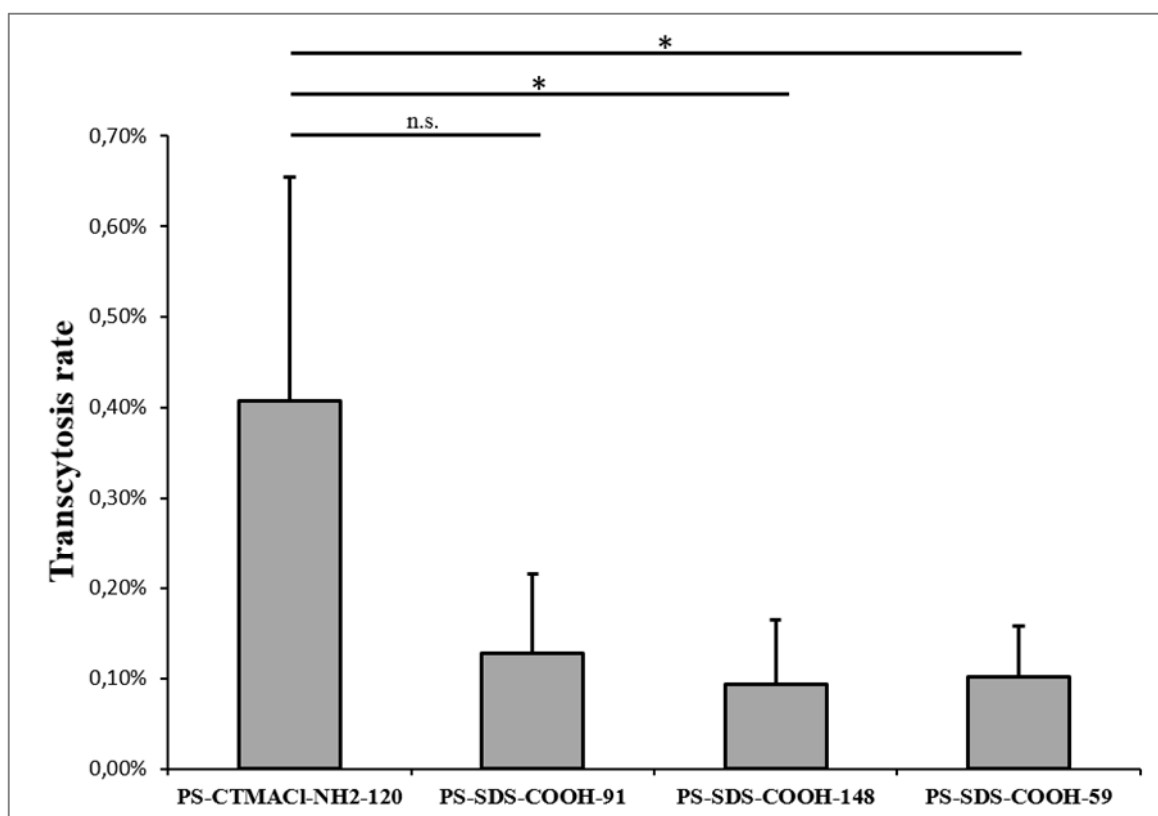
7.7 Transcytosis in different transwell plates



SI Fig. 10: Transcytosis rate through different transwell materials.

Caco-2 cells were seeded into different transwell inserts in a density of 1.5×10^5 cells / mL and cultivated for 14 days. Afterwards, polystyrene nanoparticles were added in a concentration of 150 µg/mL and incubated for 24 h. Transcytosis rate was determined via fluorescence measurement at a plate reader. PolyE = Polyester membrane, Coll = Collagen-coated membrane, PolyC = Polycarbonate membrane.

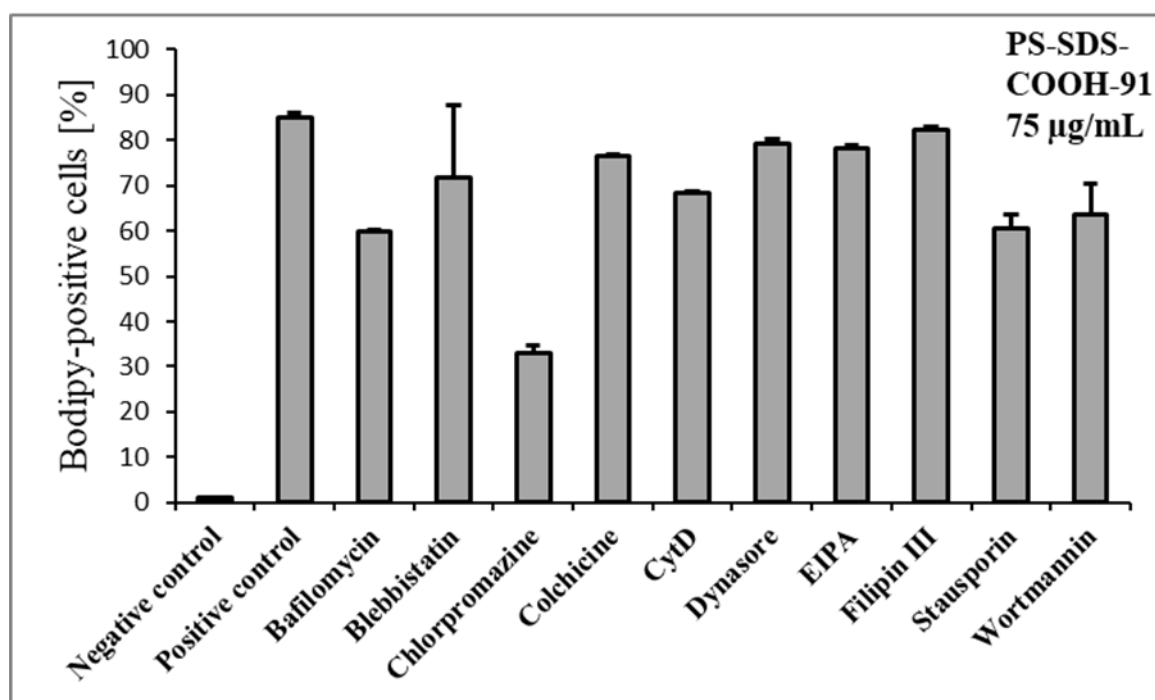
7.8 Transcytosis of differently charged SDS-stabilized nanoparticles



SI Fig. 11: Transcytosis of differently charged SDS-stabilized polystyrene nanoparticles.

This figure depicts the rate of transcytosis of differently charged SDS-stabilized polystyrene nanoparticles. Transcytosis rate was slightly increased for aminated nanoparticles. A student's t-test was used to determine significance levels, where $p < 0.05$ was considered significant.

7.9 Endocytosis inhibition by various pharmacological inhibitors



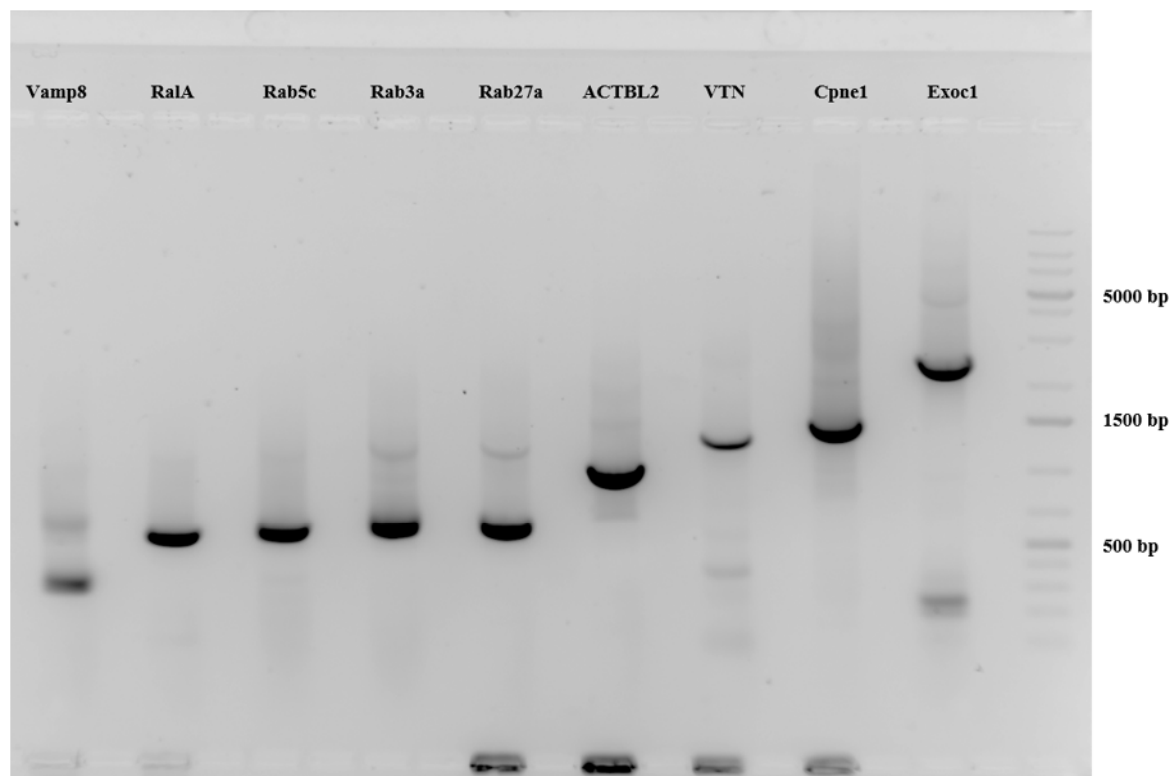
SI Fig. 12: Endocytosis inhibition via pharmacological inhibitors.

Cells were seeded in a density of 2×10^5 cells/mL in 12 well plates in DMEM with 10% FBS. Pharmacological inhibitors were added in various concentrations and incubated for 30 minutes. Then, nanoparticles were added in a concentration of $75 \mu\text{g/mL}$ and incubated for another 2 h. The percentage of nanoparticle-positive cells was determined via flow cytometry. Bafilomycin, chlorpromazine, staupsporin and wortmannin were able to reduce cellular uptake of nanoparticles.

7.10 Choice of Rab3a as representative for the Rab3 family

Our mass spectrometry data indicated a mean enrichment of Rab3c in the nanoparticle positive fraction by 514%. However, we were not able to amplify Rab3c from our total cDNA of Caco-2 cells. The transfection via commercial eGFP-tagged Rab3c resulted in a strange homogeneous signal in the cells. Nanoparticles did not show co-localization to Rab3c at any tested time points. So we re-examined the identified peptides from our mass spectrometry data for Rab3c. Both peptides assigned to Rab3c by the software did also match 100% to Rab3a. In addition, the proteins of the Rab3 family are very homologous (77-85% identical amino acids[232]). Consequently, in contrast to Rab3c, we were able to amplify Rab3a from our total cDNA of Caco-2 cells and since the transfection showed vesicular structures, we proceeded to work with Rab3a as representative for the Rab3 family.

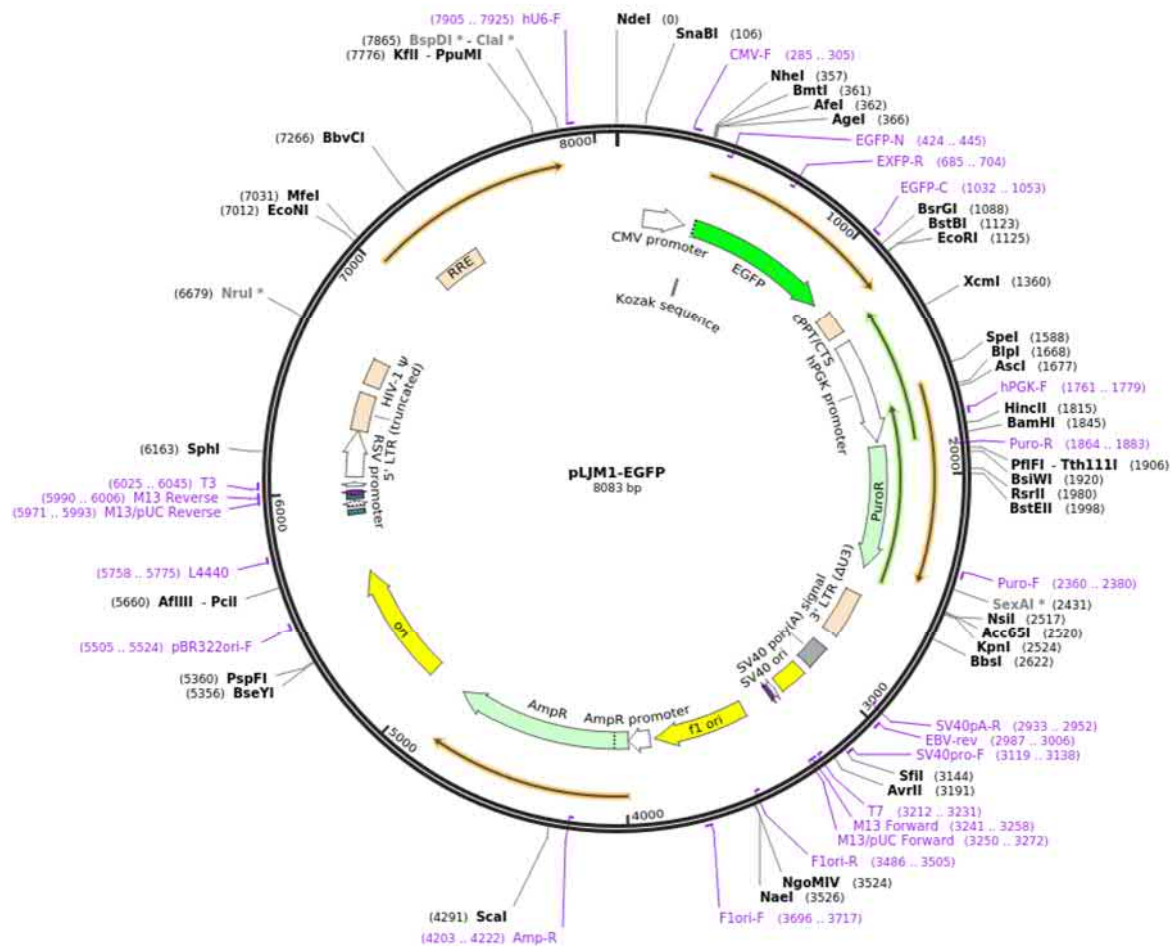
7.11 Amplification of putative transcytosis relevant cDNAs



SI Fig. 13: Amplification of putative transcytosis relevant cDNAs via polymerase chain reaction.

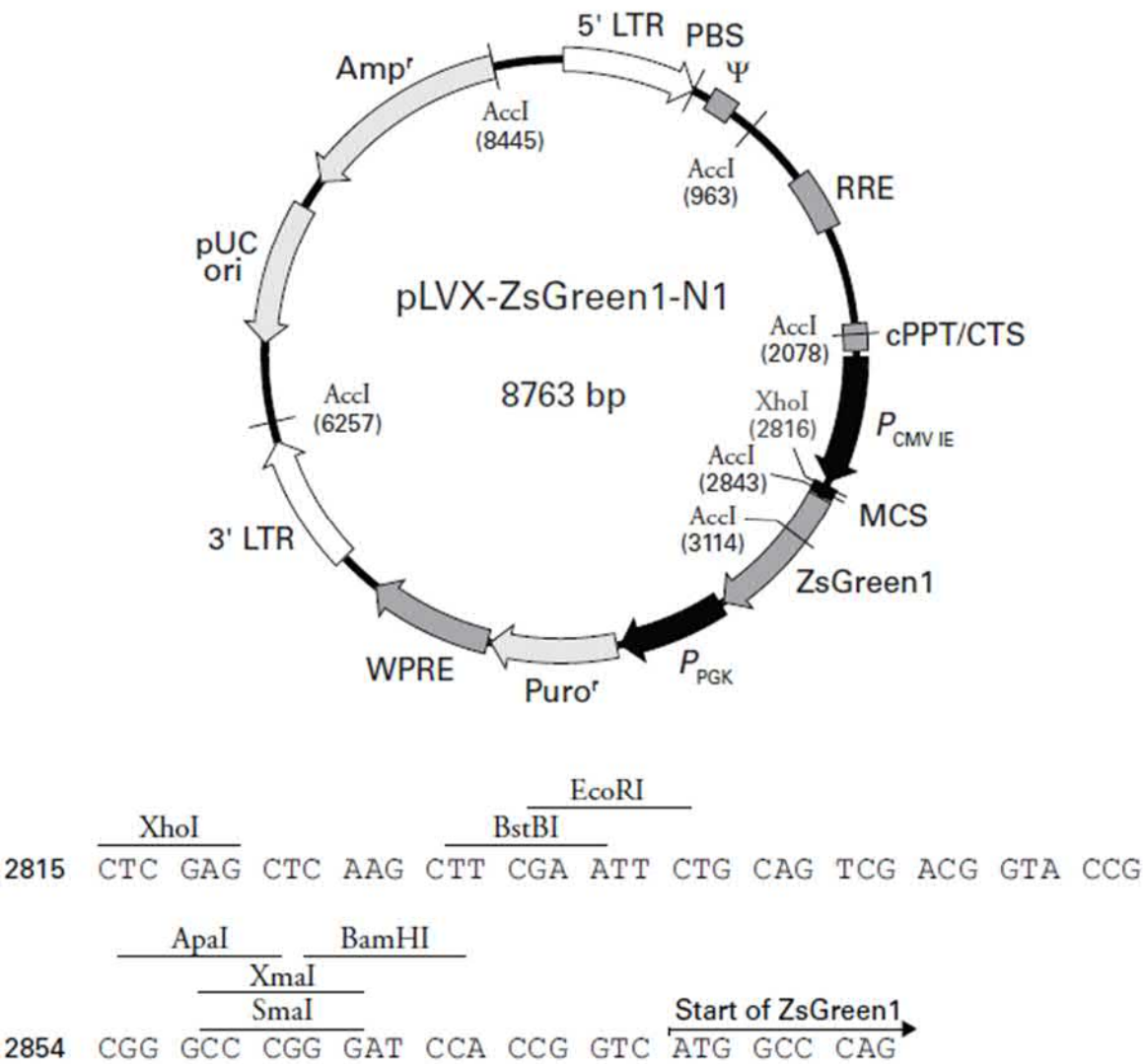
This figure depicts an agarose gel electrophoresis of putative transcytosis or exocytosis relevant cDNAs from total extracted Caco-2 RNA. All cDNAs could be amplified. Expected lengths: Vamp8: 300 bp, RalA: 618 bp, Rab5c: 648 bp, Rab3a: 660 bp, Rab27a: 663 bp, ACTBL2: 1128 bp, VTN: 1344 bp, Cpne1: 1611 bp, Exoc1: 2682 bp.

7.12 Vector maps

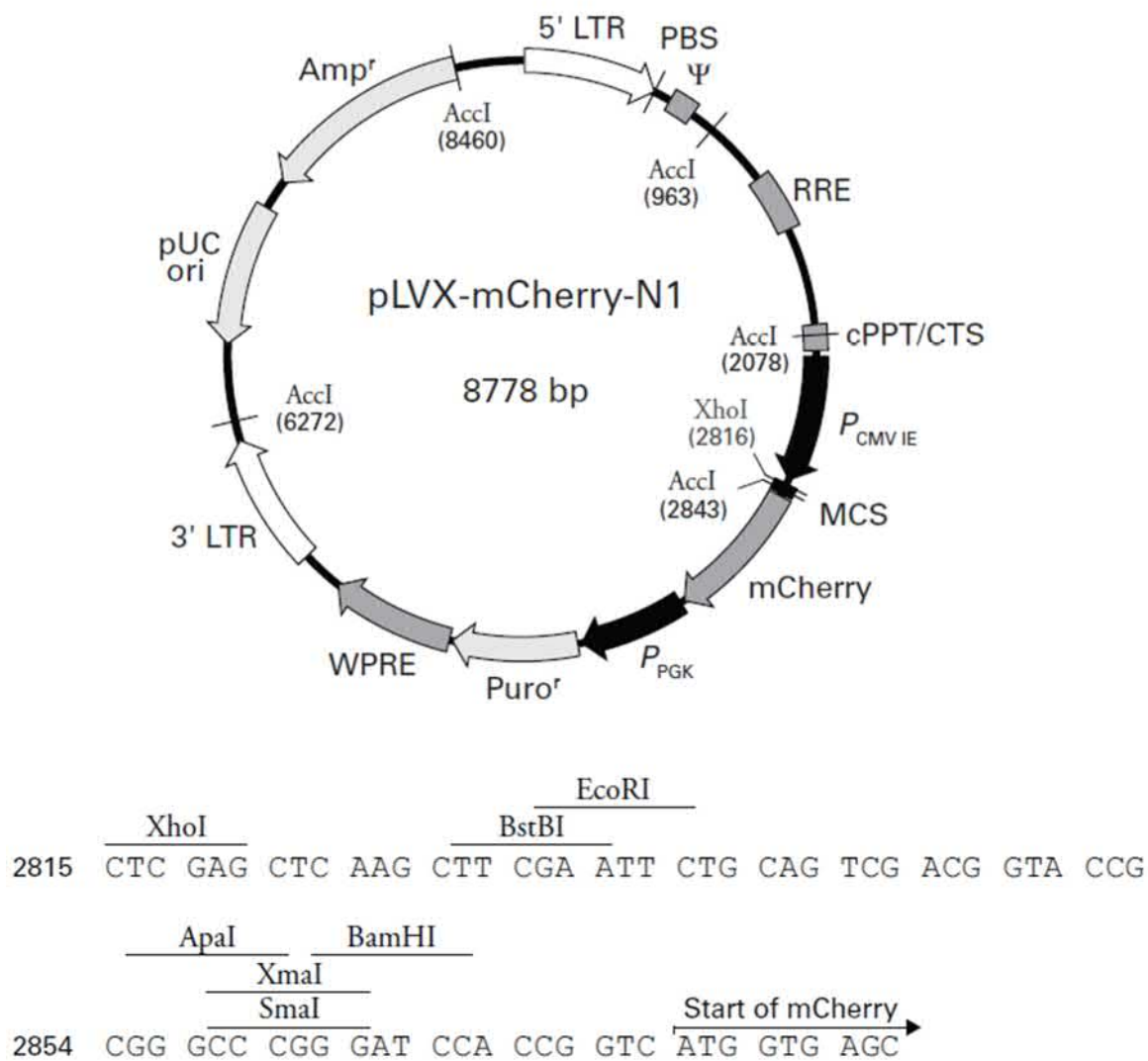


SI Fig. 14: Lentiviral transfer plasmid pLJM1-EGFP.

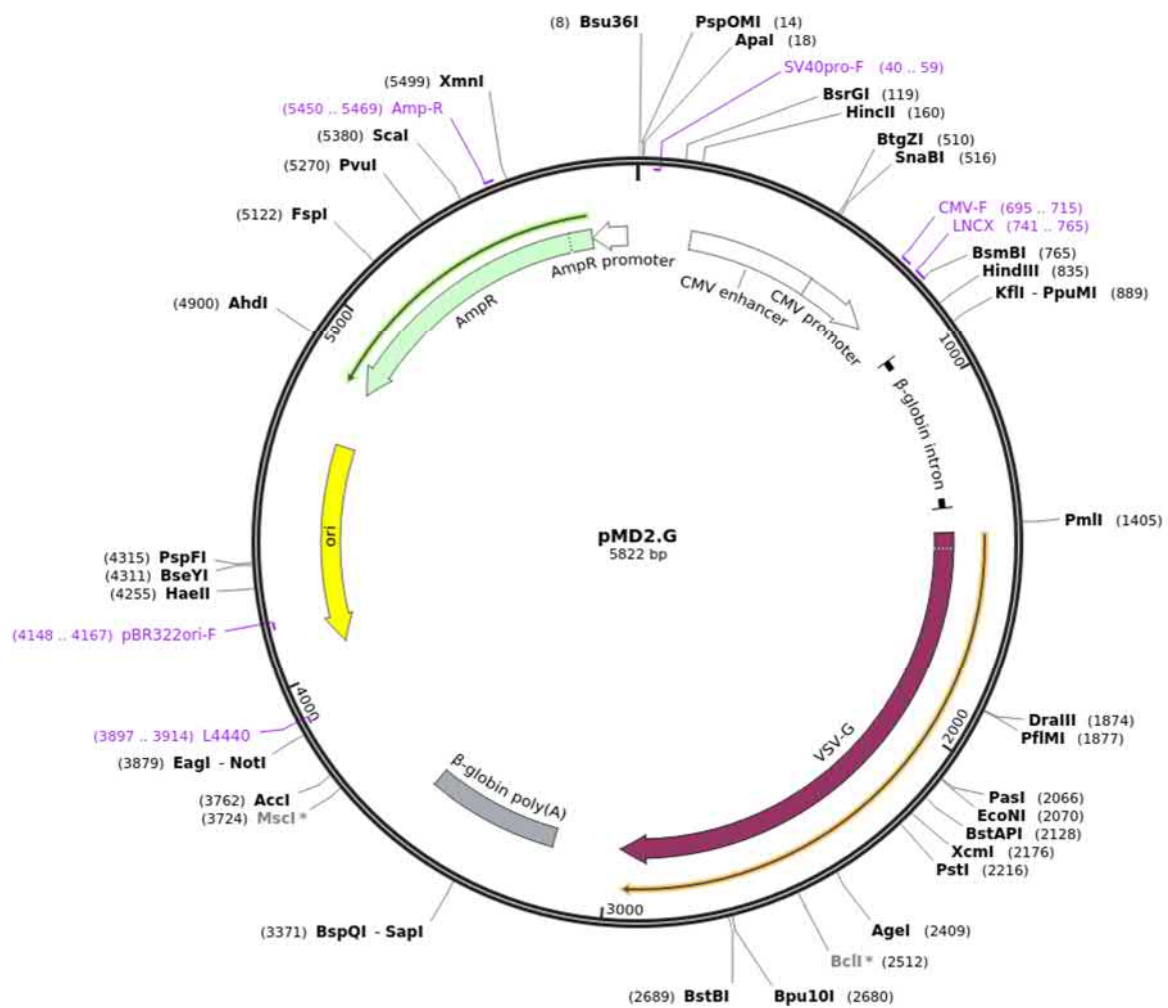
This figure depicts the vector map of the lentiviral transfer plasmid pLJM1-EGFP. The map was obtained from <https://www.addgene.org/19319/>.



SI Fig. 15: Lentiviral transfer plasmid pLVX-ZsGreen1-N1.
This figure depicts the vector map of the lentiviral transfer plasmid pLVX-ZsGreen1-N1. The map was obtained from <http://www.biofeng.com/zaiti/manbingdu/pLVX-ZsGreen1-N1.html>.



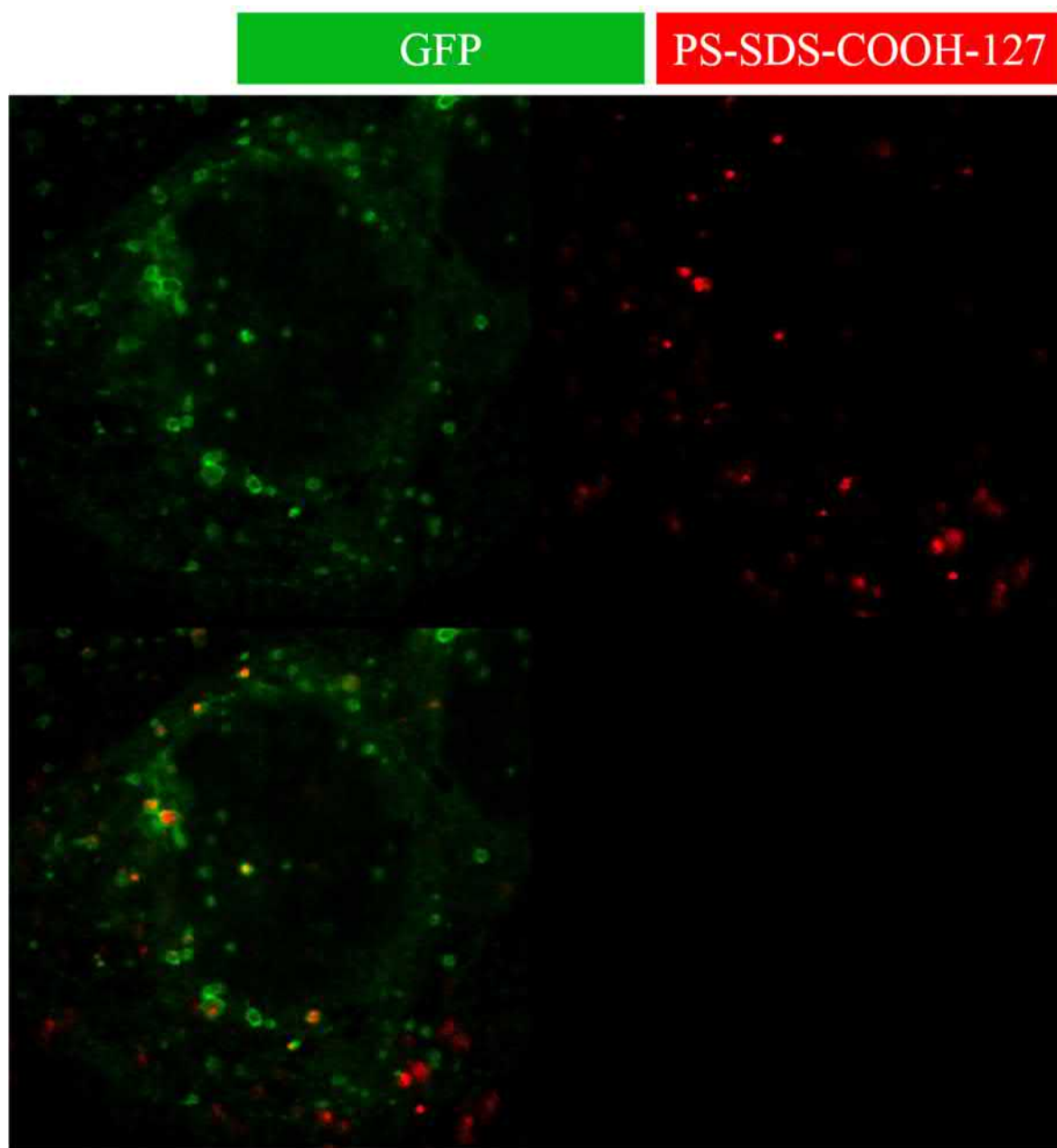
SI Fig. 16: Lentiviral transfer plasmid pLVX-mCherry-N1.
This figure depicts the vector map of the lentiviral transfer plasmid pLVX-mCherry-N1. The map was obtained from <http://www.biofeng.com/zaiti/manbingdu/pLVX-mCherry-N1.html>.



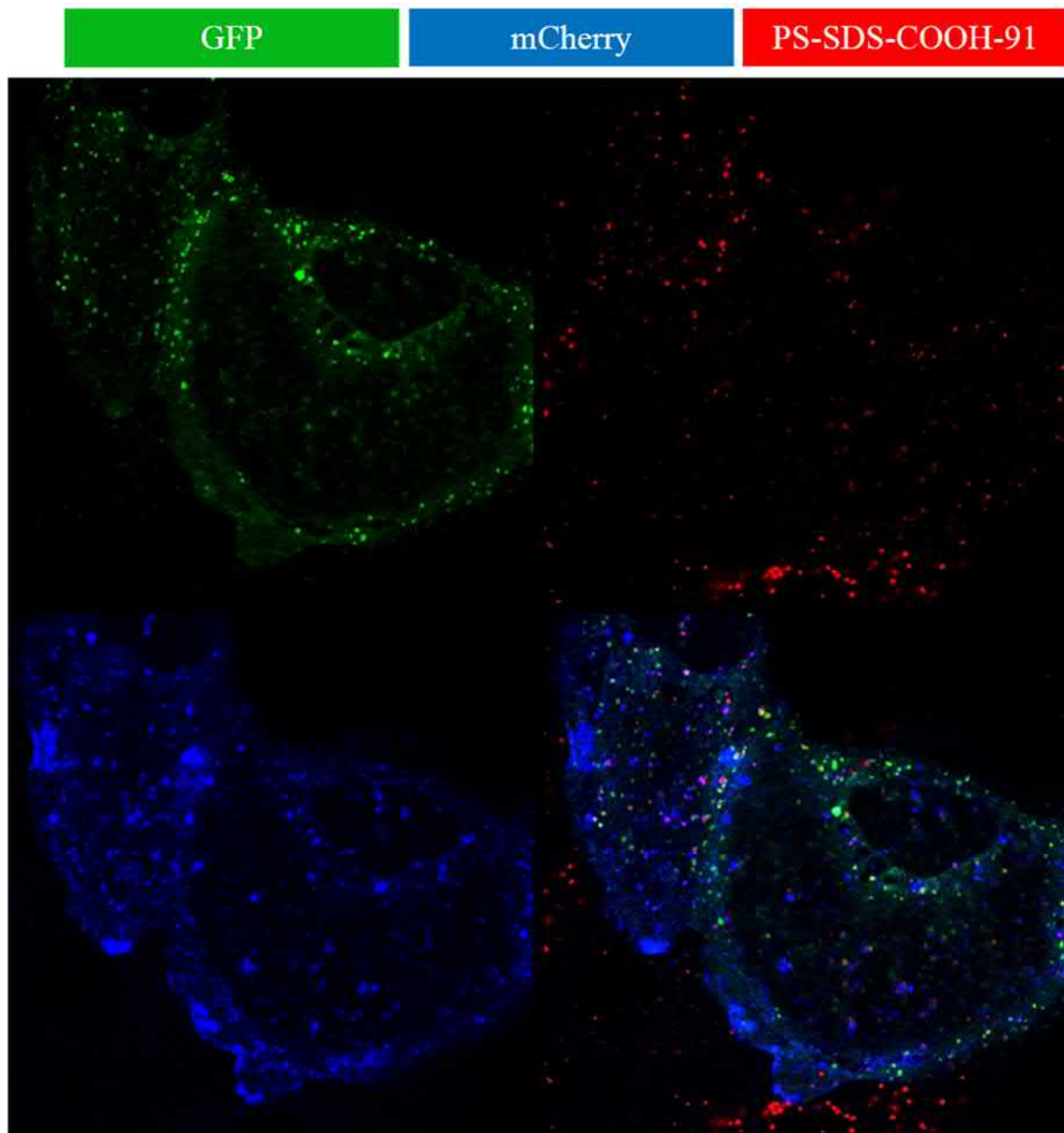
SI Fig. 17: Lentiviral envelope expressing plasmid pMD2.G.

This figure depicts the vector map of the lentiviral envelope expressing plasmid pMD2.G. The map was obtained from <https://www.addgene.org/12259/>.

7.13 Analysis of potential bleed through

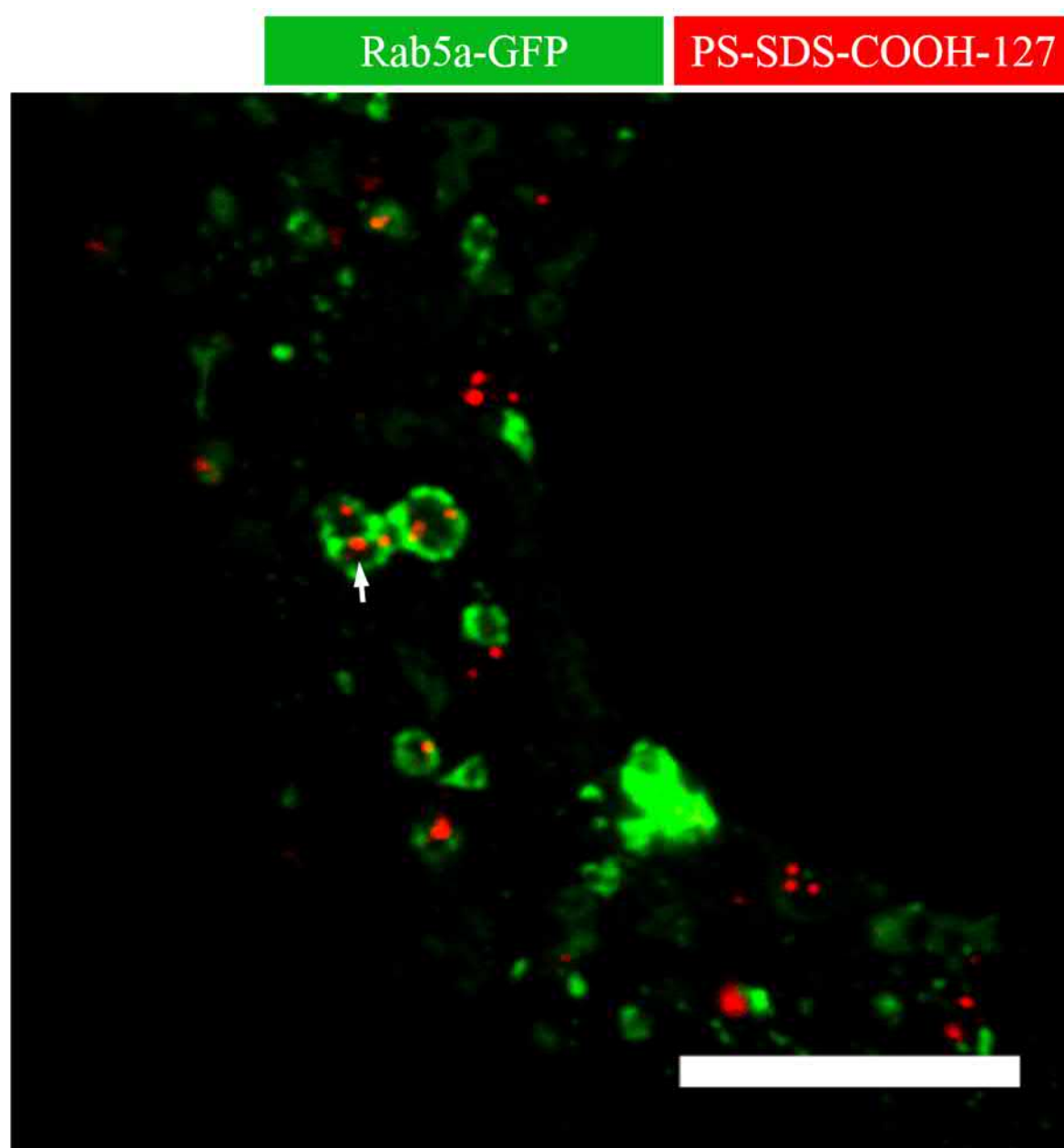


SI Fig. 19: Separate channels and overlap of GFP and PS-SDS-COOH-127 in cLSM.
Both Channels did not show major bleed through of the respective fluorescent dyes.




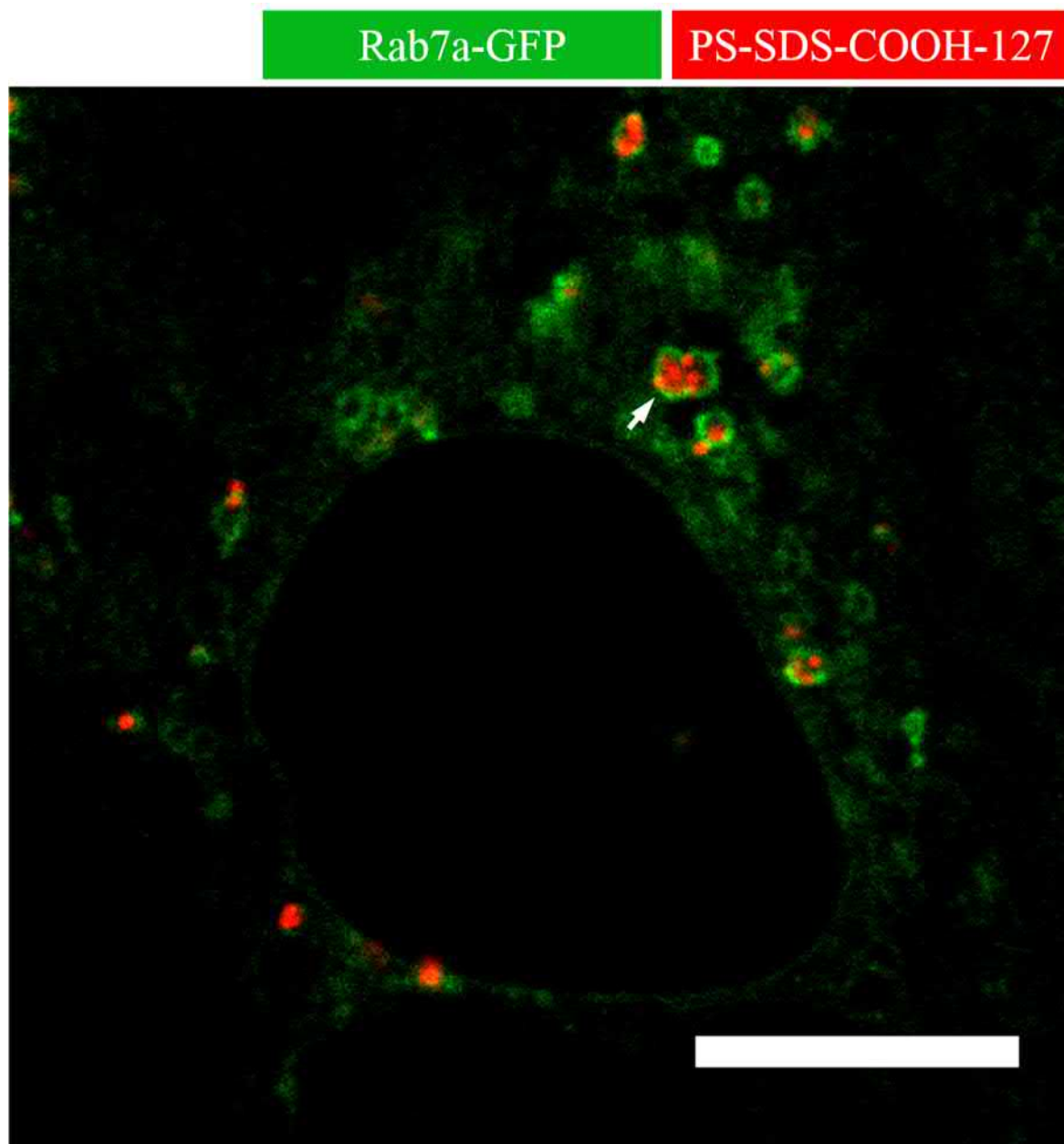
SI Fig. 20: Separate channels and overlap of GFP, mCherry and PS-SDS-COOH-91 in cLSM.
All three channels did not show major bleed through of the other respective fluorescent dyes.

7.14 Close-ups of co-localization studies




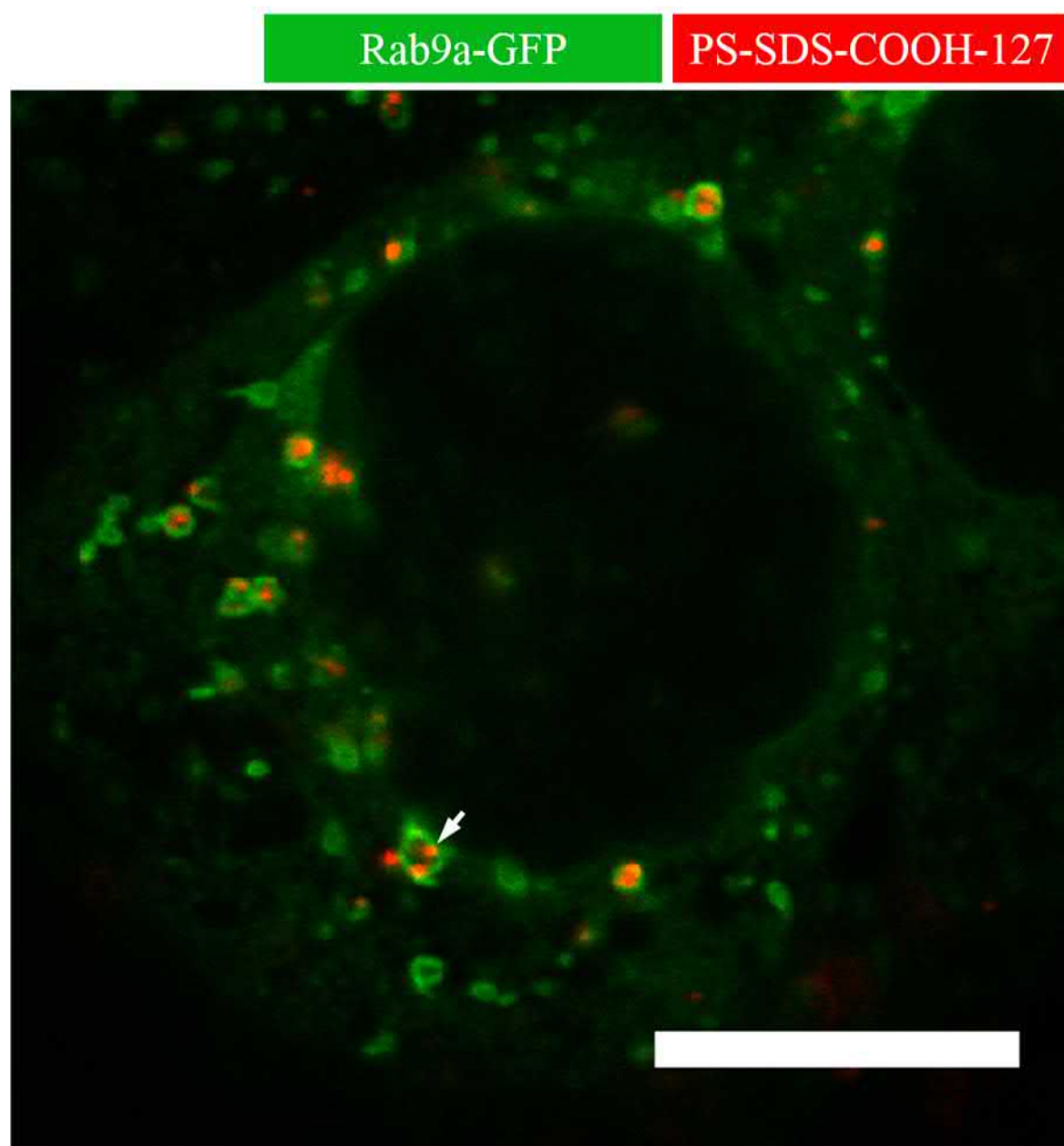
SI Fig. 21: Magnification of Figure 37: Co-Localization of Rab5a-GFP and polystyrene nanoparticles.

 = NP in Co-Localization with the marker protein. Scale bar = 10 μ m.



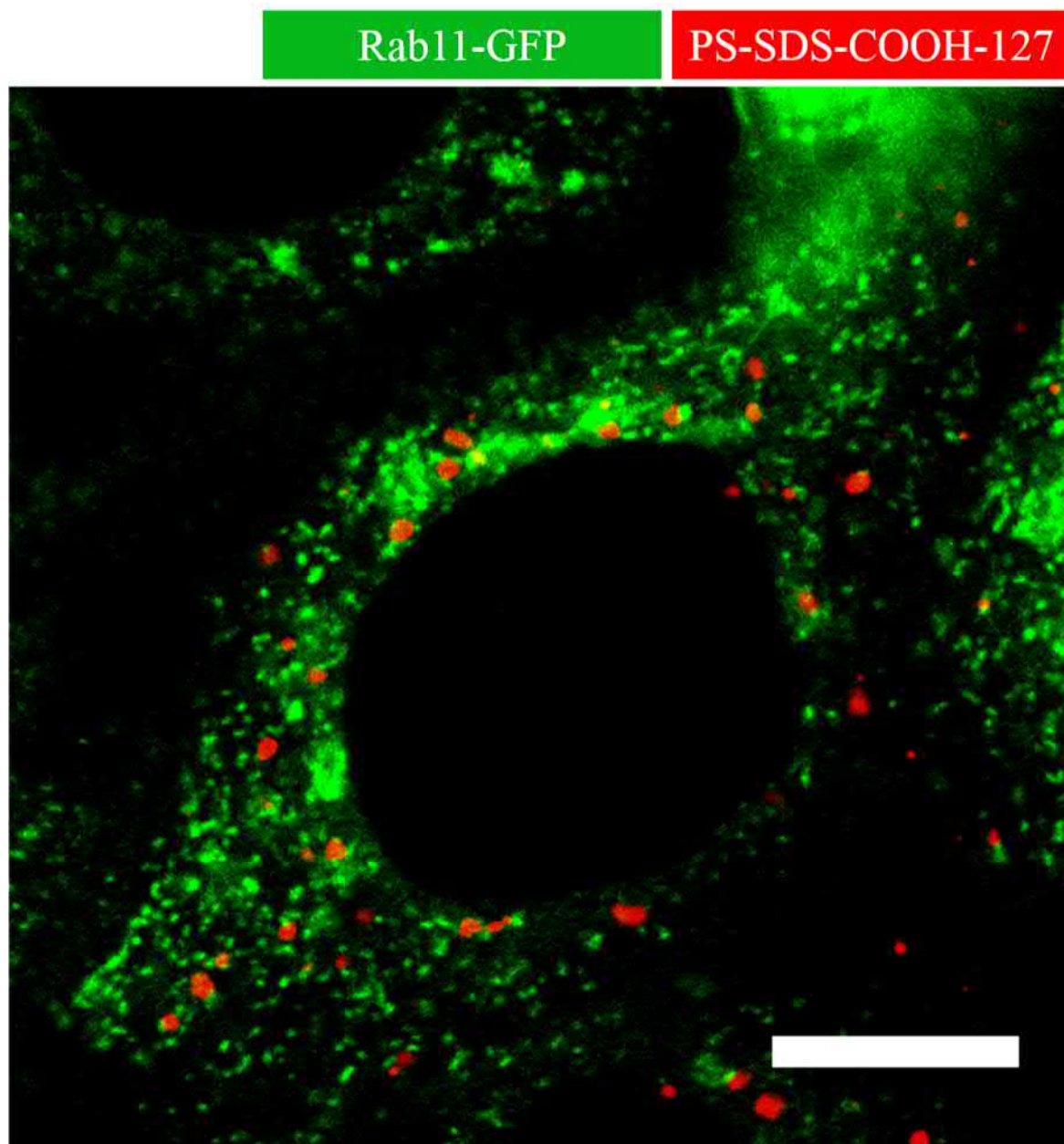
SI Fig. 22: Magnification of Figure 38: Co-Localization of Rab7a-GFP and polystyrene nanoparticles.

 = NP in Co-Localization with the marker protein. Scale bar = 10 μ m.



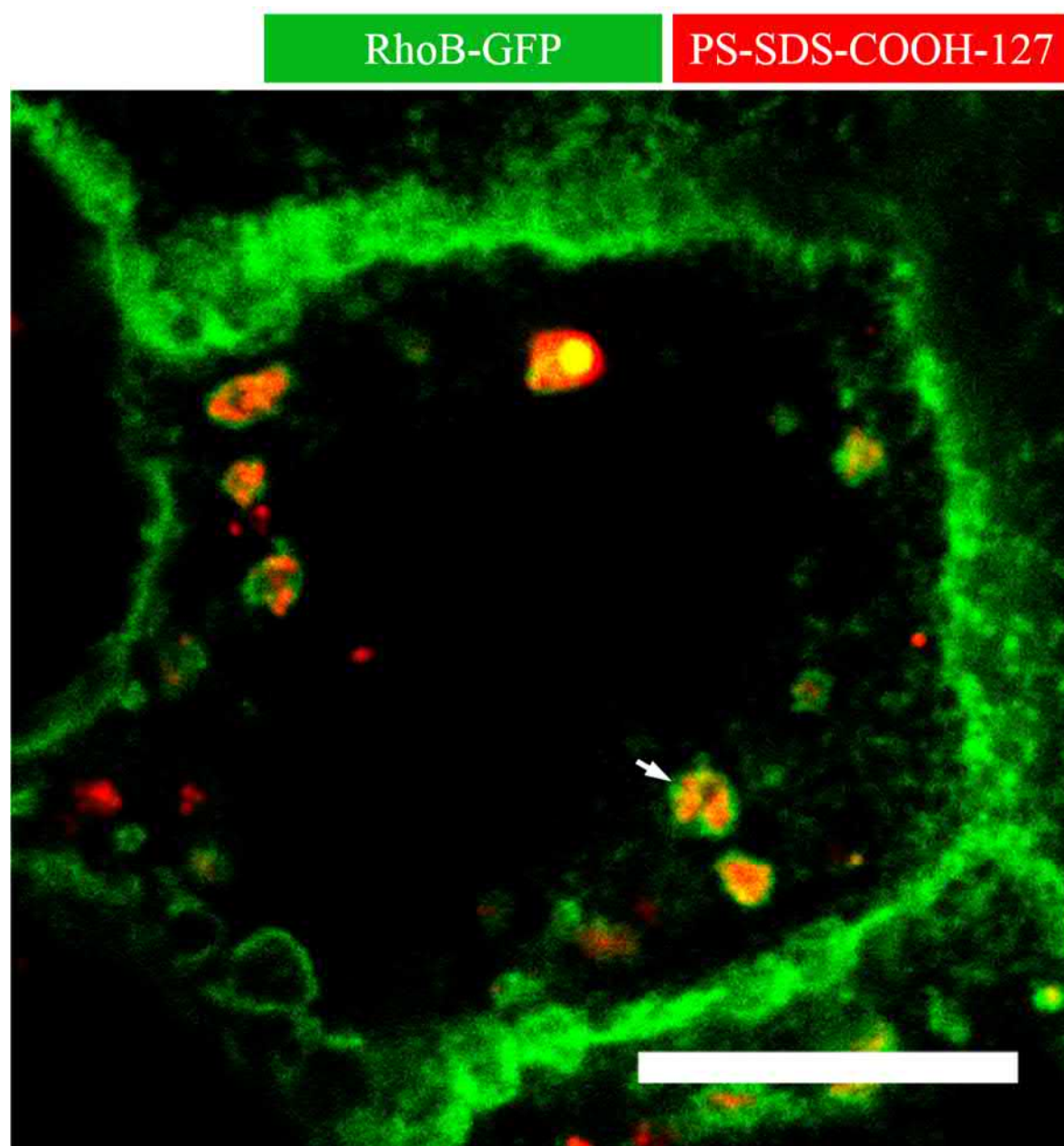
SI Fig. 23: Magnification of Figure 38: Co-Localization of Rab9a-GFP and polystyrene nanoparticles.

▣ = NP in Co-Localization with the marker protein. Scale bar = 10μm.




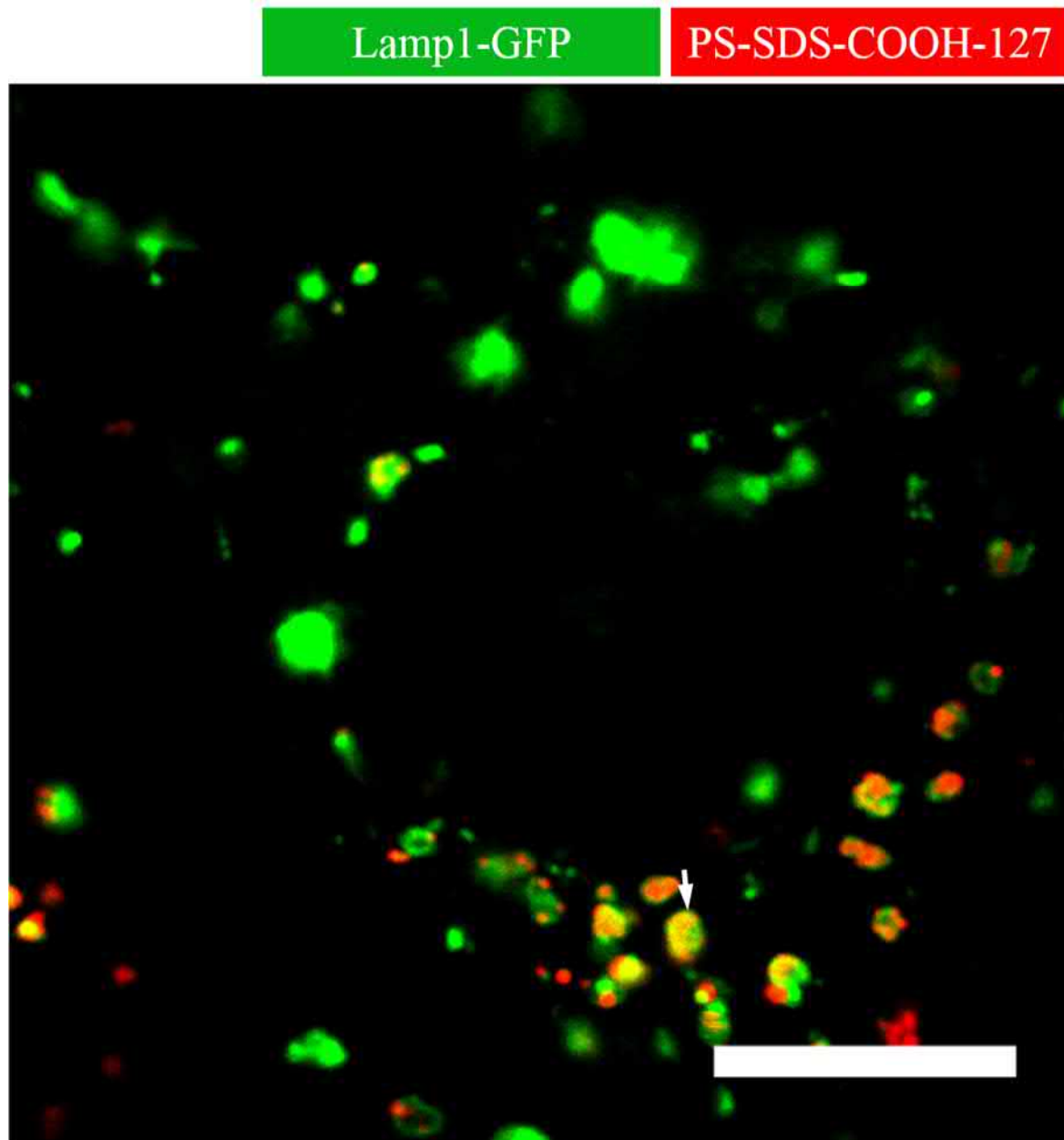
SI Fig. 24: Magnification of Figure 38: Co-Localization of Rab11-GFP and polystyrene nanoparticles.

No co-localization was observed. Scale bar = 10 μ m.




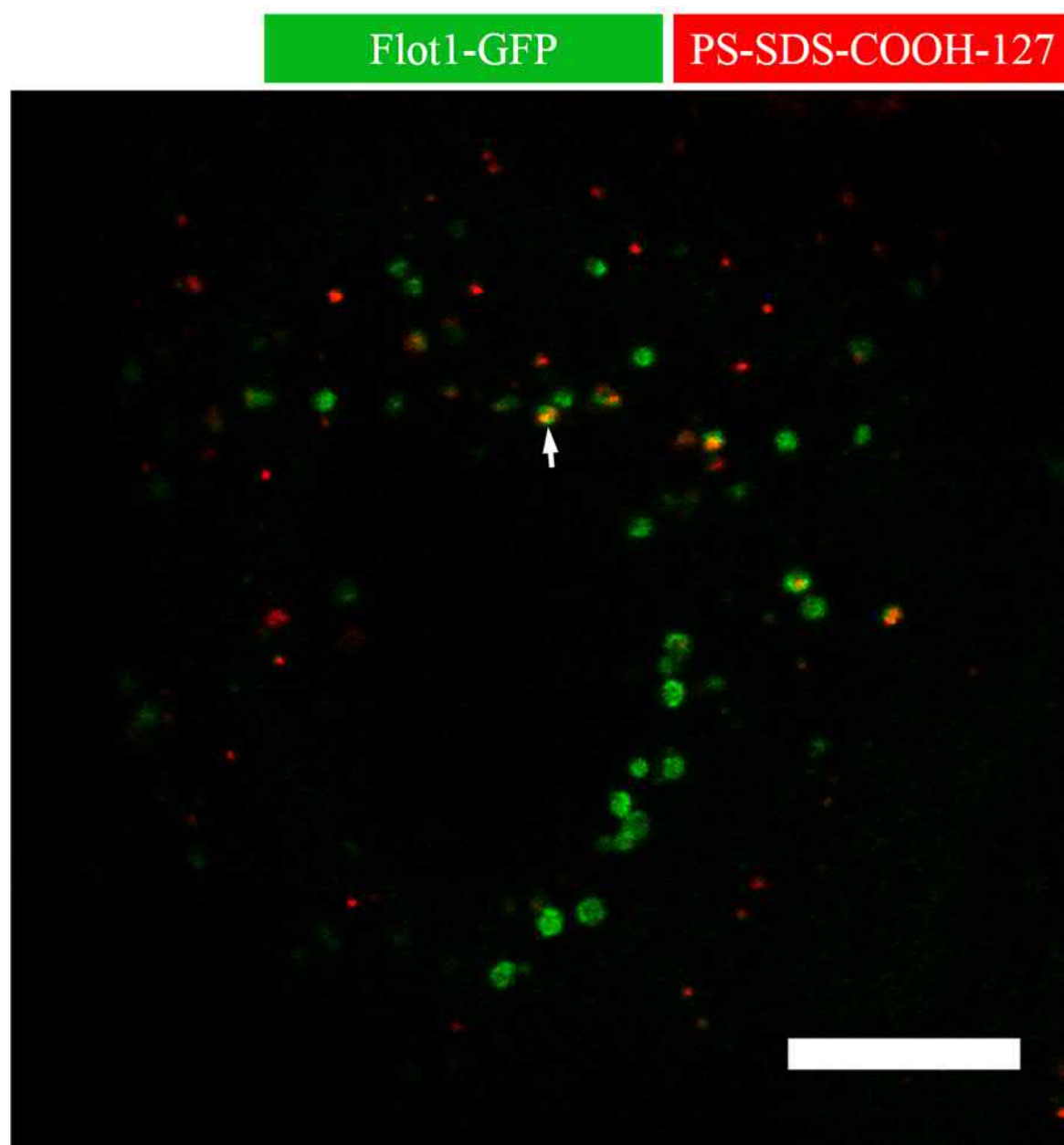
SI Fig. 25: Magnification of Figure 38: Co-Localization of RhoB-GFP and polystyrene nanoparticles.

 = NP in Co-Localization with the marker protein. Scale bar = 10 μ m.




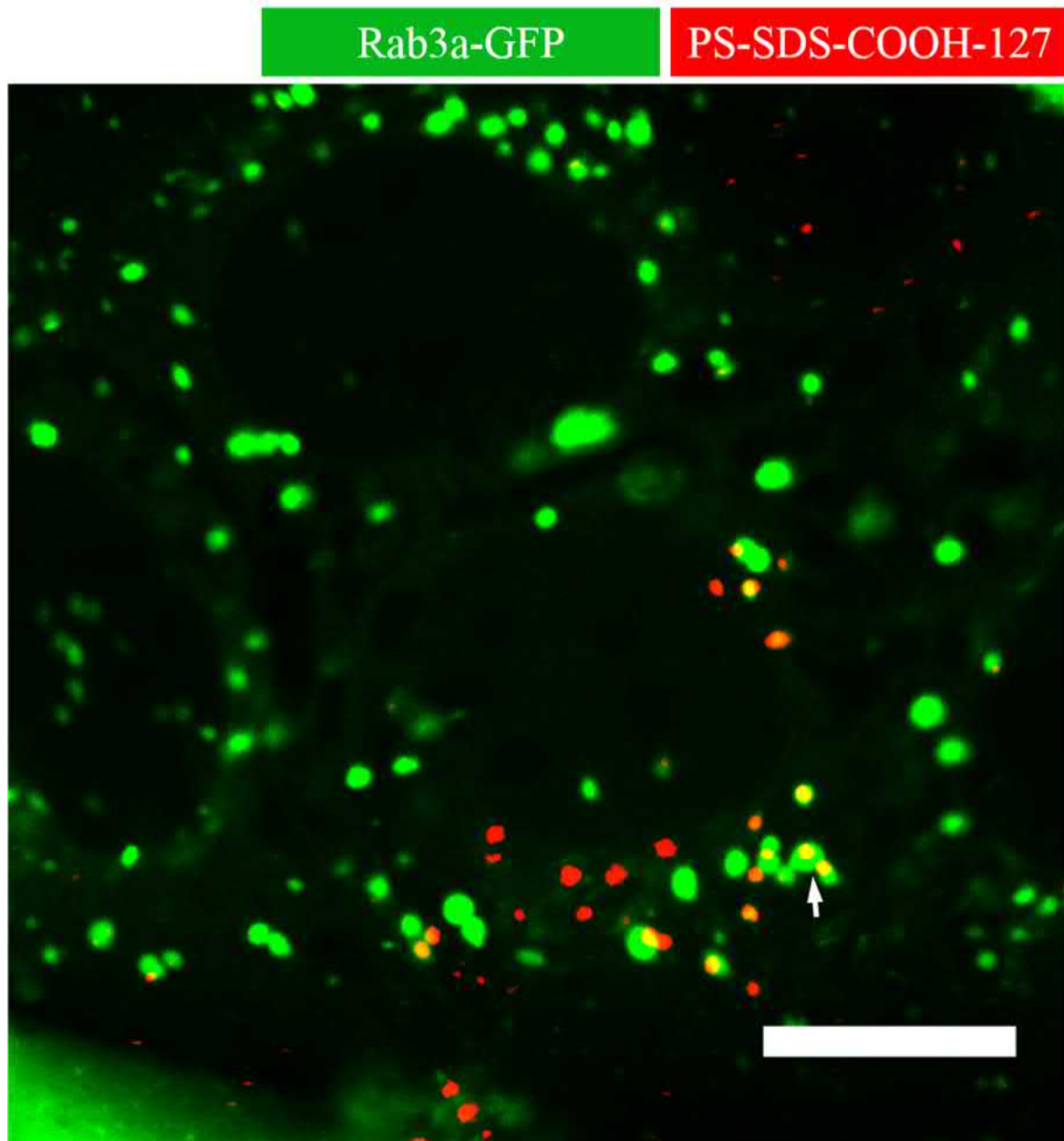
SI Fig. 26: Magnification of Figure 38: Co-Localization of Lamp1-GFP and polystyrene nanoparticles.

 = NP in Co-Localization with the marker protein. Scale bar = 10 μ m.




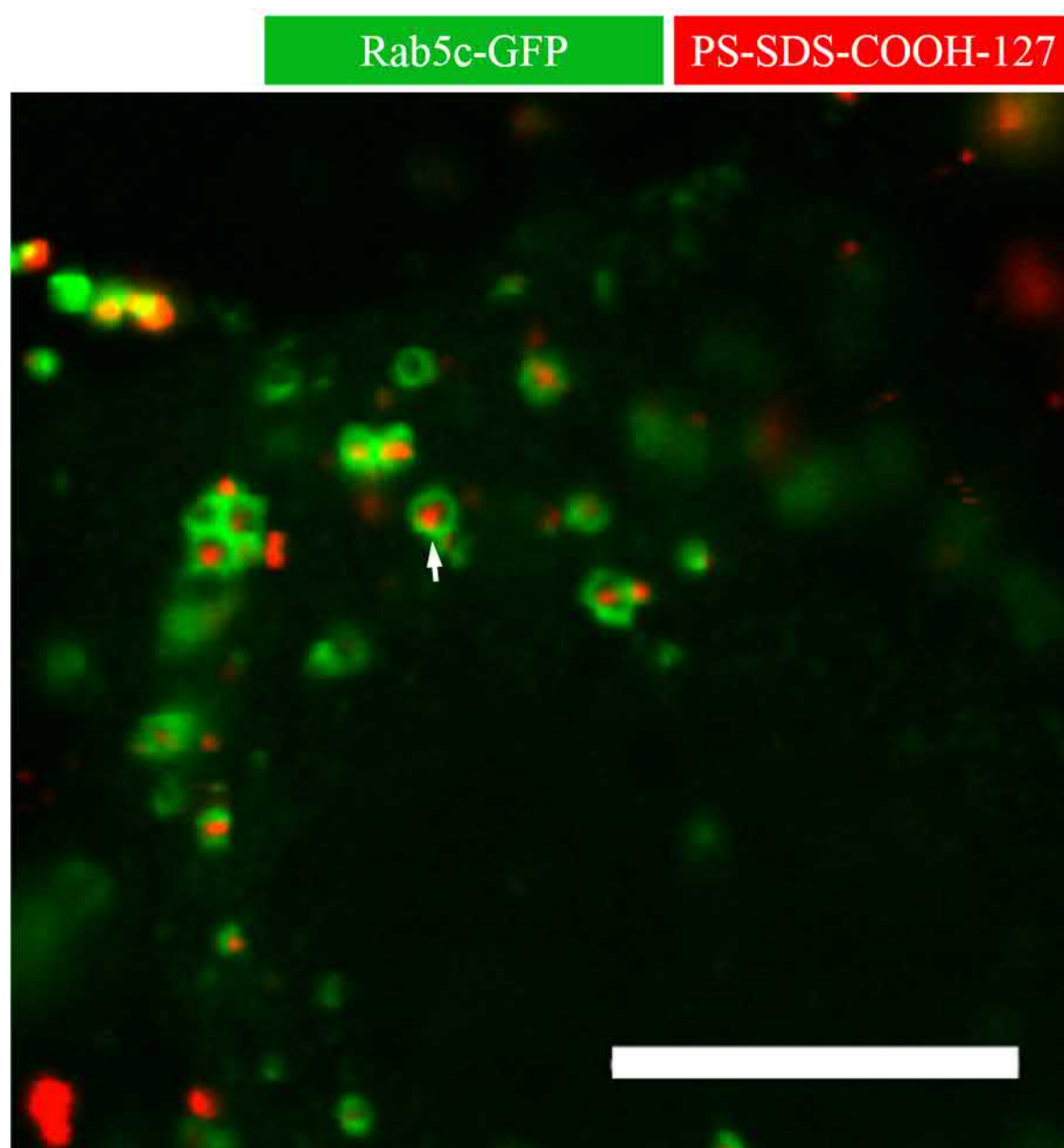
SI Fig. 27: Magnification of Figure 38: Co-Localization of Flot1-GFP and polystyrene nanoparticles.

 = NP in Co-Localization with the marker protein. Scale bar = 10 μ m.




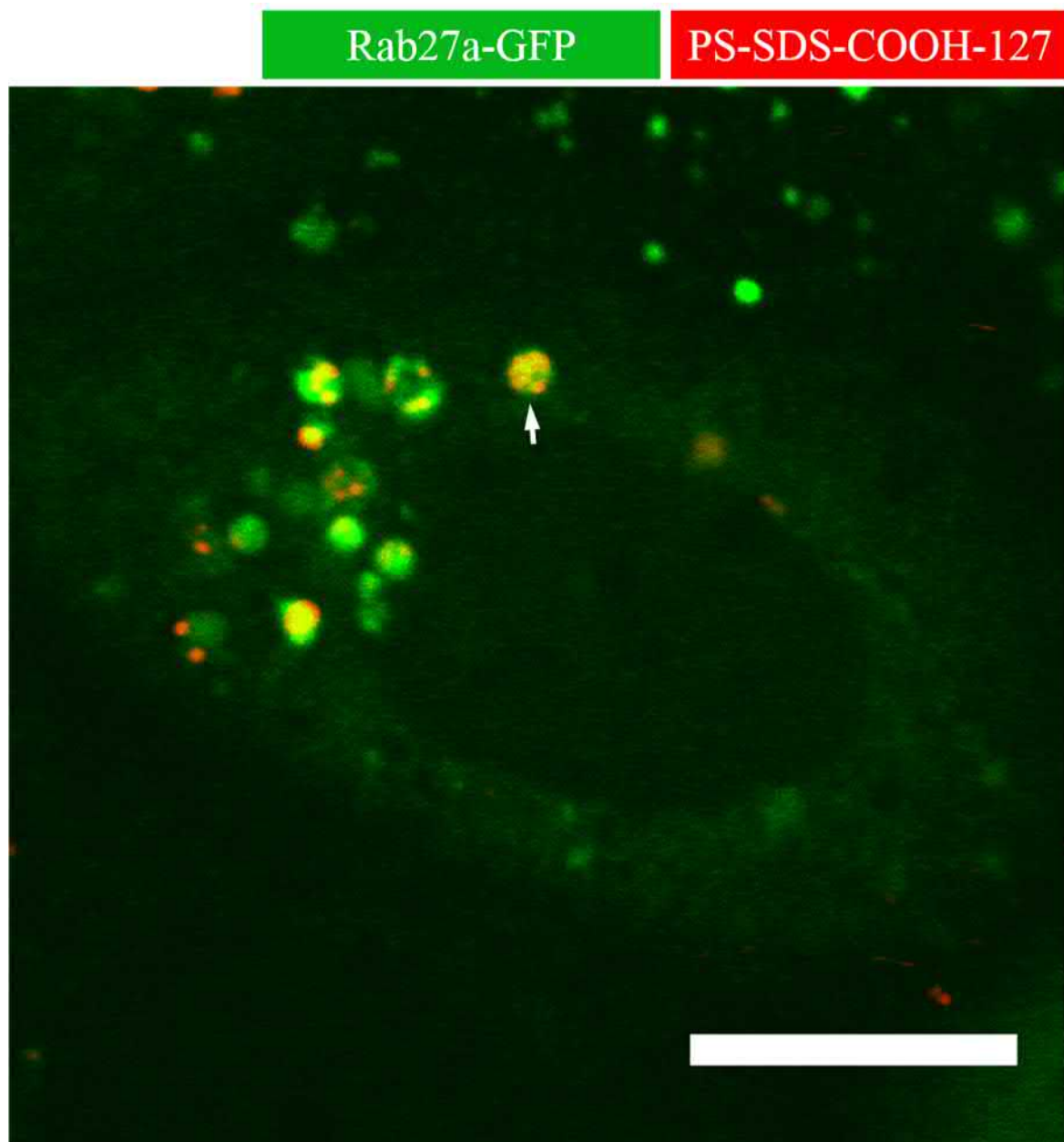
SI Fig. 28: Magnification of Figure 38: Co-Localization of Rab3a-GFP and polystyrene nanoparticles.

 = NP in Co-Localization with the marker protein. Scale bar = 10 μ m.




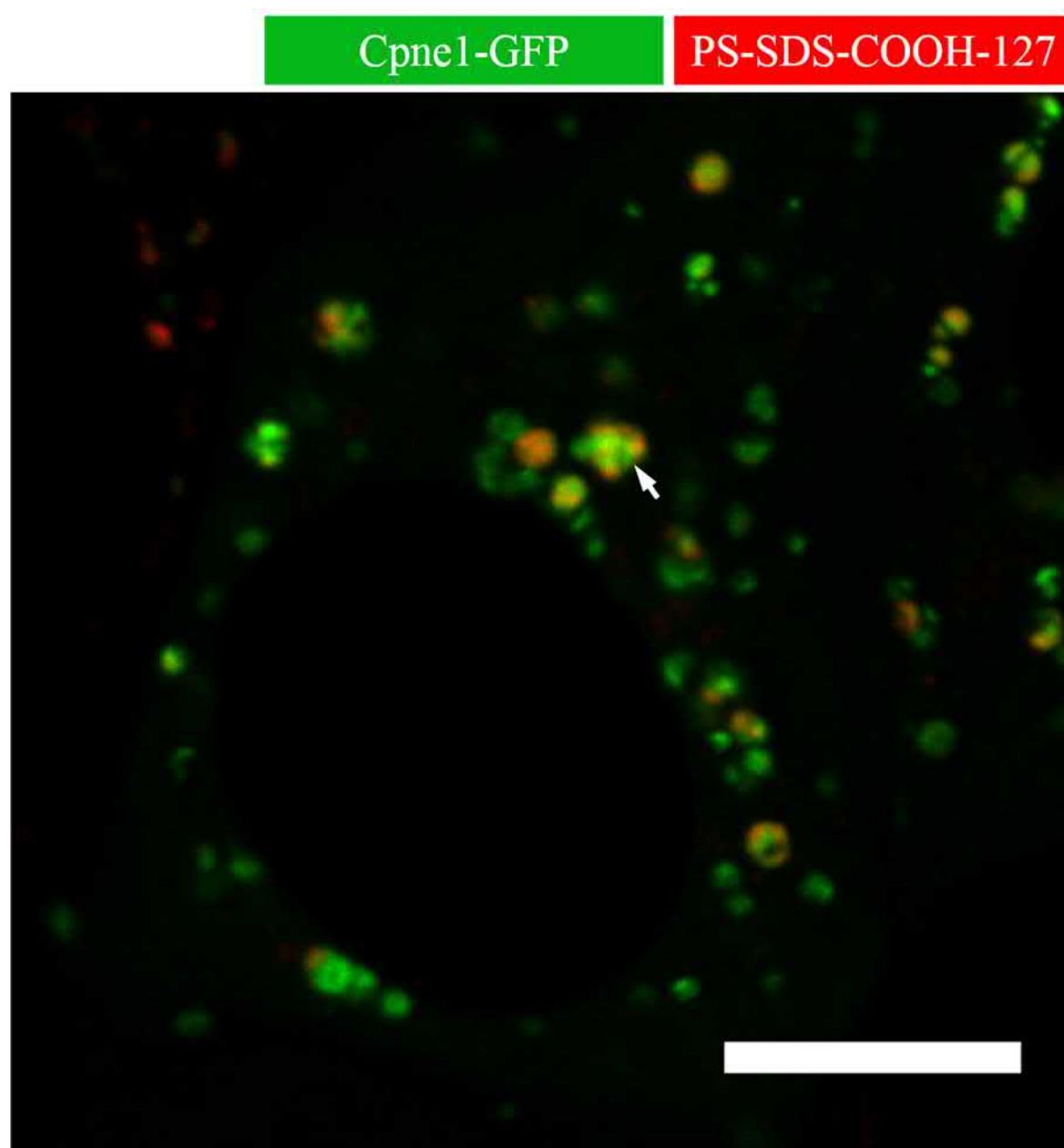
SI Fig. 29: Magnification of Figure 38: Co-Localization of Rab5c-GFP and polystyrene nanoparticles.

 = NP in Co-Localization with the marker protein. Scale bar = 10 μ m.




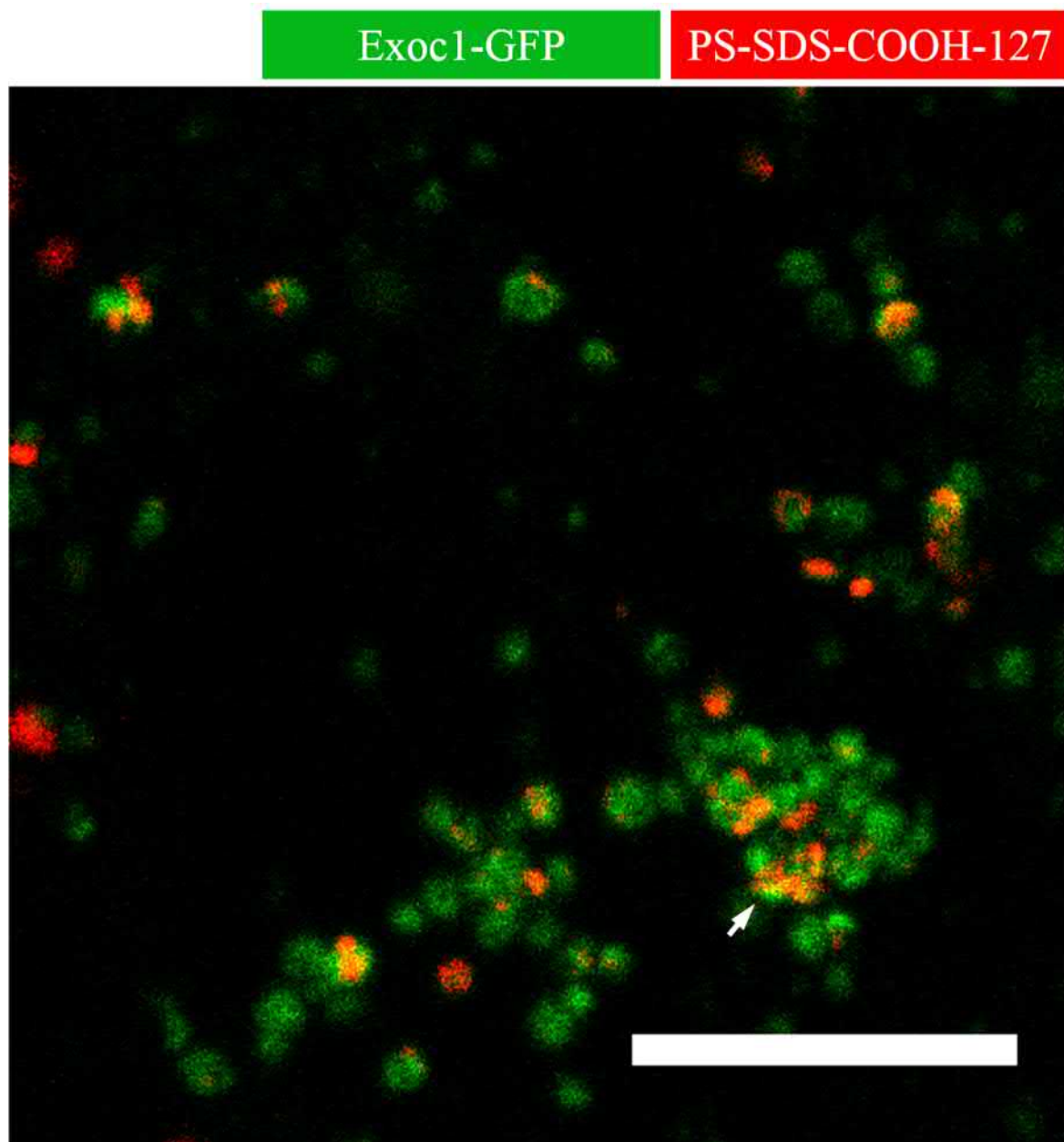
SI Fig. 30: Magnification of Figure 38: Co-Localization of Rab27a-GFP and polystyrene nanoparticles.

 = NP in Co-Localization with the marker protein. Scale bar = 10 μ m.



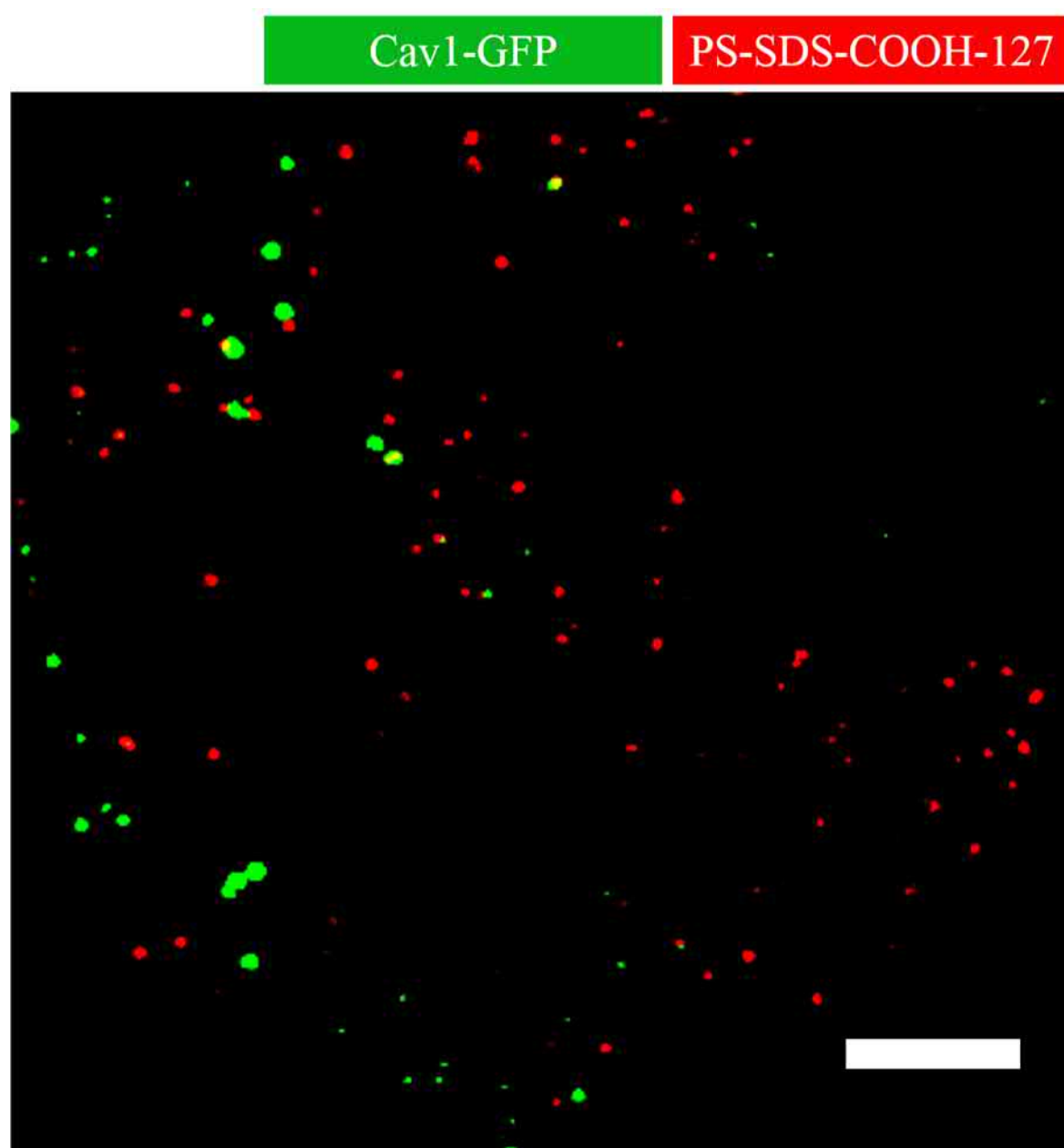
SI Fig. 31: Magnification of Figure 38: Co-Localization of Cpne1-GFP and polystyrene nanoparticles.

 = NP in Co-Localization with the marker protein. Scale bar = 10 μ m.



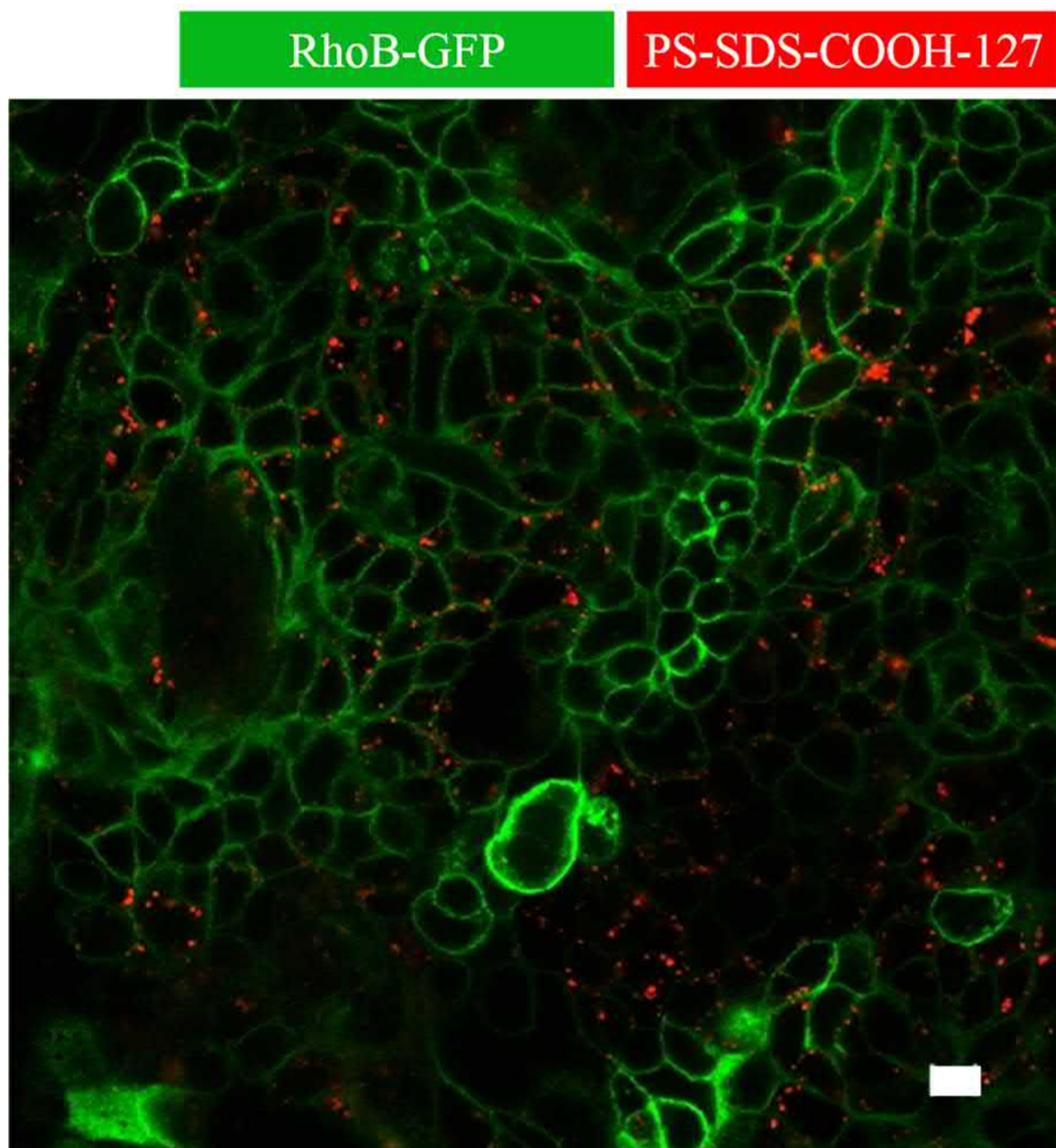
SI Fig. 32: Magnification of Figure 38: Co-Localization of Exoc1-GFP and polystyrene nanoparticles.

➡ = NP in Co-Localization with the marker protein. Scale bar = 10 μ m.



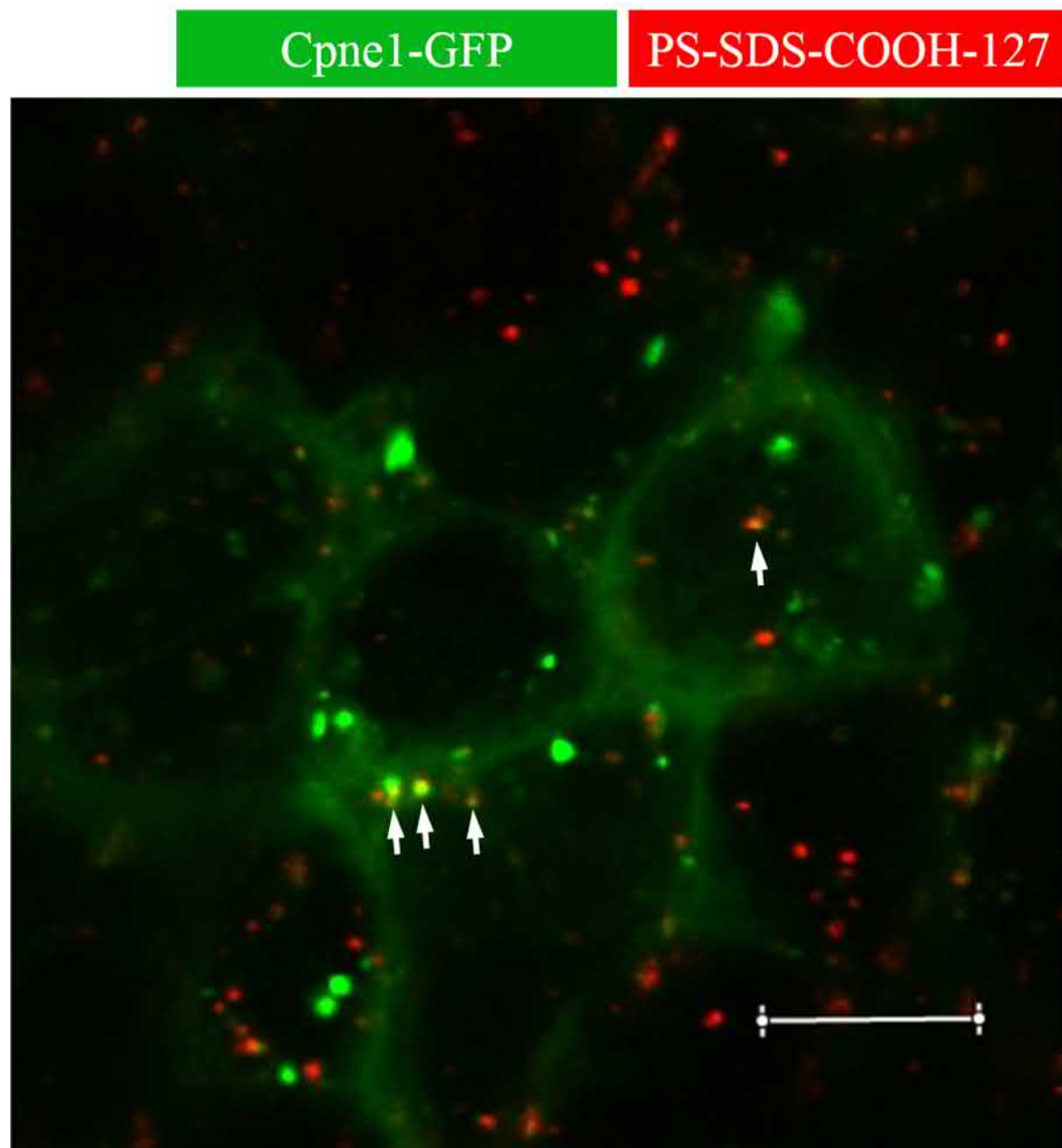
SI Fig. 33: Magnification of Figure 38: Co-Localization of Cav1-GFP and polystyrene nanoparticles.

No co-localization was observed. Scale bar = 10 μ m.

7.15 Nanoparticle treatment on transwell filters

SI Fig. 34: Localization of RhoB and PS-SDS-COOH-127 on transwell filters.

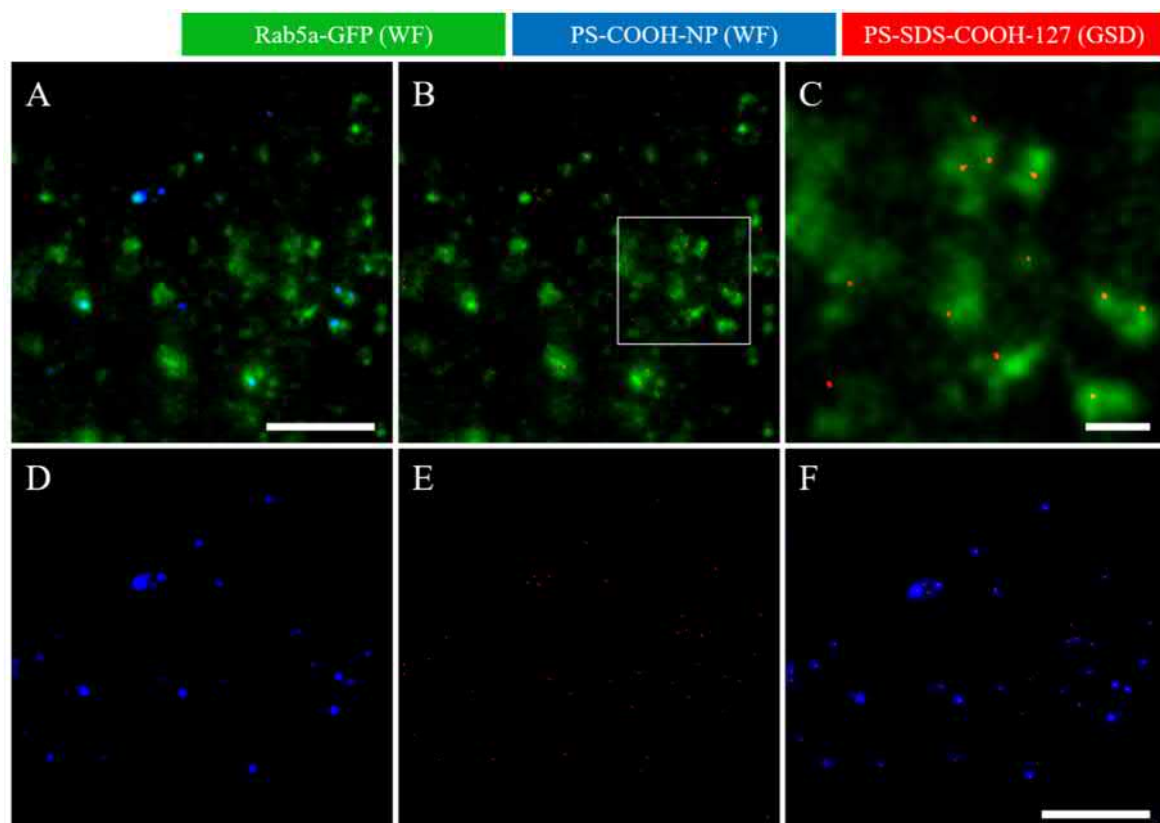
500 $\mu\text{g/mL}$ PS-SDS-COOH-127 were added for 24 hours into the apical medium. Afterwards, transwell filters were cut out with a scalpel and fixed on microscope slides. RhoB was mostly localized in the cell membrane and smaller vesicles. Nanoparticles exhibited almost no co-localization to RhoB after 24 hours incubation on transwells. Scale bar = 10 μm .



SI Fig. 35: Localization of Cpne1 and PS-SDS-COOH-127 on transwell filters.

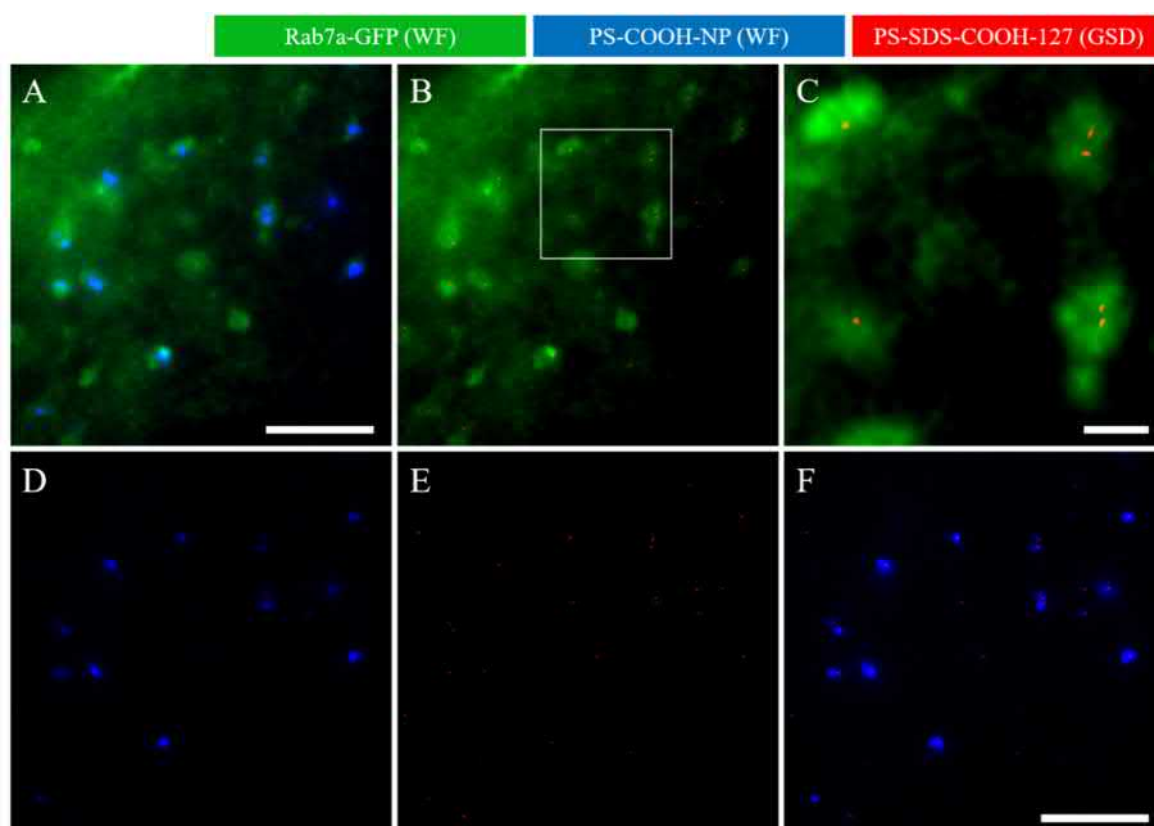
500 $\mu\text{g/mL}$ PS-SDS-COOH-127 were added for 24 hours into the apical medium. Afterwards, transwell filters were cut out with a scalpel and fixed on microscope slides. Cpne1 was mostly localized on smaller vesicles and cell membrane. Nanoparticles exhibited minor co-localization to Cpne1 after 24 hours incubation on transwells. Scale bar = 10 μm .

7.16 GSD Microscopy



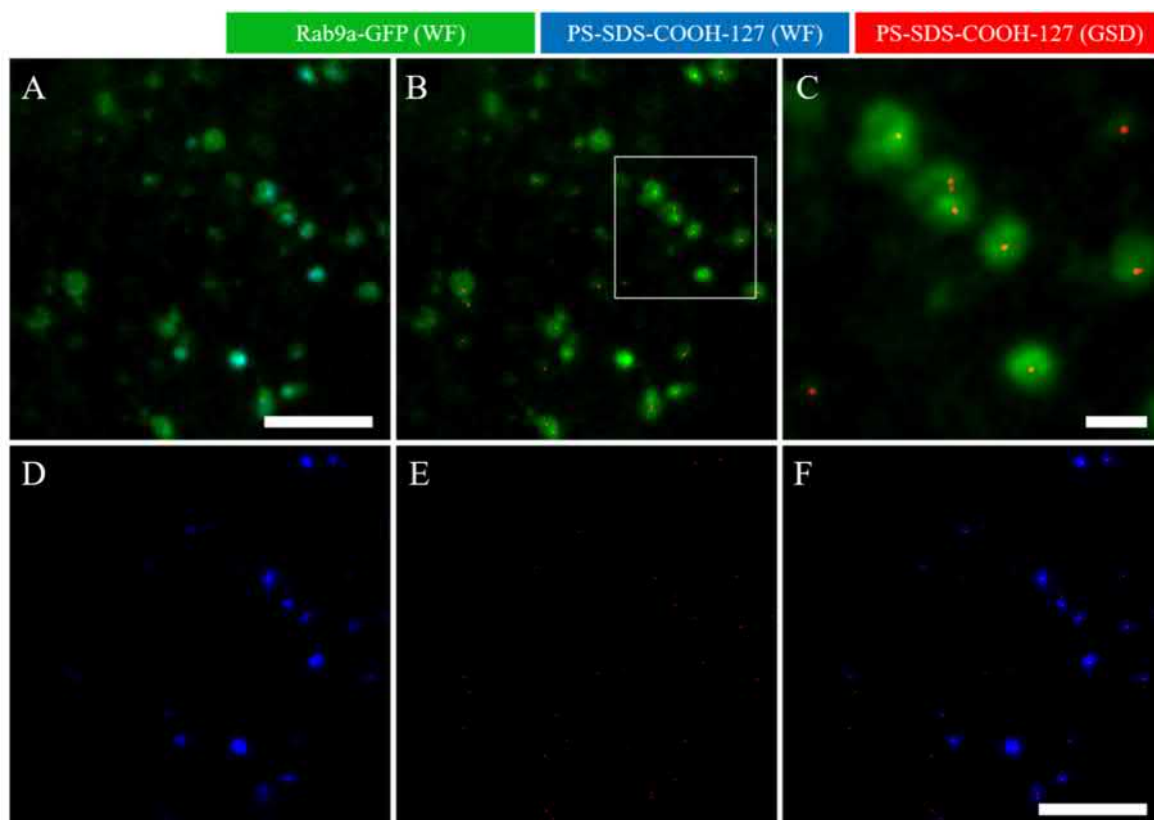
SI Fig. 36: Comparison of nanoparticle imaging via Widefield and high resolution GSD-Microscopy (Rab5a).

Caco-2 cells were incubated for 4 h in DMEM with FBS and 75 $\mu\text{g/mL}$ nanoparticles. (A) Overlay of Rab5a-GFP (WF) and PS-SDS-COOH-127 (WF). (B) Overlay of GFP (Widefield) and PS-SDS-COOH-127 (GSD). (C) Close up of Rab5a-GFP (WF) and PS-SDS-COOH-127 (GSD). (D) Nanoparticles in Widefield. (E) Nanoparticles in GSD mode. (F) Overlay of PS-SDS-COOH-127 in Widefield and GSD mode. Scale bar = 5 μm in (A), 1 μm in (C), 5 μm in (F).



SI Fig. 37: Comparison of nanoparticle imaging via Widefield and high resolution GSD-Microscopy (Rab7a).

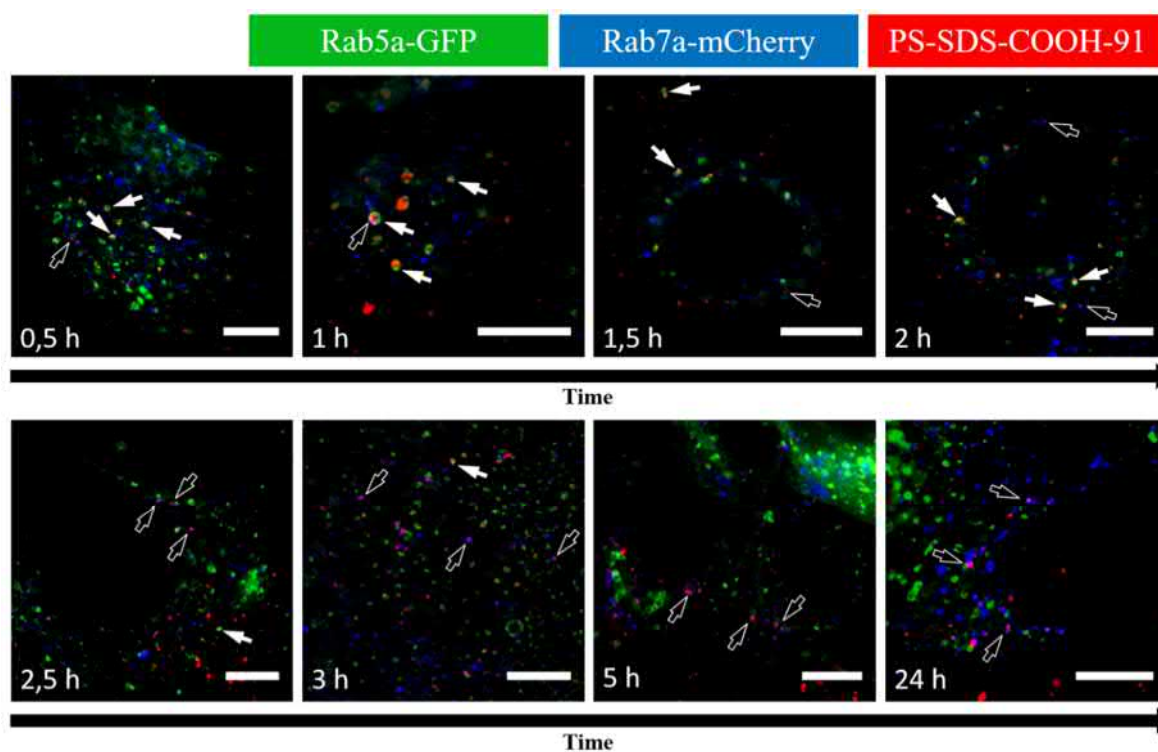
Caco-2 cells were incubated for 4 h in DMEM with FBS and 75 µg/mL nanoparticles. (A) Overlay of Rab7a-GFP (WF) and PS-SDS-COOH-127 (WF). (B) Overlay of GFP (Widefield) and PS-SDS-COOH-127 (GSD). (C) Close up of Rab7a-GFP (WF) and PS-SDS-COOH-127 (GSD). (D) Nanoparticles in Widefield. (E) Nanoparticles in GSD mode. (F) Overlay of PS-SDS-COOH-127 in Widefield and GSD mode. Scale bar = 5 µm in (A), 1 µm in (C), 5 µm in (F).





SI Fig. 38: Comparison of nanoparticle imaging via Widefield and high resolution GSD-Microscopy.

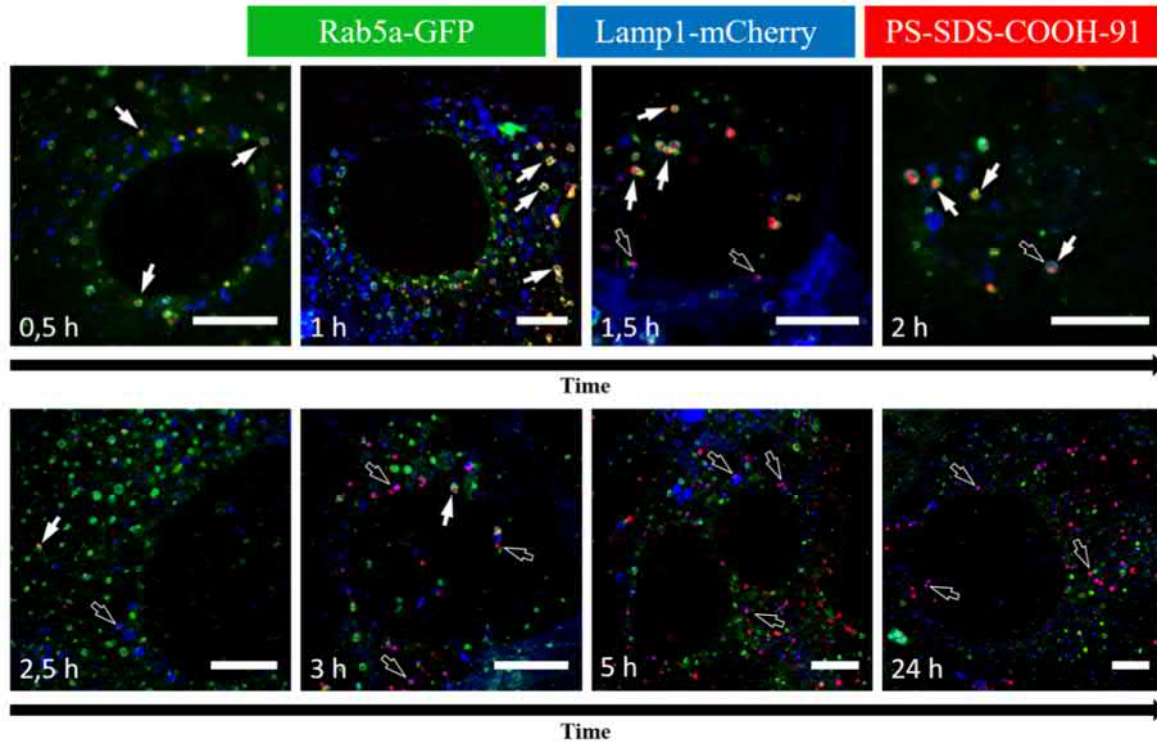
Caco-2 cells were incubated for 4 h in DMEM with FBS and 75 $\mu\text{g/mL}$ nanoparticles. (A) Overlay of Rab9a-GFP (WF) and PS-SDS-COOH-127 (WF). (B) Overlay of GFP (Widefield) and PS-SDS-COOH-127 (GSD). (C) Close up of Rab5a-GFP (WF) and PS-SDS-COOH-127 (GSD). (D) Nanoparticles in Widefield. (E) Nanoparticles in GSD mode. (F) Overlay of PS-SDS-COOH-127 in Widefield and GSD mode. Scale bar = 5 μm in (A), 1 μm in (C), 5 μm in (F).

7.17 Double transgenic cells


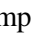


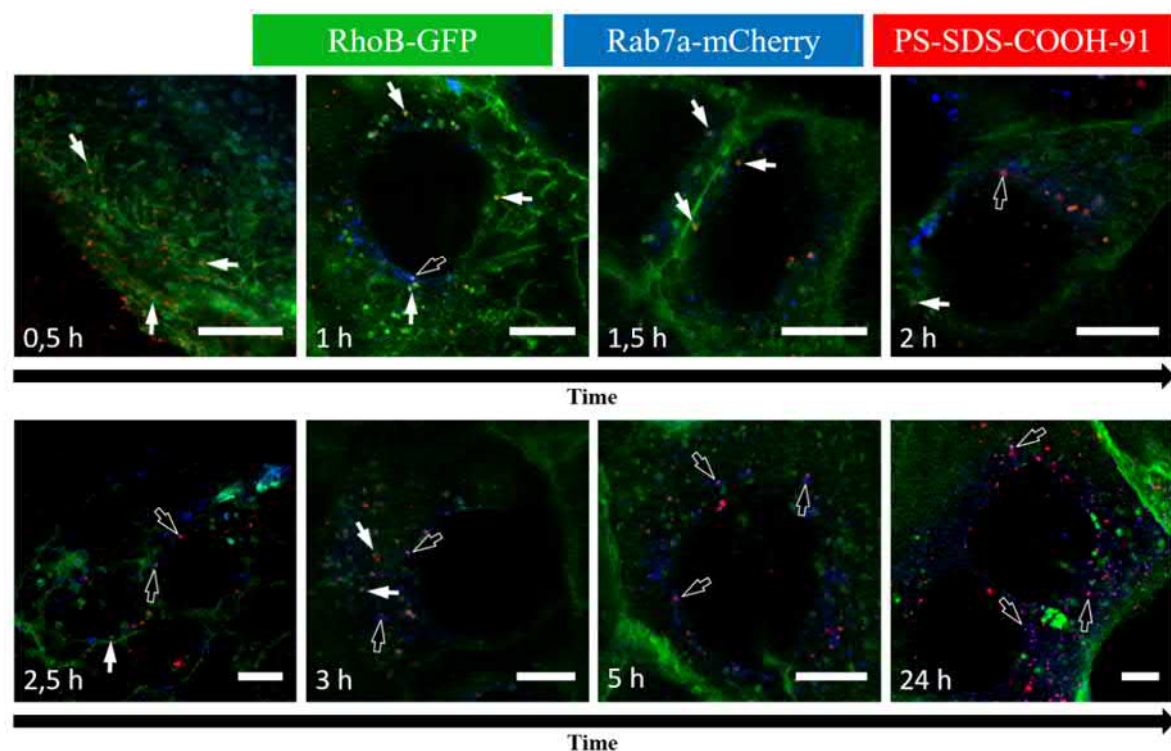
SI Fig. 39: Co-localization of polystyrene nanoparticles with Rab5a-GFP and Rab7a-mCherry.

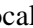
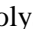
PS-NP started to co-localize with macropinocytosis marker Rab5a after uptake into Caco-2 cells. During the further monitoring, co-localization with Rab5a strongly decreased, while co-localization with late endosome marker Rab7a increased. After 24 h, nearly all of the nanoparticles are trapped in Rab7a positive vesicles.  = Co-Localization of Rab5a-GFP and polystyrene nanoparticles.  = Co-Localization of Rab7a and polystyrene nanoparticles. Scale bar = 10 μ m.



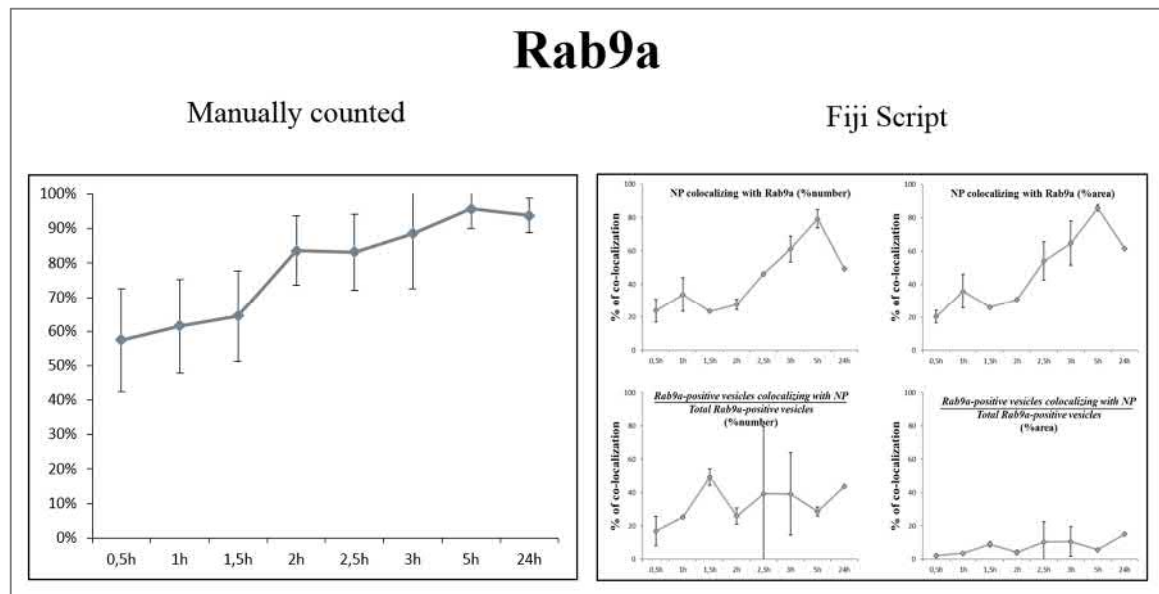
SI Fig. 40: Co-localization of polystyrene nanoparticles with Rab5a-GFP and Lamp1-mCherry.

Caco-2 cells were cultivated until they reached 100% confluence. 100 $\mu\text{g/mL}$ PS-SDS-COOH-91 were added into DMEM containing 10% FBS and cells were monitored for 0.5 – 24 h. After a maximum incubation time of 2 hours, cells were washed with PBS to eliminate any further nanoparticle uptake. EGFP-tagged proteins are pseudocolored in green, mCherry-tagged proteins are pseudocolored in blue and polystyrene nanoparticles are pseudocolored in red. Co-Localization of GFP and nanoparticles resulted in an orange color, while co-localization of mCherry and nanoparticles resulted in violet spots.  = Co-Localization of Rab5a-GFP and polystyrene nanoparticles.  = Co-Localization of Lamp1-mCherry and polystyrene nanoparticles. Rare co-localization between GFP and mCherry resulted in light blue color. Scale bar = 10 μm .



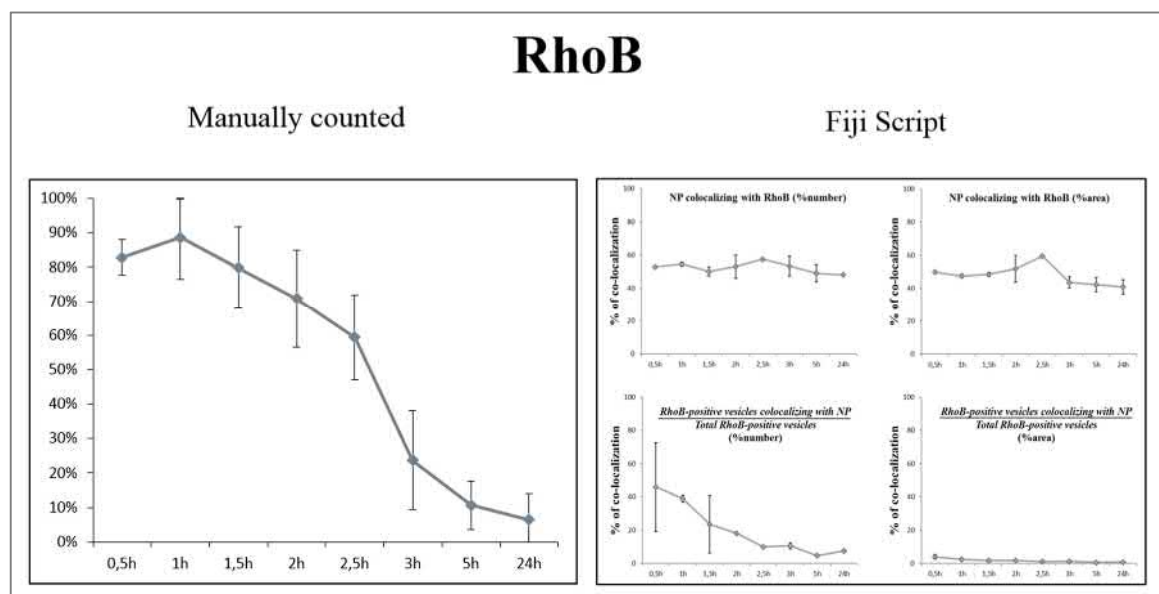
SI Fig. 41: Co-localization of polystyrene nanoparticles with RhoB-GFP and Rab7a-mCherry. PS-NP were internalized by a RhoB positive, putative macropinocytotic machinery. After 1.5 h, co-localization with RhoB strongly decreased and shifted to late endosome marker Rab7a. After 24 h, nearly 100% of the nanoparticles were trapped in Rab7a positive vesicles.  = Co-Localization of RhoB-GFP and polystyrene nanoparticles.  = Co-Localization of Rab7a-GFP and polystyrene nanoparticles. Scale bar = 10 μ m.

7.18 Fiji analysis



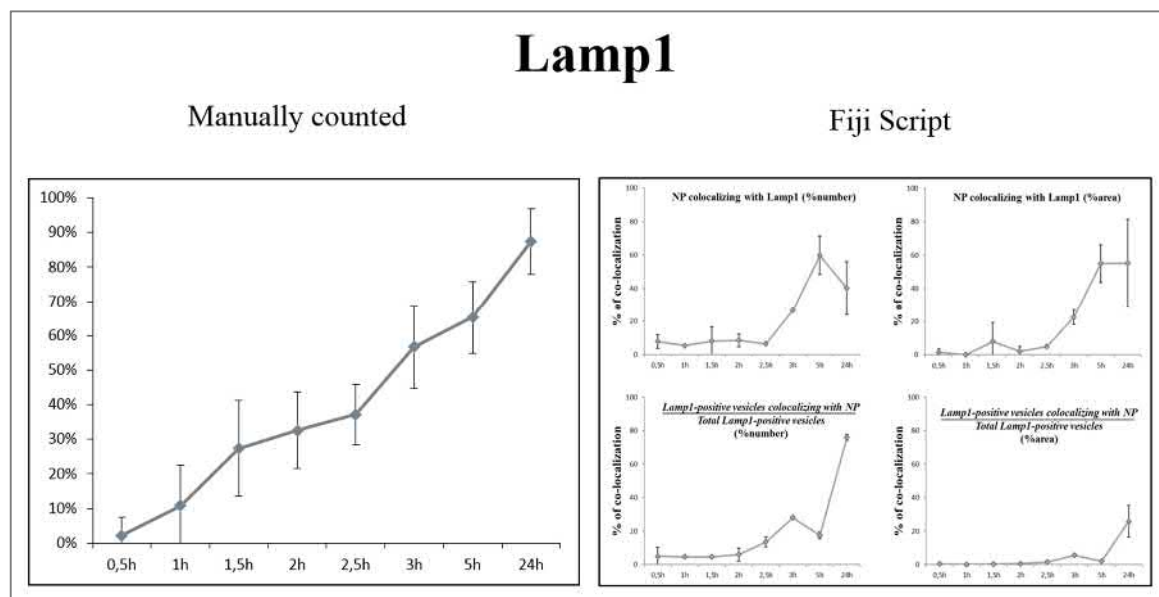
SI Fig. 42: Comparison of manually counted vs Fiji Script determined NP co-localization with Rab9a.

Tendency of Rab9a starting with a low level of co-localization which increased over time was confirmed via automatic counting using a Fiji Script. Automatic calculated relative percentages are possibly lower due to the fact that the script also counted nanoparticles on top and between cells which were not internalized.



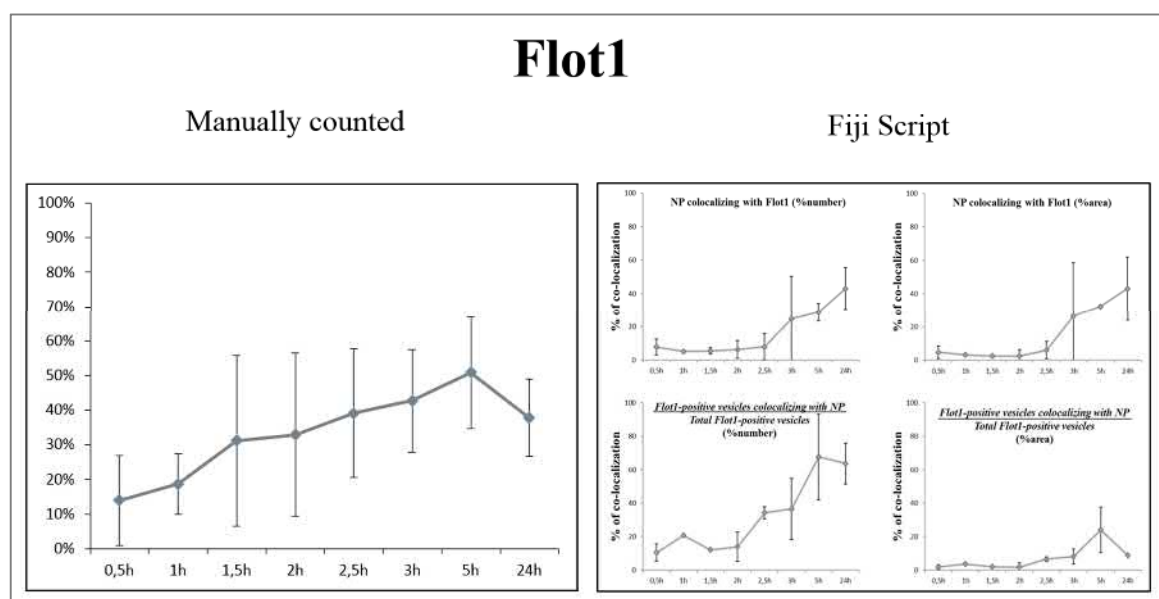
SI Fig. 43: Comparison of manually counted vs Fiji Script determined NP co-localization with RhoB.

Tendency of RhoB starting with a high level of co-localization which decreased over time was partially confirmed via automatic counting using a Fiji Script. Automatic calculated relative percentages are possibly lower due to the fact that the script also counted nanoparticles on top and between cells which were not internalized. RhoB signal and co-localization was difficult to detect due to the fact that RhoB is also part of the cell membrane and other compartments than vesicles.



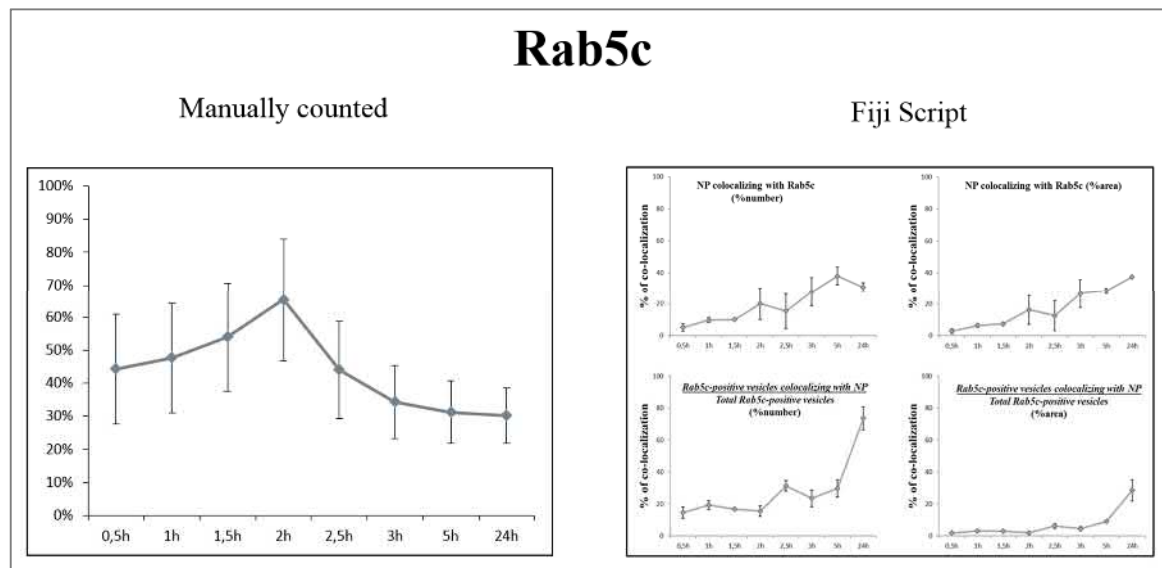
SI Fig. 44: Comparison of manually counted vs Fiji Script determined NP co-localization with Lamp1.

Tendency of Lamp1 starting with a low level of co-localization which increased over time was confirmed via automatic counting using a Fiji Script. Automatic calculated relative percentages are possibly lower due to the fact that the script also counted nanoparticles on top and between cells which were not internalized.



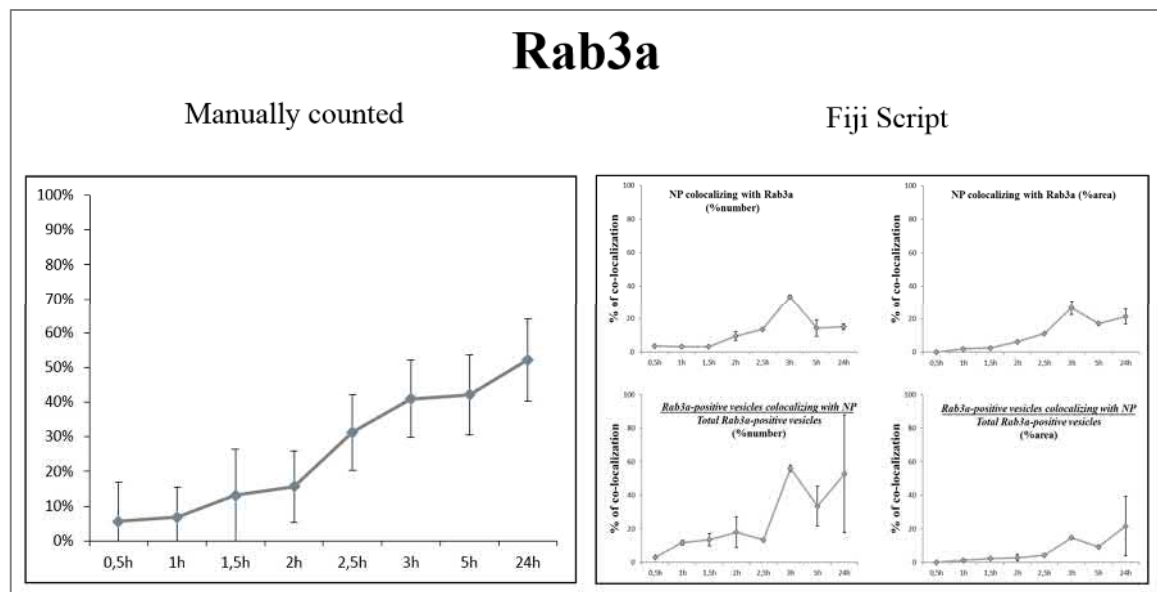
SI Fig. 45: Comparison of manually counted vs Fiji Script determined NP co-localization with Flot1.

Tendency of Flot1 starting with a low level of co-localization which increased over time with a minor peak at 5 h was partially confirmed via automatic counting using a Fiji Script. Automatic calculated relative percentages are possibly lower due to the fact that the script also counted nanoparticles on top and between cells which were not internalized.



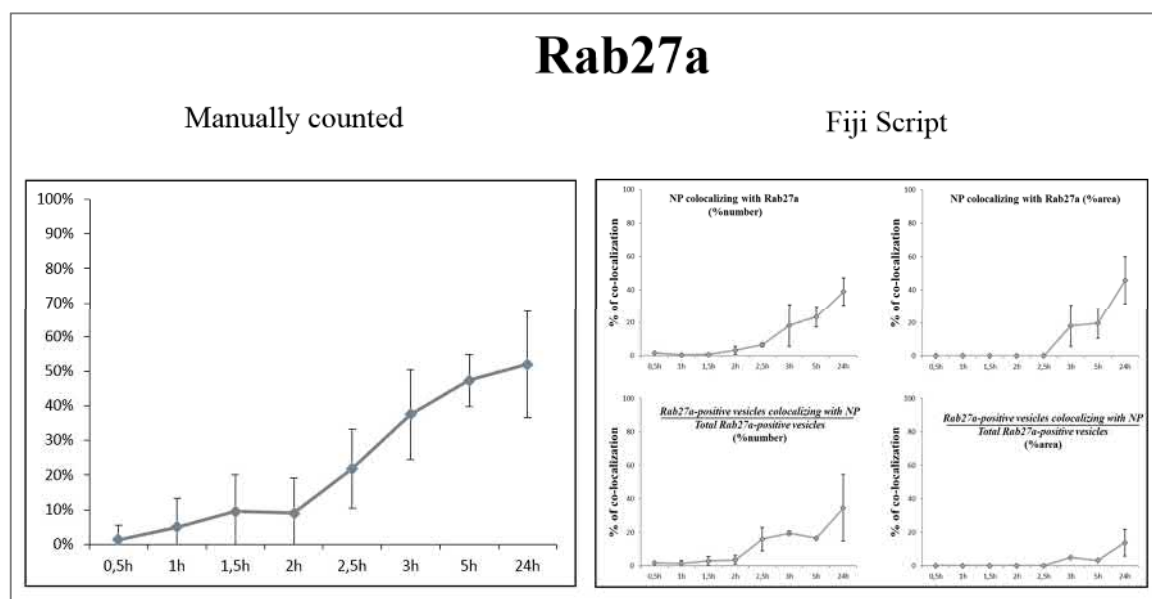
SI Fig. 46: Comparison of manually counted vs Fiji Script determined NP co-localization with Rab5c.

Tendencies of Rab5c co-localizations appeared slightly different via automatic counting using a Fiji Script. Instead a minor peak at 2 h, the script quantified co-localization as an increasing trend. Automatic calculated relative percentages are possibly lower due to the fact that the script also counted nanoparticles on top and between cells which were not internalized.



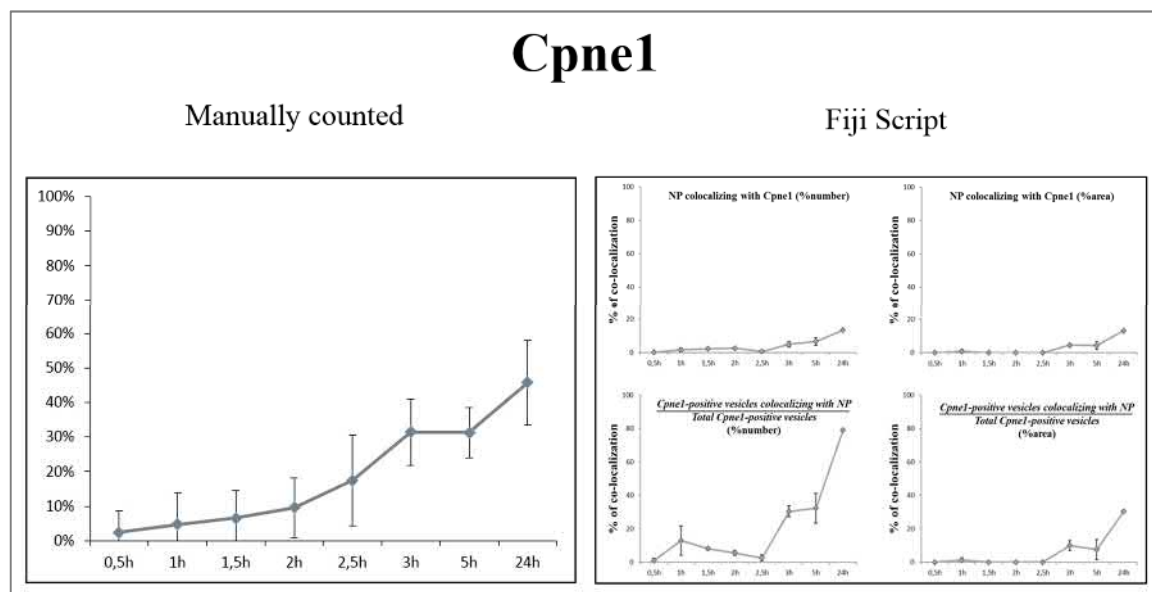
SI Fig. 47: Comparison of manually counted vs Fiji Script determined NP co-localization with Rab3a.

Tendency of Rab3a starting with a low level of co-localization which slowly increased over time was confirmed via automatic counting using a Fiji Script. Automatic calculated relative percentages are possibly lower due to the fact that the script also counted nanoparticles on top and between cells which were not internalized.



SI Fig. 48: Comparison of manually counted vs Fiji Script determined NP co-localization with Rab27a.

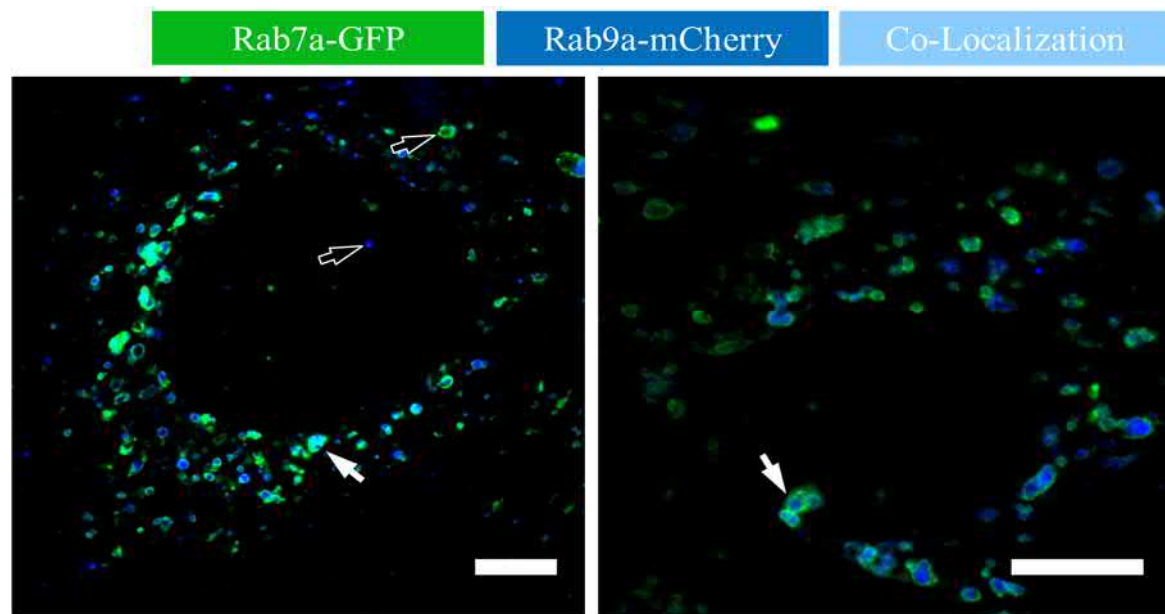
Tendency of Rab27a starting with a low level of co-localization which slowly increased over time was confirmed via automatic counting using a Fiji Script. Automatic calculated relative percentages are possibly lower due to the fact that the script also counted nanoparticles on top and between cells which were not internalized.




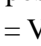
SI Fig. 49: Comparison of manually counted vs Fiji Script determined NP co-localization with Cpne1.

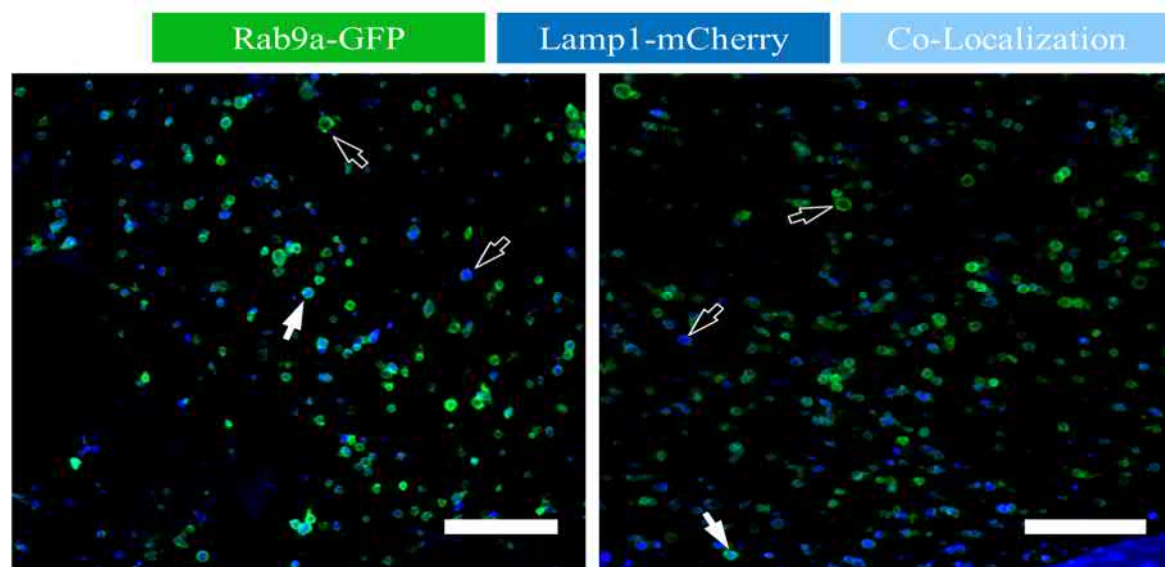
Tendency of Cpne1 starting with a low level of co-localization which slowly increased over time was confirmed via automatic counting using a Fiji Script. Automatic calculated relative percentages are possibly lower due to the fact that the script also counted nanoparticles on top and between cells which were not internalized.

7.19 Double transgenic cells without nanoparticles


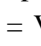


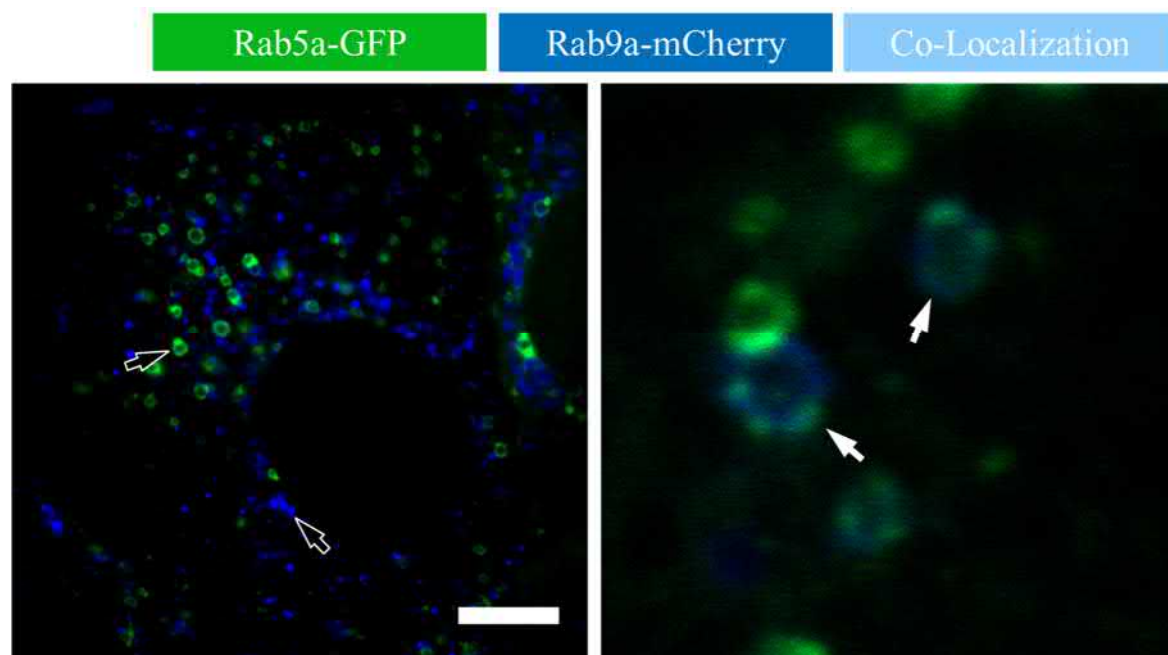
SI Fig. 50: Intracellular localization of Rab7a and Rab9a.

Late endosome markers Rab7a and Rab9a showed nearly the same localization. Virtually all vesicles positive for Rab7a were also positive for Rab9a and vice versa, explaining their similar nanoparticle co-localization profiles.  = Vesicles featuring co-localization between both marker proteins.  = Vesicles only positive for one of the marker proteins. Scale bar = 10 μ m.



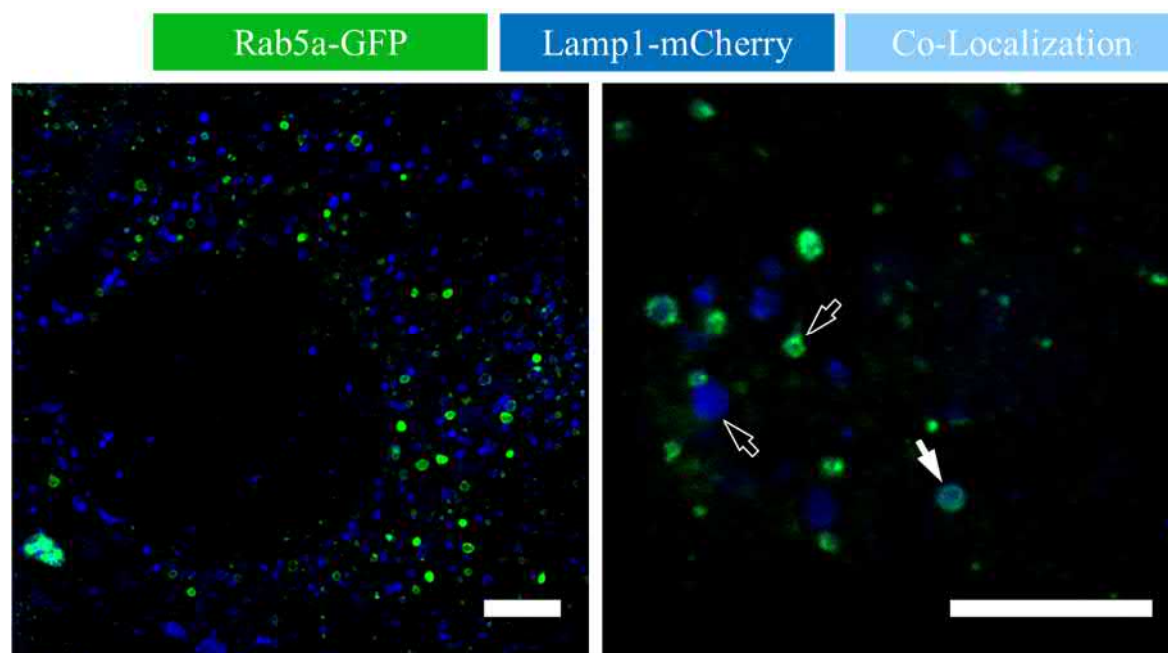
SI Fig. 51: Intracellular localization of Rab9a and Lamp1.

Approximately 50% of all Lamp1 positive vesicles were also positive for late endosome marker Rab9a (white arrows mark the three different variants).  = Vesicles featuring co-localization between both marker proteins.  = Vesicles only positive for one of the marker proteins. Scale bar = 10 μ m.


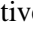


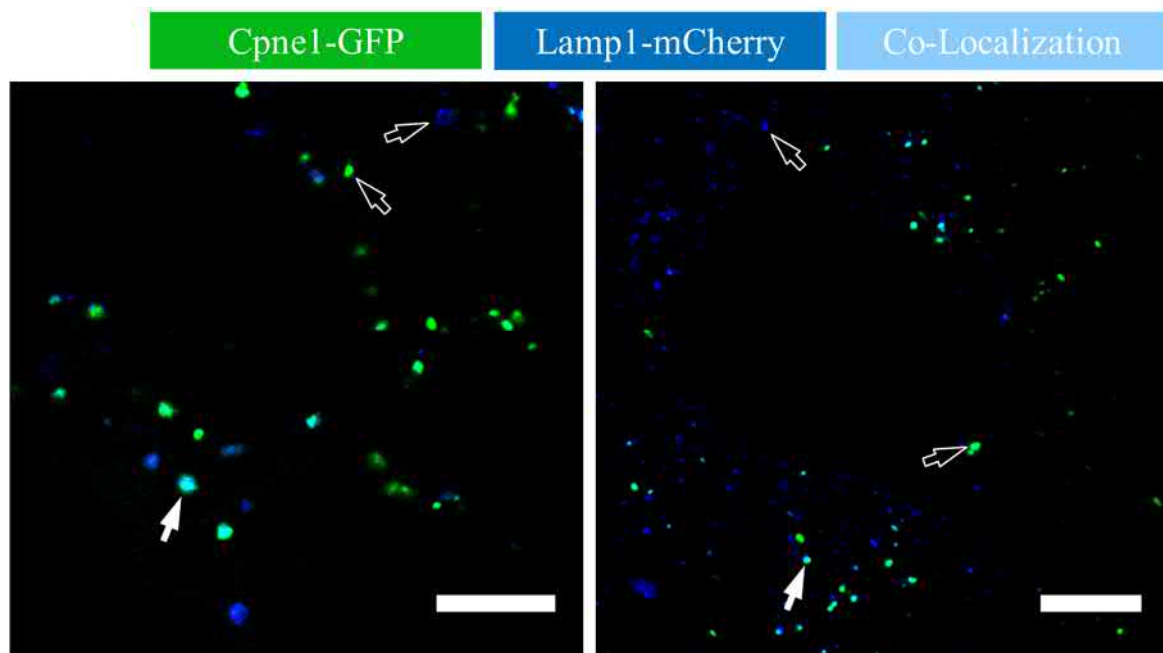
SI Fig. 52: Intracellular localization of Rab5a and Rab9a.

Rab5a and Rab9a showed nearly no co-localization. A few hybrid vesicles could be detected (white arrows). Scale bar = 10 μ m.



SI Fig. 53: Intracellular localization of Rab5a and Lamp1.

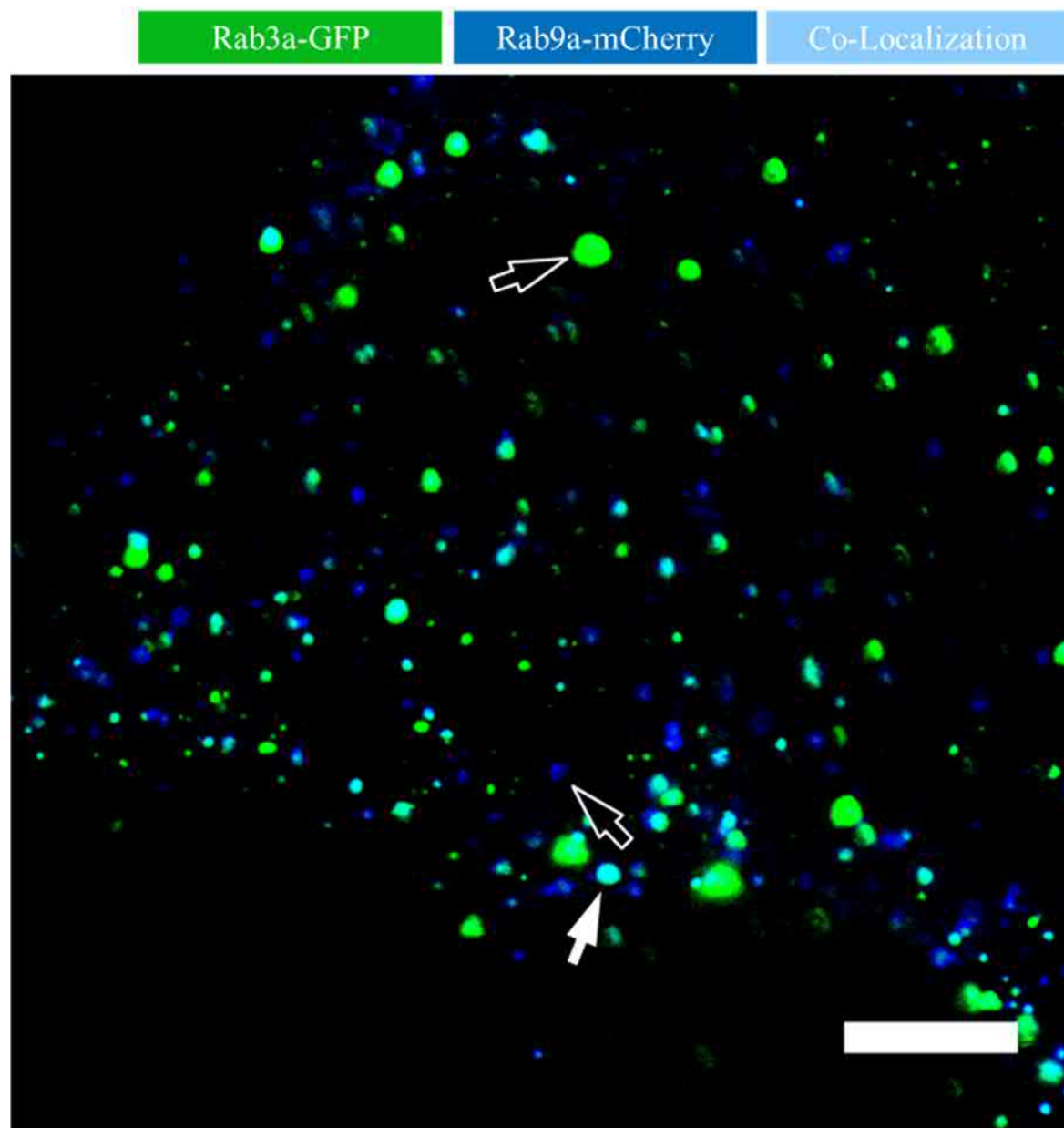
Rab5a positive and Lamp1 positive vesicles were also normally strictly separated. However, we were also able to detect hybrid vesicles (white arrows).  = Vesicles featuring co-localization between both marker proteins.  = Vesicles only positive for one of the marker proteins. Scale bar = 10 μ m.


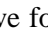


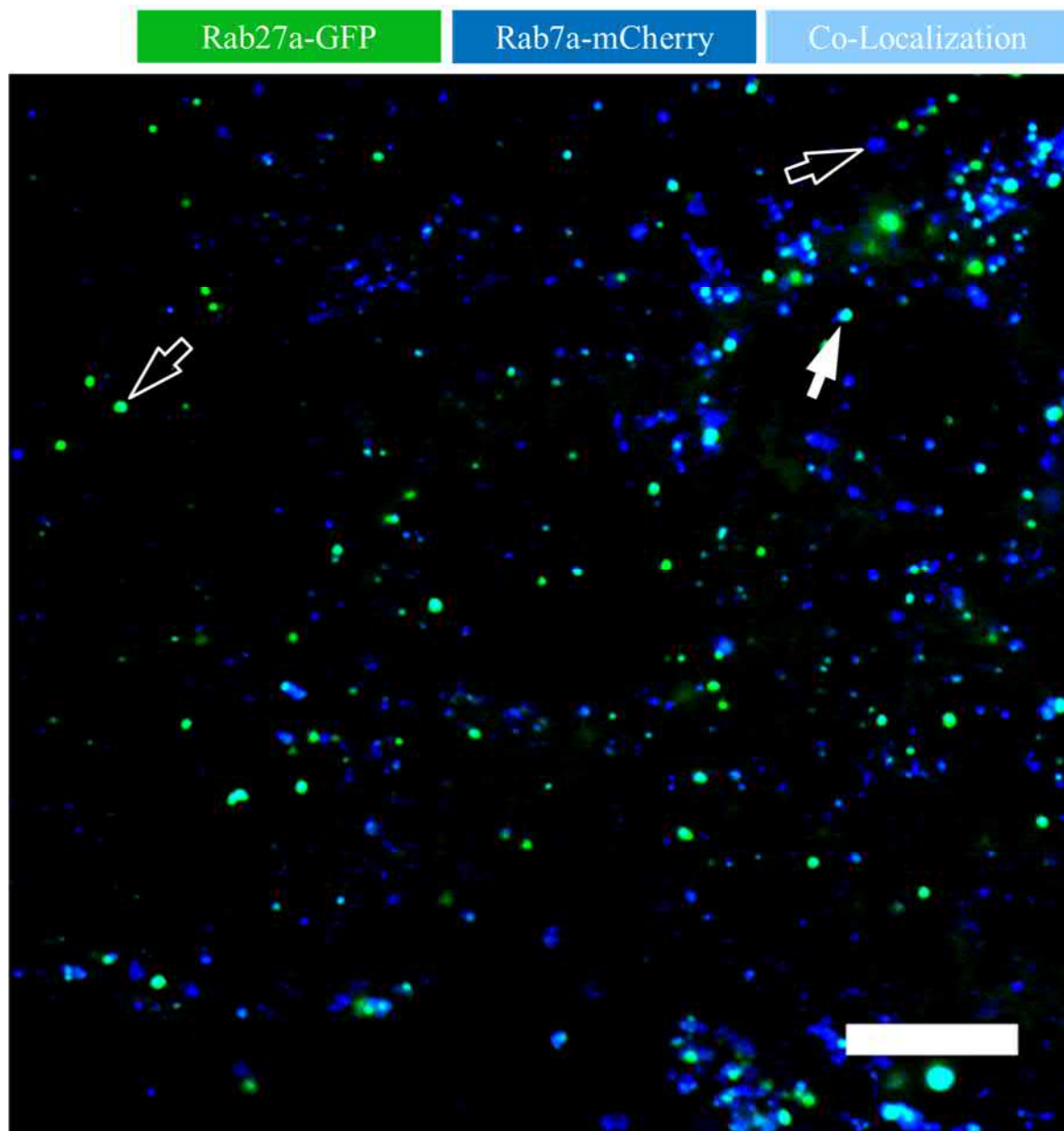
SI Fig. 54: Intracellular localization of Cpne1 and Lamp1.

Approximately 50% of Copine1 positive vesicles were also positive for lysosomal marker Lamp1.


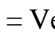
◼◼ = Vesicles featuring co-localization between both marker proteins. ◼◻ = Vesicles only positive for one of the marker proteins. Scale bar = 10 μ m.

**SI Fig. 55: Intracellular localization of Rab3a and Rab9a.**

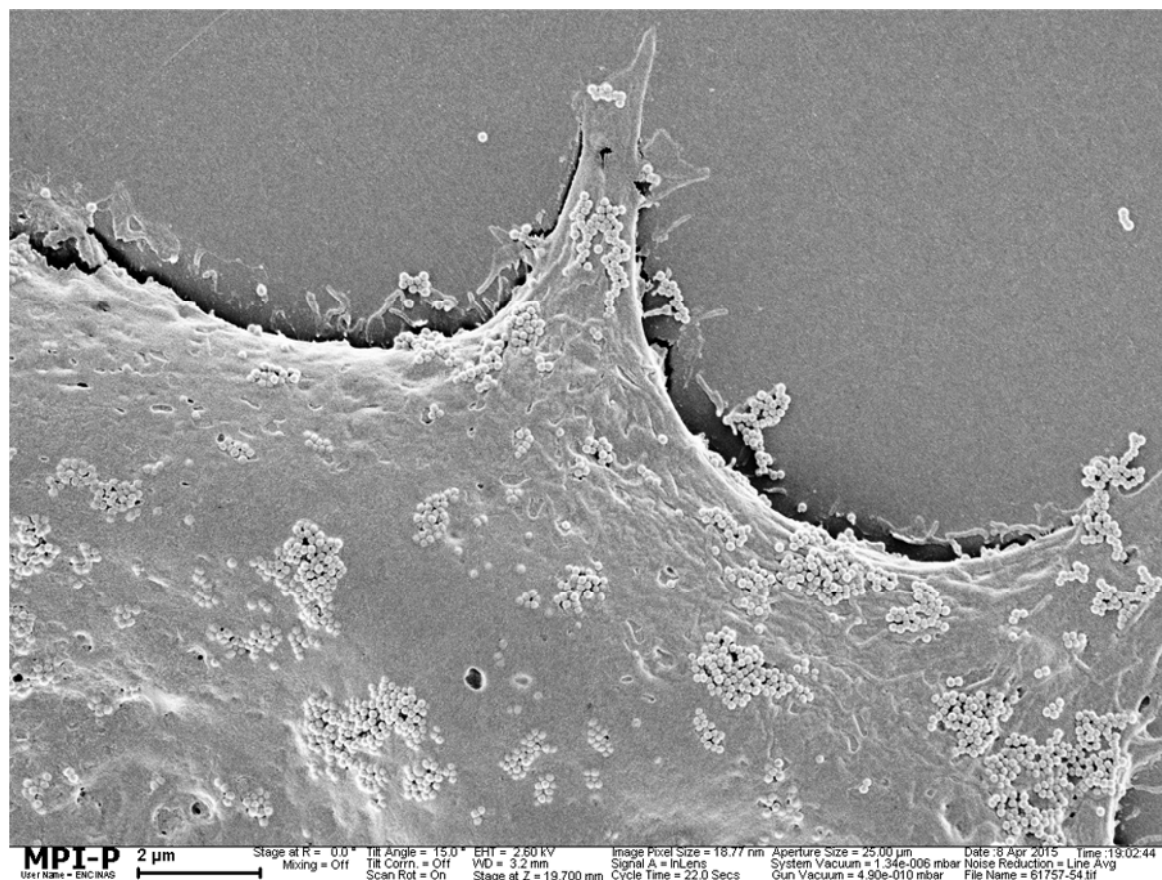
Approximately 50% of Rab3a positive vesicles were also positive for late endosome marker Rab9a. Some Rab3a positive vesicles were of huge size.  = Vesicles featuring co-localization between both marker proteins.  = Vesicles only positive for one of the marker proteins. Scale bar = 10 μm .



SI Fig. 56: Intracellular localization of Rab27a and Rab7a.

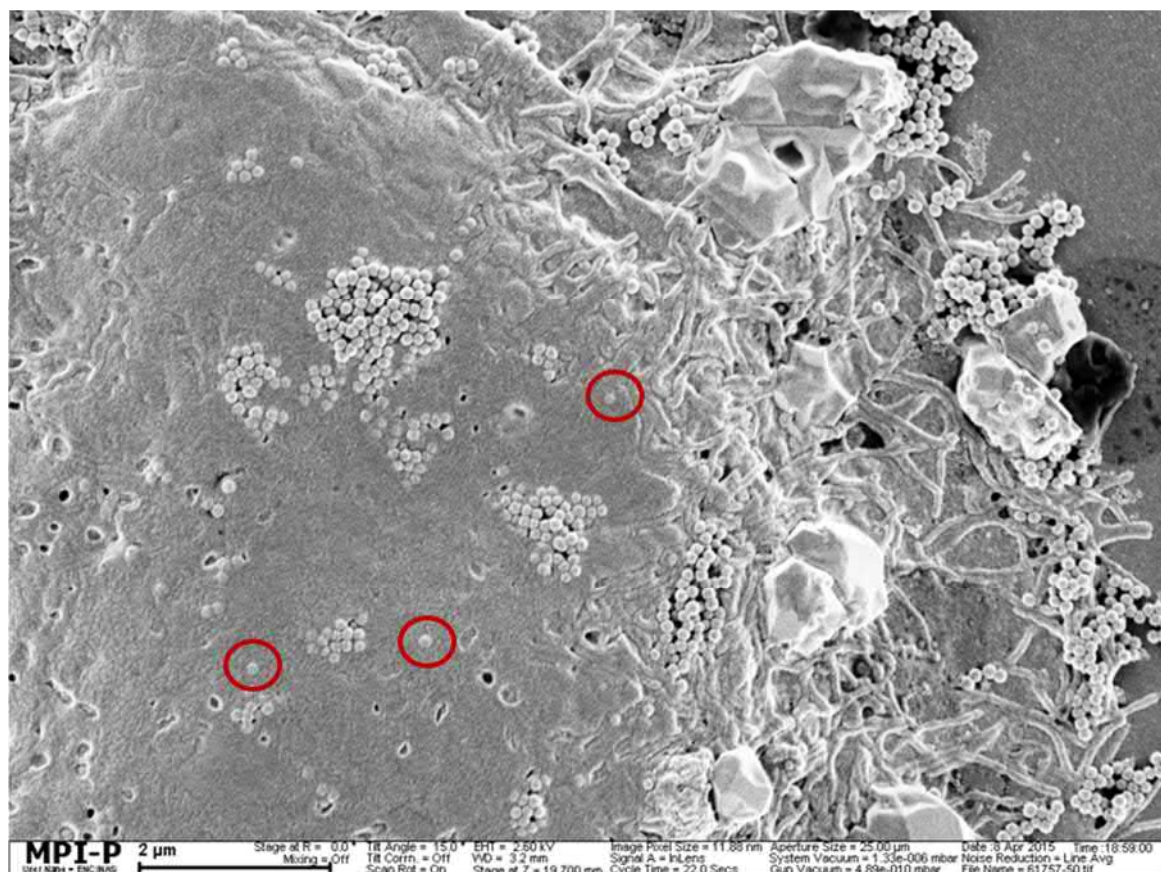
Approximately 50% of Rab27a positive vesicles also co-localized with late endosome marker Rab7a.  = Vesicles featuring co-localization between both marker proteins.  = Vesicles only positive for one of the marker proteins. Scale bar = 10 μ m.

7.20 Scanning electron microscopy



SI Fig. 57: Polystyrene nanoparticles adhered to the Caco-2 cell surface.

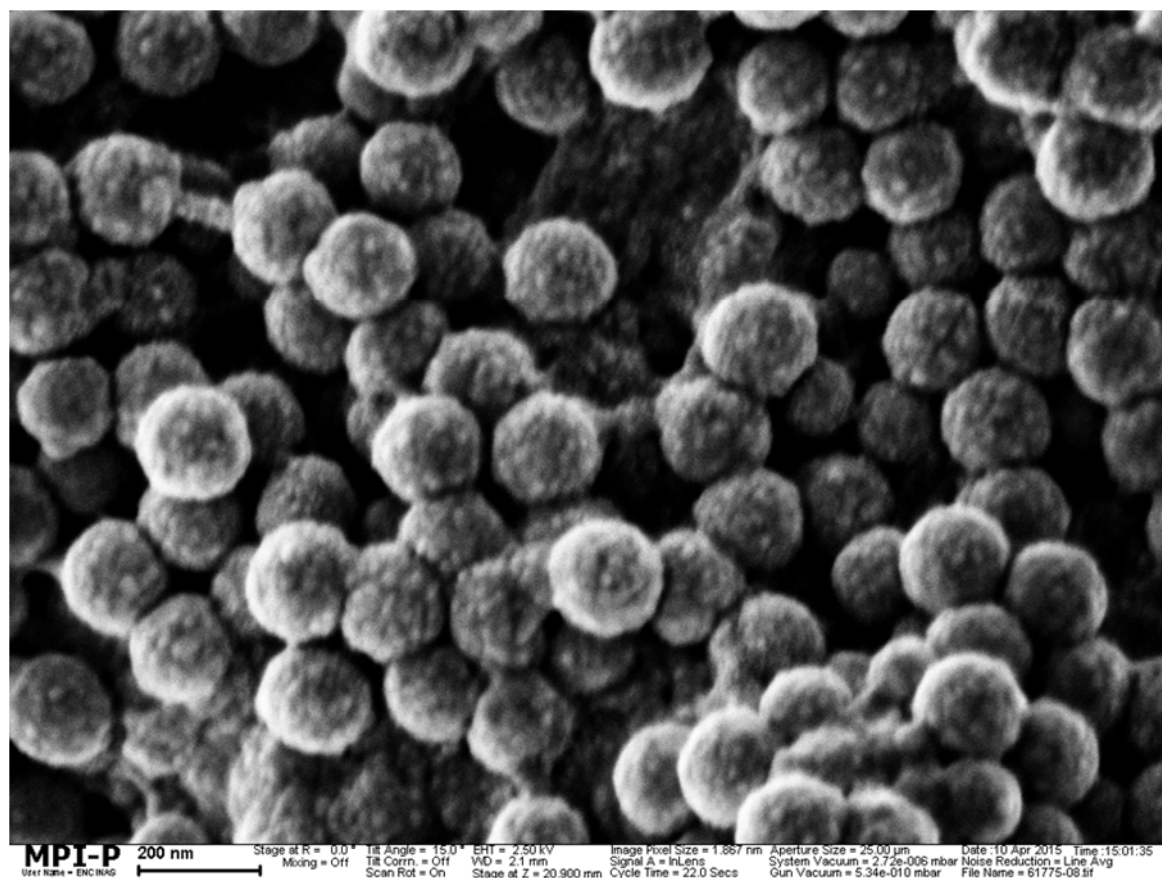
Cells were treated with 500 $\mu\text{g}/\text{mL}$ carboxylic polystyrene nanoparticles for 4 h and analyzed via scanning electron microscopy. Nanoparticle aggregates were mainly detected on the cell surface while several single nanoparticles were detected putatively internalized. Scale bar = 2 μm . Scanning electron microscopy was performed by Dr. Noemí Encinas García (Max Planck Institute for Polymer Research, Germany).



SI Fig. 58: Polystyrene nanoparticles adhered to the Caco-2 cell surface.

Cells were treated with 500 $\mu\text{g/mL}$ carboxylic polystyrene nanoparticles for 4 h and analyzed via scanning electron microscopy. Nanoparticle aggregates were mainly detected on the cell surface while several single nanoparticles were detected putatively internalized (red circles). Crystal structures were probably artefacts from SEM preparation. Scale bar = 2 μm . Scanning electron microscopy was performed by Dr. Noemí Encinas García (Max Planck Institute for Polymer Research, Germany).

7.21 Nanoparticles in cell culture medium



SI Fig. 59: Nanoparticles incubated in DMEM containing 10% FBS.

This figure depicts a scanning electron microscopy image of carboxylic nanoparticles incubated in DMEM with 10% FBS. Major clusters of nanoparticle aggregates could be observed. Scale bar = 200 nm. Scanning electron microscopy was performed by Dr. Noemí Encinas García (Max Planck Institute for Polymer Research, Germany).

7.22 Proposed KEGG-pathways of downregulated genes after ovalbumin-nanocapsule treatment

5 chart records [Download File](#)

Sublist	Category	Term	RT	Genes	Count	%	P-Value	Benjamini
	KEGG_PATHWAY	Bladder cancer	RT		4	1,6	2,0E-2	8,3E-1
	KEGG_PATHWAY	Neuroactive ligand-receptor interaction	RT		9	3,6	2,6E-2	6,9E-1
	KEGG_PATHWAY	Cell cycle	RT		6	2,4	3,1E-2	6,1E-1
	KEGG_PATHWAY	Cell adhesion molecules (CAMs)	RT		6	2,4	6,0E-2	7,5E-1
	KEGG_PATHWAY	Oocyte meiosis	RT		5	2,0	7,3E-2	7,4E-1

SI Fig. 60: Proposed KEGG-pathways of downregulated genes.

This figure depicts the KEGG (Kyoto Encyclopedia of Genes and Genomes)-pathways that were downregulated for murine BMDCs after (Adj)-Ova-nanocapsule treatment. Only genes that were at least downregulated by a factor of 2 were inserted into the analysis. The “count” column symbolizes the number of genes represented in the respective pathway. Analysis was performed with DAVID 6.7[276, 277].

8 Curriculum vitae

PERSONAL INFORMATION

Date of birth	13/10/1988
Place of birth	Mainz
Nationality	German

EDUCATION

07/2014 – 06/2018	PhD thesis <i>“Intracellular trafficking of polymeric nanocarriers in eukaryotic cells with emphasis on transcytotic processes”</i> Max-Planck-Institute for Polymer Research, Mainz
06/2013 – 02/2014	External Masterthesis <i>“Etablierung einer Methode für die genetische Untersuchung der hypervariablen D-Loop-Bereiche bei Katzen für den Einsatz in der kriminaltechnischen Fallarbeit”</i> Federal Criminal Police Office, Wiesbaden
04/2012 – 04/2014	M. Sc. in Biology Johannes Gutenberg-University, Mainz Overall grade: very good (1.0)
11/2011 – 04/2012	Bachelorthesis <i>“Untersuchung der intrazellulären Lokalisation des murinen und Quantifizierung der Expression des humanen Androglobins”</i> Institute of Molecular Genetics, Mainz
04/2009 – 08/2012	B. Sc. in Biology Johannes Gutenberg-University, Mainz Overall grade: good (1.6)

9 Publications

J. Reinholz, C. Diesler, S. Schöttler, M. Kokkinopoulou, S. Ritz, K. Landfester, V. Mailänder, Protein Machineries defining Pathways of Nanocarrier Exocytosis and Transcytosis, *Acta biomaterialia* 71 (2018) 432-443.

J. Reinholz, K. Landfester, V. Mailänder, The challenges of oral drug delivery via nanocarriers, Article accepted in *Drug Delivery* (2018). DOI: 10.1080/10717544.2018.1501119.

J. Reinholz, D. Paßlick, K. Piradashvili, S. Jiang M. Li, K. Landfester, V. Mailänder, RNA-Seq reveals upregulated pathways of dendritic cells after (adjuvant-filled) ovalbumin nanocapsule treatment, Manuscript in preparation (2018).

M. Tonigold, J. Simon, D. Estupinan, M. Kokkinopoulou, **J. Reinholz**, U. Kintzel, A. Kaltbeitzel, P. Renz, M. Domogalla, K. Steinbrink, I. Lieberwirth, D. Crespy, K. Landfester, V. Mailänder, Preadsorption of antibodies enables targeting of nanocarriers despite a biomolecular corona, Article accepted in *Nature Nanotechnology* (2018). DOI: 10.1038/s41565-018-0171-6.

S. Jiang, B.C. Ma, **J. Reinholz**, Q. Li, J. Wang, K.A. Zhang, K. Landfester, D. Crespy, Efficient nanofibrous membranes for antibacterial wound dressing and UV protection, *ACS applied materials & interfaces* 8(44) (2016) 29915-29922.

C. Yang, N. Encinas, F. Geyer, A. Kaltbeitzel, P. Baumli, **J. Reinholz**, V. Mailänder, D. Vollmer, H-J. Butt, Sub-micrometer sized roughness suppresses bacteria adhesion, Manuscript submitted to *Angewandte Chemie* (2018).

10 Affidavit

This doctoral thesis was carried out from 01.07.2014 till 30.06.2018 at the Max-Planck-Institute for Polymer Research under the supervision of Prof. Dr. Volker Mailänder and Prof. Dr. Katharina Landfester.

I herewith declare that this thesis *“Intracellular trafficking of polymeric nanocarriers in eukaryotic cells with emphasis on transcytotic processes”* was written without any unauthorized assistance and used only sources acknowledged in this work. The thesis has never been submitted to any other faculties.

Hereby, I accept the examination regulations of the Faculty of Biology (Johannes Gutenberg-Universität, Mainz).

City, Date

Jonas Reinholz

11 Acknowledgements

I am deeply grateful to Prof. Dr. Volker Mailänder and Prof. Dr. Katharina Landfester for giving me the opportunity to work in this interesting research field under their supervision and guidance.

Furthermore, I would like to thank PD Dr. Joachim Urban for the second expert opinion on my thesis.

A special thanks goes to Dr. Sandra Ritz, who performed the Ground State Depletion studies with me and assisted me with the automatic Co-localization analysis.

I acknowledge all other collaborators: Dr. Susanne Schöttler, Dr. Ketí Piradashvili, Dr. Shuai Shuai Jiang, Dr. Johanna Simon, Dr. Manuel Tonigold, David Paßlick, Christopher Diesler, Dr. Maria Kokkinopoulou and Dr. Noemí Encinas García.

I would also like to thank Katja Klein for nanoparticle synthesis.

My sincere thanks goes to the “Bio-group”, including Daniel, Susanne, Maria, Manuel, Marleen, Johanna, Jorge, Carole, David, Gabor, Artur, Adelina and Raweewan.

Thank you also my dear office colleagues Minghan, Shuai, Johanna, Carole, Kristin, Saman, Katta and Oksana.

Last but not least, I want to thank my family for always supporting and believing in me and my girlfriend Alexandra for suffering with me in the times of writing.